Gait and Morphology Optimization for Articulated Bodies in Fluids

David William Allen

Dissertation submitted to the Faculty of the
Virginia Polytechnic Institute and State University
in partial fulfillment of the requirements for the degree of

Doctor of Philosophy
in
Aerospace Engineering

Craig A. Woolsey, Chair
Muhammad R. Hajj
Mayuresh J. Patil
Michael K. Philen

July 12, 2016
Blacksburg, Virginia

Keywords: Bio-inspired Vehicles, Optimization, Averaging, Geometric Control
Copyright 2016, David William Allen

Gait and Morphology Optimization for Articulated Bodies in Fluids

David William Allen

(ABSTRACT)

This dissertation presents novel results related to the optimization of articulated bodies in fluids. This work is divided into three main components: input waveform optimization, pisciform locomotion and optimization, and bio-inspired flight. Novel contributions were developed for each of these topics and are presented herein.

The first topic is input waveform optimization, which was developed along with Dr. Sevak Tahmasian. The novel contributions presented in this dissertation relate to a new means of defining input waveforms to enable increased flexibility and the application of new cost functionals. The new definition relies on the use of truncated Fourier series to define input waveforms. With this definition, the free parameters for optimization problem are the Fourier coefficients, enabling very complex input waveforms to be considered. Two new cost functionals were considered: input energy and impulse. The input energy cost functional seeks to minimize the input "energy" in the traditional optimization sense. This should be interpreted as the signal energy. The impulse impulse cost functional seeks to minimize the integral of the absolute values of the inputs over one period. Sinusoids were proven to be the energy minimizing input waveforms. The truncated Fourier series definition of input waveforms was used to determine the optimal input waveforms for the input impulse function.

The next topic is pisciform locomotion and optimization. This work is divided into two parts: locomotion and optimization. The locomotion component focuses on the development of a new model for pisciform locomotion. This model uses multiple fins and peduncles to approximate the spectrum from undulatory to oscillatory locomotion. Apart from the structure of the model, novel contributions include a downwash model and a dynamic-feedback-inversion technique that defines the inputs the the dynamics of the group coordinates as the shape coordinates. The optimization technique is loosely based on the response surface technique. Using the optimization technique, the optimal families of gaits for various morphologies and choices of cost functional were determined. These families of gaits represent the optimal stroke amplitude and tail beat rate for traveling at desired speeds. After optimizing the gaits, it was determined that, regardless of the morphology or choice of cost functional, the optimal tail beat rate varied linearly with desired speed and the optimal stroke amplitude depended on the ratio of another linear function of speed with the tail beat rate.

The final topic is bio-inspired flight. This study takes the shape of an experimental study of the performance of an ornithopter. Wind tunnel tests were performed on an off-the-shelf model ornithopter whose electronics were replaced with standard laboratory equipment. These tests determined the forces acting on the ornithopter at different Reynolds numbers, flapping frequencies, and angles of attack. The results of these tests were placed in a conventional aircraft performance framework, which yielded novel results. Most notably, by placing the ornithopter in a conventional framework the effect of changing the reduced frequency of the flapping can be considered as both a thrust generating and a lift enhancement mechanism. This purposefully obfuscates many of the interesting unsteady phenomena that occur during flapping flight to yield something of practical value: a means of approximately describing the performance of an ornithopter in a framework that is approachable for a wide community.

This work was supported by the NSF grant No. CMMI-1435484

Gait and Morphology Optimization for Articulated Bodies in Fluids

David William Allen

(GENERAL AUDIENCE ABSTRACT)

The contributions of this dissertation can be divided into three primary foci: input waveform optimization, the modeling and optimization of fish-like robots, and experiments on a flapping wing robot. Novel contributions were made in every focus.

The first focus was on input waveform optimization. This goal of this research was to develop a means by which the optimal input waveforms can be selected to vibrationally stabilize a system. Vibrational stabilization is the use of high-frequency, high-amplitude periodic waveforms to stabilize a system about a desired state. The contributions presented herein develop a technique to choose the "best" input waveform and a discussion of how the "best" input waveform changes with the definition of "best."

The next focus was the optimization of a fish-like robot. In order to optimize such robots, a new model for fish-like locomotion is developed. An optimization technique that uses numerous simulations of fish-like locomotion was used to determine the best gaits for traveling at various speeds. Based on these results, trends were found that can determine the optimal gait using a couple relatively simple functions.

The final focus was experimentation on a flapping wing robot in a wind tunnel. These experiments determined the performance of the flapping wing robot at a variety of flight conditions. The results of this research were presented in manner that is accessible to the larger aircraft design community rather than only to those specializing in flapping flight.

Acknowledgments

I would first like to thank my advisor, Dr. Craig Woolsey, for all of his support. I began researching under Dr. Woolsey as an undergraduate and continued through my MS and now my PhD. In addition to helping me to secure funding for my graduate studies, Dr. Woolsey provided consistent advice that made me a better writer, researcher, and scholar.

I would also like to thank my committee members: Dr. Muhammad Hajj, Dr. Michael Philen, and Dr. Mayuresh Patil. All of my committee members provided me advice and guidance that substantially improved my research. In addition to my current committee, I would also like to thank the members of my MS committee, Dr. Leigh McCue-Weil and Dr. William Moore, for their support during the early part of my graduate work.

In addition to my committee members, I would like to thank the faculty of the departments of Aerospace and Ocean Engineering (AOE), Mechanical Engineering (ME), Biomedical Engineering And Mechanics (BEAM), and Mathematics for the numerous classes courses that provided me with the knowledge that proved invaluable for my research and that will serve me well in the years to come. I would also like to thank the staff of the AOE department, BEAM department, and the Graduate School for their assistance in handling the (sometimes confusing) procedures necessary to complete a graduate education.

Furthermore, I would like to thank my friends and family for their love and support. Without their assistance, this dissertation would not be possible. I would also like to thank my research collaborators. Through interactions with and advice from my collaborators, my research became immeasurably better.

Lastly, I would like to thank all of the groups that have sponsored my graduate education. My MS was primarily funded by NASA Innovative Advanced Concepts.[a] During the first portion of my PhD research, my graduate education was sponsored through Virginia Tech's Technology-enhanced Learning and Online Strategies (TLOS) group (for work developing an online course) and through the Department of Engineering (for working as the instructor of a course for freshman engineers). The latter portion of my graduate education was sponsored by the National Science Foundation.[b] Finally, I would like to thank the Virginia Space Grant Consortium for providing me with a fellowship to supplement my graduate education.

[a]Under grant NNX12AR07G
[b]Under grant CMMI-1435484

Contents

List of Figures

List of Tables

Chapter 1

Introduction

As the title of this dissertation is "Gait and Morphology Optimization for Articulated Bodies in Fluids", a useful first step is to fully parse the meaning of the title. The term "articulated bodies" provides a structure for the systems of interest. Articulated bodies are multi-body mechanical systems where the bodies are joined by rotational joints. Articulated bodies can be thought of as skeletal bodies. One of the best example of an articulated body is the skeletal body of vertebrates. The motion of a skeleton is prescribed by muscle movements that rotate the bones of the skeleton with respect to each other.

Placing the articulated bodies in fluids provides a setting for the bodies to generate forces. Since the body is in a fluid, it cannot contact a hard surface, and, therefore, all forces must be aero/hydrodynamic in nature. Thus, when considering the motion of articulated bodies in fluids, aero/hydrodynamic effects are paramount.

When designing articulated bodies, there are two primary design categories: morphology and gait. The morphology typically refers to the biological study of the physical form and structure of animals, but is used herein to refer to the form and structure of any articulated body. Of particular interest is the size and shape of components whose primary purpose is the production of aero/hydrodynamic forces. The gait of an articulated body refers to the periodic motion of the body. Gait is more commonly used to refer to the sequence of foot-falls for walking or running. For example, "walk", "trot", "cantor", and "gallop" are four distinct gaits that horses naturally exhibit, although they are capable of others through training. When discussing articulated bodies in fluids, gait refers to the movement of the joints that produces the desired aero/hydrodynamic forces.

So now the meaning of the title, "Gait and Morphology Optimization for Articulated Bodies in Fluids", is more clear. The purpose is of this document is to describe techniques by which the "best" morphology and gait can be chosen for animal-like systems that are flying or swimming. These tools will provide a framework for the preliminary design of vehicles that fly or swim. The aim is to rapidly explore the design space, deferring the challenge of detailed design optimization (using conventional, but costly high fidelity modeling tools) until a promising candidate design has been identified using lower fidelity methods.

There is currently significant interest in building small unmanned vehicles. Small, remotely-piloted aerial vehicles in particular have risen in popularity for both civilian and military applications over the past several years. Additionally, interest in unmanned aerial and underwater vehicles has also risen. Most current designs are based on conventional vehicles, e.g. submarines, fixed-wing aircraft, and rotorcraft.[a] These systems all have dedicated propulsion systems and are not articulated bodies. Unmanned systems have several benefits over piloted systems. They are able to enter environments where it may be dangerous or impossible to send a person.

To date, the primary driver for studying articulated bodies in fluids has been improved performance, efficiency, or robustness. Additionally, since articulated bodies move in animal-like ways, it is possible for these vehicles to operate in areas without arousing suspicion. This ability to "hide in plain sight" is one of the primary technology development drivers from the defense community, but there are potential civilian applications. There may be applications where companies and government agencies could benefit from aerial observations, but do not wish to unduly disturb the people they serve.

This dissertation is divided into several sections. This introductory chapter presents background and motivation for the research, as well as mathematical preliminaries needed for later work. The next chapter provides a description of the input waveform optimization technique that was developed in collaboration with Dr. Sevak Tahmasian. The two subsequent chapters develop a model for bio-inspired aquatic locomotion and a new optimization technique for the simultaneous gait and morphology optimization of aquatic locomotion. Finally, a chapter describing experiments on a model ornithopter is presented.

Much of this work was completed as part of a collaborative research group. Complementary efforts by collaborators are explicitly acknowledged throughout the dissertation.

1.1 Literature Review

Some of the earliest attempts at powered flight were ornithopters, vehicles that emulated the flight of birds. These attempts were failures, and most of the development of powered flight has focused on fixed wing vehicles and rotorcraft. Today, however, technology has progressed to the point where developing small ornithopters on the scale of birds and insects is practical. Prior to discussing the development of man-made devices, the related literature from biology will be discussed. The author divides the biological research into three approaches: allometry,

[a] Also growing in popularity are underwater gliders, which are an appealing system for many interesting scientific applications. The use of underwater gliders with the added capability of swimming as an articulated body was the topic of the author's Master of Science Thesis. See Allen et al. [2013a,b,c, 2015]; Allen [2014] for more information.

energetics, and biomechanics. Allometry attempts to finds trends in the morphology of animals with respect to physical behaviors. Energetics analyzes locomotion as an energy balance. Biomechanics is used to refer to the approach where the performance is evaluated by detailed analysis of the system dynamics. These three approaches all have their respective merits and demerits, and some studies have characteristics of multiple approaches.

Many of the early related studies were biological studies of the allometry of flying animals. [Greenewalt, 1962] provides a comprehensive collection of much of the data collected in the late nineteenth and early twentieth centuries.[b] [Greenewalt, 1962] is representative of the allometry approach to understanding the flight of animals. This approach attempts to identify trends that represent the "design" of flying animals. Farney and Fleharty [1969]; Norberg [1981] perform allometric analysis on bats and compare the results for bats to birds. Brower and Veinus [1981]; Corben [1983]; Hazlehurst and Rayner [1992]; Hedenstrom and Moller [1992]; Morgado [1987]; Warham [1977] also use this methodology. Greenewalt [1975] shows that aerodynamic effects dominate dimensional similarities for birds. Pennycuick [1983] shows the limitation of allometry: the morphology of birds is the product of evolution, not design. Pennycuick [1983] provides the example of three dissimilar species of tropical birds that show the same behavior: thermal soaring. This shows that there are dissimilar "designs" that can achieve similar performance. Thus, the capabilities of a flying animal are determined by more than the morphology. One of the advantages of allometry is that it does not require a living specimen to study the flight of an animal. Therefore, it can be applied to extinct animals to gain an understanding of how they flew [Alexander, 1994; Brower and Veinus, 1981; Hazlehurst and Rayner, 1992]. Hazlehurst and Rayner [1992] provides a striking example of this capability. Although we cannot know the exact shape of the wings of pterosaurs because soft tissues are rarely preserved during fossilization, we can use approximations to roughly describe their flight. Hazlehurst and Rayner [1992] show that pterosaurs tended to be slow, highly efficient and maneuverable flyers with good soaring performance. They were also unlikely to be able to fly underwater like diving birds, such as auks. Hazlehurst and Rayner [1992] also show the limitations of using allometry to study extinct animals; all of the pterosaurs studied were found in marine or lagoonal sediments and none showed arboreal adaptations. It is not possible to determine from allometric analysis that the lack of observed arboreal adaptations is the result of limitations of pterosaur adaptation or a selection effect due to the preferential preservation of non-arboreal pterosaurs.

Another approach used to understand the flight of animals is by analyzing the power requirements for different flight strategies. Wilkie [1959] provides an early, interesting, tangential study of this topic; their goal is to study the question "why can't large mammals (e.g. humans) fly?" The solution is that, as the size of the animal increases, the power generation capability increases at a slower rate than the power required for flight. The power/energetic approach is very useful for describing why certain morphologies correspond to certain flight

[b]Importantly, the data is published in tables, which enabled the extraction of the data. Many contemporary studies simply cite private data sets and present only figures, making replication and data extraction impractical.

strategies. Adams et al. [1986]; Aldridge [1988]; Berg and Rayner [1995]; Berman and Wang [2007]; Ellington [1985]; Frasier [1984]; Hedenstrom and Alerstam [1995]; Weis-Fogh [1972, 1973] take this approach.

A final approach, which is primarily used in this research, is to directly analyze the mechanics of the systems. The "Aerodynamics of Hovering Insect Flight" series, Ellington [1984a,b,c,d,e,f], presents a comprehensive example of this technique. This series also demonstrates how the allometry and energetics techniques can be used to inform further study. [Ellington, 1984f] is a study of allometry and [Ellington, 1984d] is an energetics study. As using the biomechanics approach requires the dynamics of the system to be considered, the chosen models are very important. In general, there are three broad classes of models for the biomechanics approach: system-level, quasi-steady, and unsteady. System-level analyses tend to be used to provide quick estimates of performance as in Weis-Fogh [1973], but can also be more detailed. One system-level technique analyzes flight by using the interaction of shed vortexes such as in [Rayner, 1979]. This has proven to be a fruitful approach and is used in later studies [Ellington, 1984b; Sane, 2003; Taylor et al., 2003]. Unsteady analysis is the most complicated biomechanics approach because the models used are significantly more complex than those used for system-level or quasi-steady analysis. Studies using unsteady analysis tend to be more explanatory than predictive. That is, unsteady biomechanics rely primarily on experiment [Tian et al., 2006; Tobalske et al., 2007; van den Berg and Ellington, 1997] or computational fluid dynamics [Liu et al., 1998] to describe the behavior of real-world systems. The results of these studies can be applied to new systems to provide predictive capabilities, but this is a difficult and time consuming process. The final approach is quasi-steady aerodynamics. This approach assumes that the motion of the wings does not affect the aerodynamics apart from local velocity changes. This is a very common approach and is used in Dhawan [1991]; Ellington [1984a,c]; Morgansen et al. [2007] among others. This research will primarily use this quasi-steady approach because it results in equations of motion that are amenable to the geometric averaging technique that will be described in Section 1.2.2.

1.1.1 Pisciform Locomotion

For the type of analysis presented in this dissertation, the models used for describing pisciform (or "fish-like") locomotion are less complicated than those used for aerial locomotion. There is significant nuance in the specifics of fish locomotion, including location, quantity, and shape of fins, but the author is primarily concerned with fish that propel themselves with body and caudal fin movements, rather than fish that use their pectoral fins. Webb [1984] provides a summary of the types of fish locomotion. In general, fish locomotion occurs on a spectrum from undulatory to oscillatory locomotion. Undulatory locomotion is characterized by approximately continuous waves propagating along the body, while oscillatory locomotion is characterized by a few more rigid segments moving relative to each other.

Sfakiotakis et al. [1999] provide a detailed overview of fish locomotion. For Body and/or Caudal Fin (BCF) propulsion, there are five swimming modes. Listed in order of the most undulatory to most oscillatory, these swimming modes are anguilliform, subcarangiform, carangiform, thunniform, and ostraciiform. In anguilliform locomotion the entire body undergoes large amplitude lateral undulations to create a standing wave propagating along the body with a wavelength less than the length of the body. The most common example of anguilliform locomotion is eels. Anguilliforms tend to be slow moving and highly maneuverable. By changing the direction of the wave propagation, anguilliforms are capable of swimming backwards. Subcarangiform locomotion is similar to anguilliform locomotion, but the amplitude of the lateral undulations is smaller at the anterior, only becoming large in the posterior half of the body. Carangiform locomotion further restricts lateral undulations to the posterior third of the body. Fish that use carangiform locomotion typically have a relatively stiff caudal tail, which provides additional thrust. In thunniform locomotion, lateral movements are mostly restricted to a stiff tail. In general, as the locomotion goes from more undulatory to more oscillatory, fish become faster and more efficient at the cost of maneuverability. Breaking this trend is ostraciiform locomotion, which is characterized by a fairly rigid body and tail and is the most oscillatory form of locomotion. Typically, fish utilizing ostraciiform locomotion use their medial or pectoral fins for low speed maneuvering and use their caudal fin as an auxiliary thrust generator for specific circumstances.

Much of the research into the design of swimming vehicles focuses on carangiform locomotion. Kelly et al. [1998] developed a model that approximates carangiform locomotion as three articulated rigid links: a body, a small peduncle, and a caudal fin. Thus, the models used by Kelly et al. [1998] and later works assume more oscillatory motion than likely exists in nature in the interest of mechanical and modeling simplicity. The work by Kelly et al. [1998] was continued by Mason and Burdick [2000] which began to look for forward and turning gaits. The work by Mason and Burdick [2000] was then used by Morgansen et al. [2001] to begin to develop optimal controllers. This work was then analyzed using the geometric averaging approach presented by Vela et al. [2002a,b] (which is a higher-order extension of [Bullo, 2001]) in [Morgansen et al., 2002]. Morgansen et al. [2002] to generate optimal articulations for performing desired maneuvers. This has proven to be a productive approach and was used to develop a free swimming carangiform robot [Morgansen et al., 2007].

One interesting technique for describing the motion of articulated bodies in fluids, mostly applied to fish, was presented by Kanso et al. [2005]; Kanso and Marsden [2005], who approached the locomotion of articulated bodies in perfect (irrotational) fluids from an analytical mechanics framework. Interestingly, it shows that articulated bodies in fluids can induce movement without generating lift. This work was later expanded to include circulation (i.e. lift) by Kanso and Oskouei [2008]; Vankerschaver et al. [2009, 2010]. Unfortunately, this technique leads to a boundary value problem, which may be difficult to solve analytically, so Kanso and Marsden [2005] suggests using the Discrete Mechanics and Optimal Control (DMOC) approach presented in Junge et al. [2005] to find numerical solutions. The necessity for numerical solutions means that this analytical mechanics technique is not useful for this research.

1.1.2 Bio-inspired Flight

The flight of different animals has fascinated scientists and engineers for many centuries. The flapping motion seen in many natural flyers has been presented as the most efficient flight mode for small objects. One of the earliest working flapping wing vehicles, or ornithopters, was built by Gustave Trouvé in the nineteenth century [Chanute, 1894.]. However, designs for ornithopters predate Trouvé. Leonardo DaVinci designed a potentially viable ornithopter, but there is no evidence that he attempted to build it. There may be an upper limit on the size of flapping wing vehicles as the largest known flying animal ever was smaller than a typical human [Templin, 2000]. In contrast, small powered ornithopters were built in the nineteenth century [Chanute, 1899]. These were open-loop devices, but modern microelectronics have made unmanned small ornithopters possible.

Along with most small aerial vehicles, small ornithopters and flapping wing micro-air vehicles (FWMAVs) have been heavily studies recent years. As such, there have been several excellent surveys of significant advances in FWMAVs. Ward et al. [2015] present a comprehensive survey of the last three decades research, ending after the first quarter of 2014. Ward et al. [2015] make the assumption that all flapping wing vehicles are biomimetic, and therefore refers to flapping wing vehicles as "biomimetic aerial vehicles" (BAVs). This assumption makes no distinction between "biomimetic" and "biologically inspired.[c] That is, Ward et al. [2015] assume that all flapping wing vehicles should mimic the behavior of extant biological specimens, rather than simply being inspired by them. For this reason, I will use the acronym "BAV" to refer to "bio-inspired aerial vehicle." The purpose of Ward et al. [2015] is to use a meta-analysis of existing literature which is meant to be used as a resource for interested current researchers and provide insight into what topics are most in need of further investigation. Ward et al. [2015] present a through and comprehensive review of trends in BAV research and is very current, so a summary of important findings will be presented here. As it is a meta-analysis, Ward et al. [2015] do not comment on the relative merits of individual contributions, but sets out an objective criterion and includes all papers that meet that criterion. One of the first observations is that there appear to be few relevant[d] publications before 2000 and a significant increase in the number of publications after 2008. Additionally, much of the development has focused on aerodynamics, both experimental and numerical. Ward et al. [2015] do not give a historical trend for these ratios, but indicates that the evolution of the field is indicative of a mature understanding of the aerodynamics

[c]Ward et al. [2015] use "biomimetic micro-air vehicle (BMAV)" for insect-scale vehicles and "biomimetic ornithopter vehicle (BOAV [sic])" for bird-scale vehicles, both of which are encompassed in my use of FW-MAV.

[d]Here, relevant refers to studies that focus on specifically on BAVs but not unrelated studies whose results can be applied to BAVs.

and unsteady effects. The second most popular categorization, representative of about a fifth of the research done on BAVs, is guidance and control. Ward et al. [2015] indicate that the majority of the research has been on control, rather than guidance. This work focuses on developing working that meets performance criteria, not optimizing gaits per se. Furthermore, the least studied topic (less than 10%), system design, is the only topic that focuses specifically on the optimization of design. System design will become increasingly important as physical vehicles are built. Based on this meta-data, the research presented in this paper sits in a useful niche, bridging the gap between control and system design.

1.2 Mathematical Preliminaries

This section provides some background information on the mathematics used in this research.

1.2.1 The Averaging Theorem

Bullo [2002] presents a summary of work on first order averaging based on [Sanders et al., 2007] and [Guckenheimer and Holmes, 1983]. Consider the system

$$\dot{\boldsymbol{x}} = \epsilon \boldsymbol{f}\left(\boldsymbol{x}, t\right) \qquad \boldsymbol{x}(0) = \boldsymbol{x}_0 \tag{1.1}$$

where $\boldsymbol{x} \in \mathbb{R}^n$, ϵ is a (small) constant, and $\boldsymbol{f}\left(\boldsymbol{x}, t\right) : \mathbb{R}^n \times \mathbb{R}_+ \to \mathbb{R}^n$ is T-periodic in its second argument.[e] The first order averaged system is

$$\dot{\boldsymbol{y}} = \epsilon \boldsymbol{F}\left(\boldsymbol{y}\right) \qquad \boldsymbol{y}(0) = \boldsymbol{x}_0 \tag{1.2}$$

where

$$\boldsymbol{F}\left(\boldsymbol{y}\right) = \frac{1}{T}\int_0^T \boldsymbol{f}\left(\boldsymbol{y}, t\right)\, dt$$

The estimate of (1.1) provided by (1.2) is said to be *on the time scale* $\delta^{-1}\left(\epsilon\right)$ if the estimate holds for t such that $0 < \delta^{-1}\left(\epsilon\right) t < L$ where L is a constant that is independent of ϵ. Bullo [2002] states the (first order) averaging theorem as

Theorem 1.1 *There exists a positive* ϵ_0 *such that, for all* $0 < \epsilon \leq \epsilon_0$, $\boldsymbol{x}(t) - \boldsymbol{y}(t) = \mathcal{O}\left(\epsilon\right)$ *as* $\epsilon \to 0$ *on time scale* $1/\epsilon$. *If the origin is a hyperbolically stable critical point for* $\boldsymbol{F}$, *then* $\boldsymbol{x}(t) - \boldsymbol{y}(t) = \mathcal{O}\left(\epsilon\right)$ *as* $\epsilon \to 0\ \forall\ t \in \mathbb{R}_+$, *and* (1.1) *possesses a unique periodic orbit which is hyperbolically stable and belongs to an* $\mathcal{O}\left(\epsilon\right)$ *neighborhood of the origin.*

[e] For the development of the averaging theorem and geometric averaging it is assumed that the system is nondimensionalized such that ϵ is unit-less.

The averaging theorem provides a technique by which hyperbolically stable periodic orbits of a nonlinear time-varying system can be predicted by finding hyperbolically stable critical points of a nonlinear time-invariant system. Unfortunately, the averaging theorem does not provide any direction on determining ϵ_0. Meerkov [1973] present a method for estimating the value of ϵ_0, although this method provides a very conservative estimate [Bellman et al., 1985a]. Berg and Manjula Wickramasinghe [2015] found that there may be $\epsilon > \epsilon_0$ for which stable periodic orbits exist, but these are not predicted by the averaging theorem. Furthermore, the averaging theorem provides a sufficient condition for the existence of hyperbolically stable periodic orbits of (1.1), but does not provide a necessary condition.

1.2.2 Geometric Averaging of Vibrational Control Systems

Bullo [2001, 2002]; Bullo and Lewis [2005] presented a method for averaging control affine systems. This method utilizes the averaging theorem and exploits the structure of mechanical control affine system to aid the analysis of vibrationally controlled systems. The framework for this method was presented in [Bullo, 2001] and applied to mechanical systems is [Bullo, 2002]. The method was later improved by Bullo and Lewis [2005]. This method exploits the structure of mechanical systems and properties of Lie brackets of homogeneous vector fields to compute the first order averaged dynamics of a mechanical system. Vela et al. [2002a]; Vela [2003] expands on Bullo's approach by incorporating second order averaging, but utilizes the same structure. As the approach presented by Bullo and expanded by Vela are described using differential geometry, it is referred to in this document as *geometric averaging*.

The primary source of the information presented in this section is [Bullo and Lewis, 2005]. The insight provided by Bullo and Lewis [2005] is that the average dynamics of a class of simple mechanical systems can be determined using the variation of constants formula and a series expansion of the pullback.

As their name implies, mechanical control affine systems are mechanical systems which are affine in their control inputs. The general form of a mechanical control affine system is

$$\ddot{\boldsymbol{q}} = \boldsymbol{f}\left(\boldsymbol{q}, \dot{\boldsymbol{q}}\right) + \sum_{i=1}^{m} \boldsymbol{g}_i\left(\boldsymbol{q}, \dot{\boldsymbol{q}}\right) u_i(t) \tag{1.3}$$

where $\boldsymbol{q}, \dot{\boldsymbol{q}} \in \mathbb{R}^n$ are the generalized position and velocities, respectively, $\boldsymbol{f}\left(\boldsymbol{q}, \dot{\boldsymbol{q}}\right) : \mathbb{R}^n \times \mathbb{R}^n \to \mathbb{R}^n$ is the *drift vector field*, $\boldsymbol{g}_i\left(\boldsymbol{q}, \dot{\boldsymbol{q}}\right) : \mathbb{R}^n \times \mathbb{R}^n \to \mathbb{R}^n$ are the *input vector fields*, and $u_i(t) : \mathbb{R}_+ - \to \mathbb{R}$ is the input. For reasons that will become apparent later, assume that the drift vector field is polynomial of degree two or less in the generalize velocities and that the input vector fields depend only on the generalized positions, i.e. $\boldsymbol{g}_i\left(\boldsymbol{q}, \dot{\boldsymbol{q}}\right) = \boldsymbol{g}_i\left(\boldsymbol{q}\right) : \mathbb{R}^n \to \mathbb{R}^n$.

While the input here is stated to be a function of only time, state-dependent inputs can be included in the drift vector field provided they conform to the assumption that they are polynomial of degree two or less in the generalized velocities. So consider the inputs

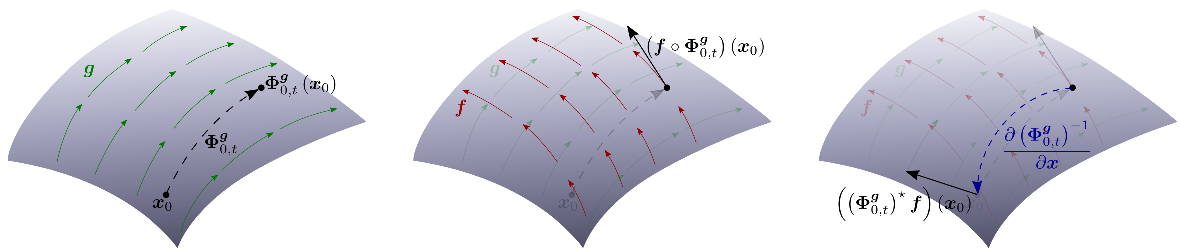

(a) Starting at $\boldsymbol{x}_0$, flow along $\boldsymbol{g}$ (b) Evaluate $\boldsymbol{f}$ at $\boldsymbol{\Phi}^{\boldsymbol{g}}_{0,t}(\boldsymbol{x}_0)$ (c) "Pull" $\boldsymbol{f}\circ\boldsymbol{\Phi}^{\boldsymbol{g}}_{0,t}(\boldsymbol{x}_0)$ back to $\boldsymbol{x}_0$

Figure 1.1: Illustration of the pullback.

$u_i(t) = u_{\mathrm{s},i}\left(\boldsymbol{q}(t), \dot{\boldsymbol{q}}(t)\right) + u_{\mathrm{t},i}(t)$ where $u_{\mathrm{s},i}\left(\boldsymbol{q}, \dot{\boldsymbol{q}}\right)$ are the state-dependent inputs and $u_{\mathrm{t},i}(t)$ are the time dependent inputs. The general control affine system (1.3) can be written as

$$\ddot{\boldsymbol{q}} = \boldsymbol{f}\left(\boldsymbol{q}, \dot{\boldsymbol{q}}\right) + \sum_{i=1}^{m} \boldsymbol{g}_i\left(\boldsymbol{q}\right) u_{\mathrm{s},i}\left(\boldsymbol{q}, \dot{\boldsymbol{q}}\right) + \sum_{i=1}^{m} \boldsymbol{g}_i\left(\boldsymbol{q}, \dot{\boldsymbol{q}}\right) u_{\mathrm{t},i}(t) \tag{1.4}$$

Notice that, under the assumption that $u_{\mathrm{s},i}\left(\boldsymbol{q}, \dot{\boldsymbol{q}}\right)$ is polynomial of degree two or less in the generalized velocities, $\boldsymbol{f}\left(\boldsymbol{q}, \dot{\boldsymbol{q}}\right) + \sum_{i=1}^{m} \boldsymbol{g}_i\left(\boldsymbol{q}\right) u_{\mathrm{s},i}\left(\boldsymbol{q}, \dot{\boldsymbol{q}}\right)$ is polynomial of degree two or less in the generalized velocities. Thus, the development of geometric averaging for (1.3) can be applied to (1.4).

1.2.2.1 The Variation of Constants Formula

Bullo [2002] presents a method where the variation of constants formula[f] is used to provide a means by which a general nonlinear time-varying system can be expressed in terms of two equations. One of these equations has the form of (1.1), enabling the Theorem 1.1 to be applied. The variation of the constants formula utilizes the pullback.

Definition 1.2 *Given a vector field* $\boldsymbol{g}$ *and a diffeomorphism* $\boldsymbol{\phi}$*, the* pullback *of* g *along* ϕ*, denoted by* $\boldsymbol{\phi}^{\star}\boldsymbol{g}$ *is*

$$\left(\boldsymbol{\phi}^{\star}\boldsymbol{g}\right)(\boldsymbol{x}) \triangleq \left(\frac{\partial\boldsymbol{\phi}^{-1}}{\partial\boldsymbol{x}} \circ \boldsymbol{g} \circ \boldsymbol{\phi}\right)(\boldsymbol{x})$$

The pullback is illustrated in Figure 1.1.

Consider the system $\dot{\boldsymbol{y}} = \boldsymbol{\psi}\left(\boldsymbol{y}, t\right)$. The flow along a vector field $\boldsymbol{\psi}$ from $t = 0$ to t is denoted $\boldsymbol{\Phi}^{\boldsymbol{\psi}}_{0,t}$.[g] The flow represents the effect of a vector field $\boldsymbol{\psi}$ on the evolution of $\boldsymbol{y}$, i.e.

[f] The variation of constants formula that is referred to is the nonlinear formulation of the variation of constants formula, which reduces to the formula familiar from linear systems theory when considering the dynamics of a linear control system.

[g] In linear systems theory, the flow is often called the "state transition matrix".

$\boldsymbol{y}(t) = \boldsymbol{\Phi}_{0,t}^{\boldsymbol{\psi}}(\boldsymbol{y}(0))$. The flow along a smooth vector field is a diffeomorphism. Consider the general nonlinear initial value problem:

$$\dot{\boldsymbol{x}} = \boldsymbol{f}(\boldsymbol{x}, t) + \boldsymbol{g}(\boldsymbol{x}, t) \qquad \boldsymbol{x}(0) = \boldsymbol{x}_0 \tag{1.5}$$

If $\boldsymbol{f}$ is regarded as a perturbation on $\boldsymbol{g}$, then the flow along $\boldsymbol{f} + \boldsymbol{g}$ from $t = 0$ to t can be found using the variation of constants formula:

$$\boldsymbol{\Phi}_{0,t}^{\boldsymbol{f}+\boldsymbol{g}} = \boldsymbol{\Phi}_{0,t}^{\boldsymbol{g}} \circ \boldsymbol{\Phi}_{0,t}^{\left(\boldsymbol{\Phi}_{0,t}^{\boldsymbol{g}}\right)^{\star}\boldsymbol{f}} \tag{1.6}$$

where $\left(\boldsymbol{\Phi}_{0,t}^{\boldsymbol{g}}\right)^{\star}\boldsymbol{f}$ is the pullback of $\boldsymbol{f}$ along the flow of $\boldsymbol{g}$. The variation of constants formula can be used to express (1.5) as

$$\begin{aligned} \dot{\boldsymbol{z}}(t) &= \left(\left(\boldsymbol{\Phi}_{0,t}^{\boldsymbol{g}}\right)^{\star}\boldsymbol{f}\right)(\boldsymbol{z}) & \boldsymbol{z}(0) &= \boldsymbol{x}_0 \\ \dot{\boldsymbol{x}}(t) &= \boldsymbol{g}(\boldsymbol{x}, t) & \boldsymbol{x}(0) &= \boldsymbol{z}(t) \end{aligned}$$

The variation of constants formula is depicted in Figure 1.2. The flow along $\boldsymbol{f} + \boldsymbol{g}$ can be

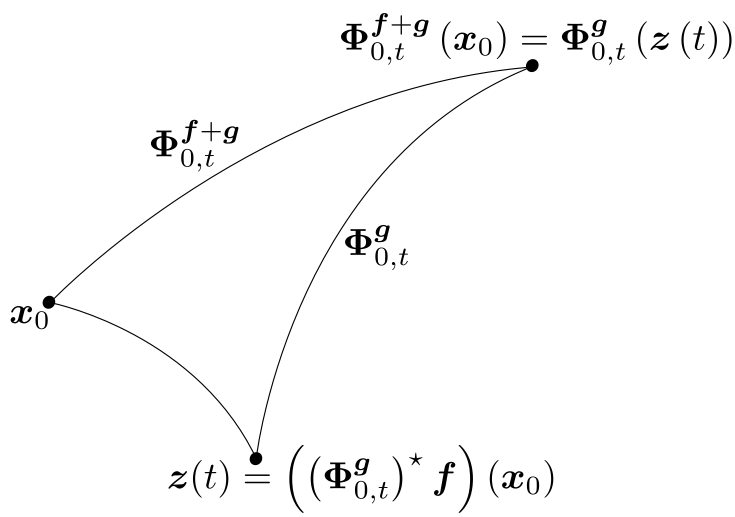

Figure 1.2: Graphic depicting the variation of constants formula. Based on [Bullo and Lewis, 2005].

determined by allowing $\boldsymbol{x}_0$ to evolve along the pullback of $\boldsymbol{f}$ along $\boldsymbol{g}$ yielding $\boldsymbol{z}(t)$ and then allowing $\boldsymbol{z}(t)$ to flow along $\boldsymbol{g}$.

1.2.2.2 Series Expansion of the Pullback

Computing analytical expressions for the flow along nonlinear vector fields is generally not possible. Thus, it is not always possible to compute the pullback using the expression in definition 1.2. Agračev and Gamkrelidze [1979] provides an alternative by using the chronological calculus to develop series expansions for the pullback. Specifically, for a system of the form (1.5) the pullback of $\boldsymbol{f}$ along the flow of $\boldsymbol{g}$ is

$$\left(\boldsymbol{\Phi}_{0,t}^{\boldsymbol{g}}\right)^{\star} \boldsymbol{g}(\boldsymbol{x},t) = \boldsymbol{f}\left(\boldsymbol{x},t\right) + \sum_{k=1}^{\infty} \int_0^t \cdots \int_0^{s_{k-1}} \left(\mathrm{ad}_{\boldsymbol{g}(\boldsymbol{x},s_k)} \ldots \mathrm{ad}_{\boldsymbol{g}(\boldsymbol{x},s_1)} \boldsymbol{f}\left(\boldsymbol{x},t\right)\right) ds_k \ldots ds_1 \tag{1.7}$$

At first glance, it appears that this expansion appears to substitute one problem without an analytical solution (integrating arbitrary nonlinear ODE) for another (finding the sum of an infinite series of integrals). However, this infinite series can terminate if all terms

$$\int_0^t \cdots \int_0^{s_{k-1}} \left(\mathrm{ad}_{\boldsymbol{g}(\boldsymbol{x},s_k)} \ldots \mathrm{ad}_{\boldsymbol{g}(\boldsymbol{x},s_1)} \boldsymbol{f}\left(\boldsymbol{x},t\right)\right) ds_k \ldots ds_1 = \boldsymbol{0}_{2n\times 1}$$

for all k greater than some constant. This is the case for simple mechanical control affine systems with the structure described in the following section [Bullo, 2002].

1.2.2.3 Properties of Homogeneous Vector Fields

Definition 1.3 *The set $\mathcal{H}_i$ is the set of scalar functions on $\mathbb{R}^n \times \mathbb{R}^n$ which are arbitrary functions of $\boldsymbol{q}$ and homogeneous polynomials of degree i in $\dot{\boldsymbol{q}}$. The set of homogeneous polynomial vectors fields, denoted $\boldsymbol{\mathcal{P}}_i$, is the set vector fields in $\mathbb{R}^{2n}$ whose first n elements are in $\mathcal{H}_i$ and whose second n elements are in $\mathcal{H}_{i+1}$. Note that i can be any integer.*

Remark 1.4 *[Bullo and Lewis, 2005] The homogeneous polynomial vector fields obey the following properties:*

1. $[\boldsymbol{\mathcal{P}}_i, \boldsymbol{\mathcal{P}}_j] \subset \boldsymbol{\mathcal{P}}_{i+j}$;
2. $\boldsymbol{\mathcal{P}}_k = \{\boldsymbol{0}\}\ \forall\ k \leq -2$;
3. *if* $k \geq 1$, *then* $\boldsymbol{X}\left(\boldsymbol{q},\boldsymbol{0}\right) = \boldsymbol{0}$ *for all* $\boldsymbol{X} \in \boldsymbol{\mathcal{P}}_k$;
4. *every* $\boldsymbol{X} \in \boldsymbol{\mathcal{P}}_{-1}$ *is the vertical lift of a vector field that is a function of only* $\boldsymbol{q}$.

Consider simple mechanical control affine systems with the form

$$\ddot{\boldsymbol{q}} = \boldsymbol{f}\left(\boldsymbol{q},\dot{\boldsymbol{q}}\right) + \sum_{i=1}^{m} \boldsymbol{g}_i\left(\boldsymbol{q}\right) u_i\left(t\right) \tag{1.8}$$

where $\boldsymbol{q} \in \mathbb{R}^n$ and $\dot{\boldsymbol{q}} \in \mathbb{R}^n$ are the generalized positions and velocities, respectively. Notice that the elements of $\boldsymbol{g}$ are in $\mathcal{H}_0$ and, since this is a mechanical system, the elements of $\boldsymbol{f}$ are in $\mathcal{H}_2$. Let $\boldsymbol{x} = \left[\boldsymbol{q}^T, \dot{\boldsymbol{q}}^T\right]^T$ and so (1.8) can be written as

$$\dot{\boldsymbol{x}} = \boldsymbol{Y}_0(\boldsymbol{x}) + \sum_{i=1}^{m} \boldsymbol{Y}_i(\boldsymbol{x})\, u_i(t) \tag{1.9}$$

where

$$\boldsymbol{Y}_0(\boldsymbol{x}) = \begin{bmatrix} \dot{\boldsymbol{q}} \\ \boldsymbol{f}(\boldsymbol{q}, \dot{\boldsymbol{q}}) \end{bmatrix} \in \boldsymbol{\mathcal{P}}_1 \qquad \text{and} \qquad \boldsymbol{Y}_i(\boldsymbol{x}) = \begin{bmatrix} \mathbf{0}_{n\times 1} \\ \boldsymbol{g}(\boldsymbol{q}) \end{bmatrix} \in \boldsymbol{\mathcal{P}}_{-1}$$

The series of iterated Lie brackets in (1.7) can be expressed using Lie brackets:

$$\begin{aligned} &\text{for } k=1 && \sum_{i=1}^{m} [\boldsymbol{Y}_i, \boldsymbol{Y}_0] \\ &\text{for } k=2 && \sum_{i,j=1}^{m} [\boldsymbol{Y}_j, [\boldsymbol{Y}_i, \boldsymbol{Y}_0]] \\ &\text{for } k=3 && \sum_{i,j,l=1}^{m} [\boldsymbol{Y}_l, [\boldsymbol{Y}_j, [\boldsymbol{Y}_i, \boldsymbol{Y}_0]]] \end{aligned}$$

and so on. For $k = 3$, notice that, since $\boldsymbol{Y}_i \in \boldsymbol{\mathcal{P}}_{-1}$ and $\boldsymbol{Y}_0 \in \boldsymbol{\mathcal{P}}_1$, $[\boldsymbol{Y}_l, [\boldsymbol{Y}_j, [\boldsymbol{Y}_i, \boldsymbol{Y}_0]]] \in \boldsymbol{\mathcal{P}}_{-2}$. By the properties in remark 1.4, $[\boldsymbol{Y}_l, [\boldsymbol{Y}_j, [\boldsymbol{Y}_i, \boldsymbol{Y}_0]]] = \mathbf{0}$. The same property holds for all $k \geq 3$. Therefore, the infinite series in (1.7) terminates after $k = 2$.

1.2.2.4 Averaging with Vibrational Inputs

Definition 1.5 *The symmetric product between* $\mathbf{Y}_i$ *and* $\mathbf{Y}_j$*, denoted* $\langle \mathbf{Y}_i : \mathbf{Y}_j \rangle$*, is*

$$\langle \mathbf{Y}_i : \mathbf{Y}_j \rangle \triangleq [\mathbf{Y}_j, [\mathbf{Y}_0, \mathbf{Y}_i]]$$

$\langle \mathbf{Y}_i : \mathbf{Y}_j \rangle$ *is called the symmetric product because* $\langle \mathbf{Y}_i : \mathbf{Y}_j \rangle = \langle \mathbf{Y}_j : \mathbf{Y}_i \rangle$*.*

Remark 1.6 *The symmetric product is defined with respect to vector fields in* $\mathbb{R}^{2n}$ *in Definition 1.5. Usually, the symmetric product is defined with respect to vector fields in* $\mathbb{R}^n$*. For the systems of interest, lifting this symmetric product in* $\mathbb{R}^n$ *to* $\mathbb{R}^{2n}$ *yields the same result as Definition 1.5 [Bullo, 2002]. That is,*

$$\langle \mathbf{Y}_i : \mathbf{Y}_j \rangle = \langle \boldsymbol{g}_i : \boldsymbol{g}_j \rangle^{\text{lift}}$$

where $\langle \mathbf{Y}_i : \mathbf{Y}_j \rangle \in \mathbb{R}^{2n}$ *is the symmetric product from Definition 1.5 and* $\langle \boldsymbol{g}_i : \boldsymbol{g}_j \rangle \in \mathbb{R}^n$ *is the symmetric product as defined by Bullo [2002].*

Definition 1.7 *The waveform shape parameters are defined as*

$$\begin{aligned}
\kappa_i &\triangleq \frac{1}{T}\int_0^T \int_0^t v_i(\tau)\,d\tau dt \\
\lambda_{ij} &\triangleq \frac{1}{T}\int_0^T \left(\int_0^t v_i(s_i)\,ds_i\right)\left(\int_0^t v_j(s_j)\,ds_j\right)dt \\
\mu_{ij} &\triangleq \frac{1}{2}\left(\lambda_{ij} - \kappa_i\kappa_j\right)
\end{aligned}$$

Let the input waveforms $v_i(t)$ be zero-mean, T-periodic functions.[h] Consider (1.9) with high-frequency, high-amplitude, zero-mean, periodic inputs $u_i(t) = (1/\epsilon)\, v_i\,(t/\epsilon)$ for a small ϵ.[i] These are referred to as vibrational inputs. Bullo and Lewis [2005] showed that using the properties of homogeneous vector fields and the series expansion of the pullback, the averaged dynamics of (1.9) with initial condition $\boldsymbol{x}_0 = \boldsymbol{x}\,(0)$ can be expressed as

$$\dot{\overline{\boldsymbol{x}}} = \boldsymbol{Y}_0\,(\overline{\boldsymbol{x}}) - \sum_{i,j=1}^{m} \mu_{ij}\,\langle \boldsymbol{Y}_i : \boldsymbol{Y}_j\rangle\,(\overline{\boldsymbol{x}}) \qquad \overline{\boldsymbol{x}}\,(0) = \boldsymbol{x}_0 + \sum_{i=1}^{k} \kappa_i \boldsymbol{Y}_i\,(\boldsymbol{x}_0) \tag{1.10}$$

where $\langle \boldsymbol{Y}_i : \boldsymbol{Y}_j\rangle$ is the *symmetric product* between $\boldsymbol{Y}_i$ and $\boldsymbol{Y}_j$ (see Definition 1.5) and κ_i and μ_{ij} are waveform shape parameters (see definition 1.7). The waveform shape parameters represent the effect of the shape of the input waveforms and the interaction between input waveforms. The geometric averaging technique can be stated in the form of a theorem:

Theorem 1.8 *(Adapted from [Bullo and Lewis, 2005, Ch. 9]): Consider control-affine system* (1.3) *with high-frequency, high-amplitude inputs defined as $u_i = \omega v_i(\omega t)$ where $\omega = 1/\epsilon$ and v_i is a zero-mean, T-periodic function, and its first order form of* (1.9)*. Suppose that $\boldsymbol{f}(\boldsymbol{q}, \dot{\boldsymbol{q}})$ and $\boldsymbol{g}_i(\boldsymbol{q})$ depend polynomially on their arguments, are twice differentiable in $\boldsymbol{q}$, and that the components of $\boldsymbol{f}(\boldsymbol{q}, \dot{\boldsymbol{q}})$ are homogeneous in $\dot{\boldsymbol{q}}$ of degree two and less. Consider the time-invariant system*

$$\dot{\overline{\boldsymbol{x}}} = \boldsymbol{Z}(\overline{\boldsymbol{x}}) - \sum_{i,j=1}^{m} \mu_{ij}\langle \boldsymbol{Y}_i : \boldsymbol{Y}_j\rangle(\overline{\boldsymbol{x}}) \tag{1.11}$$

with the initial condition $\overline{\boldsymbol{x}}(0) = \overline{\boldsymbol{x}}_0 = \boldsymbol{x}_0 + \sum_{i=1}^{m} \kappa_i \boldsymbol{Y}_i(\boldsymbol{x}_0)$, where $\overline{\boldsymbol{x}} = (\overline{\boldsymbol{q}}^T,\ \dot{\overline{\boldsymbol{q}}}^T)^T$ is the state vector. There exists a positive ϵ_0 (corresponding to a frequency ω_0) such that for all $0 < \epsilon \leq \epsilon_0$ ($\omega \geq \omega_0$), $\boldsymbol{q}(t) = \overline{\boldsymbol{q}}(t) + O(\epsilon)$ as $\epsilon \to 0$ on the time scale 1. Furthermore if the system (1.11) *possesses a hyperbolically stable equilibrium point $\overline{\boldsymbol{x}}_{\mathrm{e}}$, then the system* (1.9) *possesses a unique, hyperbolically stable periodic orbit within an $O(\epsilon)$ neighborhood of the equilibrium point $\overline{\boldsymbol{x}}_{\mathrm{e}}$, and the approximation $\boldsymbol{q}(t) = \overline{\boldsymbol{q}}(t) + O(\epsilon)$ is valid for all time $t \geq 0$.*

[h] The amplitude and period, T, of v_i are on the order of 1, i.e. $T = \mathcal{O}(1)$.

[i] The period of u_i is on the order of ϵ and the amplitude is on the order of $1/\epsilon$.

Remark 1.9 *[Bullo and Lewis, 2005] With waveform shape parameters defined as in definition 1.7, if all of the input waveforms are phase shifted equally, the value of μ_{ij} does not change, while the values of κ_i and λ_{ij} change. Furthermore, the value of μ_{ij} depends only on the* relative phase *between v_i and v_j, while κ_i and λ_{ij} depend on the individual phases of v_i and v_j.*

Using Theorem 1.1 and the variation of constants formula, some of the hyperbolically stable periodic orbits of (1.9) can be found by finding hyperbolically stable fixed points of (1.10).[j] Examining (1.10), μ_{ij} appears in a way similar to control inputs. Thus, the problem of finding input waveforms that produce hyperbolically stable periodic orbits of (1.9) can be approached as finding inputs that stabilize (1.10) about some equilibrium where the inputs are the shape and phasing of the input waveforms.

One useful property of μ_{ij} is provided in Theorem 1.10. This theorem presents constraints on the possible values of μ_{ij} and will be useful for discussing input waveform optimization in Chapter 2

Theorem 1.10 *For any T-periodic, zero mean functions $v_i(t)$ and $v_j(t)$ the waveform shape parameters (Definition 1.7) obey the following properties:*

- $\mu_{ii} \geq 0$ *and* $\mu_{jj} \geq 0$
- $\mu_{ij}^2 \leq \mu_{ii}\mu_{jj}$

Proof: See Tahmasian et al. [2016].

1.3 Overview of Contributions

This section contains a brief list of the contributions of this dissertation. This list is meant to provide a brief overview of the contributions, more detailed descriptions are provided at the end of each chapter. A citation is included for work that has been presented in other publications.

- A method was developed numerically approximating the symmetric product of vector fields.
- In collaboration with Dr. Sevak Tahmasian, a technique was developed for optimizing the input waveforms to vibrationally stabilize an equilibrium. [Tahmasian et al., 2016]

[j] As the Theorem 1.1 provides a sufficient but not necessary condition for the existence of a hyperbolically stable periodic orbit, there may be hyperbolically stable periodic orbits note predicted by Theorem 1.1.

- A technique for generating approximations of arbitrary waveforms using truncated Fourier series was developed. These waveforms approximate the solution to input waveform optimization problems.[Tahmasian et al., 2016]
- An input energy input waveform optimization problem developed and its solution was proven to be sinusoids. [Tahmasian et al., 2016]
- An impulse input waveform optimization problem was developed and the truncate Fourier series definition of input waveforms were used to approximate a solution.
- A new model of fish locomotion that can be used to approximate the spectrum of fish locomotion from undulatory to oscillatory locomotion was developed.
- The new model of fish locomotion and a modified response surface optimization technique were utilized to find the optimal gaits for a representative of Thunniform locomotion. This optimization was performed on multiple variations of the morphology and cost functional.
- The optimization results were used to find trends for the optimal gait, and these trends were parameterized using linear functions of speed.
- Wind tunnel experiments were performed on a model ornithopter and results were presented using a traditional aircraft performance framework.[Zakaria et al., 2016]
- A framework for estimating the effects of flapping flight as relatively simple functions of reduced frequency was developed.[Zakaria et al., 2016]
- Data of over 1600 flying animals were collected. A text-based user interface to extract the data was built enabling easy access to the database. [Allen, 2015]

Chapter 2

Input Waveform Optimization

Using the geometric averaging techniques described in Section 1.2.2, a method for choosing the optimal input waveforms for stabilizing a system of the form (1.9) in a periodic orbit around a desired equilibrium was developed.[a] This method uses a constrained optimization problem whose free parameters define the input waveforms and whose constraint is that the input waveforms induce a stable periodic orbit about some desired state. The cost functional can be any reasonable cost functional one desires. Two general methods for parameterizing input waveforms are presented in Section 2.1 and a few choices of cost functional are presented in Section 2.2. The optimization problem's constraints are presented in Section 2.3 and the limitations of this method are presented in Section 2.4. Finally, an illustrative example is provided in Section 2.5.

2.1 Parameterization of Input Waveforms

There are two methods for parameterizing the input waveforms presented here. One uses archetypal waveforms (e.g. square waves or sinusoids) and adjusts the amplitude and phase, while the other approximates arbitrary input waveforms using truncated Fourier series.

2.1.1 Amplitude and Phase Method

One method of describing the input waveform is to define a basic waveform and adjust its amplitude and phase. Some examples of basic waveforms are square waves and sinusoids. A development for square waves and sinusoids is presented in this section. Although this dissertation will only discusses square waves and sinusoids, any archetypal waveform can be used.

[a]This method was developed in collaboration with Dr. Sevak Tahmasian.

In this work sinusoids are defined as a cosine function with three parameters: an amplitude, a frequency, and a phase shift. That is, an input waveform, v_i, can be defined as

$$v_i(t) = B_i \cos(\Omega t + \phi_i) \tag{2.1}$$

where $B_i \geq 0$ is the amplitude, $\Omega = 2\pi/T$ is the frequency (with T being the period), and $\phi_i \in [0, 2\pi)$ is the phase shift. In order yield more compact results, let $B_i = \Omega \widetilde{B}_i$. With input waveforms defined as in (2.1) the waveform shape parameters from definition 1.7 are

$$\kappa_i = -\widetilde{B}_i \sin(\phi_i) \qquad \text{and} \qquad \mu_{ij} = \frac{1}{4}\widetilde{B}_i \widetilde{B}_j \cos(\phi_{ij}) \tag{2.2}$$

where $\phi_{ij} = \phi_i - \phi_j$ is the *relative phase*. Notice that μ_{ij} depends only on relative phase, as is stated in Remark 1.9.

Now consider square waves, which can be defined as

$$S_B(t) = \begin{cases} B & \text{if } t \in [0, T/2) \\ -B & \text{if } t \in [T/2, T) \end{cases}$$

where B is the amplitude and T is the period. If the input waveforms defined as square waves are parametrized as

$$v_i(t) = S_{B_i}(t + \phi_i) = \begin{cases} B_i & \text{if } t + \phi_i \in [0, T/2) \\ -B_i & \text{if } t + \phi_i \in [T/2, T) \end{cases} \tag{2.3}$$

where B_i defines the amplitude, ϕ_i is the phase, and T is the period. Unlike sinusoids, B_i is allowed to be positive or negative and $\phi_i \in [0, T/2]$.[b] If the input waveforms are defined as square waves,

$$\kappa_i = B_i\left(\frac{T}{4} - \phi_i\right) \qquad \text{and} \qquad \mu_{ij} = \frac{T^2 B_i B_j}{96}\left(32\left(\frac{\phi_{ij}}{T}\right)^3 - 24\left(\frac{\phi_{ij}}{T}\right)^2 + 1\right) \tag{2.4}$$

where $\phi_{ij} = \phi_i - \phi_j$ [Tahmasian et al., 2016].

2.1.2 Truncated Fourier Series Method

Any continuous zero-mean, T-periodic function can be expressed as a Fourier series:

$$v_i(t) = \sum_{n=1}^{\infty} A_{i,n} \cos(\Omega n t) + B_{i,n} \sin(\Omega n t) \tag{2.5}$$

[b] This change is required so that Equation (2.4) is valid. A negative value of B_i is equivalent to a phase shift of more than $T/2$. Also note that in this case, B_i is not the amplitude, which must be positive; the amplitude is $|B_i|$.

where $\Omega = 2\pi/T$ and $A_{i,n}$, $B_{i,n}$ are *Fourier coefficients*. Since $A_{i,n}$ and $B_{i,n}$ tend to converge to zero for a large class of zero-mean, T-periodic functions, such functions can be approximated as *truncated Fourier series*, i.e.

$$v_i(t) = \sum_{n=1}^{l} A_{i,n}\cos(\Omega n t) + B_{i,n}\sin(\Omega n t) \tag{2.6}$$

for some finite l. Notice that $\Omega = \mathcal{O}(1)$. For later simplicity, let $A_{i,n} = \Omega a_{i,n}$ and $B_{i,n} = \Omega b_{i,n}$. With input waveforms defined as truncated Fourier series, it is possible to express the waveform shape parameters from definition 1.7 as

$$\kappa_i = \sum_{n=1}^{l} \frac{b_{i,n}}{n} \qquad \text{and} \qquad \mu_{ij} = \frac{1}{4}\sum_{i,j=1}^{l} \frac{1}{n^2}\left(a_{i,n}a_{j,n} + b_{i,n}b_{j,n}\right) \tag{2.7}$$

See Appendix A.1 for a proof of (2.7).[c]

2.2 Cost Functionals

This section discusses the choices of the cost functional presented herein. The choice of cost function is among the most important aspects of optimization problems.[d] The cost functional represents the metric by which the solutions to the optimization problem will be evaluated (i.e. it is the metric by which the optimal solution is optimal). Therefore, choosing the right optimization metric is very important; if an inappropriate cost function is chosen, the solution to the optimization is useless. The three cost functionals presented in this section are the input amplitude, input energy, and input impulse.

2.2.1 Input Amplitude

One choice of cost function is to minimize amplitude of input waveforms. This is well motivated; in general, minimizing the mass of the system is an important objective [Chedmail and Gautier, 1990; Karpelson et al., 2008] and the size of an actuator scales with its maximum output. So, minimizing the magnitude of the forces and moments required to operate the system may allow one to minimize the size of the actuators, thus minimizing the mass of the system. While the definition of the amplitude is clear for waveforms defined using the amplitude and phase method (Section 2.1.1), the notion of amplitude is more subtle for waveforms defined as truncated Fourier series.

[c] This proof is lengthy but relies on straightforward algebraic manipulation and simple calculus.

[d] The structure chosen for optimization problems herein is minimization. Other optimization problems, e.g. maximization problems, are equivalent, so the term "cost functional" may not be relevant for all optimization problem.

Definition 2.1 *The amplitude of a T-periodic waveform $v(t)$ is*

$$\mathbf{amp}\ (v(t)) \triangleq \frac{1}{2}\left(\max_{t\in[0,T)} v(t) - \min_{t\in[0,T)} v(t)\right)$$

The cost functional that minimizes the sum of the amplitudes of the input waveforms is

$$J(\boldsymbol{v}(t)) = \sum_{i=1}^{m} \mathbf{amp}\ (v_i(t)) \tag{2.8}$$

where $\boldsymbol{v}(t) = [v_1(t), v_2(t), \ldots, v_m(t)]^T$ is the vector of the input waveforms.

Remark 2.2 *If $B_i = \mathbf{amp}\ (v_i(t))$ and $\boldsymbol{B} = [B_1, B_2, \ldots, B_m]^T$ is the vector of input amplitudes, then the cost functional* (2.8) *can be expressed as*

$$J(\boldsymbol{v}(t)) = \sum_{i=1}^{m} B_i = \|\boldsymbol{B}\|_1$$

While Remark 2.2 may seem trivial, its significance is discussed in Section 2.2.4.1.

2.2.2 Input Energy

Another well motivated optimization objective is minimizing the input energy. As the inputs are not necessarily forces, the term "input energy" can be misleading. It can also be interpreted as the "signal energy" of the inputs. The word "energy" does not imply that it has units of energy, e.g. Joules. Suppose $\boldsymbol{u}(t)$ is a set of inputs that drives a system, $\dot{\boldsymbol{x}} = \boldsymbol{f}\,(t, \boldsymbol{x}(t), \boldsymbol{u}(t))$, from $\boldsymbol{x}_0$ at time $t = 0$ to $\boldsymbol{x}_f$ at time $t = t_f$. The input energy of such a controller is [Burns, 2014]

$$E = \frac{1}{2}\int_0^{t_f} \boldsymbol{u}^T(t)\boldsymbol{u}(t)dt \tag{2.9}$$

If the inputs are T-periodic and $t_f = kT$ for some $k \in \mathbb{Z}^+$, then

$$E = \frac{k}{2}\int_0^{T} \boldsymbol{u}^T(t)\boldsymbol{u}(t)dt \tag{2.10}$$

Definition 2.3 *The T-averaged p-norm of a vector signal $\boldsymbol{u}(t)$ is*

$$\|\boldsymbol{u}(t)\|_{T,p} = \left(\frac{1}{T}\int_0^{T} \sum_{i=1}^{m} |u_i(t)|^p dt\right)^{\frac{1}{p}}$$

where $u_i(t)$ is the i^{th} element of $\boldsymbol{u}(t)$.

Using this definition, the T-averaged 2-norm is equal to

$$\|\boldsymbol{u}(t)\|_{T,2} = \sqrt{\frac{1}{T}\int_0^T \boldsymbol{u}^T(t)\boldsymbol{u}(t)dt}$$

The T-averaged p-norm defined in Definition 2.3 satisfies the required properties of a norm function for a signal defined on the interval $[0,T]$ [Khalil, 2001].

Theorem 2.4 *Let $\boldsymbol{v}(t) = [v_1(t),\ldots,v_m(t)]^T$ be a vector of zero-mean, T-periodic input waveforms. Minimizing the input energy over the time interval $[0,kT]$ is equivalent to minimizing the T-averaged 2-norm of the input waveforms.*

Proof: Recalling the definition of the input energy over k periods in equation (2.10), the input energy of the input waveforms is

$$E = \frac{k}{2}\int_0^T \|\boldsymbol{v}(t)\|_2^2\, dt = \frac{k}{2}\int_0^T \boldsymbol{v}^T(t)\boldsymbol{v}(t)dt$$

When solving the minimum input energy optimization problem, E is used as a cost functional. Notice that E is strictly positive except if $\boldsymbol{v}(t) \equiv \mathbf{0}$ and that multiplying E by a constant scalar yields an equivalent optimization problem [Boyd and Vandenberghe, 2004]. Multiplying E by $2/kT$ yields

$$\frac{2}{kT}E = \frac{1}{T}\int_0^T \boldsymbol{v}^T(t)\boldsymbol{v}(t)dt = \|\boldsymbol{v}(t)\|_{T,2}^2$$

□

Remark 2.5 *: If $v_i(t)$ is defined as a truncated Fourier series as in equation (2.5), i.e.*

$$v_i(t) = \Omega\sum_{n=1}^{l}\left(a_{i,n}\cos(\Omega nt) + b_{i,n}\sin(\Omega nt)\right)$$

then the T-averaged 2-norm can be expressed as

$$\|\boldsymbol{v}(t)\|_{T,2} = \sqrt{\frac{1}{T}\int_0^T \boldsymbol{v}^T(t)\boldsymbol{v}(t)dt} = \frac{\Omega}{\sqrt{2}}\sqrt{\sum_{i=1}^{m}\sum_{n=1}^{l}\left(a_{i,n}^2 + b_{i,n}^2\right)}$$

2.2.3 Input Impulse

An additional cost function is minimizing the impulse of the inputs. Impulse is the measure of the net change in momentum of a system over time. For spacecraft using thrusters, impulse is equivalent to fuel use, but clear equivalences may not exist for other systems. I define the impulse for a single time-varying input $f(t)$ from an initial time t_0 to a final time t_f is

$$\int_{t_0}^{t_f} f(t)dt$$

If $f(t)$ is a force, then this impulse is the net change in momentum due to $f(t)$. Note that the impulse over one period for a zero-mean periodic force is zero. Thus, a slight modification is needed in order to have a meaningful cost functional based on the impulse of inputs waveforms because input waveforms are zero-mean periodic functions. This modification is accomplished by integrating the absolute value of the input waveform over time, i.e.

$$\int_{t_0}^{t_f} |f(t)|\, dt$$

which will not be zero unless $f(t) = 0$ for all $t \in [t_0, t_f]$ except at a finite number of points. Translating this to a cost functional, the input impulse minimizing cost functional is

$$J\left(\boldsymbol{v}(t)\right) = \sum_{i=1}^{m} \int_0^T |v_i(t)|\, dt \tag{2.11}$$

2.2.4 Known Solutions

For specific choices of cost functionals, there are known optimal waveforms.

Theorem 2.6 *[Tahmasian et al., 2016] Let $\boldsymbol{v}(t) = [v_1(t), \ldots, v_m(t)]^T$ be a vector of continuous, zero-mean, T-periodic input waveforms satisfying the conditions in equation* (2.15)*. For the corresponding values of μ_{ij}, the square waves achieve these values with the minimum sum of amplitudes. Square waves are defined in* (2.3)*.*

Proof: As Theorem 2.6 and its proof was primarily developed by Dr. Sevak Tahmasian as part of his and the author's collaboration, the reader is referred to [Tahmasian et al., 2016] for the proof of Theorem 2.6.

Theorem 2.7 *Let $\boldsymbol{v}(t) = [v_1(t), \ldots, v_m(t)]^T$ be a vector of continuous, zero-mean, T-periodic input waveforms satisfying the conditions in equation* (2.15)*. For the corresponding values of μ_{ij}, the minimum input energy corresponds to sinusoidal input waveforms, i.e. $v_i(t) = B_i \cos\left(\Omega t + \phi_i\right)$.*

Proof: Consider the problem of minimizing the input energy of $v_i(t)$ with $\mu_{ii} = \mu^\star$ which satisfies the constraint in equation (2.15). Assume that $v_i(t)$ is a continuous, zero-mean, T-periodic function. $v_i(t)$ can therefore be expressed as a Fourier series, i.e.

$$v_i(t) = \Omega \sum_{n=1}^{\infty} \left(a_{i,n}\cos(\Omega n t) + b_{i,n}\sin(\Omega n t)\right)$$

Since $v_i(t)$ is defined as a Fourier series, one finds that

$$\mu_{ii} = \mu^\star = \frac{1}{4}\sum_{n=1}^{\infty} \frac{1}{n^2}\left(a_{i,n}^2 + b_{i,n}^2\right) \tag{2.12}$$

and the input energy of this waveform is (see Theorem 2.4)

$$\|v_i(t)\|_{T,2}^2 = \frac{\Omega^2}{2}\sum_{n=1}^{\infty}\left(a_{i,n}^2 + b_{i,n}^2\right) \tag{2.13}$$

Notice that the summands of (2.12) and (2.13) differ only by a factor of $1/n^2$. Minimizing (2.13) subject to (2.12) is equivalent to minimizing $\sum_{n=1}^{\infty}\left(a_{i,n}^2 + b_{i,n}^2\right)$ subject to $\sum_{n=1}^{\infty}\frac{1}{n^2}\left(a_{i,n}^2 + b_{i,n}^2\right) = \mu^\star$. Notice that

$$\begin{aligned}
\sum_{n=1}^{\infty}\left(a_{i,n}^2 + b_{i,n}^2\right) &= \sum_{n=1}^{\infty}\left(\frac{1}{n^2}\left(a_{i,n}^2 + b_{i,n}^2\right) + \frac{n^2-1}{n^2}\left(a_{i,n}^2 + b_{i,n}^2\right)\right)\\
&= \sum_{n=1}^{\infty}\left(\frac{1}{n^2}\left(a_{i,n}^2 + b_{i,n}^2\right)\right) + \sum_{n=1}^{\infty}\left(\frac{n^2-1}{n^2}\left(a_{i,n}^2 + b_{i,n}^2\right)\right)
\end{aligned}$$

Applying the constraint yields

$$\sum_{n=1}^{\infty}\left(a_{i,n}^2 + b_{i,n}^2\right) = \mu^\star + \sum_{n=1}^{\infty}\left(\frac{n^2-1}{n^2}\left(a_{i,n}^2 + b_{i,n}^2\right)\right)$$

Since $\mu^\star$ is a constant and $\left(n^2-1\right)/n^2 = 0$ if $n = 1$, minimizing the input energy of $v_i(t)$ subject to $\mu_{ii} = \mu^\star$ is equivalent to minimizing

$$\sum_{n=2}^{\infty}\frac{n^2-1}{n^2}\left(a_{i,n}^2 + b_{i,n}^2\right) \tag{2.14}$$

Notice that $\left(n^2-1\right)/n^2 > 0$ for all $n > 1$, so the minimum of (2.14) occurs when $a_{i,n}^2 + b_{i,n}^2 = 0$ for all $n \geq 2$ which occurs when $a_{i,n}, b_{i,n} = 0$ for all $n \geq 2$.

Therefore, the minimum input energy continuous, zero-mean, T-periodic waveform corresponding to $\mu_{ii} = \mu^\star$ can be expressed as a Fourier series where all of the Fourier coefficients except for the first pair are zero. Such Fourier series represents a sinusoid, i.e.

$$v_i(t) = \widetilde{B}_i\Omega\cos(\Omega t + \phi_i) = \Omega\sum_{n=1}^{\infty}\left(a_{i,n}\cos(\Omega n t) + b_{i,n}\sin(\Omega n t)\right)$$

where $a_{i,1} = \widetilde{B}_i \cos(-\phi_i)$, $b_{i,1} = \widetilde{B}_i \sin(-\phi_i)$, and $a_{i,n}, b_{i,n} = 0$ for all $n > 1$. Thus, the minimum input energy continuous, zero-mean, T-periodic waveform corresponding to $\mu_{ii} = \mu^\star$ is a sinusoid.

Assume that $\boldsymbol{v}(t) = [v_1(t), \ldots, v_m(t)]^T$ is a vector of continuous, zero-mean, T-periodic input waveforms satisfying the conditions in equation (2.15). This assumption constrains the possible input waveforms $v_i(t)$ such that each input waveform has a prescribed value of μ_{ii}. Furthermore, each pair of input waveforms have a prescribed value of μ_{ij}.

Since every μ_{ij} only depends on the relative phase of the inputs, the value of μ_{ii} is constant regardless of phase shifts because the relative phase between a waveform and itself is always zero. Thus, the value of μ_{ii} is determined by the shape and amplitude of $v_i(t)$. Theorem 1.10 states that $\mu_{ij}^2 \leq \mu_{ii}\mu_{jj}$. Therefore, since μ_{ii} and μ_{jj} are described by the shape and amplitude of $v_i(t)$ and $v_j(t)$, respectively, μ_{ij} is determined primarily by the relative phase between $v_i(t)$ and $v_j(t)$.

The input energy of $\boldsymbol{v}(t)$, $\|\boldsymbol{v}(t)\|_{T,2}^2$, does not depend on the phase of the input waveforms. Therefore, changing the value of μ_{ij} by changing the relative phase of the inputs does not affect the input energy. The input energy of $\boldsymbol{v}(t)$ is the sum of the input energies of each individual $v_i(t)$, so the interaction of the input waveforms does not affect the input energy. Therefore, minimizing the input energy of $\boldsymbol{v}(t)$ with μ_{ij} satisfying equation (2.15) is equivalent to minimizing the input energy of each $v_i(t)$ with μ_{ii} satisfying equation (2.15).

As previously stated, for $v_i(t)$ with μ_{ii} satisfying equation (2.15) the minimum input energy input waveform corresponds to sinusoids. Therefore, if $\boldsymbol{v}(t) = [v_1(t), \ldots, v_m(t)]^T$ is a vector of continuous, zero-mean, T-periodic input waveforms satisfying the conditions in equation (2.15), the minimum input energy corresponds to sinusoidal input waveforms, i.e. $v_i(t) = \widetilde{B}_i \Omega \cos(\Omega t + \phi_i)$. □

2.2.4.1 Equivalence of Cost Functionals

Recall that the amplitude cost functional considered earlier was $\sum_{i=1}^m (\mathbf{amp}\, v_i(t))^2$. For square waves or sinusoids, this can be written as $\sum_{i=1}^m B_i^2$. Notice that the input energy for square waves and sinusoids is proportional to the sum of the square of the amplitudes, i.e. for input waveforms expressed as square waves or sinusoids $\|\boldsymbol{v}(t)\|_{T,2}^2 \propto \sum_{i=1}^m B_i^2$. Therefore, if the input waveforms are defined as square waves, the same input waveforms minimize both $\sum_{i=1}^m (\mathbf{amp}\, v_i(t))^2$ and $\|\boldsymbol{v}(t)\|_{T,2}^2$, and likewise for input waveforms defined as sinusoids. The proportionality constant is different when considering square waves and sinusoids. This difference leads to Theorem 2.6 stating that square waves are the best choice for minimizing $\sum_{i=1}^m (\mathbf{amp}\, v_i(t))^2$ and Theorem 2.7 stating that sinusoids are the best choice for minimizing the input energy. Similarly, the input impulse cost functional (2.11) is equivalent to both the amplitude and energy cost functionals.

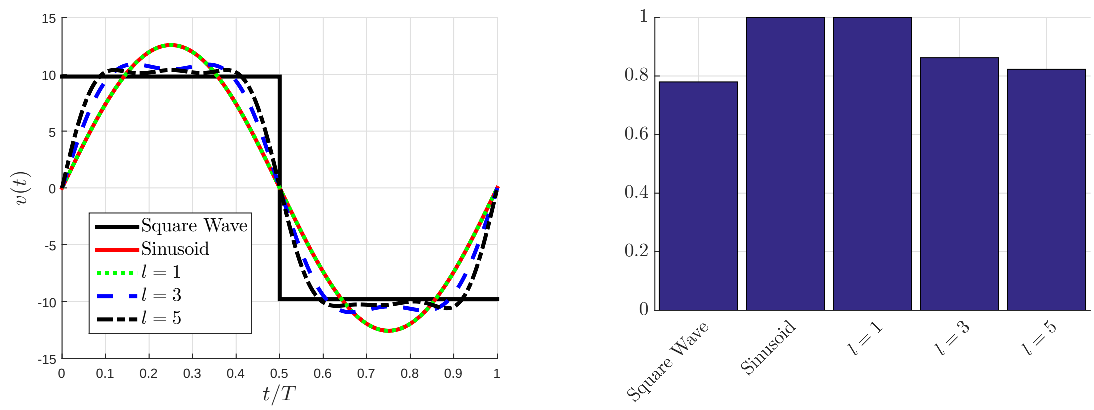

(a) $v(t)$ (b) Normalized Cost

Figure 2.1: Input amplitude minimizing waveforms. Five different input waveforms, corresponding to square waves, sinusoids, and truncated Fourier series with $l = 1, 3, 5$. As stated by Theorem 2.6, square waves are the input amplitude minimizing input waveforms. Sinusoids and truncated Fourier series with $l = 1$ have the highest cost, and increasing l yields better approximations of square waves and thus a lower cost.

2.2.4.2 Comparison of Solutions

As stated previously, the amplitude, energy, and impulse cost functionals are equivalent in the sense that the solution to one can be readily applied to another. However the best choice of waveform varies based on the cost functional. To illustrate this point, a vastly simplified problem is presented. Specifically, only one input waveform is considered with the constraint that $\mu = 1$. The input waveform optimization was then preformed using the three different cost functionals. The results are shown in Figures 2.1, 2.2, and 2.3.

Each figure shows the optimal input waveforms on the left and a normalized cost. The normalized cost[e] is the results of the optimization for different definitions of the input waveforms. Square waves, sinusoids, and truncated Fourier series with $l = 1, 3, 5$ are used to demonstrate the optimization. Notice that the results for the sinusoid and truncated Fourier series with $l = 1$ are the same.

In Figure 2.1, the square wave has the minimum cost, as is expected from Theorem 2.6. The sinusoid has the highest cost, and increasing the length of the truncated Fourier series results in increasingly accurate approximations of the square wave.

Figure 2.2 shows the optimal input waveforms with respect to the input energy cost functional. As expected from Theorem 2.7, the optimal input waveform is the sinusoid. Also

[e]The normalized cost is the cost normalized such that the greatest cost of a waveform is 1. This is done to avoid confusion over units. That is, the amplitude, impulse, and energy all have different units, so comparing their values directly can lead to confusion.

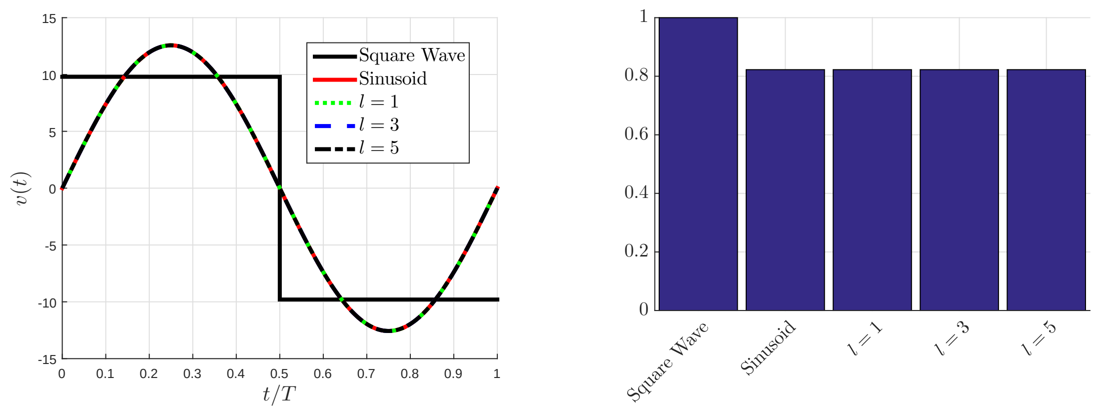

(a) $v(t)$ (b) Normalized Cost

Figure 2.2: Input energy minimizing waveforms. Five different input waveforms, corresponding to square waves, sinusoids, and truncated Fourier series with $l = 1, 3, 5$. As stated by Theorem 2.7, sinusoids minimize the input energy. As truncated Fourier series of any length are capable of exactly expressing sinusoids, all of the truncated Fourier series have the same cost as the sinusoid. The square wave has the highest cost.

as expected, all of the truncated Fourier series are the same as the sinusoid.[f]

Unlike the amplitude and energy cost functionals, there is not a clear optimal input waveform for impulse cost functional. All of the truncated Fourier series are an improvement on the square waves and sinusoid. In fact, the truncated Fourier series appears to be converging to an interesting optimum. This optimum is a large, short-duration pulse in one direction and then an equally large and short-duration pulse in opposite direction one half period later.

2.3 Constraints

The remaining essential part of a constrained optimization problem is the constraint. While there are numerous implicit constraints that will be discussed (i.e. limits on the values of ϕ_{ij}), the primary constraint for input waveform optimization is that the input waveforms achieve the desired behavior. If the desired behavior is defined as maintaining a stable periodic orbit about a desired state, Theorem 1.1 and the geometric averaging technique described in Section 1.2.2 can be used to establish this constraint.

Let the desired behavior be defined as "the system has a hyperbolically stable periodic orbit about $\boldsymbol{x}_e$." If the frequency of the input is high enough (i.e. $\epsilon < \epsilon_0$) and the averaged

[f] See the proof of Theorem 2.7 for more information.

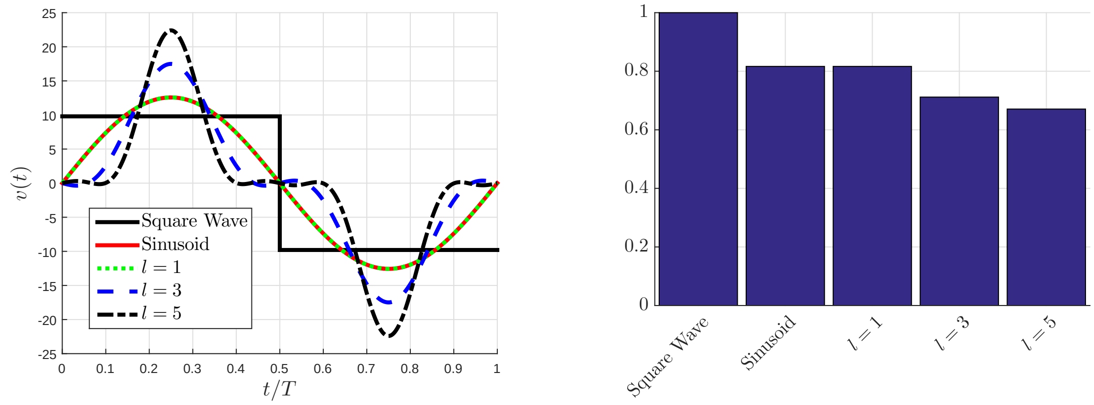

(a) $v(t)$ (b) Normalized Cost

Figure 2.3: Input impulse minimizing waveforms. Five different input waveforms, corresponding to square waves, sinusoids, and truncated Fourier series with $l = 1, 3, 5$. The optimal input waveform is a short, high-amplitude input one direction then another short, high amplitude input the other direction half of a period later. The truncated Fourier series approximate this waveform, with the accuracy of the approximation increasing with l. Thus, increasing l yields a lower cost with the lowest cost of displayed input waveforms corresponding to $l = 5$.

dynamics have a hyperbolically stable equilibrium at $\boldsymbol{x}_e$, then Theorem 1.1 states the actual dynamics will have a hyperbolically stable periodic orbit about $\boldsymbol{x}_e$. Using the geometric averaging technique described in Section 1.2.2, if $\boldsymbol{x}_e$ is a hyperbolically stable fixed point of the averaged dynamics, then, from (1.10),

$$\mathbf{Y}_0\left(\boldsymbol{x}_e\right) - \sum_{i,j=1}^{m} \mu_{ij} \left\langle \mathbf{Y}_i : \mathbf{Y}_j \right\rangle \left(\boldsymbol{x}_e\right) = \mathbf{0}_{2n\times 1} \tag{2.15}$$

must hold. This condition only guarantees that $\boldsymbol{x}_e$ is a fixed point, not that it is a hyperbolically stable fixed point. Therefore, the stability must be assessed separately. Also, this constraint does not allow for non-zero average velocities.

2.4 Limitations of Input Averaging

This technique of input averaging is very versatile, but has several limitations. These can be addressed by careful analysis, iterative testing, or extension of techniques. The limitations are as follows:

- The averaging theorem requires $\epsilon < \epsilon_0$ for some small ϵ_0, but does not provide any insight into how to determine ϵ_0. Bellman et al. [1985b] present a method for determining

ϵ_0, but their method yields conservative results.

- There may exist periodic orbits not predicted by the averaging theorem. These could occur when $\epsilon < \epsilon_0$. That is, a periodic orbit could exist that does not correspond to an equilibrium of the averaged dynamics. Furthermore, there could exist periodic orbits which are stable for a (perhaps small) range of $\epsilon > \epsilon_0$ [Berg and Manjula Wickramasinghe, 2015]. These are not predicted by the averaging theorem and thus are not considered.

- The constraint (2.15) does not allow for non-zero average velocities. Future work should extend the input waveform optimization technique to allow for non-zero average velocities.

2.5 Example

Consider the planar two-link mechanism on a cart depicted in Figure 2.4.[g] Each link is a uniform bar with mass m_i, $i \in \{1, 2\}$, length l_i, and mass moment of inertia $I_i = \frac{1}{12} m_i l_i^2$ about its center of mass. The mass of the cart is m_c. The system is a 3-DOF system with two inputs and moves in a horizontal plane; gravity does not affect the motion. The inputs are the force $F(t)$ acting on the cart and the torque $\tau(t)$ acting on the first link. We assume the system is subject to linear damping with coefficients of k_{d_1} and k_{d_2} in the first and second joints, respectively. Considering $\boldsymbol{q} = [x, \theta_1, \theta_2]^T$ as the vector of generalized coordinates, the goal is to generate a stable periodic orbit in a $O(\epsilon)$ neighborhood of a desired configuration $\boldsymbol{q}_\mathrm{d} = [x_\mathrm{d}, \theta_{d_1}, \theta_{d_2}]^T$, while using inputs with minimum amplitudes.

The dynamics of the system can be written as

$$\boldsymbol{M}\left(\boldsymbol{q}\right)\ddot{\boldsymbol{q}} = \boldsymbol{f}\left(\boldsymbol{q}, \dot{\boldsymbol{q}}\right) + \boldsymbol{F}_c(t)$$

where the mass matrix is

$$\boldsymbol{M}(\boldsymbol{q}) = \begin{bmatrix} m_\mathrm{c} + m_1 + m_2 & -\frac{1}{2}(m_1 + 2m_2) l_1 \sin\theta_1 & -\frac{1}{2} m_2 l_2 \sin\theta_2 \\ -\frac{1}{2}(m_1 + 2m_2) l_1 \sin\theta_1 & I_1 + \frac{1}{4}(m_1 + 4m_2) l_1^2 & \frac{1}{2} m_2 l_1 l_2 \cos(\theta_1 - \theta_2) \\ -\frac{1}{2} m_2 l_2 \sin\theta_2 & \frac{1}{2} m_2 l_1 l_2 \cos(\theta_1 - \theta_2) & I_2 + \frac{1}{4} m_2 l_2^2 \end{bmatrix}$$

and the vector of inputs

$$\boldsymbol{F}_\mathrm{c}(t) = \begin{bmatrix} F(t) \\ \tau(t) \\ 0 \end{bmatrix}$$

Consider the following inputs

$$\begin{aligned} F(t) &= -k_{\mathrm{p_c}}(x - x_\mathrm{d}) - k_{\mathrm{d_c}}\dot{x} + \omega v_1(\omega t) \\ \tau(t) &= \tau_\mathrm{s} - k_{p_1}(\theta_1 - \theta_{d_1}) + \omega v_2(\omega t + \phi) \end{aligned} \tag{2.16}$$

[g] This example was developed in collaboration with Dr. Sevak Tahmasian.

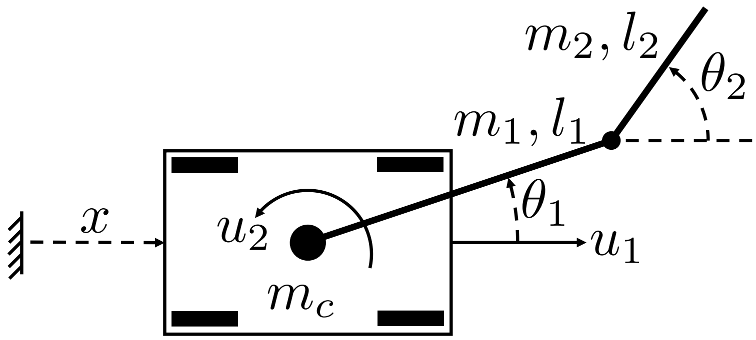

Figure 2.4: A two-link mechanism on a cart in a horizontal plane

where $v_1(t)$ and $v_2(t)$ are T-periodic, zero-mean functions, $k_{\mathrm{p_c}}$, k_{p_1}, and $k_{\mathrm{d_c}}$ are control parameters, and τ_{s} is a nonzero constant.

Using the state vector $\boldsymbol{x} = (\boldsymbol{q}^T, \dot{\boldsymbol{q}}^T)^T$, one may transform the equations of motion of the system into the form (1.9) with $m = 2$, and determine the averaged dynamics using Theorem 1.8. The averaged dynamics is in the form

$$\dot{\overline{\boldsymbol{x}}} = \boldsymbol{Y}_0(\overline{\boldsymbol{x}}) - \sum_{i,j=1}^{2} \mu_{ij} \langle \boldsymbol{Y}_i : \boldsymbol{Y}_j \rangle (\overline{\boldsymbol{x}}) \tag{2.17}$$

where $\boldsymbol{Y}_i$ is the i^{th} column of $\boldsymbol{M}^{-1}(\boldsymbol{q})$, and

$$\boldsymbol{Y}_0(\boldsymbol{x}) = \begin{bmatrix} \dot{\boldsymbol{q}} \\ \boldsymbol{M}^{-1}(\boldsymbol{q})\big(\boldsymbol{f}(\boldsymbol{q}, \dot{\boldsymbol{q}}) + \boldsymbol{g}(\boldsymbol{q}, \dot{\boldsymbol{q}})\big) \end{bmatrix}$$

where

$$\boldsymbol{g}(\boldsymbol{q}, \dot{\boldsymbol{q}}) = \begin{bmatrix} -k_{\mathrm{p_c}}(x - x_{\mathrm{d}}) - k_{\mathrm{d_c}}\dot{x} \\ \tau_s - k_{p_1}(\theta_1 - \theta_{d_1}) \\ 0 \end{bmatrix}.$$

Using the inputs (2.16), the system may possess a stable periodic orbit in an $O(\frac{1}{\omega})$ neighborhood of $\boldsymbol{q}_{\mathrm{d}}$. This happens if the point $\boldsymbol{x}_{\mathrm{e}} = \left[\boldsymbol{q}_{\mathrm{d}}^T, \boldsymbol{0}_{1\times 3}\right]^T$ is a hyperbolically stable equilibrium point of the averaged dynamics. For the point $\boldsymbol{x}_{\mathrm{e}}$ to be an equilibrium point of the averaged system, it must satisfy

$$\boldsymbol{Y}_0(\boldsymbol{x}_{\mathrm{e}}) - \sum_{i,j=1}^{2} \mu_{ij} \langle \boldsymbol{Y}_i : \boldsymbol{Y}_j \rangle (\boldsymbol{x}_{\mathrm{e}}) = \boldsymbol{0} \tag{2.18}$$

The set of algebraic equations (2.18) contains six equations, the first three being satisfied automatically because of the system structure. For the point $\boldsymbol{q}_{\mathrm{d}}$ to be an equilibrium point of the averaged dynamics, one needs to choose parameters to satisfy the last three equations of (2.18).

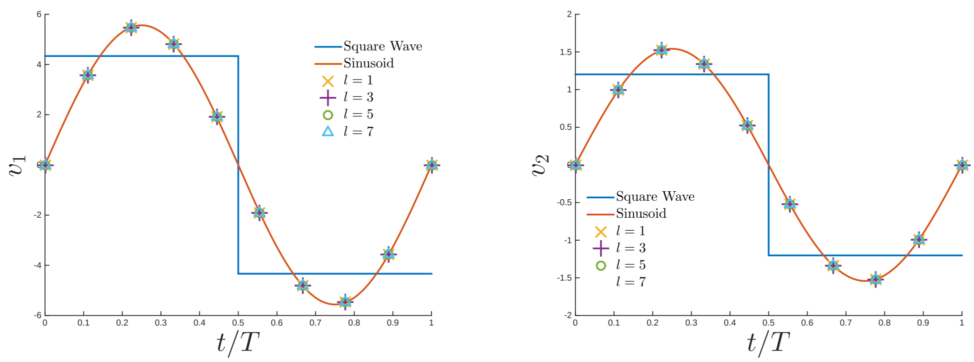

Figure 2.5: Optimal input waveforms for the two-link mechanism on a cart.

To follow a periodic orbit about the point $\boldsymbol{q}_{\mathrm{d}}$ one should choose a value for τ_{s} and find μ_{ij}, $i, j \in \{1, 2\}$, to satisfy equations (2.18). Depending on the physical parameters of the system, there may be no acceptable solution for μ_{ij}.

One important observation is that only two of the last three equations of (2.18) are independent. Therefore there is a set of two independent equations in three unknowns $\mu_{ij} = \mu_{ji}$. The equations yield a one-parameter family of solutions. There is thus parametric freedom available for further optimization.

Consider the case where the links have mass per unit length ρ_m. For the physical parameters

$$
\begin{array}{lllll}
m_{\mathrm{c}} = 1 \text{ kg}, & \rho_m = 1 \text{ kg/m}, & l_1 = 0.8 \text{ m}, & l_2 = 1 \text{ m} & \\
k_{\mathrm{p_c}} = 5, & k_{\mathrm{d_c}} = 2, & k_{p_1} = 10, & k_{d_1} = 2, & k_{d_2} = 1
\end{array}
$$

and for $x_{\mathrm{d}} = 0$, $\theta_{d_1} = -\frac{\pi}{9}$ rad, $\theta_{d_2} = \frac{\pi}{9}$ rad, and $\tau_s = 1$ N.m, the set of equations (2.18) to be satisfied are

$$
\begin{aligned}
0.2271\mu_{11} - 0.6111\mu_{12} - 1.5465\mu_{22} &= -0.4727 \\
1.0179\mu_{11} - 3.1218\mu_{12} - 5.9772\mu_{22} &= -2.3732 \\
1.4390\mu_{11} - 3.0137\mu_{12} - 11.9323\mu_{22} &= -2.4241
\end{aligned}
\tag{2.19}
$$

The set of equations in Equation (2.19) contain two independent equations and three unknowns. There are infinite number of possible inputs $v_1(t)$ and $v_2(t)$ to be chosen. The cost functional is chosen to be the input energy (see Section 2.2.2). Both the amplitude and phase method and the truncated Fourier series method were used to minimize the input energy. Square wave, sinusoids, and truncate Fourier series of various lengths were considered, although Theorem 2.7 states that sinusoids minimize the input energy.

The optimal input waveforms are shown in Figure 2.5. The sinusoid is the optimal solution, as shown in Theorem (2.7), and every truncated Fourier series lies on the sinusoid.

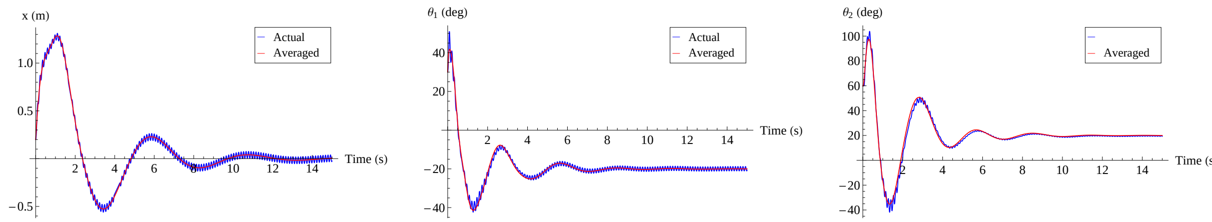

Figure 2.6: Simulation of the dynamics of the two-link mechanism on a cart with input waveforms defined as square waves.

This is the expected result as truncated Fourier series can exactly replicate a sinusoid (this fact was utilized in the proof of Theorem 2.7). The square waves have the lowest amplitude (as expected from Theorem 2.6), but have greater input energy.

The dynamics of system were simulated using square waves as the input waveforms. These simulations are shown in Figure 2.6[h]. These show that although the system did not begin at the desired point, the input waveforms created a stable periodic orbit about the desired equilibrium. Figure 2.6 also shows the relationship between the averaged and actual dynamics; the actual dynamics appear a rapid oscillation in the neighborhood of the averaged dynamics.

2.6 Contributions

In this section, a technique for input waveform optimization was developed. Much of this work was first present in [Tahmasian et al., 2016]. This technique built on the geometric averaging technique presented by Bullo and Lewis [2005]. This technique, which was developed along with Dr. Sevak Tahmasian, differs from previous work in that it uses the structure provided by Bullo and Lewis [2005] in order to determine the optimal input waveforms that will vibrationally stabilize a desired equilibrium. This is accomplished by posing the problem as a constrained optimization problem.

This dissertation develops two parameterizations for input waveforms. The first being a relatively simple parameterization that modulates the amplitude and phase of archetypal waveforms. e.g. square waves or sinusoids. The other parameterization is a truncated Fourier series. This truncated Fourier series is capable of approximating a large class of input waveform. Unlike the former parameterization, the constrained optimization problem must be solved numerically when using truncated Fourier series. Unfortunately, increasing the

[h]Figure 2.6 was generated by Dr. Sevak Tahmasian as part of a collaborative work and appears in [Tahmasian et al., 2016].

number of parameters greatly increases the computational expense of solving the constrained optimization problem.

Two new cost functionals were developed, input energy and impulse. For the input energy optimization problem, sinusoids were shown to be the optimal input waveforms. Truncated Fourier series were used to demonstrate that the optimal input waveforms for the input impulse optimization problem are alternating impulses.

Chapter 3

Pisciform Locomotion

The purpose of this section is to develop a model of pisciform locomotion. That is, the primary objective of this section is to develop a model than can be used to approximate the spectrum of fish locomotion. The model must be computationally inexpensive, requiring only modest computer hardware to preform numerous simulations, but be able to capture the complex undulatory motion of pisciform locomotors. This is accomplished by having multiple hydrofoils connected by rigid links that do not interact hydrodynamically. The hydrofoils produce downwash, which affects the flow on other hydrofoils. A new control methodology is introduced that allows the control inputs to be the shape coordinates, rather than joint torques. This chapter is divided into four sections: 1) a section discussing the pisciform locomotion in the context of examples of extant species of fish, 2) a section developing the model and control methodology, 3) a section presenting simulations of a representative thunniform system, and 4) a section discussing related experimental results performed by others.

3.1 Examples from Biology

In nature, there are countless variations in the locomotion of aquatic animals. There are many methods of swimming, but this research will focus on Body and Caudal Fin (BCF) locomotion. Sfakiotakis et al. [1999] describe the different types of BCF locomotion along a spectrum from undulatory to oscillatory locomotion, as shown in Figure 3.1. As the name implies, BCF locomotion primarily involves body and caudal fin movement for propulsion and maneuvering. Other types of locomotion are described by Sfakiotakis et al. [1999] that primarily use other fins, e.g. anal, dorsal, or pectoral fins, for propulsion and maneuvering. These other types of locomotion will not be considered as they cannot be represented by the BCF model described in Section 3.2.

There are five types of BCF locomotion. Listed in order from the most undulatory to

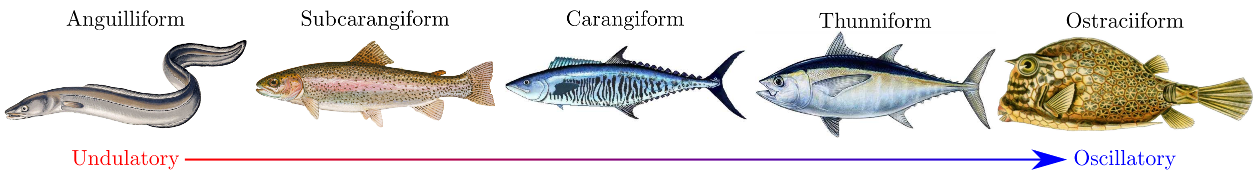

Figure 3.1: Spectrum of body and caudal fin locomotion. Images of fish are in the public domain, either out of copyright or derivative works of the US Government.

Table 3.1: Types of Fish Locomotion and Associated Taxonomical Group.

Locomotion Type	Taxonomical Group	Example
Ostraciiform	Family Ostraciidae	Box-fish
Thunniform	Genus Thunnus	Tunas
Carangiform	Family Carangidae	Pompano
Subcarangiform	—	Trout
Anguilliform	Family Anguillidae	Freshwater Eels

the most oscillatory, they are anguilliform, subcarangiform, carangiform, thunniform, and ostraciiform. The names of these types of locomotion refer to the taxonomical group most associated with the type of locomotion.[a] This association is shown in Table 3.1.

3.2 Model

The system model is shown in Figure 3.2. This model is meant to represent a fish that uses BCF locomotion for propulsion and maneuvering. The model has three types of components: a body, peduncles, and fins. Figure 3.2 shows four fins, each with a peduncle, but the model will be made adaptable to an arbitrary number of fins. If only one fin and peduncle is included, this model is analogous to the models presented by Mason and Burdick [2000]; Morgansen et al. [2001, 2002, 2007]. All components are assumed to be thin along their lengths and have a uniform mass distribution. The body has a mass m_b and a length l_b. the ith peduncle has a mass and length of $m_{\mathrm{p},i}$ and $l_{\mathrm{p},i}$, respectively. Similarly, the ith fin has a mass and length of $m_{\mathrm{f},i}$ and $l_{\mathrm{f},i}$, respectively. The number of fins (which is the same as the number of peduncles) is denoted by L. Since this is a planar problem all masses, inertias, moments, and forces are per unit depth. That is, all components are assumed to have an infinite aspect ratio.

[a]Subcarangiform means "below"-carangiform, thus it exists somewhere in the spectrum between anguilliform and carangiform.

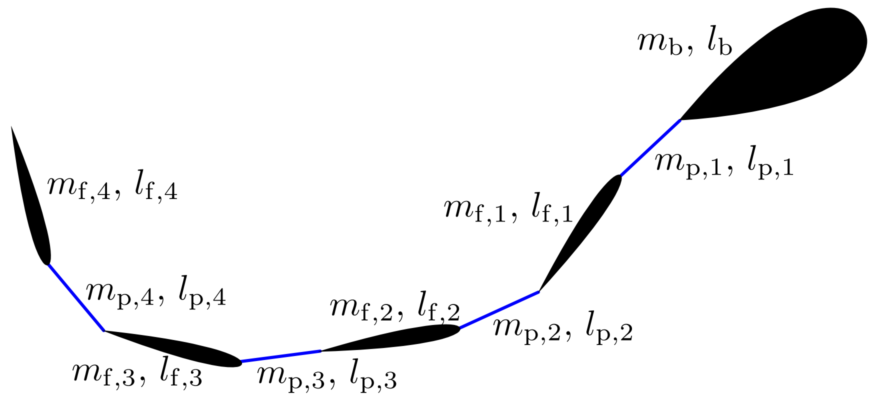

Figure 3.2: Multi-link model of a fish with four fins, i.e. $L = 4$.

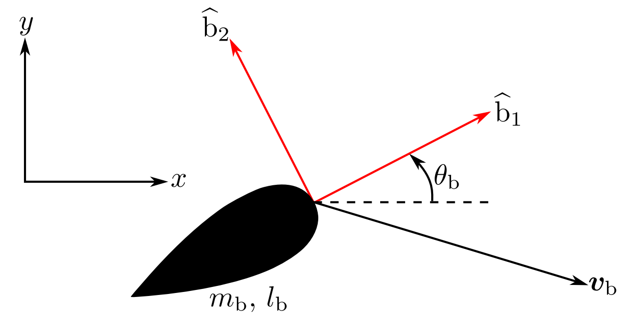

Figure 3.3: Coordinate conventions for the body of the multi-link fish

3.2.1 Kinematics

The configuration of the body is an element of $\mathrm{SE}\,(2)$ and is parameterized by three coordinates, x, y, and θ_{b} as shown in Figure 3.3. Note that x and y are measured relative to an inertial coordinate system and θ_{b} is measured relative to the inertial x-axis. The position vector connecting the inertial origin to the leading edge of the body is $\boldsymbol{r}_{\mathrm{b}}$. The velocity of the body is an element of $\mathfrak{se}(2)$ and is parameterized by $\mathbf{v}_{\mathrm{b}}$ and $\dot{\theta}_{\mathrm{b}}$. There is a body-fixed coordinate system, $\widehat{\mathrm{b}}_1$, $\widehat{\mathrm{b}}_2$, which is aligned to the inertial coordinate system when $\theta_{\mathrm{b}} = 0$.

The coordinate conventions for the ith fin and peduncle are shown in Figure 3.4. Note that if $i = 1$, then the $(i-1)$th fin is the body (and there is no $(i-1)$th peduncle). The green axes, $\widehat{\mathrm{p}}_{i,1}, \widehat{\mathrm{p}}_{i,2}$ and $\widehat{\mathrm{f}}_{i,1}, \widehat{\mathrm{f}}_{i,2}$, are axes fixed to the ith peduncle and fin, respectively. The multi-link fish model is an articulated body, so the shape of the body is determined by a finite number of angles. Specifically, the number of angles that define the shape of the body is $2L$ in this case.

There are three different choices for the joint angles, only one of which is shown in Figure 3.4. The angles shown in Figure 3.4, denoted $\theta_{\mathrm{p},i}$ and $\theta_{\mathrm{f},i}$, are called the *joint relative angles*.

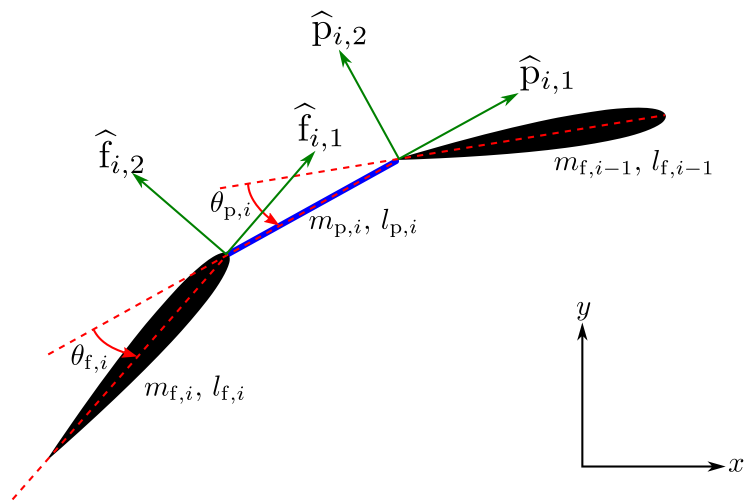

Figure 3.4: Coordinate conventions for the ith peduncle and fin of the multi-link fish. The dashed red lines are the centerlines of appropriate bodies.

Another useful set of angles are the *inertial angles*, which are measured relative to the inertial x-axis and denoted with ψ. It is straightforward to calculate these angles by summing the joint relative angles, specifically,

$$\psi_{\mathrm{p},i} = \pi + \theta_{\mathrm{b}} + \theta_{\mathrm{p},i} + \sum_{j=1}^{i-1} \theta_{\mathrm{p},j} + \theta_{\mathrm{f},j} \qquad \psi_{\mathrm{f},i} = \pi + \theta_{\mathrm{b}} + \sum_{j=1}^{i} \theta_{\mathrm{p},j} + \theta_{\mathrm{f},j} \tag{3.1}$$

Lastly, the *body relative angles*, denoted with ϕ, are angles measured relative to the $-\widehat{\mathrm{b}}_1$ axis and can be found using

$$\phi_{\mathrm{p},i} = \psi_{\mathrm{p},i} - \pi - \theta_{\mathrm{b}} = \theta_{\mathrm{p},i} + \sum_{j=1}^{i-1} \theta_{\mathrm{p},j} + \theta_{\mathrm{f},j} \qquad \phi_{\mathrm{f},i} = \psi_{\mathrm{f},i} - \pi - \theta_{\mathrm{b}} = \sum_{j=1}^{i} \theta_{\mathrm{p},j} + \theta_{\mathrm{f},j} \tag{3.2}$$

The choice of which set of angles is used is entirely based on what is most convenient.

3.2.1.1 Velocities

For each link, there are several translational velocities that are necessary for later analysis. For the hydrodynamics surfaces, i.e. the fins and body, the velocity of the quarter chord point is necessary. For all links, the velocities of the midpoints, leading edges, and trailing edges are necessary. Since this is an articulated body, the velocity of the leading edge of a link is the same as the velocity of the trailing edge of the preceding link. Thus, the velocities of the leading and trailing edges of the links can be defined in series. Specifically, the velocity of the trailing edge of each peduncle and fin (in the inertial frame[b]) can be defined as

$$\mathbf{v}_{\mathrm{p},i,\mathrm{TE}} = \mathbf{v}_{\mathrm{p},i,\mathrm{LE}} + l_{\mathrm{p},i}\dot{\psi}_{\mathrm{p},i}\begin{bmatrix} -\sin\psi_{\mathrm{p},i} \\ \cos\psi_{\mathrm{p},i} \\ 0 \end{bmatrix} \qquad \mathbf{v}_{\mathrm{f},i,\mathrm{TE}} = \mathbf{v}_{\mathrm{f},i,\mathrm{LE}} + l_{\mathrm{f},i}\dot{\psi}_{\mathrm{f},i}\begin{bmatrix} -\sin\psi_{\mathrm{f},i} \\ \cos\psi_{\mathrm{f},i} \\ 0 \end{bmatrix} \tag{3.3}$$

where $\mathbf{v}_{\mathrm{p},i,\mathrm{LE}}$ and $\mathbf{v}_{\mathrm{f},i,\mathrm{LE}}$ are the velocities of the leading edges of the ith peduncle and fin, respectively. Since this is an articulated body, it can be seen that $\mathbf{v}_{\mathrm{f},i,\mathrm{LE}} = \mathbf{v}_{\mathrm{p},i,\mathrm{TE}}$ and $\mathbf{v}_{\mathrm{p},i,\mathrm{LE}} = \mathbf{v}_{\mathrm{f},i-1,\mathrm{TE}}$. Using these properties, it is possible to determine the velocities of the leading and trailing edges of every fin and peduncle in series, so all that is needed is the velocity of the leading edge of the first peduncle, $\mathbf{v}_{\mathrm{p},1,\mathrm{LE}}$. Since the first peduncle is attached to the body, the $\mathbf{v}_{\mathrm{p},1,\mathrm{LE}} = \mathbf{v}_{\mathrm{b},\mathrm{TE}}$. Notice from Figure 3.3, $\mathbf{v}_{\mathrm{b}}$ is the velocity of the leading edge of the body, so the velocities of the trailing edge of the body (and the velocity of the leading edge of the first peduncle) is

$$\mathbf{v}_{\mathrm{b},\mathrm{TE}} = \mathbf{v}_{\mathrm{p},1,\mathrm{LE}} = \mathbf{v}_{\mathrm{b}} + l_{\mathrm{b}}\dot{\theta}_{\mathrm{b}}\begin{bmatrix} \sin\theta_{\mathrm{b}} \\ -\cos\theta_{\mathrm{b}} \\ 0 \end{bmatrix}$$

Now that the velocity of every leading and trailing edge is known, it is straightforward to determine the velocity of the midpoints and quarter chord points. The velocity of the midpoints of the ith fin and peduncle are

$$\mathbf{v}_{\mathrm{p},i,\mathrm{m}} = \mathbf{v}_{\mathrm{p},i,\mathrm{LE}} + \frac{l_{\mathrm{p},i}}{2}\dot{\psi}_{\mathrm{p},i}\begin{bmatrix} -\sin\psi_{\mathrm{p},i} \\ \cos\psi_{\mathrm{p},i} \\ 0 \end{bmatrix} \quad \text{and} \quad \mathbf{v}_{\mathrm{f},i,\mathrm{m}} = \mathbf{v}_{\mathrm{f},i,\mathrm{LE}} + \frac{l_{\mathrm{f},i}}{2}\dot{\psi}_{\mathrm{f},i}\begin{bmatrix} -\sin\psi_{\mathrm{f},i} \\ \cos\psi_{\mathrm{f},i} \\ 0 \end{bmatrix}$$

respectively. As the peduncle is assumed to have no hydrodynamic loading, it is not necessary to find the velocity of its quarter chord point. The fins, however, are hydrodynamic surfaces and the velocities of their quarter chord points are important because the hydrodynamic model assumes that lift and drag act at the quarter chord point. The velocity of the quarter chord point of the ith fin is

$$\mathbf{v}_{\mathrm{f},i,\mathrm{qc}} = \mathbf{v}_{\mathrm{f},i,\mathrm{LE}} + \frac{l_{\mathrm{f},i}}{4}\dot{\psi}_{\mathrm{f},i}\begin{bmatrix} -\sin\psi_{\mathrm{f},i} \\ \cos\psi_{\mathrm{f},i} \\ 0 \end{bmatrix} \tag{3.4}$$

The velocity of the midpoint and quarter chord point of the body can be found using similar expressions, accounting for the difference between θ_{b} and $\psi_{\mathrm{f},i}$. Specifically, the velocity of the midpoint and quarter chord point of the body are

$$\mathbf{v}_{\mathrm{b},\mathrm{m}} = \mathbf{v}_{\mathrm{b}} + \frac{l_{\mathrm{b}}}{2}\dot{\theta}_{\mathrm{b}}\begin{bmatrix} \sin\theta_{\mathrm{b}} \\ -\cos\theta_{\mathrm{b}} \\ 0 \end{bmatrix} \quad \text{and} \quad \mathbf{v}_{\mathrm{b},\mathrm{qc}} = \mathbf{v}_{\mathrm{b}} + \frac{l_{\mathrm{b}}}{4}\dot{\theta}_{\mathrm{b}}\begin{bmatrix} \sin\theta_{\mathrm{b}} \\ -\cos\theta_{\mathrm{b}} \\ 0 \end{bmatrix} \tag{3.5}$$

respectively.

[b] All velocities denoted with a $\mathbf{v}$ are in the inertial frame.

3.2.1.2 Positions

For reasons that will be explained later, it is necessary to define the positions of the important points along the articulated body. As before, these points are the leading edge, trailing edge, midpoint, and quarter chord of the various bodies. These positions are relative to the same inertial frame that defined $\boldsymbol{r}_{\mathrm{b}}$ before.[c] Recall that $\boldsymbol{r}_{\mathrm{b}}$ is the position vector indicating the position of the leading edge of the body, thus the position of the trailing edge, midpoint, and quarter chord are

$$\boldsymbol{r}_{\mathrm{b,TE}} = \boldsymbol{r}_{\mathrm{b}} + l_{\mathrm{b}} \begin{bmatrix} -\cos\theta_{\mathrm{b}} \\ -\sin\theta_{\mathrm{b}} \\ 0 \end{bmatrix} \quad \boldsymbol{r}_{\mathrm{b,m}} = \boldsymbol{r}_{\mathrm{b}} + \frac{l_{\mathrm{b}}}{2} \begin{bmatrix} -\cos\theta_{\mathrm{b}} \\ -\sin\theta_{\mathrm{b}} \\ 0 \end{bmatrix} \quad \boldsymbol{r}_{\mathrm{b,qc}} = \boldsymbol{r}_{\mathrm{b}} + \frac{l_{\mathrm{b}}}{4} \begin{bmatrix} -\cos\theta_{\mathrm{b}} \\ -\sin\theta_{\mathrm{b}} \\ 0 \end{bmatrix}$$

respectively. Notice that the position of the trailing edge of the body is the position of the leading edge of the first peduncle, i.e. $\boldsymbol{r}_{\mathrm{b,TE}} = \boldsymbol{r}_{\mathrm{p,1,LE}}$. Again, since this is an articulated body, the position of the leading edge of one link is the same as the position of the trailing edge of the preceding link. Thus,

$$\boldsymbol{r}_{\mathrm{p},i,\mathrm{LE}} = \boldsymbol{r}_{\mathrm{f},i-1,\mathrm{TE}} \qquad \text{and} \qquad \boldsymbol{r}_{\mathrm{f},i,\mathrm{LE}} = \boldsymbol{r}_{\mathrm{p},i,\mathrm{TE}}$$

The positions of the midpoint and trailing edge of the ith peduncle are

$$\boldsymbol{r}_{\mathrm{p},i,\mathrm{m}} = \boldsymbol{r}_{\mathrm{p},i,\mathrm{LE}} + \frac{l_{\mathrm{p},i}}{2} \begin{bmatrix} \cos\psi_{\mathrm{p},i} \\ \sin\psi_{\mathrm{p},i} \\ 0 \end{bmatrix} \qquad \text{and} \qquad \boldsymbol{r}_{\mathrm{p},i,\mathrm{TE}} = \boldsymbol{r}_{\mathrm{p},i,\mathrm{LE}} + l_{\mathrm{p},i} \begin{bmatrix} \cos\psi_{\mathrm{p},i} \\ \sin\psi_{\mathrm{p},i} \\ 0 \end{bmatrix}$$

respectively. Similarly, the positions of the quarter chord, midpoint, and trailing edge of the ith fin are

$$\boldsymbol{r}_{\mathrm{f},i,\mathrm{qc}} = \boldsymbol{r}_{\mathrm{f},i,\mathrm{LE}} + \frac{l_{\mathrm{f},i}}{4} \begin{bmatrix} \cos\psi_{\mathrm{f},i} \\ \sin\psi_{\mathrm{f},i} \\ 0 \end{bmatrix} \quad \boldsymbol{r}_{\mathrm{f},i,\mathrm{m}} = \boldsymbol{r}_{\mathrm{f},i,\mathrm{LE}} + \frac{l_{\mathrm{f},i}}{2} \begin{bmatrix} \cos\psi_{\mathrm{f},i} \\ \sin\psi_{\mathrm{f},i} \\ 0 \end{bmatrix} \quad \boldsymbol{r}_{\mathrm{f},i,\mathrm{TE}} = \boldsymbol{r}_{\mathrm{f},i,\mathrm{LE}} + l_{\mathrm{f},i} \begin{bmatrix} \cos\psi_{\mathrm{f},i} \\ \sin\psi_{\mathrm{f},i} \\ 0 \end{bmatrix}$$

respectively.

3.2.2 Rigid Body Mechanics

The rigid body mechanics will be determined using Lagrangian mechanics. The first step is to define the generalized coordinates. The generalized coordinates are separated into group coordinates, $\mathbf{r}$ and shape coordinates $\mathbf{s}$. The group coordinates define the state of the body and are generally the coordinates of the most interest for motion planning. That is, when

[c] All position vectors denoted by $\boldsymbol{r}$ are with respect to this inertial frame.

describing the "velocity" of the multi-link fish, one is typically referring to the rate of change of the group coordinates. The group coordinates are

$$\mathbf{r} = \begin{bmatrix} x \\ y \\ \theta_{\mathrm{b}} \end{bmatrix} \tag{3.6}$$

The shape coordinates, $\mathbf{s}$, define the shape of the multi-link fish. Since the fish is an articulated body, the shape coordinates are the joint angles. For reasons that will be made clear later, the body-relative angles will be used. Thus the shape coordinates are

$$\mathbf{s} = \begin{bmatrix} \phi_{\mathrm{p},1} \\ \phi_{\mathrm{f},1} \\ \phi_{\mathrm{p},2} \\ \phi_{\mathrm{f},2} \\ \vdots \\ \phi_{\mathrm{p},L} \\ \phi_{\mathrm{f},L} \end{bmatrix} \tag{3.7}$$

The generalized coordinates, $\boldsymbol{q}$, are the group and shape coordinates, specifically $\boldsymbol{q} = \left[\mathbf{r}^T, \mathbf{s}^T\right]^T$. The generalized velocities are therefore $\dot{\boldsymbol{q}} = \left[\dot{\mathbf{r}}^T, \dot{\mathbf{s}}^T\right]^T$ where

$$\dot{\mathbf{r}} = \begin{bmatrix} \dot{x} \\ \dot{y} \\ \dot{\theta}_{\mathrm{b}} \end{bmatrix} \qquad \text{and} \qquad \dot{\mathbf{s}} = \begin{bmatrix} \dot{\phi}_{\mathrm{p},1} \\ \dot{\phi}_{\mathrm{f},1} \\ \dot{\phi}_{\mathrm{p},2} \\ \dot{\phi}_{\mathrm{f},2} \\ \vdots \\ \dot{\phi}_{\mathrm{p},L} \\ \dot{\phi}_{\mathrm{f},L} \end{bmatrix}$$

Note that the body relative angles, e.g. $\phi_{\mathrm{p},i}$ and $\phi_{\mathrm{f},i}$, are not measured relative to an inertial frame. So a change of variables, see Equation (3.2), is needed to convert between body relative and inertial angles.

As the mass in each of the links is assumed to be uniformly distributed, the center of mass of each body is at its midpoint.[d] Let I_{b} be the moment of inertia about the center of mass of the body and let $I_{\mathrm{p},i}$ and $I_{\mathrm{f},i}$ be the moment of inertia about the centers of mass of the ith peduncle and fin, respectively. Using this, along with the inertial velocities of the midpoints[e] described in Section 3.2.1, it is straightforward to compute the total kinetic

[d]The body and fins are assumed to be slender, so the thickness variation along the length of the fins and body is assumed to not affect mass distribution.

[e]The midpoints are assumed to be the centers of mass.

energy of the system with respect to the inertial coordinates

$$T(\mathbf{r},\boldsymbol{\psi},\dot{\mathbf{r}},\dot{\boldsymbol{\psi}}) = \frac{1}{2}\left(m_{\mathrm{b}}\left\|\mathbf{v}_{\mathrm{b,m}}\right\|_2^2 + I_{\mathrm{b}}\dot{\theta}_{\mathrm{b}}^2 + \sum_{i=1}^{L} m_{\mathrm{p},i}\left\|\mathbf{v}_{\mathrm{p},i,\mathrm{m}}\right\|_2^2 + I_{\mathrm{p},i}\dot{\psi}_{\mathrm{p},i}^2 + m_{\mathrm{f},i}\left\|\mathbf{v}_{\mathrm{f},i,\mathrm{m}}\right\|_2^2 + I_{\mathrm{f},i}\dot{\psi}_{\mathrm{f},i}^2\right)$$

where $\boldsymbol{\psi}$ is the vector of inertial angles, i.e. $\boldsymbol{\psi} = \left[\psi_{\mathrm{p},1},\psi_{\mathrm{f},1},\psi_{\mathrm{p},2},\psi_{\mathrm{f},2},\ldots,\psi_{\mathrm{p},L},\psi_{\mathrm{f},L}\right]^T$. From (3.2), we have

$$\psi_{\mathrm{p},i} = \phi_{\mathrm{p},i} + \pi + \theta_{\mathrm{b}} \qquad\qquad \psi_{\mathrm{f},i} = \phi_{\mathrm{f},i} + \pi + \theta_{\mathrm{b}}$$

and therefore

$$\dot{\psi}_{\mathrm{p},i} = \dot{\phi}_{\mathrm{p},i} + \dot{\theta}_{\mathrm{b}} \qquad\qquad \dot{\psi}_{\mathrm{f},i} = \dot{\phi}_{\mathrm{f},i} + \dot{\theta}_{\mathrm{b}}$$

Using these expressions, it is straightforward to express the total kinetic energy of the system as a function of the group and shape coordinates, i.e. $T = T(\mathbf{r},\mathbf{s},\dot{\mathbf{r}},\dot{\mathbf{s}})$, by simple substitution. Specifically

$$\begin{aligned} T = T(\mathbf{r},\mathbf{s},\dot{\mathbf{r}},\dot{\mathbf{s}}) =& \frac{1}{2}\Bigg(m_{\mathrm{b}}\left\|\mathbf{v}_{\mathrm{b,m}}\right\|_2^2 + I_{\mathrm{b}}\dot{\theta}_{\mathrm{b}}^2 + \sum_{i=1}^{L}\left[m_{\mathrm{p},i}\left\|\mathbf{v}_{\mathrm{p},i,\mathrm{m}}\right\|_2^2 + I_{\mathrm{p},i}\left(\dot{\phi}_{\mathrm{p},i}+\dot{\theta}_{\mathrm{b}}\right)^2\right] \\ &+ \sum_{i=1}^{L}\left[m_{\mathrm{f},i}\left\|\mathbf{v}_{\mathrm{f},i,\mathrm{m}}\right\|_2^2 + I_{\mathrm{f},i}\left(\dot{\phi}_{\mathrm{f},i}+\dot{\theta}_{\mathrm{b}}\right)^2\right]\Bigg) \end{aligned} \tag{3.8}$$

The summation in (3.8) is split for the purposes of clarity. There is no potential energy stored in the system. Thus, the Lagrangian of the system is the kinetic energy:

$$L = T + T_{\mathrm{A}}$$

where T_{A} is the energy required to accelerate the fluid around the body. This additional energy, referred to as added mass, is described in Section 3.2.2.1.

3.2.2.1 Added Mass

The added mass is the proportionality constant between the pressure-induced forces and moments and the accelerations [Fossen, 1994]. For the model of the multi-link fish presented here, only the body and fins will be considered to have added mass. Based on the added mass of a slender ellipse presented by Fossen [1994], the added mass in the direction of the 1-axis of the body is zero (i.e. $m_{\mathrm{A},1} = 0$), and the added mass in the direction of the 2-axis and the added inertia are

$$m_{\mathrm{A},2} = \pi\rho l^2 \qquad\qquad m_{\mathrm{A},3} = \frac{1}{8}\pi\rho l^4 \tag{3.9}$$

where ρ is the density of the fluid, l is the (chord) length of the component, and A is the planform area of the component. The kinetic energy due to the added mass is therefore

$$\begin{aligned} T_{\mathrm{A}} =& \frac{1}{2}\left(m_{\mathrm{A,b},2}\left(\widehat{\mathrm{b}}_2 \cdot \mathbf{v}_{\infty,\mathrm{rel,b,m}}\right)^2 + m_{\mathrm{A,b},3}\dot{\theta}_{\mathrm{b}}^2\right. \\ &\left. + \sum_{i=1}^{L}\left[m_{\mathrm{A,f},i,2}\left(\widehat{\mathrm{f}}_{i,2} \cdot \mathbf{v}_{\infty,\mathrm{rel,f},i,\mathrm{m}}\right)^2 + m_{\mathrm{A,f},i,3}\left(\dot{\phi}_{\mathrm{f},i} + \dot{\theta}_{\mathrm{b}}\right)^2\right]\right) \end{aligned} \tag{3.10}$$

where

$$m_{\mathrm{A,b},2} = \pi\rho l_{\mathrm{b}}^2 \qquad m_{\mathrm{A,f},i,2} = \pi\rho l_{\mathrm{f},i}^2 \qquad m_{\mathrm{A,b},3} = \frac{1}{8}\pi\rho l_{\mathrm{b}}^4 \qquad m_{\mathrm{A,f},i,3} = \frac{1}{8}\pi\rho l_{\mathrm{f},i}^4$$

and where

$$\mathbf{v}_{\infty,\mathrm{rel,b,m}} = -\mathbf{v}_{\mathrm{b,m}} + \mathbf{v}_{\infty} \qquad \text{and} \qquad \mathbf{v}_{\infty,\mathrm{rel,f},i,\mathrm{m}} = -\mathbf{v}_{\mathrm{f},i,\mathrm{m}} + \mathbf{v}_{\infty,\mathrm{f},i,\mathrm{m}} \tag{3.11}$$

with $\mathbf{v}_\infty$ being the free stream velocity of the fluid and $\mathbf{v}_{\infty,\mathrm{rel,f},i}$ being the local free stream velocity at the midpoint of the ith fin, which includes downwash. For reasons that will be explained in detail in Section 3.2.3.4,

$$\mathbf{v}_{\infty,\mathrm{f},i,\mathrm{m}} = \mathbf{v}_\infty + \sum_{j=0}^{i-1} \frac{C_{\Gamma,\mathrm{f},j} C_{\mathrm{L,f},j} l_{\mathrm{f},j}}{2\pi \left\|\boldsymbol{r}_{\mathrm{qc,m},ji}\right\|^2}\left[\boldsymbol{r}_{\mathrm{qc,m},ji} \times \left(\mathbf{v}_{\infty,\mathrm{rel,f},j} \times \widehat{\mathrm{f}}_{j,1}\right)\right] \tag{3.12}$$

where $\boldsymbol{r}_{\mathrm{qc,m},ji}$ is the position vector between the *quarter chord point* of the jth fin[f] and the *midpoint* of the ith fin, that is

$$\boldsymbol{r}_{\mathrm{qc,m},ji} = \boldsymbol{r}_{\mathrm{f},i,\mathrm{m}} - \boldsymbol{r}_{\mathrm{f},j,\mathrm{qc}} \tag{3.13}$$

The remaining terms are $C_{\mathrm{L,f},j}$, $C_{\Gamma,\mathrm{f},j}$, and $\mathbf{v}_{\infty,\mathrm{rel,f},j}$. $C_{\mathrm{L,f},j}$ is the lift coefficient of the jth fin, and $C_{\Gamma,\mathrm{f},j}$ is a term included in the downwash model primarily to enable easier study of the effects of downwash. Lastly, $\mathbf{v}_{\infty,\mathrm{rel,f},j}$ is velocity of the quarter chord point of the jth fin.

Although it is straightforward to compute the kinetic energy due to added mass, the results are quite lengthy. Thus, the calculations are performed using numerical computation software, e.g. *Mathematica*.

3.2.2.2 Euler-Lagrange Equations

The dynamics of the system can be found using the Euler-Lagrange equations:

$$\frac{d}{dt}\left(\frac{\partial L}{\partial \dot{\boldsymbol{q}}}\right) - \frac{\partial L}{\partial \boldsymbol{q}} = \boldsymbol{F}_{\mathrm{ext}}$$

[f]The body is considered to be the 0th fin.

where $\boldsymbol{F}_{\text{ext}}$ are the generalized external forces (and torques). In this case, the external forces will be hydrodynamic forces and joint torques. Since this is a mechanical system, the equations of motion will take the form

$$\boldsymbol{M}(\boldsymbol{q})\,\ddot{\boldsymbol{q}} + \boldsymbol{C}(\boldsymbol{q}, \dot{\boldsymbol{q}}) = \boldsymbol{F}_{\text{ext}} \tag{3.14}$$

where $\boldsymbol{M}(\boldsymbol{q})$ is the mass matrix[g] and $\boldsymbol{C}(\boldsymbol{q}, \dot{\boldsymbol{q}})$ is a vector field. For simplicity, $\boldsymbol{M}$ will be partitioned as

$$\boldsymbol{M} = \begin{bmatrix} \boldsymbol{M}_{\mathbf{r}} & \boldsymbol{M}_{\mathbf{rs}} \\ \boldsymbol{M}_{\mathbf{rs}}^T & \boldsymbol{M}_{\mathbf{s}} \end{bmatrix} + \boldsymbol{M}_{\mathrm{A}}$$

where $\boldsymbol{M}_{\mathbf{r}} \in \mathbb{R}^{3\times3}$, $\boldsymbol{M}_{\mathbf{rs}} \in \mathbb{R}^{3\times2L}$, $\boldsymbol{M}_{\mathbf{s}} \in \mathbb{R}^{2L\times2L}$, and $\boldsymbol{M}_{\mathrm{A}} \in \mathbb{R}^{3+2L\times3+2L}$. Note that, since $\boldsymbol{M}$ is symmetric, $\boldsymbol{M}_{\mathbf{r}}$ and $\boldsymbol{M}_{\mathbf{s}}$ are also symmetric. $\boldsymbol{M}_{\mathrm{A}}$ contains the added mass. Expressions for the elements of $\boldsymbol{M}_{\mathbf{r}}$, $\boldsymbol{M}_{\mathbf{rs}}$, and $\boldsymbol{M}_{\mathbf{s}}$ are contained in Appendix B.1.1.

The vector field $\boldsymbol{C}(\boldsymbol{q}, \dot{\boldsymbol{q}})$ can be expressed as

$$\boldsymbol{C}(\boldsymbol{q}, \dot{\boldsymbol{q}}) = \begin{bmatrix} \sum_{i=1}^{n} \sum_{j=i}^{n} -c_{i,j}^{1} \dot{q}_i \dot{q}_j \\ \sum_{i=1}^{n} \sum_{j=i}^{n} -c_{i,j}^{2} \dot{q}_i \dot{q}_j \\ \vdots \\ \sum_{i=1}^{n} \sum_{j=i}^{n} -c_{i,j}^{n} \dot{q}_i \dot{q}_j \end{bmatrix} + \boldsymbol{C}_{\mathrm{A}}(\boldsymbol{q}, \boldsymbol{q})$$

where $\boldsymbol{C}_{\mathrm{A}}(\boldsymbol{q}, \boldsymbol{q})$ are the forces related to the added mass. The expressions for $c_{i,j}^{k}$ are included in Appendix B.1.2.

3.2.3 Hydrodynamics

The body and every fin is assumed to be a thin hydrofoil in an ideal fluid. Thus, the body and every fin produces lift and drag. This situation is similar to the model presented by Morgansen et al. [2001, 2002], but allows for drag and lift on the same surfaces. As the elements are assumed to be thin, symmetric hydrofoils in ideal fluids and only planar dynamics are considered, two dimensional thin hydrofoil theory is used as a basis for the hydrodynamic model. Thin airfoil theory on symmetric hydrodynamics leads to the following simplifications: the hydrodynamic center is at the quarter chord point and there is no hydrodynamic moment about the hydrodynamic center [Bertin and Cummings, 2009].[h] The hydrodynamic model will consider each element independently, but the hydrodynamics of the elements will be coupled by their effect on the ambient flow, as detailed in Section 3.2.3.4. That is, the fins cannot "perceive" the actions of the other fins, but, since every fin influences the flow, the actions of one fin affects the flow around another.

[g] Also called the kinetic energy metric

[h] The term "thin airfoil theory" refers to the more common application (airfoils), but is equally applicable to hydrofoils and airfoils.

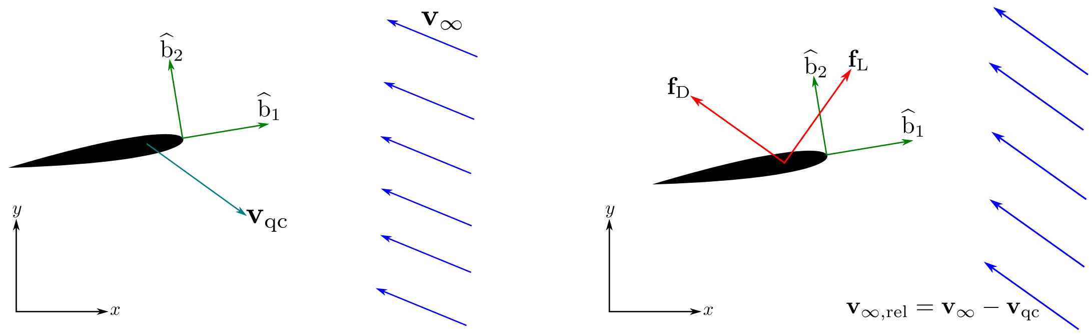

(a) Velocity Conventions (b) Force Convetions

Figure 3.5: Conventions used for Pisciform Hydrodynamic Model.

Before developing expressions for the hydrodynamic forcing around each hydrodynamic, it is necessary to defined conventions used for the calculations. Figure 3.5 shows these conventions, with 3.5(a) showing the conventions for the free stream velocity, $\mathbf{v}_\infty$, the velocity of the quarter chord point, $\mathbf{v}_{\mathrm{qc}}$, and the body axes of the hydrodynamic, $\widehat{\mathrm{b}}_1$ and $\widehat{\mathrm{b}}_2$. The velocities are measured with respect to the inertial $x - y$ basis. Figure 3.5(b) shows the relative velocity of the quarter chord point with respect to the flow, $\mathbf{v}_{\infty,\mathrm{rel}} = \mathbf{v}_\infty - \mathbf{v}_{\mathrm{qc}}$, and the lift and drag force vectors, $\mathbf{f}_\mathrm{L}$ and $\mathbf{f}_\mathrm{D}$. Note that the lift force $\mathbf{f}_\mathrm{L}$ is perpendicular to the *relative* flow $\mathbf{v}_{\infty,\mathrm{rel}}$, not the free stream flow velocity $\mathbf{v}_\infty$. Similarly, $\mathbf{f}_\mathrm{D}$ is parallel to $\mathbf{v}_{\infty,\mathrm{rel}}$ rather than $\mathbf{v}_\infty$. This distinction allows a moving hydrodynamic to produce forward thrust as will be describe in Section 3.2.3.5.

3.2.3.1 Lift

The lift force $\mathbf{f}_\mathrm{L}$ is, by definition, perpendicular to $\mathbf{v}_{\infty,\mathrm{rel}}$. Since the hydrodynamic is symmetric, the lift force at zero angle of attack is zero. The lift force should also scale with the dynamic pressure, which depends on the velocity squared. Morgansen et al. [2002] present an expression that accommodates these properties of the lift force; the hydrodynamic lift model presented herein is a modified version of the model presented by Morgansen et al. [2002]. Specifically,

$$\mathbf{f}_\mathrm{L} = \frac{\rho l}{2} C_\mathrm{L} \left(\mathbf{v}_{\infty,\mathrm{rel}} \times \widehat{\mathrm{b}}_1 \right) \times \mathbf{v}_{\infty,\mathrm{rel}} \tag{3.15}$$

Figure 3.6 is provided to demonstrate that this model behaves as desired with respect to changes in angle of attack and free stream velocity. Figure 3.6(a) shows that the force of the lift increases with angle of attack, reaching a maximum value. The performance at high angles of attack is better than expected from reality, but this is acceptable for this model because such high angles of attack are not encountered. Figure 3.6(b) shows that the variation of lift force with the free stream velocity. As expected, the lift force depends on

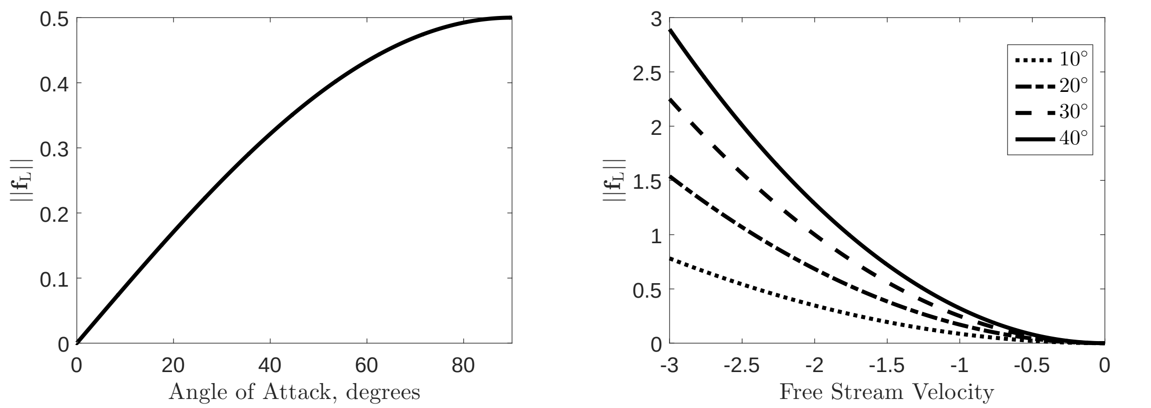

(a) Behavior of lift force with respect to changes in angle of attack. Free stream velocity is set to a magnitude of 1.

(b) Behavior of lift force with respect to changes in free stream velocity at several angles of attack.

Figure 3.6: Behavior of the magnitude of the lift force of the fish hydrodynamic model. Arbitrary parameters are chosen for constants, specifically, $C_\mathrm{L} = \rho = l = 1$, for illustrative purposes only. These choices are not meant to represent realistic values.

the velocity square.

3.2.3.2 Drag

Using [Morgansen et al., 2002] as a basis, one potential drag model is

$$\mathbf{f}_\mathrm{D} = \frac{\rho l}{2}\left(C_\mathrm{D,linear}\mathbf{v}_{\infty,\mathrm{rel}} + C_\mathrm{D}\left\|\mathbf{v}_{\infty,\mathrm{rel}} \times \widehat{\mathrm{b}}_1\right\|\mathbf{v}_{\infty,\mathrm{rel}}\right) \tag{3.16}$$

Similar to Figure 3.6, Figure 3.7 shows the behavior of the drag with respect to changes in parameters. This behavior is what is expected; increasing angle of attack or free stream velocity increases the drag. Also, the drag at zero angle of attack is not zero. The nonzero drag at zero angle of attack is due to the term that includes $C_\mathrm{D,linear}$ in (3.16). This apparent in Figure 3.7(b); the drag at zero angle of attack varies linearly with the free stream velocity.

3.2.3.3 Rotational Damping

Although thin airfoil theory predicts zero moment about the hydrodynamic center of symmetric hydrofoils, linear rotational damping is included. That is, if the angular velocity of a component is $\dot{\theta}$, there is a moment of $-C_\mathrm{M}\dot{\theta}$ opposing the rotational velocity.

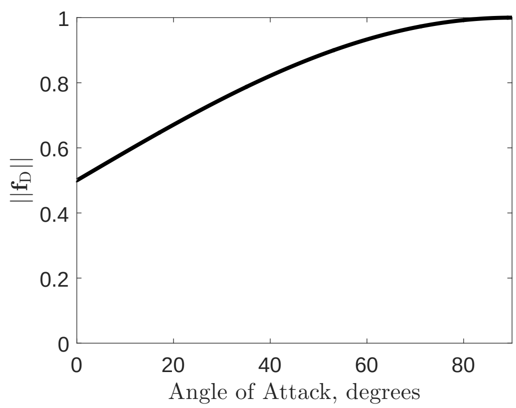

(a) Behavior of drag force with respect to changes in angle of attack. Free stream velocity is set to a magnitude of 1.

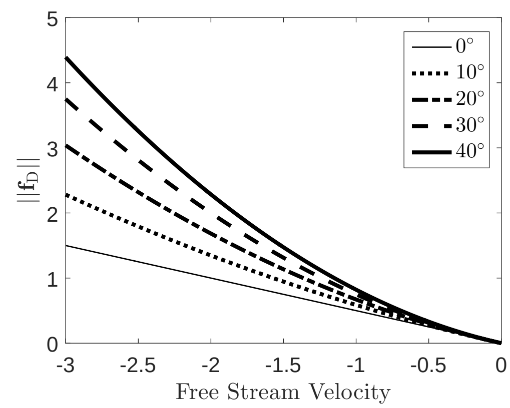

(b) Behavior of drag force with respect to changes in free stream velocity at several angles of attack.

Figure 3.7: Behavior of the magnitude of the drag force of the fish hydrodynamic model. Arbitrary parameters are chosen for constants, specifically, $C_{\mathrm{D,linear}} = C_{\mathrm{D}} = \rho = l = 1$, for illustrative purposes only. These choices are not meant to represent realistic values.

3.2.3.4 Downwash

Among the effects that influence the flow around a moving hydrofoil are vortex shedding and the formation of leading edge vortexes. In particular, the interaction of a hydrofoil with a shed vortex may substantially affect the hydrodynamic forcing. See [Chopra, 1976; Chopra and Kambe, 1977; Ellington, 1984a; Lighthill, 1969; Mason and Burdick, 2000; Rayner, 1979; Wang et al., 2008; Weis-Fogh, 1972] for examples of this effect. Instead of attempting to directly account for vortex shedding and other effects, the approach commonly used in aircraft stability is utilized. That is, the "downwash" created via the generation of lift by an upstream hydrofoil changes the free stream velocity of the flow for downstream hydrofoils. This is a common approach for analyzing the dynamics of fixed wing aircraft [Etkin and Reid, 1995].

From [Bertin and Cummings, 2009], the lift produced by a hydrofoil is proportional to the circulation, i.e.

$$L \propto u_\infty \Gamma \Rightarrow \Gamma \propto \frac{L}{u_\infty} \tag{3.17}$$

where L is the lift force, u_∞ is the free stream airspeed, and Γ is the circulation. Furthermore, the downwash velocity is is proportional to negative of the circulation,i.e.

$$w \propto -\Gamma \tag{3.18}$$

where w is the downwash velocity. From (3.17) and (3.18), it can be seen that the downwash

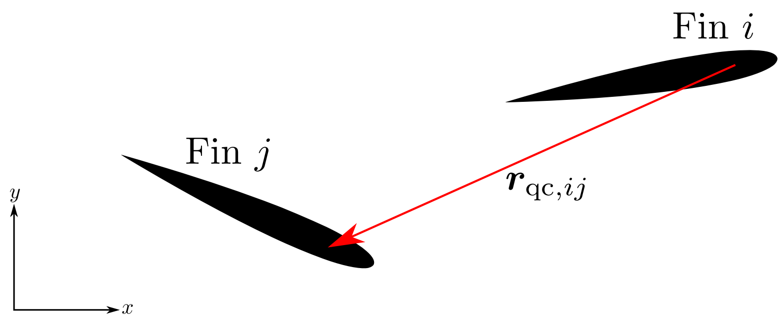

Figure 3.8: Relative position of two airfoils.

velocity should be proportional to the lift divided by the free stream velocity[i], so, since the lift force is quadratic with respect to the free stream velocity, the downwash velocity should be linear with respect to the free stream velocity.

It is reasonable to assume that the downwash velocity should decrease as the distance to the lifting surface increases. Using motivation from the Law of Biot and Savart [Bertin and Cummings, 2009], the downwash velocity will decrease with the distance from the quarter chord point. The relative position vector between the quarter chord points from the ith to the jth hydrofoil is $\boldsymbol{r}_{\mathrm{qc},ij}$ and is shown in Figure 3.8.

From (3.15), it can be seen that

$$\frac{\|\mathbf{f}_{\mathrm{L}}\|}{\|\mathbf{v}_{\infty,\mathrm{rel}}\|} = \frac{\rho l}{2} C_{\mathrm{L}} \left\| \mathbf{v}_{\infty,\mathrm{rel}} \times \widehat{\mathrm{b}}_1 \right\|$$

for $\mathbf{v}_{\infty,\mathrm{rel}} \neq 0$. Thus, following Bertin and Cummings [2009], the circulation vector can be expressed as

$$\boldsymbol{\Gamma} = \frac{l}{2} C_{\mathrm{L}} \left(\mathbf{v}_{\infty,\mathrm{rel}} \times \widehat{\mathrm{b}}_1 \right) \tag{3.19}$$

The parameter C_Γ is included primarily to provide a simple mechanism to determine the effects of the downwash. When examining the analytical expressions that define the model, all terms related to the downwash will have a C_Γ coefficient. When downwash is included in simulations, $C_\Gamma = 1$. The Law of Biot and Savart provides that for a vortex filament of finite length, the downwash speed at a point a distance h from the filament is

$$w = \frac{\Gamma}{4\pi h} \left(\cos\vartheta_1 - \cos\vartheta_2 \right)$$

where ϑ_1 and ϑ_2 are the angles made between the vortex filament and the line connecting the ends of the filament to the point of interest [Karamcheti, 1966]. This induced velocity is shown in Figure 3.9. This figure shows the downwash ($\boldsymbol{w}$) produced by the point vortex ($\boldsymbol{\Gamma}$) at a point some distance away from the vortex. The downwash at two different points is shown, with the speed of the downwash decreasing with distance from the point vortex.

[i]Note that (3.17) and (3.18) are a scalar equations and are only used to justify the model of the downwash.

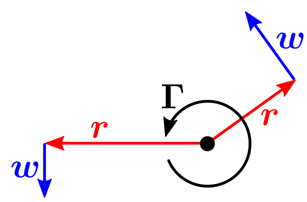

Figure 3.9: Illustration of downwash from a point vortex.

Temporarily neglecting the assumption of planar dynamics, let the span of the fin is b and let the fin be symmetric across the x-y plane, i.e. the midpoint of the fin lies in the x-y plane, then the angles ϑ_1 and ϑ_2 can be computed as

$$\vartheta_1 = \arctan\left(\frac{2\left\|\boldsymbol{r}_{\mathrm{qc},ij}\right\|}{b}\right) \qquad \text{and} \qquad \vartheta_2 = \pi - \vartheta_1$$

Notice that $\cos(\pi - \vartheta_1) = -\cos\vartheta_1$. Therefore under these assumptions,

$$w = \frac{\Gamma}{2\pi h}\cos\arctan\left(\frac{2\left\|\boldsymbol{r}_{\mathrm{qc},ij}\right\|}{b}\right)$$

where w is the speed of the downwash in the x-y plane.

Note that $\boldsymbol{\Gamma}$ is out of the x-y plane and $\boldsymbol{r}_{\mathrm{qc},ij}$ is in the x-y plane. Thus, it is possible to combine the previous development and express the downwash velocity as

$$\begin{aligned} \boldsymbol{w} &= \frac{C_\Gamma}{2\pi\left\|\boldsymbol{r}_{\mathrm{qc},ij}\right\|}\left(\frac{\boldsymbol{r}_{\mathrm{qc},ij}}{\left\|\boldsymbol{r}_{\mathrm{qc},ij}\right\|}\times\boldsymbol{\Gamma}\right)\cos\arctan\left(\frac{2\left\|\boldsymbol{r}_{\mathrm{qc},ij}\right\|}{b}\right) \\ &= C_\Gamma\frac{\boldsymbol{r}_{\mathrm{qc},ij}\times\boldsymbol{\Gamma}}{2\pi\left\|\boldsymbol{r}_{\mathrm{qc},ij}\right\|^2}\cos\arctan\left(\frac{2\left\|\boldsymbol{r}_{\mathrm{qc},ij}\right\|}{b}\right) \end{aligned} \tag{3.20}$$

where C_Γ is a coefficient. As stated before, the primary purpose of C_Γ is to identify what terms are associated with the downwash. In general, $C_\Gamma = 1$, but could be varied to account for additional effects. When applied to the multi-link fish model, downwash only affects downstream components.[j] Notice that although this is a planar hydrodynamics problem, formulating the downwash using a finite vortex filament and including C_Γ allows for some design optimization of the fins, most notably aspect ratio, to take place.

Reintroducing the assumption of planar flow, the results predicted by potential flow theory are recovered. Allowing the length of the vortex filament (i.e. the span of the hydrofoil) to approach infinity, $b \to \infty$, yields

$$\lim_{b\to\infty}\cos\arctan\left(\frac{2\left\|\boldsymbol{r}_{\mathrm{qc},ij}\right\|}{b}\right) = 1$$

Thus, the prediction from two dimensional ideal flow theory is that the downwash is

$$\boldsymbol{w} = C_\Gamma\frac{\boldsymbol{r}_{\mathrm{qc},ij}\times\boldsymbol{\Gamma}}{2\pi\left\|\boldsymbol{r}_{\mathrm{qc},ij}\right\|^2} \tag{3.21}$$

[j]This assumption is necessary to avoid algebraic recursion.

3.2.3.5 Thrust Generation

While it is not possible for a stationary hydrofoil in a flow to produce thrust in the direction of the flow, i.e. "fight the current," it is possible for a hydrofoil that is moving perpendicularly to the flow to produce forward thrust. This is because the lift is perpendicular to the *relative* flow velocity, as seen in (3.15). The thrust generation is discussed in this section through the use of two illustrative examples.

Consider the illustrative example of a hydrofoil with the characteristics in Table 3.2. The motion of the hydrofoil in this example is defined by

$$\begin{aligned} x(t) =& a_x \cos(t + \phi_x) \\ y(t) =& a_y \cos(t + \phi_y) \\ \theta(t) =& a_\theta \cos(t + \phi_\theta) \end{aligned} \tag{3.22}$$

where $x(t)$ and $y(t)$ define the position of the quarter chord point with respect to the inertial frame and $\theta(t)$ is the angle between the chord line and the inertial x axis. The parameters for these equations are defined in Table 3.2 with the exception of ϕ_θ as it will be varied later. The velocity of the free stream relative to the inertial frame is $\boldsymbol{v}_\infty = [v_{\infty,x}, v_{\infty,u}, 0]^T$. As the motion of the system is perpendicular to the free stream velocity, some of the lift generated is directed into the free stream. This can be seen in the montages in Figure 3.20; as the velocity of the hydrofoil increases, more of the lift is directed into the free stream.[k] The net effect of this deflection of the lift also depends on the phase ϕ_θ as can be seen in Figure 3.10. Notice that for some values of ϕ_θ a net thrust is generated, i.e. the amount of deflected lift overcomes the drag, which is indicated by a positive slope of a line in Figure 3.10(a). However, for some values of ϕ_θ the amount of deflected lift does not overcome the drag, resulting in net drag. Also note that in Figure 3.10(b), after every period the net force in the y direction is zero. Thus regardless of the value of ϕ_θ, no net y force is generated. That is, by coupling the pitching and lateral (with respect to the free stream) motion of a hydrofoil, it is possible to generate net forward thrust without also generating net lateral thrust. This phenomenon is further studied in the following example.

For a more illustrative example, consider the system in Figure 3.11. This system consists of a hydrofoil attached to a moving cart. The cart is restricted to only moving in the x-direction and the fin can translate only in the y-direction while rotating about its quarter chord point. The velocity of the cart and the velocity of the quarter chord point of the fin relative to the cart are

$$\boldsymbol{v}_{\text{cart}} = \begin{bmatrix} \dot{x} \\ 0 \\ 0 \end{bmatrix} \qquad \text{and} \qquad \boldsymbol{v}_{\text{fin}} = \begin{bmatrix} 0 \\ \dot{y} \\ 0 \end{bmatrix}$$

[k] Figure 3.20 was appended to the end of this section due to its size.

Table 3.2: Characteristics of a hydrofoil used as an example. Parameters are nondimensional and are chosen arbitrarily and not meant to approximate a real system.

Parameter	Value
C_{L}	1.5
$C_{\mathrm{D,linear}}$	0.5
C_{D}	0.5
ρ	1
l	1
a_x	0
a_y	1.5
a_θ	30°
ϕ_x	90°
ϕ_y	0°
$v_{\infty,x}$	-3
$v_{\infty,y}$	0

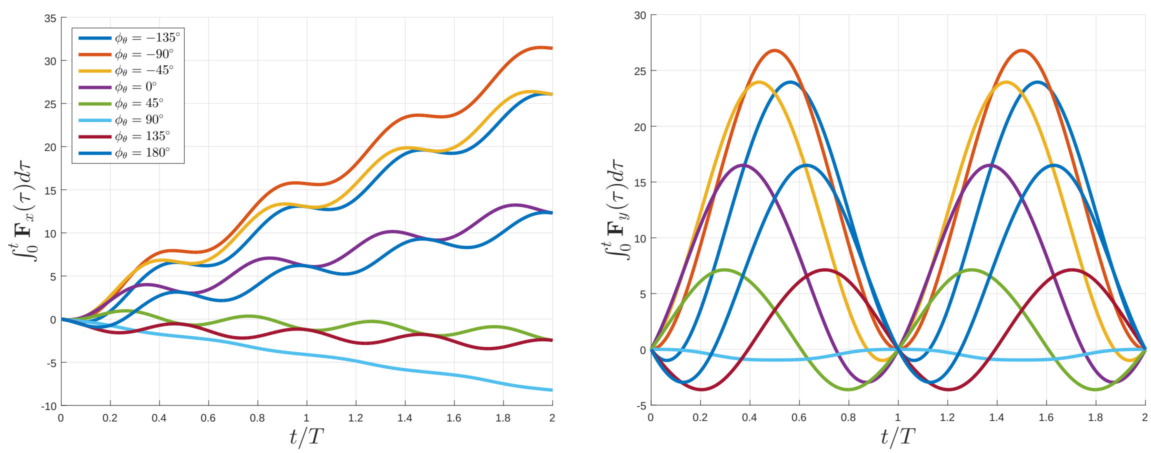

(a) Net Force in x direction

(b) Net Force in y direction

Figure 3.10: Net forces generated by moving hydrofoils with different phases ϕ_θ

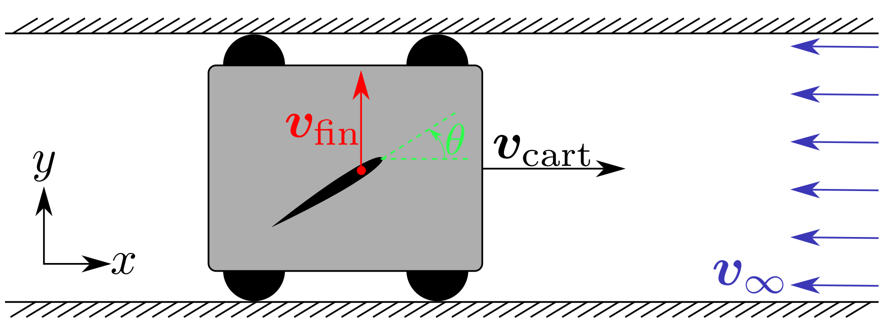

Figure 3.11: Example system for thrust generation from a single moving fin.

respectively. Thus, the velocity of the quarter chord point, relative to the inertial frame is

$$\boldsymbol{v}_{\mathrm{qc}} = \boldsymbol{v}_{\mathrm{cart}} + \boldsymbol{v}_{\mathrm{fin}} = \begin{bmatrix} \dot{x} \\ \dot{y} \\ 0 \end{bmatrix}$$

and, since the free stream velocity is $\boldsymbol{v}_\infty = [-v_{\infty,x}, 0, 0]^T$, the free stream velocity relative to the quarter chord point of the fin is

$$\boldsymbol{v}_{\infty,\mathrm{rel,qc}} = \boldsymbol{v}_\infty - \boldsymbol{v}_{\mathrm{qc}} = \begin{bmatrix} -v_{\infty,x} - \dot{x} \\ -\dot{y} \\ 0 \end{bmatrix}$$

The angle between the chord line of the fin and the inertial x-axis is θ. The $\widehat{\mathrm{b}}_1$ axis of the fin can be expressed as $\widehat{\mathrm{b}}_1 = [\cos\theta, \sin\theta, 0]^T$. Noting that $\rho l = 2$, the lift and drag forces produced by the fin can be computed as

$$\mathbf{f}_{\mathrm{L}} = C_{\mathrm{L}} \left(\boldsymbol{v}_{\infty,\mathrm{rel}} \times \widehat{\mathrm{b}}_1 \right) \times \boldsymbol{v}_{\infty,\mathrm{rel}}$$

and

$$\mathbf{f}_{\mathrm{D}} = C_{\mathrm{D,linear}} \boldsymbol{v}_{\infty,\mathrm{rel}} + C_{\mathrm{D}} \left\| \boldsymbol{v}_{\infty,\mathrm{rel}} \times \widehat{\mathrm{b}}_1 \right\| \boldsymbol{v}_{\infty,\mathrm{rel}}$$

Assume unit depth and that $\rho l = 2$. Let the fin be massless and the cart have mass m. Let $\boldsymbol{v}_{\mathrm{fin}}$ and θ be specified. That is, y and θ (or their derivatives) can be used as control inputs. Since the cart is restricted only to move in the x-direction, the equation of motion of the system is

$$m\ddot{x} = \mathrm{f}_{\mathrm{L},x} + \mathrm{f}_{\mathrm{D},x}$$

or

$$\ddot{x} = \frac{1}{m} \left(\mathrm{f}_{\mathrm{L},x} + \mathrm{f}_{\mathrm{D},x} \right)$$

where $\mathrm{f}_{\mathrm{L},x}$ and $\mathrm{f}_{\mathrm{D},x}$ are the x-components of $\mathbf{f}_{\mathrm{L}}$ and $\mathbf{f}_{\mathrm{D}}$, respectively.

Let y and θ be specified as

$$y(t) = y_0 \cos(\Omega t) \qquad \theta(t) = \theta_0 \cos(\Omega t + \phi_\theta)$$

where $\Omega = 2\pi/T$, with T being the period, and, without loss of generality, let $x(0) = 0$. Let the lift and drag coefficients be defined as in Table 3.2. Let the mass of the cart be $m = 7$ and the free stream velocity is $v_{\infty,x} = 0.15$.

Although this system is not well posed for the geometric averaging technique presented in Section 1.2.2, direct averaging as described in Section 1.2.1 is applicable. Let $y(t)$ and $\theta(t)$ vary on the time scale τ, i.e.

$$y(\tau) = y_0 \cos(\Omega \tau) \qquad \theta(\tau) = \theta_0 \cos(\Omega \tau + \phi_\theta)$$

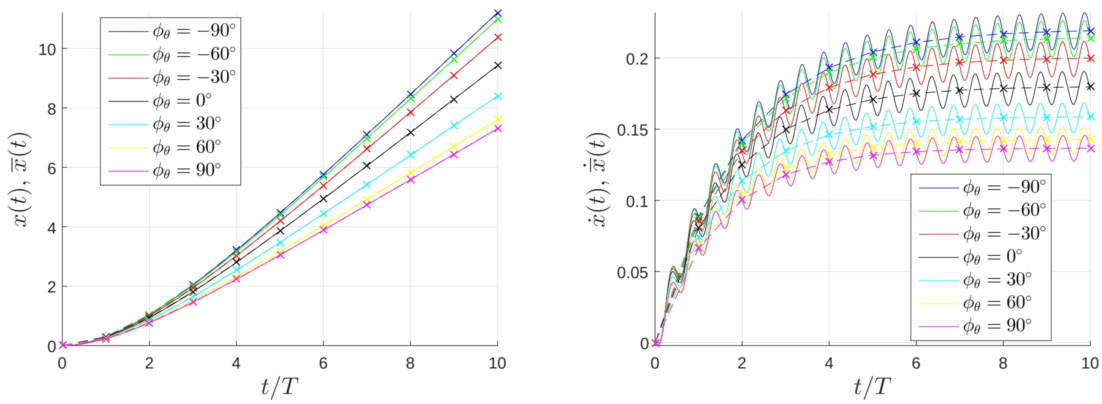

(a) $x(t)$ (b) $\dot{x}(t)$

Figure 3.12: Simulation of system shown in Figure 3.11. The actual dynamics are shown as solid lines, while the averaged dynamics are shown as dashed lines with a marker indicating the periods.

The average dynamics can be computed as

$$\ddot{\overline{x}} = \frac{1}{T}\int_0^T \frac{1}{m}\left(\mathrm{f}_{\mathrm{L},x} + \mathrm{f}_{\mathrm{D},x}\right) d\tau$$

with the same initial conditions. Figure 3.12 shows the results of numerically simulating the actual dynamics and average dynamics of the system shown in Figure 3.11. It is immediately clear that the actual dynamics are a periodic oscillation around the averaged dynamics. Therefore, the behavior of the system over long time scales can be described using the average dynamics.

3.2.4 Model Synthesis

Now that the rigid body mechanics and hydrodynamic models have been defined, it is possible to synthesize these models into a single model. For this model, the shape of the body shall be defined directly. That is, the angles between all of the fins and peduncles can be defined directly. Morgansen et al. [2001, 2002] use a similar method for a simpler model of a carangiform fish, but their shape control methodology makes assumptions that are not justified for the model presented herein. Notably, Morgansen et al. [2001, 2002] assume that the hydrodynamic forces on the fin do not affect the torques required to control the shape of the fish. The shape control methodology used here uses a feedback-inversion technique where the prescribed joint torques are the torques required to generate the desired shape while counteracting the hydrodynamic and inertial forcing.

Equation (3.14) provides the equations of motion for the system. The term $\boldsymbol{F}_{\text{ext}}$ refers to the external (non-inertial) forcing on the system, which, in this case, is hydrodynamic forcing and torques between links. To better discuss the hydrodynamic forcing, it can be divided into several components. Specifically,

$$\boldsymbol{F}_{\text{ext}} = \mathbf{f}_{\text{L}} + \mathbf{f}_{\text{D}} + \mathbf{m}_{\text{L}} + \mathbf{m}_{\text{D}} + \mathbf{m}_{\text{damp}} + \mathbf{u}(t) \tag{3.23}$$

where $\mathbf{f}_{\text{L}}$ and $\mathbf{f}_{\text{D}}$ are the hydrodynamic forces due to lift and drag, respectively, $\mathbf{m}_{\text{L}}$ and $\mathbf{m}_{\text{D}}$ are the hydrodynamic moments due to lift and drag, respectively, and $\mathbf{m}_{\text{damp}}$ is rotational damping. $\mathbf{u}(t)$ are the torques acting at each link. The nuance associated with each of these terms will be elucidated in subsequent sections, but a few general comments should be made about these terms. First is that these terms depend only on the generalized positions $\boldsymbol{q}$ and velocities $\dot{\boldsymbol{q}}$ of the system. Also, the system parameters, such as lengths of segments, mass of components, and forcing coefficients, are included in a vector $\mathfrak{p}$. As the forces and moments are both generated by the hydrodynamics, the partitioning of the hydrodynamic forcing into force and torque terms as in (3.23) is somewhat artificial in nature, but it can be useful for discussing the effects of the hydrodynamics.

3.2.4.1 Lift and Drag Forces

The forces arising from hydrodynamic lift and drag, i.e. $\mathbf{f}_{\text{L}}$ and $\mathbf{f}_{\text{D}}$, are due to the sum of the lift and drag forces on each component. These forces depend on the velocity of each component relative to the ambient flow, which includes downwash as described in Section 3.2.3.4. This section will be structured as follows:

1. The lift and drag forces produced by the body will be described.
2. The lift and drag forces produced by each fin will be described. This description will include terms that correspond to the downwash, which will be described later.
3. The downwash on each component will be computed.
4. The method for computing the lift and drag forces in the presence of downwash for each component will be presented procedurally.

The first step is to determine the hydrodynamic forcing created by the body. The velocity of the quarter chord point, $\mathbf{v}_{\text{b,qc}}$, is defined in (3.5). Notice that $\mathbf{v}_{\text{b}} = [\dot{x}, \dot{y}, 0]^T$. Since there are no upstream components to create downwash, the velocity of the quarter chord point of the body relative to the ambient flow is

$$\mathbf{v}_{\infty,\text{rel,b}} = \boldsymbol{v}_{\infty} - \mathbf{v}_{\text{b,qc}} \tag{3.24}$$

Thus the lift and drag forces generated by the body are, from (3.15),

$$\mathbf{f}_{\text{L,b}} = \frac{\rho l_{\text{b}}}{2} C_{\text{L,b}} \left(\mathbf{v}_{\infty,\text{rel,b}} \times \widehat{\text{b}}_1 \right) \times \mathbf{v}_{\infty,\text{rel,b}} \tag{3.25}$$

where l_{b} is the length of the lifting surface of the body, and $C_{\mathrm{L,b}}$ is the lift coefficient of the body. Note that $\widehat{\mathrm{b}}_1$ follows the definition in Figure 3.3 (See also Figure 3.5). Similarly, the drag created by the body is

$$\mathbf{f}_{\mathrm{D,b}} = \frac{\rho l_{\mathrm{b}}}{2}\left(C_{\mathrm{D,linear,b}}\mathbf{v}_{\infty,\mathrm{rel,b}} + C_{\mathrm{D,b}}\left\|\mathbf{v}_{\infty,\mathrm{rel,b}} \times \widehat{\mathrm{b}}_1\right\|\mathbf{v}_{\infty,\mathrm{rel,b}}\right) \tag{3.26}$$

where $C_{\mathrm{D,linear,b}}$ and $C_{\mathrm{D,b}}$ are the linear and quadratic drag coefficients of the body.

For the purpose of simplicity, the body is considered to be the "zeroth" fin, that is the subscript "b" is equivalent to the subscript "$\mathrm{f},0$". The free stream flow velocity at the quarter chord of point of the ith fin (for $i \geq 1$) is

$$\mathbf{v}_{\infty,\mathrm{f},i} = \boldsymbol{v}_{\infty} + \sum_{j=0}^{i-1}\boldsymbol{w}_{j,i} \tag{3.27}$$

where $\boldsymbol{w}_{j,i}$ is the downwash velocity created by the jth hydrofoil at the quarter chord point of the ith hydrofoil. Formal expressions for $\boldsymbol{w}_{j,i}$ will be provided later. Thus the velocity of the quarter chord point of the ith hydrofoil relative to the free stream is

$$\mathbf{v}_{\infty,\mathrm{rel,f},i} = \mathbf{v}_{\infty,\mathrm{f},i} - \mathbf{v}_{\mathrm{f},i,\mathrm{qc}} \tag{3.28}$$

where $\mathbf{v}_{\mathrm{f},i,\mathrm{qc}}$ is defined in (3.4). Using this, the lift and drag produced by the ith fin are

$$\mathbf{f}_{\mathrm{L,f},i} = \frac{\rho l_{\mathrm{f},i}}{2}C_{\mathrm{L,f},i}\left(\mathbf{v}_{\infty,\mathrm{rel,f},i} \times \widehat{\mathrm{f}}_{i,1}\right) \times \mathbf{v}_{\infty,\mathrm{rel,f},i} \tag{3.29}$$

and

$$\mathbf{f}_{\mathrm{D,f},i} = \frac{\rho l_{\mathrm{f},i}}{2}\left(C_{\mathrm{D,linear,f},i}\mathbf{v}_{\infty,\mathrm{rel,f},i} + C_{\mathrm{D,f},i}\left\|\mathbf{v}_{\infty,\mathrm{rel,f},i} \times \widehat{\mathrm{f}}_{i,1}\right\|\mathbf{v}_{\infty,\mathrm{rel,f},i}\right) \tag{3.30}$$

respectively, where $l_{\mathrm{f},i}$ is the length of the lifting surface, $C_{\mathrm{L,f},i}$ is the lift coefficient, $C_{\mathrm{D,linear,f},i}$ is the linear drag coefficient, and $C_{\mathrm{D,f},i}$ is the quadratic drag coefficient, all of the ith fin. $\widehat{\mathrm{f}}_{i,1}$ is defined in Figure 3.4.

Note that the downwash on the ith fin depends only on the lift produced by the fins indexed by $j < i$. That is, the downwash on the first fin results only from the lift produced by the body, the downwash on the second fin results from the lift produced by the body and the first fin, and so on. Using this procedure, it is possible to compute the total downwash on each fin sequentially. The $\boldsymbol{w}_{j,i}$ terms in Equation (3.27) can be expressed, using Equations (3.19) and (3.20), as

$$\boldsymbol{w}_{j,i} = \frac{C_{\Gamma,\mathrm{f},j}C_{\mathrm{L,f},j}l_{\mathrm{f},j}}{2\pi\left\|\boldsymbol{r}_{\mathrm{qc},ji}\right\|^2}\left[\cos\arctan\left(\frac{2\left\|\boldsymbol{r}_{\mathrm{qc},ji}\right\|}{b_{\mathrm{f},j}}\right)\right]\left[\boldsymbol{r}_{\mathrm{qc},ji} \times \left(\mathbf{v}_{\infty,\mathrm{rel,f},j} \times \widehat{\mathrm{f}}_{j,1}\right)\right] \tag{3.31}$$

where $C_{\Gamma,\mathrm{f},j}$ is an efficiency parameter related to the ellipticity of the lift distribution of the ith fin in three dimensions. Notice that $\boldsymbol{r}_{\mathrm{qc},ji}$ is the position vector measured from the quarter chord point of the jth hydrofoil to the quarter chord point of the ith hydrofoil.

Procedurally, the previous expressions can be used to compute the lift and drag for each component. The steps are as follows:

1. Using the generalized positions and velocities, compute $\mathbf{v}_{\mathrm{b,qc}}$ and $\mathbf{v}_{\mathrm{f},i,\mathrm{qc}}$ for every fin. For later use, let $\mathbf{v}_{\mathrm{f,0,qc}} \triangleq \mathbf{v}_{\mathrm{b,qc}}$.
2. Use equation (3.24) to compute the free stream velocity relative to the quarter chord point of the body.
3. Compute the lift and drag produced by the body using Equations (3.25) and (3.26).
4. Starting with the first fin, compute the downwash created at the quarter chord point of the ith fin for all fins $j \in \{0, 1, 2, \ldots, i-1\}$ which equation (3.31).
5. Use equation (3.27) to compute the free stream flow velocity at the quarter chord point of the ith fin.
6. Use the generalized positions and velocities to compute $\mathbf{v}_{\mathrm{f},i,\mathrm{qc}}$.
7. Use equation (3.28) to compute $\mathbf{v}_{\infty,\mathrm{rel,f},i,\mathrm{qc}}$.
8. Use equations (3.29) and (3.30) to compute the lift and drag produced by the ith fin.
9. Repeat the steps 4 through 8 for every fin.

3.2.4.2 Principle of Virtual Work

Due to the nature of having multiple non-conservative forces applied to the various links in a multi-body system, the method used by Morgansen et al. [2001] cannot be used. Morgansen et al. [2001] effectively assume that the masses of the tail fin and peduncle of a carangiform fish are negligible and applied all forces and moments directly to the body. This may be an appropriate assumption for carangiform and thunniform locomotion, but is unlikely to be valid for approximations of anguilliform locomotion using the multi-link fish model developed here. Therefore, the effects of forces and moments must be computed using the Principle of Virtual Work. This implies that $\boldsymbol{F}_{\mathrm{ext}}$ are the *generalized forces* acting on the system and that the terms in (3.23) are likewise components of the generalized forces.

This derivation of the principle of virtual work follows [Greenwood, 1977]. The virtual work on a system with N forces is

$$\delta\mathcal{W} = \sum_{i=1}^{N} \boldsymbol{F}_i \cdot \delta\boldsymbol{r}_i$$

where $\boldsymbol{F}_i$ is the force applied at position $\boldsymbol{r}_i$ and $\delta\boldsymbol{r}_i$ is the virtual displacement of $\boldsymbol{r}_i$. The virtual displacement $\delta\boldsymbol{r}_i$ can be computed as

$$\delta\boldsymbol{r}_i = \frac{\partial\boldsymbol{r}_i}{\partial q_j}\delta q_j$$

Thus,

$$\delta\mathcal{W} = \sum_{i=1}^{N} \boldsymbol{F}_i \cdot \sum_{j=1}^{n} \frac{\partial \boldsymbol{r}_i}{\partial q_j}\delta q_j = \sum_{j=1}^{n}\left(\sum_{i=1}^{N} \boldsymbol{F}_i \cdot \frac{\partial \boldsymbol{r}_i}{\partial q_j}\right)\delta q_j = \sum_{j=1}^{n} Q_j \delta q_j$$

where

$$Q_j \triangleq \sum_{i=1}^{N} \boldsymbol{F}_i \cdot \frac{\partial \boldsymbol{r}_i}{\partial q_j} \tag{3.32}$$

are the *generalized forces*. Notice that if $\boldsymbol{Q} = [Q_1, \ldots, Q_n]^T$, then

$$\delta\mathcal{W} = \boldsymbol{Q} \cdot \delta\boldsymbol{q}$$

That is, the generalized forces can be thought of as forces applied directly to the generalized coordinates.

For the multilink fish model, the generalized positions are $\boldsymbol{q} = \left[\mathbf{r}^T, \mathbf{s}^T\right]^T$ with $\mathbf{r}$ and $\mathbf{s}$ being the group and shape coordinates defined in (3.6) and (3.7), respectively. Let r_i and s_i be the ith elements of $\mathbf{r}$ and $\mathbf{s}$, respectively. The assumption from thin airfoil theory that the quarter chord point of a hydrofoil is its hydrodynamic center provides the fact that every lift and drag force acts at the quarter chord point of the hydrofoil. The locations of the quarter chord points of all hydrodynamic components are listed in Section 3.2.1.2 and will be restated here for clarity. The location of the quarter chord point of the body is

$$\boldsymbol{r}_{\mathrm{b,qc}} = \boldsymbol{r}_{\mathrm{b}} + \frac{l_b}{4}\begin{bmatrix} -\cos\theta_{\mathrm{b}} \\ -\sin\theta_{\mathrm{b}} \\ 0 \end{bmatrix} = \begin{bmatrix} x - (l_{\mathrm{b}}/4)\cos\theta_{\mathrm{b}} \\ y - (l_{\mathrm{b}}/4)\sin\theta_{\mathrm{b}} \\ 0 \end{bmatrix}$$

Notice that $\boldsymbol{r}_{\mathrm{b,qc}}$ does not depend on the shape coordinates $\mathbf{s}$. Thus,

$$\frac{\partial \mathbf{r}_{\mathrm{b,qc}}}{\partial \mathrm{s}_i} = \mathbf{0}_{3\times 1} \tag{3.33}$$

for all shape coordinates s_i. With respect to the group coordinates,

$$\frac{\partial \mathbf{r}_{\mathrm{b,qc}}}{\partial x} = \begin{bmatrix} 1 \\ 0 \\ 0 \end{bmatrix} \qquad \frac{\partial \mathbf{r}_{\mathrm{b,qc}}}{\partial y} = \begin{bmatrix} 0 \\ 1 \\ 0 \end{bmatrix} \qquad \frac{\partial \mathbf{r}_{\mathrm{b,qc}}}{\partial \theta_{\mathrm{b}}} = \begin{bmatrix} (l_{\mathrm{b}}/4)\sin\theta_{\mathrm{b}} \\ -(l_{\mathrm{b}}/4)\cos\theta_{\mathrm{b}} \\ 0 \end{bmatrix} \tag{3.34}$$

The position of the quarter chord point is computed using a series. First, notice that

$$\boldsymbol{r}_{\mathrm{p,1,LE}} = \boldsymbol{r}_{\mathrm{b,TE}} = \begin{bmatrix} x - l_{\mathrm{b}}\cos\theta_{\mathrm{b}} \\ y - l_{\mathrm{b}}\sin\theta_{\mathrm{b}} \\ 0 \end{bmatrix}$$

Then notice that

$$\boldsymbol{r}_{\mathrm{f},i,\mathrm{LE}} = \boldsymbol{r}_{\mathrm{p},i,\mathrm{TE}} = \boldsymbol{r}_{\mathrm{p},i,\mathrm{LE}} + l_{\mathrm{p},i}\begin{bmatrix} \cos\psi_{\mathrm{p},i} \\ \sin\psi_{\mathrm{p},i} \\ 0 \end{bmatrix}$$

and that

$$\boldsymbol{r}_{\mathrm{f},i,\mathrm{TE}} = \boldsymbol{r}_{\mathrm{f},i,\mathrm{LE}} + l_{\mathrm{f},i} \begin{bmatrix} \cos\psi_{\mathrm{f},i} \\ \sin\psi_{\mathrm{f},i} \\ 0 \end{bmatrix} = \boldsymbol{r}_{\mathrm{p},i+1,\mathrm{LE}}$$

Expressing these as a sequence yields

$$\begin{aligned}
\boldsymbol{r}_{\mathrm{p},1,\mathrm{LE}} =& \boldsymbol{r}_{\mathrm{b},\mathrm{TE}} \\
\boldsymbol{r}_{\mathrm{f},1,\mathrm{LE}} =& \boldsymbol{r}_{\mathrm{b},\mathrm{TE}} + l_{\mathrm{p},1} \begin{bmatrix} \cos\psi_{\mathrm{p},1} \\ \sin\psi_{\mathrm{p},1} \\ 0 \end{bmatrix} \\
\boldsymbol{r}_{\mathrm{p},2,\mathrm{LE}} =& \boldsymbol{r}_{\mathrm{b},\mathrm{TE}} + l_{\mathrm{p},1} \begin{bmatrix} \cos\psi_{\mathrm{p},1} \\ \sin\psi_{\mathrm{p},1} \\ 0 \end{bmatrix} + l_{\mathrm{f},1} \begin{bmatrix} \cos\psi_{\mathrm{f},1} \\ \sin\psi_{\mathrm{f},1} \\ 0 \end{bmatrix} \\
\boldsymbol{r}_{\mathrm{f},2,\mathrm{LE}} =& \boldsymbol{r}_{\mathrm{b},\mathrm{TE}} + l_{\mathrm{p},1} \begin{bmatrix} \cos\psi_{\mathrm{p},1} \\ \sin\psi_{\mathrm{p},1} \\ 0 \end{bmatrix} + l_{\mathrm{f},1} \begin{bmatrix} \cos\psi_{\mathrm{f},1} \\ \sin\psi_{\mathrm{f},1} \\ 0 \end{bmatrix} + l_{\mathrm{p},2} \begin{bmatrix} \cos\psi_{\mathrm{p},2} \\ \sin\psi_{\mathrm{p},2} \\ 0 \end{bmatrix} \\
\boldsymbol{r}_{\mathrm{p},3,\mathrm{LE}} =& \boldsymbol{r}_{\mathrm{b},\mathrm{TE}} + l_{\mathrm{p},1} \begin{bmatrix} \cos\psi_{\mathrm{p},1} \\ \sin\psi_{\mathrm{p},1} \\ 0 \end{bmatrix} + l_{\mathrm{f},1} \begin{bmatrix} \cos\psi_{\mathrm{f},1} \\ \sin\psi_{\mathrm{f},1} \\ 0 \end{bmatrix} + l_{\mathrm{p},2} \begin{bmatrix} \cos\psi_{\mathrm{p},2} \\ \sin\psi_{\mathrm{p},2} \\ 0 \end{bmatrix} + l_{\mathrm{f},2} \begin{bmatrix} \cos\psi_{\mathrm{f},2} \\ \sin\psi_{\mathrm{f},2} \\ 0 \end{bmatrix} \\
&\vdots \\
\boldsymbol{r}_{\mathrm{f},i,\mathrm{LE}} =& \begin{bmatrix} x - l_{\mathrm{b}}\cos\theta_{\mathrm{b}} \\ y - l_{\mathrm{b}}\sin\theta_{\mathrm{b}} \\ 0 \end{bmatrix} + l_{\mathrm{p},i} \begin{bmatrix} \cos\psi_{\mathrm{p},i} \\ \sin\psi_{\mathrm{p},i} \\ 0 \end{bmatrix} + \sum_{j=1}^{i-1} \left(l_{\mathrm{p},j} \begin{bmatrix} \cos\psi_{\mathrm{p},j} \\ \sin\psi_{\mathrm{p},j} \\ 0 \end{bmatrix} + l_{\mathrm{f},j} \begin{bmatrix} \cos\psi_{\mathrm{f},j} \\ \sin\psi_{\mathrm{f},j} \\ 0 \end{bmatrix} \right)
\end{aligned}$$

Lastly, notice that

$$\boldsymbol{r}_{\mathrm{f},i,\mathrm{qc}} = \boldsymbol{r}_{\mathrm{f},i,\mathrm{LE}} + \frac{l_{\mathrm{f},i}}{4} \begin{bmatrix} \cos\psi_{\mathrm{f},i} \\ \sin\psi_{\mathrm{f},i} \\ 0 \end{bmatrix}$$

Therefore, the position of the quarter chord point of the ith fin is

$$\begin{aligned}
\boldsymbol{r}_{\mathrm{f},i,\mathrm{qc}} = & \begin{bmatrix} x - l_{\mathrm{b}}\cos\theta_{\mathrm{b}} \\ y - l_{\mathrm{b}}\sin\theta_{\mathrm{b}} \\ 0 \end{bmatrix} + l_{\mathrm{p},i} \begin{bmatrix} \cos\psi_{\mathrm{p},i} \\ \sin\psi_{\mathrm{p},i} \\ 0 \end{bmatrix} + \frac{l_{\mathrm{f},i}}{4} \begin{bmatrix} \cos\psi_{\mathrm{f},i} \\ \sin\psi_{\mathrm{f},i} \\ 0 \end{bmatrix} \\
& + \sum_{j=1}^{i-1} \left(l_{\mathrm{p},j} \begin{bmatrix} \cos\psi_{\mathrm{p},j} \\ \sin\psi_{\mathrm{p},j} \\ 0 \end{bmatrix} + l_{\mathrm{f},j} \begin{bmatrix} \cos\psi_{\mathrm{f},j} \\ \sin\psi_{\mathrm{f},j} \\ 0 \end{bmatrix} \right)
\end{aligned} \tag{3.35}$$

One issue that arises is that the angles used are the inertial angles, $\psi_{\mathrm{p},i}$ and $\psi_{\mathrm{f},i}$, which are not the shape coordinates $\mathbf{s}$. The shape coordinates are expressed in terms of the body-relative angles $\phi_{\mathrm{p},i}$ and $\phi_{\mathrm{f},i}$. Fortunately, this is a simple change of variables, specifically

$$\psi_{\mathrm{p},i} = \phi_{\mathrm{p},i} + \pi + \theta_{\mathrm{b}} \qquad \psi_{\mathrm{f},i} = \phi_{\mathrm{f},i} + \pi + \theta_{\mathrm{b}}$$

Noting that $\cos(t+\pi) = -\cos(t)$ and $\sin(t+\pi) = -\sin(t)$, it is possible to rewrite (3.35) in terms of the generalized coordinates, specifically,

$$\begin{aligned}\boldsymbol{r}_{\mathrm{f},i,\mathrm{qc}} = &\begin{bmatrix} x - l_{\mathrm{b}}\cos\theta_{\mathrm{b}} \\ y - l_{\mathrm{b}}\sin\theta_{\mathrm{b}} \\ 0 \end{bmatrix} - l_{\mathrm{p},i}\begin{bmatrix} \cos(\phi_{\mathrm{p},i}+\theta_{\mathrm{b}}) \\ \sin(\phi_{\mathrm{p},i}+\theta_{\mathrm{b}}) \\ 0 \end{bmatrix} - \frac{l_{\mathrm{f},i}}{4}\begin{bmatrix} \cos(\phi_{\mathrm{f},i}+\theta_{\mathrm{b}}) \\ \sin(\phi_{\mathrm{f},i}+\theta_{\mathrm{b}}) \\ 0 \end{bmatrix} \\ &- \sum_{j=1}^{i-1}\left(l_{\mathrm{p},j}\begin{bmatrix} \cos(\phi_{\mathrm{p},j}+\theta_{\mathrm{b}}) \\ \sin(\phi_{\mathrm{p},j}+\theta_{\mathrm{b}}) \\ 0 \end{bmatrix} + l_{\mathrm{f},j}\begin{bmatrix} \cos(\phi_{\mathrm{f},j}+\theta_{\mathrm{b}}) \\ \sin(\phi_{\mathrm{f},j}+\theta_{\mathrm{b}}) \\ 0 \end{bmatrix}\right)\end{aligned} \tag{3.36}$$

It is now possible to compute $\partial\boldsymbol{r}_{\mathrm{f},i,\mathrm{qc}}/\partial q_i$ for all generalized coordinates. With respect to the group coordinates,

$$\frac{\partial\boldsymbol{r}_{\mathrm{f},i,\mathrm{qc}}}{\partial x} = \begin{bmatrix} 1 \\ 0 \\ 0 \end{bmatrix} \qquad \text{and} \qquad \frac{\partial\boldsymbol{r}_{\mathrm{f},i,\mathrm{qc}}}{\partial y} = \begin{bmatrix} 0 \\ 1 \\ 0 \end{bmatrix}$$

and

$$\begin{aligned}\frac{\partial\boldsymbol{r}_{\mathrm{f},i,\mathrm{qc}}}{\partial\theta_{\mathrm{b}}} = &l_{\mathrm{b}}\begin{bmatrix} \sin\theta_{\mathrm{b}} \\ -\cos\theta_{\mathrm{b}} \\ 0 \end{bmatrix} + l_{\mathrm{p},i}\begin{bmatrix} \sin(\phi_{\mathrm{p},i}+\theta_{\mathrm{b}}) \\ -\cos(\phi_{\mathrm{p},i}+\theta_{\mathrm{b}}) \\ 0 \end{bmatrix} + \frac{l_{\mathrm{f},i}}{4}\begin{bmatrix} \sin(\phi_{\mathrm{f},i}+\theta_{\mathrm{b}}) \\ -\cos(\phi_{\mathrm{f},i}+\theta_{\mathrm{b}}) \\ 0 \end{bmatrix} \\ &+ \sum_{j=1}^{i-1}\left(l_{\mathrm{p},j}\begin{bmatrix} \sin(\phi_{\mathrm{p},j}+\theta_{\mathrm{b}}) \\ -\cos(\phi_{\mathrm{p},j}+\theta_{\mathrm{b}}) \\ 0 \end{bmatrix} + l_{\mathrm{f},j}\begin{bmatrix} \sin(\phi_{\mathrm{f},j}+\theta_{\mathrm{b}}) \\ -\cos(\phi_{\mathrm{f},j}+\theta_{\mathrm{b}}) \\ 0 \end{bmatrix}\right)\end{aligned} \tag{3.37}$$

Notice that $\partial\boldsymbol{r}_{\mathrm{f},i,\mathrm{qc}}/\partial\theta_{\mathrm{b}}$ depends on the shape variables, in addition to θ_{b}. For the shape variables,

$$\frac{\partial\boldsymbol{r}_{\mathrm{f},i,\mathrm{qc}}}{\partial\phi_{\mathrm{p},j}} = \begin{bmatrix} \sin(\phi_{\mathrm{p},j}+\theta_{\mathrm{b}}) \\ -\cos(\phi_{\mathrm{p},j}+\theta_{\mathrm{b}}) \\ 0 \end{bmatrix}\begin{cases} l_{\mathrm{p},j} & \text{if } j \le i \\ 0 & \text{if } j > i \end{cases} \tag{3.38}$$

and

$$\frac{\partial\boldsymbol{r}_{\mathrm{f},i,\mathrm{qc}}}{\partial\phi_{\mathrm{f},j}} = \begin{bmatrix} \sin(\phi_{\mathrm{f},j}+\theta_{\mathrm{b}}) \\ -\cos(\phi_{\mathrm{f},j}+\theta_{\mathrm{b}}) \\ 0 \end{bmatrix}\begin{cases} l_{\mathrm{f},j} & \text{if } j < i \\ \frac{l_{\mathrm{f},i}}{4} & \text{if } j = i \\ 0 & \text{if } j > i \end{cases} \tag{3.39}$$

Notice that

$$\frac{\partial\boldsymbol{r}_{\mathrm{f},i,\mathrm{qc}}}{\partial\phi_{\mathrm{p},j}} = \frac{\partial\boldsymbol{r}_{\mathrm{f},i,\mathrm{qc}}}{\partial\phi_{\mathrm{f},j}} = \mathbf{0}_{3\times 1}$$

for all $j > i$. That is, the force on the ith fin does not affect $\phi_{\mathrm{p},j}$ nor $\phi_{\mathrm{p},j}$ $\forall j > i$.

3.2.4.3 Generalized Forces

Recall (3.23),

$$\boldsymbol{F}_{\text{ext}} = \mathbf{f}_{\text{L}} + \mathbf{f}_{\text{D}} + \mathbf{m}_{\text{L}} + \mathbf{m}_{\text{D}} + \mathbf{m}_{\text{damp}} + \mathbf{u}(t)$$

By definition, forces act on translational coordinates, i.e. x and y, and moments act on angular coordinates. Thus, all elements of $\mathbf{f}_{\text{L}}$ other than the first two are zero, the first element of $\mathbf{f}_{\text{L}}$, denoted $\text{f}_{\text{L},1}$ can be expressed as

$$\begin{aligned}\text{f}_{\text{L},1} =& \mathbf{f}_{\text{L,b}} \cdot \frac{\partial \boldsymbol{r}_{\text{b,qc}}}{\partial x} + \sum_{i=1}^{L} \mathbf{f}_{\text{L,f},i} \cdot \frac{\partial \boldsymbol{r}_{\text{f},i,\text{qc}}}{\partial x} = \mathbf{f}_{\text{L,b}} \cdot \begin{bmatrix} 1 \\ 0 \\ 0 \end{bmatrix} + \sum_{i=1}^{L} \mathbf{f}_{\text{L,f},i} \cdot \begin{bmatrix} 1 \\ 0 \\ 0 \end{bmatrix} \\ =& \left(\mathbf{f}_{\text{L,b}} + \sum_{i=1}^{L} \mathbf{f}_{\text{L,f},i} \right) \cdot \begin{bmatrix} 1 \\ 0 \\ 0 \end{bmatrix}\end{aligned}$$

and the second element $\text{f}_{\text{L},2}$ can be expressed as (using the same process as before)

$$\begin{aligned}\text{f}_{\text{L},2} =& \mathbf{f}_{\text{L,b}} \cdot \frac{\partial \boldsymbol{r}_{\text{b,qc}}}{\partial y} + \sum_{i=1}^{L} \mathbf{f}_{\text{L,f},i} \cdot \frac{\partial \boldsymbol{r}_{\text{f},i,\text{qc}}}{\partial y} = \mathbf{f}_{\text{L,b}} \cdot \begin{bmatrix} 0 \\ 1 \\ 0 \end{bmatrix} + \sum_{i=1}^{L} \mathbf{f}_{\text{L,f},i} \cdot \begin{bmatrix} 0 \\ 1 \\ 0 \end{bmatrix} \\ =& \left(\mathbf{f}_{\text{L,b}} + \sum_{i=1}^{L} \mathbf{f}_{\text{L,f},i} \right) \cdot \begin{bmatrix} 0 \\ 1 \\ 0 \end{bmatrix}\end{aligned}$$

Similar for $\mathbf{f}_{\text{D}}$, all elements of $\mathbf{f}_{\text{D}}$ other than the first two are zero, the first element of $\mathbf{f}_{\text{D}}$, denoted $\text{f}_{\text{D},1}$ can be expressed as

$$\begin{aligned}\text{f}_{\text{D},1} =& \mathbf{f}_{\text{D,b}} \cdot \frac{\partial \boldsymbol{r}_{\text{b,qc}}}{\partial x} + \sum_{i=1}^{L} \mathbf{f}_{\text{D,f},i} \cdot \frac{\partial \boldsymbol{r}_{\text{f},i,\text{qc}}}{\partial x} = \mathbf{f}_{\text{D,b}} \cdot \begin{bmatrix} 1 \\ 0 \\ 0 \end{bmatrix} + \sum_{i=1}^{L} \mathbf{f}_{\text{D,f},i} \cdot \begin{bmatrix} 1 \\ 0 \\ 0 \end{bmatrix} \\ =& \left(\mathbf{f}_{\text{D,b}} + \sum_{i=1}^{L} \mathbf{f}_{\text{D,f},i} \right) \cdot \begin{bmatrix} 1 \\ 0 \\ 0 \end{bmatrix}\end{aligned}$$

and the second element $\text{f}_{\text{D},2}$ can be expressed as (using the same process as before)

$$\begin{aligned}\text{f}_{\text{D},2} =& \mathbf{f}_{\text{D,b}} \cdot \frac{\partial \boldsymbol{r}_{\text{b,qc}}}{\partial y} + \sum_{i=1}^{L} \mathbf{f}_{\text{D,f},i} \cdot \frac{\partial \boldsymbol{r}_{\text{f},i,\text{qc}}}{\partial y} = \mathbf{f}_{\text{D,b}} \cdot \begin{bmatrix} 0 \\ 1 \\ 0 \end{bmatrix} + \sum_{i=1}^{L} \mathbf{f}_{\text{D,f},i} \cdot \begin{bmatrix} 0 \\ 1 \\ 0 \end{bmatrix} \\ =& \left(\mathbf{f}_{\text{D,b}} + \sum_{i=1}^{L} \mathbf{f}_{\text{D,f},i} \right) \cdot \begin{bmatrix} 0 \\ 1 \\ 0 \end{bmatrix}\end{aligned}$$

From these expressions and the fact that the third elements of the lift and drag forces are zero, it is straightforward to see that

$$\mathbf{f}_{\mathrm{L}} = \begin{bmatrix} \mathbf{f}_{\mathrm{L,b}} + \sum_{i=1}^{L} \mathbf{f}_{\mathrm{L,f},i} \\ \mathbf{0}_{2L\times 1} \end{bmatrix} \tag{3.40}$$

and

$$\mathbf{f}_{\mathrm{D}} = \begin{bmatrix} \mathbf{f}_{\mathrm{D,b}} + \sum_{i=1}^{L} \mathbf{f}_{\mathrm{D,f},i} \\ \mathbf{0}_{2L\times 1} \end{bmatrix} \tag{3.41}$$

The hydrodynamic moments can also be computed using the principle of virtual work. The moment due to lift, $\mathbf{m}_{\mathrm{L}}$, acts only on the angular coordinates, i.e. θ_{b}, $\phi_{\mathrm{p},i}$, and $\phi_{\mathrm{f},i}$. The element of $\mathbf{m}_{\mathrm{L}}$ corresponding to θ_{b}, denoted $\mathrm{m}_{\mathrm{L}}^{(\theta_{\mathrm{b}})}$, which corresponds to θ_{b} is computed as

$$\mathrm{m}_{\mathrm{L}}^{(\theta_{\mathrm{b}})} = \mathbf{f}_{\mathrm{L,b}} \cdot \frac{\partial \boldsymbol{r}_{\mathrm{b,qc}}}{\partial \theta_{\mathrm{b}}} + \sum_{i=1}^{L} \mathbf{f}_{\mathrm{L,f},i} \cdot \frac{\partial \boldsymbol{r}_{\mathrm{f},i,\mathrm{qc}}}{\partial \theta_{\mathrm{b}}} \tag{3.42}$$

with expressions for $\partial \boldsymbol{r}_{\mathrm{b,qc}}/\partial\theta_{\mathrm{b}}$ and $\partial \boldsymbol{r}_{\mathrm{f},i,\mathrm{qc}}/\partial\theta_{\mathrm{b}}$ given in (3.34) and (3.37), respectively. Similar the hydrodynamic moments due to the lift on the jth peduncle are

$$\mathrm{m}_{\mathrm{L}}^{(\phi_{\mathrm{p},j})} = \sum_{i=1}^{L} \mathbf{f}_{\mathrm{L,f},i} \cdot \frac{\partial \boldsymbol{r}_{\mathrm{f},i,\mathrm{qc}}}{\partial \phi_{\mathrm{p},j}}$$

Notice that if $i < j$, $\partial \boldsymbol{r}_{\mathrm{f},i,\mathrm{qc}}/\partial\phi_{\mathrm{p},j} = \mathbf{0}_{3\times 1}$. Therefore,

$$\begin{aligned} \mathrm{m}_{\mathrm{L}}^{(\phi_{\mathrm{p},j})} &= \sum_{i=j}^{L} \mathbf{f}_{\mathrm{L,f},i} \cdot \frac{\partial \boldsymbol{r}_{\mathrm{f},i,\mathrm{qc}}}{\partial \phi_{\mathrm{p},j}} \\ &= \sum_{i=j}^{L} \mathbf{f}_{\mathrm{L,f},i} \cdot l_{\mathrm{p},j} \begin{bmatrix} \sin(\phi_{\mathrm{p},j} + \theta_{\mathrm{b}}) \\ -\cos(\phi_{\mathrm{p},j} + \theta_{\mathrm{b}}) \\ 0 \end{bmatrix} \end{aligned} \tag{3.43}$$

Similarly,

$$\begin{aligned} \mathrm{m}_{\mathrm{L}}^{(\phi_{\mathrm{f},j})} &= \sum_{i=j}^{L} \mathbf{f}_{\mathrm{L,f},i} \cdot \frac{\partial \boldsymbol{r}_{\mathrm{f},i,\mathrm{qc}}}{\partial \phi_{\mathrm{f},j}} \\ &= \mathbf{f}_{\mathrm{L,f},i} \cdot \frac{l_{\mathrm{f},i}}{4} \begin{bmatrix} \sin(\phi_{\mathrm{p},i} + \theta_{\mathrm{b}}) \\ -\cos(\phi_{\mathrm{p},i} + \theta_{\mathrm{b}}) \\ 0 \end{bmatrix} + \sum_{i=j+1}^{L} \mathbf{f}_{\mathrm{L,f},i} \cdot l_{\mathrm{f},j} \begin{bmatrix} \sin(\phi_{\mathrm{p},j} + \theta_{\mathrm{b}}) \\ -\cos(\phi_{\mathrm{p},j} + \theta_{\mathrm{b}}) \\ 0 \end{bmatrix} \end{aligned} \tag{3.44}$$

Similarly, the hydrodynamic drag moments can be expressed as

$$\mathrm{m}_{\mathrm{D}}^{(\theta_{\mathrm{b}})} = \mathbf{f}_{\mathrm{D,b}} \cdot \frac{\partial \boldsymbol{r}_{\mathrm{b,qc}}}{\partial \theta_{\mathrm{b}}} + \sum_{i=1}^{L} \mathbf{f}_{\mathrm{D,f},i} \cdot \frac{\partial \boldsymbol{r}_{\mathrm{f},i,\mathrm{qc}}}{\partial \theta_{\mathrm{b}}} \tag{3.45}$$

$$\mathrm{m}_{\mathrm{D}}^{(\phi_{\mathrm{p},j})} = \sum_{i=j}^{L} \mathbf{f}_{\mathrm{D,f},i} \cdot l_{\mathrm{p},j} \begin{bmatrix} \sin(\phi_{\mathrm{p},j} + \theta_{\mathrm{b}}) \\ -\cos(\phi_{\mathrm{p},j} + \theta_{\mathrm{b}}) \\ 0 \end{bmatrix} \tag{3.46}$$

$$\mathrm{m}_{\mathrm{D}}^{(\phi_{\mathrm{f},j})} = \mathbf{f}_{\mathrm{D,f},i} \cdot \frac{l_{\mathrm{f},i}}{4} \begin{bmatrix} \sin(\phi_{\mathrm{p},i} + \theta_{\mathrm{b}}) \\ -\cos(\phi_{\mathrm{p},i} + \theta_{\mathrm{b}}) \\ 0 \end{bmatrix} + \sum_{i=j+1}^{L} \mathbf{f}_{\mathrm{D,f},i} \cdot l_{\mathrm{f},j} \begin{bmatrix} \sin(\phi_{\mathrm{p},j} + \theta_{\mathrm{b}}) \\ -\cos(\phi_{\mathrm{p},j} + \theta_{\mathrm{b}}) \\ 0 \end{bmatrix} \tag{3.47}$$

Therefore

$$\mathbf{m}_{\mathrm{L}} = \begin{bmatrix} 0 \\ 0 \\ \mathrm{m}_{\mathrm{L}}^{(\theta_{\mathrm{b}})} \\ \mathrm{m}_{\mathrm{L}}^{(\phi_{\mathrm{p},1})} \\ \mathrm{m}_{\mathrm{L}}^{(\phi_{\mathrm{f},1})} \\ \mathrm{m}_{\mathrm{L}}^{(\phi_{\mathrm{p},2})} \\ \mathrm{m}_{\mathrm{L}}^{(\phi_{\mathrm{f},2})} \\ \vdots \\ \mathrm{m}_{\mathrm{L}}^{(\phi_{\mathrm{p},L})} \\ \mathrm{m}_{\mathrm{L}}^{(\phi_{\mathrm{f},L})} \end{bmatrix} \quad \text{and} \quad \mathbf{m}_{\mathrm{D}} = \begin{bmatrix} 0 \\ 0 \\ \mathrm{m}_{\mathrm{D}}^{(\theta_{\mathrm{b}})} \\ \mathrm{m}_{\mathrm{D}}^{(\phi_{\mathrm{p},1})} \\ \mathrm{m}_{\mathrm{D}}^{(\phi_{\mathrm{f},1})} \\ \mathrm{m}_{\mathrm{D}}^{(\phi_{\mathrm{p},2})} \\ \mathrm{m}_{\mathrm{D}}^{(\phi_{\mathrm{f},2})} \\ \vdots \\ \mathrm{m}_{\mathrm{D}}^{(\phi_{\mathrm{p},L})} \\ \mathrm{m}_{\mathrm{D}}^{(\phi_{\mathrm{f},L})} \end{bmatrix} \tag{3.48}$$

The final hydrodynamic forcing term is the rotational damping. This is assumed to be linear damping in all of the angular coordinates. Thus,

$$\mathbf{m}_{\mathrm{damp}} = \begin{bmatrix} 0 \\ 0 \\ -b_{\mathrm{d,b}}\dot{\theta}_{\mathrm{b}} \\ -b_{\mathrm{d,p},1}\dot{\psi}_{\mathrm{p},1} \\ -b_{\mathrm{d,f},1}\dot{\psi}_{\mathrm{f},1} \\ -b_{\mathrm{d,p},2}\dot{\psi}_{\mathrm{p},2} \\ -b_{\mathrm{d,f},2}\dot{\psi}_{\mathrm{f},2} \\ \vdots \\ -b_{\mathrm{d,p},L}\dot{\psi}_{\mathrm{p},L} \\ -b_{\mathrm{d,f},L}\dot{\psi}_{\mathrm{f},L} \end{bmatrix}$$

Note that $\dot{\psi}_{\mathrm{p},i} = \dot{\phi}_{\mathrm{p},i} + \dot{\theta}_{\mathrm{b}}$ and $\dot{\psi}_{\mathrm{f},i} = \dot{\phi}_{\mathrm{f},i} + \dot{\theta}_{\mathrm{b}}$. Thus,

$$\mathbf{m}_{\mathrm{damp}} = \begin{bmatrix} 0 \\ 0 \\ -b_{\mathrm{d,b}}\dot{\theta}_{\mathrm{b}} \\ -b_{\mathrm{d,p},1}\left(\dot{\phi}_{\mathrm{p},1} + \dot{\theta}_{\mathrm{b}}\right) \\ -b_{\mathrm{d,f},1}\left(\dot{\phi}_{\mathrm{f},1} + \dot{\theta}_{\mathrm{b}}\right) \\ -b_{\mathrm{d,p},2}\left(\dot{\phi}_{\mathrm{p},2} + \dot{\theta}_{\mathrm{b}}\right) \\ -b_{\mathrm{d,f},2}\left(\dot{\phi}_{\mathrm{f},2} + \dot{\theta}_{\mathrm{b}}\right) \\ \vdots \\ -b_{\mathrm{d,p},L}\left(\dot{\phi}_{\mathrm{p},L} + \dot{\theta}_{\mathrm{b}}\right) \\ -b_{\mathrm{d,f},L}\left(\dot{\phi}_{\mathrm{f},L} + \dot{\theta}_{\mathrm{b}}\right) \end{bmatrix} \tag{3.49}$$

Note that these damping moments are applied directly to the links, so these are generalized forces. Likewise, the internal moments $\boldsymbol{\mathfrak{u}}(t)$ are generalized forces. However, unlike the hydrodynamic forcing, the internal moments can be prescribed and, assuming one has knowledge of the states, include both state and time dependence. This fact will be exploited later, but for now, simply consider $\boldsymbol{\mathfrak{u}}(t)$ of the form

$$\boldsymbol{\mathfrak{u}}(t) = \begin{bmatrix} 0 \\ 0 \\ 0 \\ \mathfrak{u}_1(t) \\ \mathfrak{u}_2(t) \\ \vdots \\ \mathfrak{u}_{2L}(t) \end{bmatrix} \qquad \text{or} \qquad \boldsymbol{\mathfrak{u}}(t) = \begin{bmatrix} 0 \\ 0 \\ 0 \\ \mathfrak{u}_{\mathrm{p},1}(t) \\ \mathfrak{u}_{\mathrm{f},1}(t) \\ \mathfrak{u}_{\mathrm{p},2}(t) \\ \mathfrak{u}_{\mathrm{f},2}(t) \\ \vdots \\ \mathfrak{u}_{\mathrm{p},L}(t) \\ \mathfrak{u}_{\mathrm{f},L}(t) \end{bmatrix} \tag{3.50}$$

Notice that the two forms are simply different ways of expressing the same $\boldsymbol{\mathfrak{u}}(t)$, i.e $\mathfrak{u}_{\mathrm{p},i}(t) = \mathfrak{u}_{2i-1}(t)$ and $\mathfrak{u}_{\mathrm{f},i}(t) = \mathfrak{u}_{2i}(t)$ for $i = 1, \ldots, L$, and can be used interchangeably when convenient. Again, since these moments are applied directly to the generalized coordinates, they are generalized forces, and therefore the principle of virtual work is not needed.

3.2.4.4 Parameter Vector

The parameter vector $\boldsymbol{\mathfrak{p}}$ contains all of the system parameters. The order is not particularly important; $\boldsymbol{\mathfrak{p}}$ is only represented as a vector for the purposes of inclusion in mathematics.

Table 3.3: Parameters contained within the parameter vector $\mathfrak{p}$

Parameter Name	Symbol
Lengths	$l_{\text{b}},\ l_{\text{p},1}, l_{\text{p},2}, \ldots, l_{\text{p},L},\ l_{\text{f},1}, l_{\text{f},2}, \ldots, l_{\text{f},L}$
Masses	$m_{\text{b}},\ m_{\text{p},1}, m_{\text{p},2}, \ldots, m_{\text{p},L},\ m_{\text{f},1}, m_{\text{f},2}, \ldots, m_{\text{f},L}$
Inertias	$I_{\text{b}},\ I_{\text{p},1}, I_{\text{p},2}, \ldots, I_{\text{p},L},\ I_{\text{f},1}, I_{\text{f},2}, \ldots, I_{\text{f},L}$
Circulation Coefficients	$C_{\Gamma,\text{b}}, C_{\Gamma,\text{f},1}, C_{\Gamma,\text{f},2}, \ldots, C_{\Gamma,\text{f},L}$
Lift Coefficients	$C_{\text{L},\text{b}}, C_{\text{L},\text{f},1}, C_{\text{L},\text{f},2}, \ldots, C_{\text{L},\text{f},L}$
Linear Drag Coefficients	$C_{\text{D,linear,b}}, C_{\text{D,linear,f},1}, C_{\text{D,linear,f},2}, \ldots, C_{\text{D,linear,f},L}$
Drag Coefficients	$C_{\text{D,b}}, C_{\text{D,f},1}, C_{\text{D,f},2}, \ldots, C_{\text{D,f},L}$
Rotational Damping Coefficients	$b_{\text{d,b}},\ b_{\text{d,p},1}, b_{\text{d,p},2}, \ldots, b_{\text{d,p},L},\ b_{\text{d,f},1}, b_{\text{d,f},2}, \ldots, b_{\text{d,f},L}$
Number of Fins	L

The parameter *vector* could be better thought of as the parameter *list*, a grouping of the parameters that define the system. As such, the elements of $\mathfrak{p}$ are described in Table 3.3. Although expressing $\mathfrak{p}$ as a vector does not represent a physical property, doing so allows physical constraints, e.g. all masses must be positive, to be expressed as functions of $\mathfrak{p}$. Many of these functions will be linear or affine, greatly reducing the computational overhead required to solve numerical optimization problems.

3.2.4.5 Final Synthesis

Recall from equation (3.14) that the dynamics of the multi-link fish can be expressed as

$$\boldsymbol{M}(\boldsymbol{q})\,\ddot{\boldsymbol{q}} + \boldsymbol{C}(\boldsymbol{q}, \dot{\boldsymbol{q}}) = \boldsymbol{F}_{\text{ext}}$$

If the $\boldsymbol{F}_{\text{ext}}$ is divided into the hydrodynamic forces, i.e.

$$\boldsymbol{F}_{\text{Hydro}} = \mathbf{f}_{\text{L}} + \mathbf{f}_{\text{D}} + \mathbf{m}_{\text{L}} + \mathbf{m}_{\text{D}} + \mathbf{m}_{\text{damp}}$$

and internal joint forces, i.e. $\mathfrak{u}(t)$, then the equations of motion can be expressed as

$$\boldsymbol{M}(\boldsymbol{q})\,\ddot{\boldsymbol{q}} = -\boldsymbol{C}(\boldsymbol{q}, \dot{\boldsymbol{q}}) + \boldsymbol{F}_{\text{Hydro}} + \mathfrak{u}(t)$$

or as

$$\ddot{\boldsymbol{q}} = -\boldsymbol{M}^{-1}(\boldsymbol{q})\,\boldsymbol{C}(\boldsymbol{q}, \dot{\boldsymbol{q}}) + \boldsymbol{M}^{-1}(\boldsymbol{q})\,\boldsymbol{F}_{\text{Hydro}} + \boldsymbol{M}^{-1}(\boldsymbol{q})\,\mathfrak{u}(t) \tag{3.51}$$

where $\boldsymbol{M}^{-1}(\boldsymbol{q})$ is the inverse of the symmetric matrix $\boldsymbol{M}(\boldsymbol{q})$. As $\left(A^{-1}\right)^T = \left(A^T\right)^{-1}$ for any invertible matrix A, $\boldsymbol{M}^{-1}(\boldsymbol{q})$ is symmetric because $\boldsymbol{M}(\boldsymbol{q})$ is symmetric. Let $\boldsymbol{M}^{-1}(\boldsymbol{q})$ be partitioned as

$$\boldsymbol{M}^{-1}(\boldsymbol{q}) = \begin{bmatrix} \boldsymbol{M}_{11}^{-1}(\boldsymbol{q}) & \boldsymbol{M}_{12}^{-1}(\boldsymbol{q}) \\ \left(\boldsymbol{M}_{12}^{-1}(\boldsymbol{q})\right)^T & \boldsymbol{M}_{22}^{-1}(\boldsymbol{q}) \end{bmatrix}$$

where $\boldsymbol{M}_{11}^{-1}(\boldsymbol{q}) \in \mathbb{R}^{3\times 3}$, $\boldsymbol{M}_{12}^{-1}(\boldsymbol{q}) \in \mathbb{R}^{3\times 2L}$, and $\boldsymbol{M}_{22}^{-1}(\boldsymbol{q}) \in \mathbb{R}^{2L\times 2L}$. Partitioning the group coordinates $\mathbf{r}$ and the shape coordinates $\mathbf{s}$ yields

$$\ddot{\mathrm{r}} = -\left[\boldsymbol{M}_{11}^{-1}(\boldsymbol{q}),\ \boldsymbol{M}_{12}^{-1}(\boldsymbol{q})\right](\boldsymbol{C}(\boldsymbol{q},\dot{\boldsymbol{q}}) - \boldsymbol{F}_{\mathrm{Hydro}}) + \left[\boldsymbol{M}_{11}^{-1}(\boldsymbol{q}),\ \boldsymbol{M}_{12}^{-1}(\boldsymbol{q})\right]\mathfrak{u}(t)$$

and

$$\ddot{\mathrm{s}} = -\left[\left(\boldsymbol{M}_{12}^{-1}(\boldsymbol{q})\right)^T,\ \boldsymbol{M}_{22}^{-1}(\boldsymbol{q})\right](\boldsymbol{C}(\boldsymbol{q},\dot{\boldsymbol{q}}) - \boldsymbol{F}_{\mathrm{Hydro}}) + \left[\left(\boldsymbol{M}_{12}^{-1}(\boldsymbol{q})\right)^T,\ \boldsymbol{M}_{22}^{-1}(\boldsymbol{q})\right]\mathfrak{u}(t)$$

Note that the first three elements of $\mathfrak{u}(t)$ are zero. Let $\widetilde{\mathfrak{u}}(t)$ be defined such that

$$\widetilde{\mathfrak{u}}(t) = \begin{bmatrix} \mathfrak{u}_1(t) \\ \mathfrak{u}_2(t) \\ \vdots \\ \mathfrak{u}_{2L}(t) \end{bmatrix} = \begin{bmatrix} \mathfrak{u}_{\mathrm{p},1}(t) \\ \mathfrak{u}_{\mathrm{f},1}(t) \\ \mathfrak{u}_{\mathrm{p},2}(t) \\ \mathfrak{u}_{\mathrm{f},2}(t) \\ \vdots \\ \mathfrak{u}_{\mathrm{p},L}(t) \\ \mathfrak{u}_{\mathrm{f},L}(t) \end{bmatrix}$$

Thus $\mathfrak{u}(t) = \left[\mathbf{0}_{1\times 3}, \widetilde{\mathfrak{u}}^T(t)\right]^T$. The state dynamics can therefore be expressed as

$$\ddot{\mathrm{r}} = -\left[\boldsymbol{M}_{11}^{-1}(\boldsymbol{q}),\ \boldsymbol{M}_{12}^{-1}(\boldsymbol{q})\right](\boldsymbol{C}(\boldsymbol{q},\dot{\boldsymbol{q}}) - \boldsymbol{F}_{\mathrm{Hydro}}) + \boldsymbol{M}_{12}^{-1}(\boldsymbol{q})\,\widetilde{\mathfrak{u}}(t) \tag{3.52}$$

and the shape dynamics can be expressed as

$$\ddot{\mathrm{s}} = -\left[\left(\boldsymbol{M}_{12}^{-1}(\boldsymbol{q})\right)^T,\ \boldsymbol{M}_{22}^{-1}(\boldsymbol{q})\right](\boldsymbol{C}(\boldsymbol{q},\dot{\boldsymbol{q}}) - \boldsymbol{F}_{\mathrm{Hydro}}) + \boldsymbol{M}_{22}^{-1}(\boldsymbol{q})\,\widetilde{\mathfrak{u}}(t) \tag{3.53}$$

3.2.5 Control Methodology

For control, rather than attempting to apply forces to generate desired motions, it is preferable to specify the shape coordinates directly. This makes intuitive sense; when you want to move your body, you typically do not think about what combination of muscle contractions will result in the desired motion, rather you think of the position you want your body in. Mechanically, this is equivalent to using servos.

Recall the shape dynamics from equation (3.53). If it was possible to specify the shape dynamics, (3.53) would take the form of

$$\ddot{\mathrm{s}} = \boldsymbol{u}(t) \tag{3.54}$$

where $\boldsymbol{u}(t) \in \mathbb{R}^{2L\times 1}$ are commanded accelerations of the shape coordinates. Using this definition, it can be seen that, in order to control the shape coordinates to obey (3.54) $\widetilde{\mathfrak{u}}(t)$ must obey

$$\boldsymbol{u}(t) = -\left[\left(\boldsymbol{M}_{12}^{-1}(\boldsymbol{q})\right)^T,\ \boldsymbol{M}_{22}^{-1}(\boldsymbol{q})\right](\boldsymbol{C}(\boldsymbol{q},\dot{\boldsymbol{q}}) - \boldsymbol{F}_{\mathrm{Hydro}}) + \boldsymbol{M}_{22}^{-1}(\boldsymbol{q})\,\widetilde{\mathfrak{u}}(t)$$

or, through straightforward manipulation,

$$\widetilde{\mathbf{u}}(t) = \left(\boldsymbol{M}_{22}^{-1}\right)^{-1}(\boldsymbol{q})\left[\left(\boldsymbol{M}_{12}^{-1}(\boldsymbol{q})\right)^{T},\ \boldsymbol{M}_{22}^{-1}(\boldsymbol{q})\right]\left(\boldsymbol{C}(\boldsymbol{q},\dot{\boldsymbol{q}}) - \boldsymbol{F}_{\text{Hydro}}\right) + \left(\boldsymbol{M}_{22}^{-1}\right)^{-1}(\boldsymbol{q})\,\boldsymbol{u}(t) \tag{3.55}$$

Note that $\left(\boldsymbol{M}_{22}^{-1}\right)^{-1} \neq \boldsymbol{M}_{\mathbf{s}}$. Substituting (3.55) into (3.52) yields

$$\begin{aligned}\ddot{\mathbf{r}} = &-\left[\boldsymbol{M}_{11}^{-1}(\boldsymbol{q}),\ \boldsymbol{M}_{12}^{-1}(\boldsymbol{q})\right]\left(\boldsymbol{C}(\boldsymbol{q},\dot{\boldsymbol{q}}) - \boldsymbol{F}_{\text{Hydro}}\right)\\ &+ \boldsymbol{M}_{12}^{-1}(\boldsymbol{q})\left(\boldsymbol{M}_{22}^{-1}\right)^{-1}(\boldsymbol{q})\left[\left(\boldsymbol{M}_{12}^{-1}(\boldsymbol{q})\right)^{T},\ \boldsymbol{M}_{22}^{-1}(\boldsymbol{q})\right]\left(\boldsymbol{C}(\boldsymbol{q},\dot{\boldsymbol{q}}) - \boldsymbol{F}_{\text{Hydro}}\right)\\ &+ \boldsymbol{M}_{12}^{-1}(\boldsymbol{q})\left(\boldsymbol{M}_{22}^{-1}\right)^{-1}(\boldsymbol{q})\,\boldsymbol{u}(t)\end{aligned} \tag{3.56}$$

Since the shape coordinates are specified, they are known. Therefore, let

$$\begin{aligned}\boldsymbol{f}(\boldsymbol{q},\dot{\boldsymbol{q}}) = &-\left[\boldsymbol{M}_{11}^{-1}(\boldsymbol{q}),\ \boldsymbol{M}_{12}^{-1}(\boldsymbol{q})\right]\left(\boldsymbol{C}(\boldsymbol{q},\dot{\boldsymbol{q}}) - \boldsymbol{F}_{\text{Hydro}}\right)\\ &+ \boldsymbol{M}_{12}^{-1}(\boldsymbol{q})\left(\boldsymbol{M}_{22}^{-1}\right)^{-1}(\boldsymbol{q})\left[\left(\boldsymbol{M}_{12}^{-1}(\boldsymbol{q})\right)^{T},\ \boldsymbol{M}_{22}^{-1}(\boldsymbol{q})\right]\left(\boldsymbol{C}(\boldsymbol{q},\dot{\boldsymbol{q}}) - \boldsymbol{F}_{\text{Hydro}}\right)\end{aligned} \tag{3.57}$$

and let $\boldsymbol{g}_i(\boldsymbol{q})$ be the ith column of $\boldsymbol{M}_{12}^{-1}(\boldsymbol{q})\left(\boldsymbol{M}_{22}^{-1}\right)^{-1}(\boldsymbol{q})$, that is

$$\boldsymbol{M}_{12}^{-1}(\boldsymbol{q})\left(\boldsymbol{M}_{22}^{-1}\right)^{-1}(\boldsymbol{q}) = \boldsymbol{M}_{12}^{-1}(\mathbf{r})\left(\boldsymbol{M}_{22}^{-1}\right)^{-1}(\mathbf{r}) = \left[\ \boldsymbol{g}_1(\boldsymbol{q}) \quad \boldsymbol{g}_2(\boldsymbol{q}) \quad \cdots \boldsymbol{g}_{2L}(\boldsymbol{q})\ \right] \tag{3.58}$$

Therefore, (3.56) can be expressed as

$$\ddot{\mathbf{r}} = \boldsymbol{f}(\boldsymbol{q},\dot{\boldsymbol{q}}) + \sum_{i=1}^{2L}\boldsymbol{g}_i(\boldsymbol{q})\,u_i(t) \tag{3.59}$$

where $u_i(t)$ is the ith element of $\boldsymbol{u}(t)$. This is a control affine system with the drift vector field being $\boldsymbol{f}(\boldsymbol{q},\dot{\boldsymbol{q}})$ and input vector fields being $\boldsymbol{g}_i(\boldsymbol{q})$.

3.2.6 A Note On Matrix Inverses

Suppose that the mass matrix is partitioned as

$$\boldsymbol{M} = \begin{bmatrix} \widetilde{\boldsymbol{M}}_{\mathbf{r}} & \widetilde{\boldsymbol{M}}_{\mathbf{rs}} \\ \widetilde{\boldsymbol{M}}_{\mathbf{rs}}^{T} & \widetilde{\boldsymbol{M}}_{\mathbf{s}} \end{bmatrix}$$

where the $\widetilde{(\cdot)}$ denotes the inclusion of added mass, and note that the inverse to the matrix

$$\begin{bmatrix} \boldsymbol{A} & \boldsymbol{B} \\ \boldsymbol{C} & \boldsymbol{D} \end{bmatrix}$$

is

$$\begin{bmatrix} \boldsymbol{A} & \boldsymbol{B} \\ \boldsymbol{C} & \boldsymbol{D} \end{bmatrix}^{-1} = \begin{bmatrix} \boldsymbol{A}^{-1} + \boldsymbol{A}^{-1}\boldsymbol{B}\left(\boldsymbol{D} - \boldsymbol{C}\boldsymbol{A}^{-1}\boldsymbol{B}\right)^{-1}\boldsymbol{C}\boldsymbol{A}^{-1} & -\boldsymbol{A}^{-1}\boldsymbol{B}\left(\boldsymbol{D} - \boldsymbol{C}\boldsymbol{A}^{-1}\boldsymbol{B}\right)^{-1} \\ -\left(\boldsymbol{D} - \boldsymbol{C}\boldsymbol{A}^{-1}\boldsymbol{B}\right)^{-1}\boldsymbol{C}\boldsymbol{A}^{-1} & \left(\boldsymbol{D} - \boldsymbol{C}\boldsymbol{A}^{-1}\boldsymbol{B}\right)^{-1} \end{bmatrix}$$

Therefore

$$\boldsymbol{M}^{-1} = \begin{bmatrix} \widetilde{\boldsymbol{M}}_{\mathbf{r}}^{-1} + \widetilde{\boldsymbol{M}}_{\mathbf{r}}^{-1}\widetilde{\boldsymbol{M}}_{\mathbf{rs}}\left(\widetilde{\boldsymbol{M}}_{\mathbf{s}} - \widetilde{\boldsymbol{M}}_{\mathbf{rs}}^{T}\widetilde{\boldsymbol{M}}_{\mathbf{r}}^{-1}\widetilde{\boldsymbol{M}}_{\mathbf{rs}}\right)^{-1}\widetilde{\boldsymbol{M}}_{\mathbf{rs}}^{T}\widetilde{\boldsymbol{M}}_{\mathbf{r}}^{-1} & -\widetilde{\boldsymbol{M}}_{\mathbf{r}}^{-1}\widetilde{\boldsymbol{M}}_{\mathbf{rs}}\left(\widetilde{\boldsymbol{M}}_{\mathbf{s}} - \widetilde{\boldsymbol{M}}_{\mathbf{rs}}^{T}\widetilde{\boldsymbol{M}}_{\mathbf{r}}^{-1}\widetilde{\boldsymbol{M}}_{\mathbf{rs}}\right)^{-1} \\ -\left(\widetilde{\boldsymbol{M}}_{\mathbf{s}} - \widetilde{\boldsymbol{M}}_{\mathbf{rs}}^{T}\widetilde{\boldsymbol{M}}_{\mathbf{r}}^{-1}\widetilde{\boldsymbol{M}}_{\mathbf{rs}}\right)^{-1}\widetilde{\boldsymbol{M}}_{\mathbf{rs}}^{T}\widetilde{\boldsymbol{M}}_{\mathbf{r}}^{-1} & \left(\widetilde{\boldsymbol{M}}_{\mathbf{s}} - \widetilde{\boldsymbol{M}}_{\mathbf{rs}}^{T}\widetilde{\boldsymbol{M}}_{\mathbf{r}}^{-1}\widetilde{\boldsymbol{M}}_{\mathbf{rs}}\right)^{-1} \end{bmatrix}$$

where $\widetilde{\boldsymbol{M}}_{\mathbf{s}} - \widetilde{\boldsymbol{M}}_{\mathbf{rs}}^{T}\widetilde{\boldsymbol{M}}_{\mathbf{r}}^{-1}\widetilde{\boldsymbol{M}}_{\mathbf{rs}}$ is called the Schur complement of $\widetilde{\boldsymbol{M}}_{\mathbf{r}}$ in $\boldsymbol{M}$. Since both $\widetilde{\boldsymbol{M}}_{\mathbf{r}}$ and the Schur complement are symmetric,

$$\left(\widetilde{\boldsymbol{M}}_{\mathbf{r}}^{-1}\widetilde{\boldsymbol{M}}_{\mathbf{rs}}\left(\widetilde{\boldsymbol{M}}_{\mathbf{s}} - \widetilde{\boldsymbol{M}}_{\mathbf{rs}}^{T}\widetilde{\boldsymbol{M}}_{\mathbf{r}}^{-1}\widetilde{\boldsymbol{M}}_{\mathbf{rs}}\right)^{-1}\right)^{T} = \left(\widetilde{\boldsymbol{M}}_{\mathbf{s}} - \widetilde{\boldsymbol{M}}_{\mathbf{rs}}^{T}\widetilde{\boldsymbol{M}}_{\mathbf{r}}^{-1}\widetilde{\boldsymbol{M}}_{\mathbf{rs}}\right)^{-1}\widetilde{\boldsymbol{M}}_{\mathbf{rs}}^{T}\widetilde{\boldsymbol{M}}_{\mathbf{r}}^{-1}$$

Therefore, the inverse of the mass matrix can be expressed as

$$\boldsymbol{M}^{-1} = \begin{bmatrix} \widetilde{\boldsymbol{M}}_{\mathbf{r}}^{-1} + \widetilde{\boldsymbol{M}}_{\mathbf{r}}^{-1}\widetilde{\boldsymbol{M}}_{\mathbf{rs}}\left(\widetilde{\boldsymbol{M}}_{\mathbf{s}} - \widetilde{\boldsymbol{M}}_{\mathbf{rs}}^{T}\widetilde{\boldsymbol{M}}_{\mathbf{r}}^{-1}\widetilde{\boldsymbol{M}}_{\mathbf{rs}}\right)^{-1}\widetilde{\boldsymbol{M}}_{\mathbf{rs}}^{T}\widetilde{\boldsymbol{M}}_{\mathbf{r}}^{-1} & -\widetilde{\boldsymbol{M}}_{\mathbf{r}}^{-1}\widetilde{\boldsymbol{M}}_{\mathbf{rs}}\left(\widetilde{\boldsymbol{M}}_{\mathbf{s}} - \widetilde{\boldsymbol{M}}_{\mathbf{rs}}^{T}\widetilde{\boldsymbol{M}}_{\mathbf{r}}^{-1}\widetilde{\boldsymbol{M}}_{\mathbf{rs}}\right)^{-1} \\ -\left(\widetilde{\boldsymbol{M}}_{\mathbf{r}}^{-1}\widetilde{\boldsymbol{M}}_{\mathbf{rs}}\left(\widetilde{\boldsymbol{M}}_{\mathbf{s}} - \widetilde{\boldsymbol{M}}_{\mathbf{rs}}^{T}\widetilde{\boldsymbol{M}}_{\mathbf{r}}^{-1}\widetilde{\boldsymbol{M}}_{\mathbf{rs}}\right)^{-1}\right)^{T} & \left(\widetilde{\boldsymbol{M}}_{\mathbf{s}} - \widetilde{\boldsymbol{M}}_{\mathbf{rs}}^{T}\widetilde{\boldsymbol{M}}_{\mathbf{r}}^{-1}\widetilde{\boldsymbol{M}}_{\mathbf{rs}}\right)^{-1} \end{bmatrix} \tag{3.60}$$

Recalling the partitions of the inverted mass matrix, we find that

$$\begin{aligned} \boldsymbol{M}_{11}^{-1} &= \widetilde{\boldsymbol{M}}_{\mathbf{r}}^{-1} + \widetilde{\boldsymbol{M}}_{\mathbf{r}}^{-1}\widetilde{\boldsymbol{M}}_{\mathbf{rs}}\left(\widetilde{\boldsymbol{M}}_{\mathbf{s}} - \widetilde{\boldsymbol{M}}_{\mathbf{rs}}^{T}\widetilde{\boldsymbol{M}}_{\mathbf{r}}^{-1}\widetilde{\boldsymbol{M}}_{\mathbf{rs}}\right)^{-1}\widetilde{\boldsymbol{M}}_{\mathbf{rs}}^{T}\widetilde{\boldsymbol{M}}_{\mathbf{r}}^{-1} \\ \boldsymbol{M}_{12}^{-1} &= -\widetilde{\boldsymbol{M}}_{\mathbf{r}}^{-1}\widetilde{\boldsymbol{M}}_{\mathbf{rs}}\left(\widetilde{\boldsymbol{M}}_{\mathbf{s}} - \widetilde{\boldsymbol{M}}_{\mathbf{rs}}^{T}\widetilde{\boldsymbol{M}}_{\mathbf{r}}^{-1}\widetilde{\boldsymbol{M}}_{\mathbf{rs}}\right)^{-1} \\ \boldsymbol{M}_{22}^{-1} &= \left(\widetilde{\boldsymbol{M}}_{\mathbf{s}} - \widetilde{\boldsymbol{M}}_{\mathbf{rs}}^{T}\widetilde{\boldsymbol{M}}_{\mathbf{r}}^{-1}\widetilde{\boldsymbol{M}}_{\mathbf{rs}}\right)^{-1} \end{aligned} \tag{3.61}$$

and therefore

$$\left(\boldsymbol{M}_{22}^{-1}\right)^{-1} = \widetilde{\boldsymbol{M}}_{\mathbf{s}} - \widetilde{\boldsymbol{M}}_{\mathbf{rs}}^{T}\widetilde{\boldsymbol{M}}_{\mathbf{r}}^{-1}\widetilde{\boldsymbol{M}}_{\mathbf{rs}} \tag{3.62}$$

The computational complexity of finding the partitioned matrix inverse is significantly reduced by this partitioning. Directly computing the inverse of $\boldsymbol{M}$, then partitioning, and finally inverting $\boldsymbol{M}_{22}^{-1}$ requires the inversion of a matrix in $\mathbb{R}^{3+2L\times 3+2L}$ and a matrix in $\mathbb{R}^{2L\times 2L}$. The complexity of this operation increases dramatically as L increases. By partitioning the matrix, this is reduced to inverting $\widetilde{\boldsymbol{M}}_{\mathbf{r}} \in \mathbb{R}^{3\times 3}$ and then inverting $\widetilde{\boldsymbol{M}}_{\mathbf{s}} - \widetilde{\boldsymbol{M}}_{\mathbf{rs}}^{T}\widetilde{\boldsymbol{M}}_{\mathbf{r}}^{-1}\widetilde{\boldsymbol{M}}_{\mathbf{rs}} \in \mathbb{R}^{2L\times 2L}$ along with some matrix multiplication, significantly reducing overhead.[1]

3.2.7 Gait and Morphology Description

As the shape coordinates can be specified directly, the gait can be chosen arbitrarily. For this work, sinusoidal gaits are chosen. This choice is common for fish biolocomotion [Mason

[1]The choice of using the Schur complement of $\widetilde{\boldsymbol{M}}_{\mathbf{r}}$ in $\boldsymbol{M}$ rather than the Schur complement of $\widetilde{\boldsymbol{M}}_{\mathbf{s}}$ in $\boldsymbol{M}$ is so that $\left(\boldsymbol{M}_{22}^{-1}\right)^{-1}$ can be computed without inversion (because it is the Schur complement).

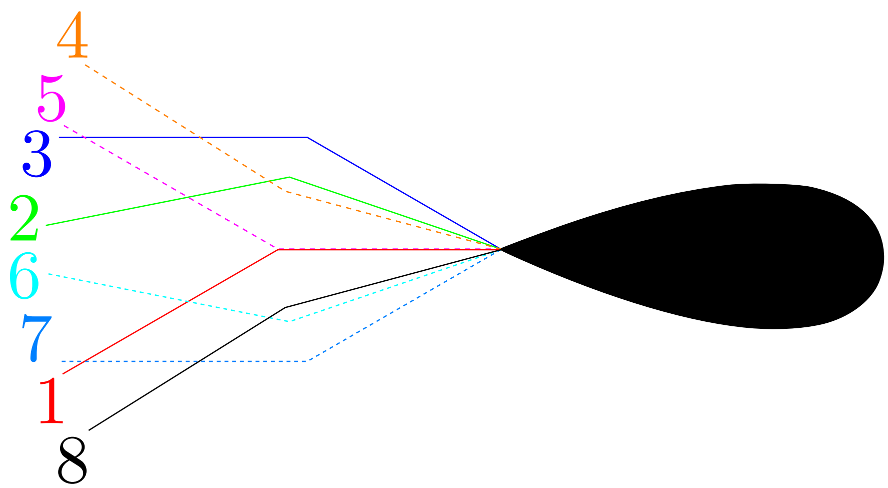

Figure 3.13: Diagram of a typical gait for $L = 1$ and $\psi_{\phi_{\mathrm{f},1}} = 90°$. The numbers correspond to the order of the sequence of tail orientations. The "upstroke" is in solid lines, while the "down stroke" is in dashed lines.

and Burdick, 2000]. For sinusoidal gaits, the shape coordinates are parameterized as

$$\begin{aligned}\phi_{\mathrm{p},i}\left(t\right) =& \overline{\phi}_{\mathrm{p},i} - \frac{\phi_{\mathrm{p},i,0}}{\Omega}\cos\left(\Omega t + \psi_{\phi_{\mathrm{p},i}}\right)\\ \phi_{\mathrm{f},i}\left(t\right) =& \overline{\phi}_{\mathrm{f},i} - \frac{\phi_{\mathrm{f},i,0}}{\Omega}\cos\left(\Omega t + \psi_{\phi_{\mathrm{f},i}}\right)\end{aligned} \tag{3.63}$$

These sinusoidal gaits lead to velocities of

$$\begin{aligned}\dot{\phi}_{\mathrm{p},i}\left(t\right) =& \phi_{\mathrm{p},i,0}\sin\left(\Omega t + \psi_{\phi_{\mathrm{p},i}}\right)\\ \dot{\phi}_{\mathrm{f},i}\left(t\right) =& \phi_{\mathrm{f},i,0}\sin\left(\Omega t + \psi_{\phi_{\mathrm{f},i}}\right)\end{aligned} \tag{3.64}$$

and required the inputs are

$$\begin{aligned}u_{2i-1}(t) = \ddot{\phi}_{\mathrm{p},i}\left(t\right) =& \phi_{\mathrm{p},i,0}\Omega\cos\left(\Omega t + \psi_{\phi_{\mathrm{p},i}}\right)\\ u_{2i}(t) = \ddot{\phi}_{\mathrm{f},i}\left(t\right) =& \phi_{\mathrm{f},i,0}\Omega\cos\left(\Omega t + \psi_{\phi_{\mathrm{f},i}}\right)\end{aligned} \tag{3.65}$$

When describing the gait, Ω is referred to as the *tail beat rate*; the quantities $\phi_{\cdot,\cdot,0}/\Omega$ are referred to as the *stroke amplitudes* (e.g. $\phi_{\mathrm{f},i,0}/\Omega$ is the "stoke amplitude of the ith fin"); and $\overline{\phi}_{\cdot,i}$ are the *mean stroke angles* (e.g. $\overline{\phi}_{\mathrm{f},i}$ is the mean stroke angle of the ith fin). For simplicity and without loss of generality, $\psi_{\phi_{\mathrm{p},1}}$ is set to be zero. Occasionally, the *tail beat period*, T, is used instead of the tail beat rate, Ω. If Ω is in units of radians per second, $T = 2\pi/\Omega$. A typical gait for $L = 1$ is shown in Figure 3.13. In Figure 3.13, the tail fin is shown as a line (instead of a hydrofoil) for clarity.

In addition to the gait, the morphology must be described using a consistent set of parameters. Instead of directly defining the length of each segment, an overall length and

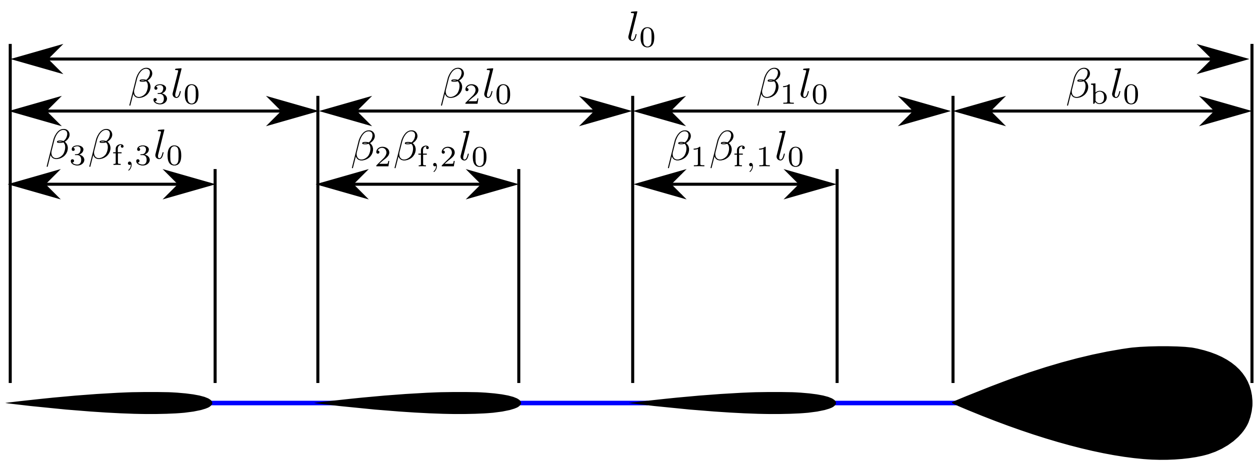

Figure 3.14: Conventions for parameterizing the morphology of the multi-link fish model with $L = 3$

several ratios are used to define the size of each component. The overall length is l_0. The the ratio of the length of the body to the overall length is β_b, i.e. $l_b = \beta_b l_0$. The ratio of combined length of the ith peduncle and fin to the overall length is β_i and the ratio of length of the ith fin to the combined length of the ith peduncle and fin is $\beta_{f,i}$. These ratios can over-define the morphology, so a few parameters are dependent on the others. Specifically,

$$\beta_1 = 1 - \beta_b - \sum_{i=2}^{L} \beta_i \tag{3.66}$$

From this it can be seen that if $L = 1$, then $\beta_1 = 1 - \beta_b$. Also, notice that by this notation, it is possible to define the ratio of length of the ith fin to the combined length of the ith peduncle and fin as $\beta_{p,i}$, but this would over-define the morphology as $\beta_{p,i} = 1 - \beta_{f,i}$. These conventions are shown in Figure 3.14.

3.3 Simulation

Prior to discussing the optimization process, general trends about the performance of this fish model are discussed in light of several simulations. These simulations are of a system that is representative of thunniform locomotion (i.e. with $L = 1$). The values chosen for system parameters are representative of *Thunnus atlanticus*, i.e. black-fin tuna, as described by Collette and Nauen [1983]:

$$\begin{aligned} m_b &= 5 \text{ kg}, & m_{p,1} &= 0.75 \text{ kg}, & m_{f,1} &= 1 \text{ kg} \\ l_b &= 80 \text{ cm}, & l_{p,1} &= 10 \text{ cm}, & l_{f,1} &= 10 \text{ cm} \\ I_b &= 2667 \text{ kg*cm}^2, & I_{p,1} &= 6.3 \text{ kg*cm}^2, & I_{f,1} &= 8.3 \text{ kg*cm}^2 \end{aligned}$$

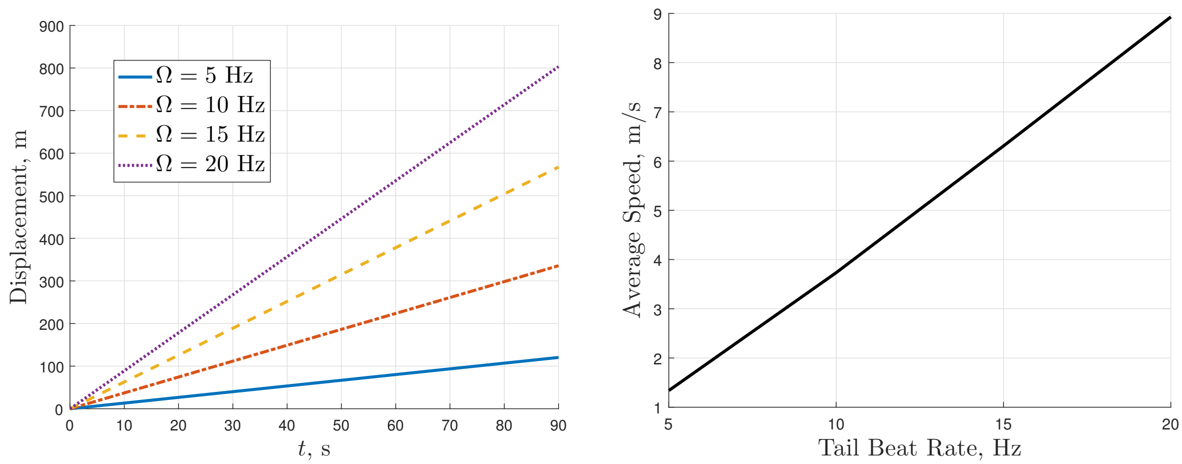

(a) Displacement (b) Speed

Figure 3.15: Variation of the displacement and speed of the fish model with respect to changes in Ω. Other gait parameters are $\overline{\phi}_{\mathrm{p},1} = 0$, $\phi_{\mathrm{p},1,0}/\Omega = 30°$, and $\psi_{\phi_{\mathrm{p},1}} = 90°$.

The lengths of the segments can be alternately described using the conventions described in Section 3.2.7

$$l_0 = 100 \text{ cm} \qquad \beta_{\mathrm{b}} = 0.8 \qquad \beta_{\mathrm{f},1} = 0.5$$

It is implicit from this parameterization $\beta_1 = 1 - \beta_{\mathrm{b}}$. The hydrodynamic parameters are chosen to yield realistic behavior and are

$$C_{\mathrm{L,b}} = 1, \quad C_{\mathrm{L,f,1}} = 6, \quad C_{\mathrm{D,b}} = 2, \quad C_{\mathrm{D,f,1}} = 2, \quad C_{\mathrm{D,linear,b}} = 2, \quad C_{\mathrm{D,linear,f,1}} = 2$$
$$b_{\mathrm{d,b}} = 0, \quad b_{\mathrm{d,p,1}} = 0, \quad b_{\mathrm{d,f,1}} = 0$$

There is assumed to be no ambient motion of the fluid and the density fluid is that of water, i.e. $\rho = 1$ g/cm^3.

Figures 3.15, 3.16, and 3.18 show the results of this simulation. Figures 3.15 and 3.16 show performance when the mean stroke angles are 0, which corresponds to swimming in a straight line, and Figure 3.18 shows the effect of varying the mean stroke angles, which corresponds to constant rate turns.

Figure 3.15 shows the effect of varying the tail beat rate with a specific stoke amplitude and phase. Figure 3.15(a) shows the displacement over time. The curves in Figure 3.15(a) are approximately linear with slopes representing the average speed of the system. These slopes are plotted in Figure 3.15(b), which shows that the swimming speed varies linearly with tail beat rate.

Figure 3.16 shows the effect of varying the phase $\psi_{\phi_{\mathrm{f},1}}$ with a specific stroke amplitude and tail beat rate on the swimming speed. As with Figure 3.15, Figure 3.16(a) shows the

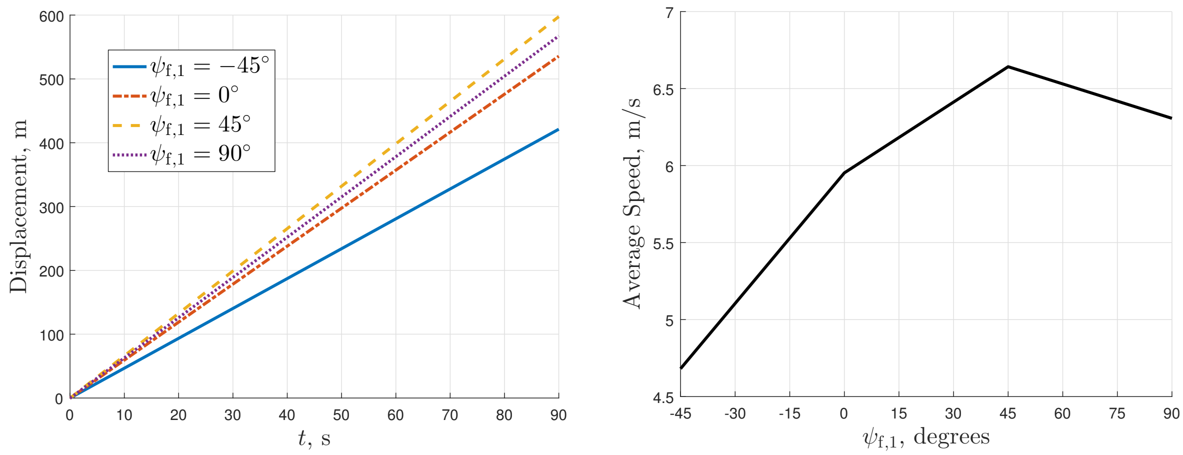

(a) Displacement (b) Speed

Figure 3.16: Variation of the displacement and speed of the fish model with respect to changes in $\psi_{\phi_{f,1}}$. Other gait parameters are $\overline{\phi}_{p,1} = 0$, $\phi_{p,1,0}/\Omega = 30°$, and $\Omega = 15$ Hz.

displacement with respect to time and Figure 3.16(b) shows the relationship between the phase and swimming speed. Figure 3.16(b) reveals that, of the phases simulated, $\psi_{\phi_{f,1}} = 45°$ achieves the fastest swimming speed. This agrees with the experimental results of Mason and Burdick [2000], which found an optimal phase angle of 45° for low-energy swimming and a slightly lower phase angle higher-energy swimming. As noted in [Mason and Burdick, 2000], this result is not seen in nature, most fish appear to have a phase angle of $\psi_{\phi_{f,1}} = 90°$. Mason and Burdick [2000] posit that this discrepancy could arise from their assumption of sinusoidal gaits, which is not be an exact model of the behavior of actual fish. As the same assumption is made in this paper, a phase angle of $\psi_{\phi_{f,1}} = 90°$ is used throughout. Further study is needed to fully illuminate the origin of this phenomenon.

Constant speed turns are achieved by having non-zero mean stroke angles as seen in Figure 3.17. By having non-zero mean stroke angles, the thrust generated by the tail is deflected, which produces a torque about the center of mass. This yields a constant rate turn at a constant speed, i.e. a circular turn. These turns are shown in Figure 3.18, with the left axes showing the Cartesian position of the "nose" of the fish model (i.e. the path the system) and the right axes show the body turning angle θ_b over time for several combinations of Ω and $\overline{\phi}_{p,1} = \overline{\phi}_{f,1}$. The right axes that every combination of Ω and $\overline{\phi}_{p,1}$ yields a constant rate turn, and the left axes show that every combination yields a circular (or linear if $\overline{\phi}_{p,1} = 0$) path, with some combinations of Ω and $\overline{\phi}_{p,1}$ completing multiple circles and others failing to complete a single circle. The reason that the paths do not appear to be exactly circular in Figure 3.18 is due to distortion of the axes. Figure 3.19 explicitly show the turning rate. Figure 3.19(a) shows the effect of changing the mean stroke angle. Positive (counter-clockwise) mean stroke angles result in negative (clockwise) turning rates, with greater mean stroke angles resulting in greater turning rates. Figure 3.19(b) shows the effect of varying

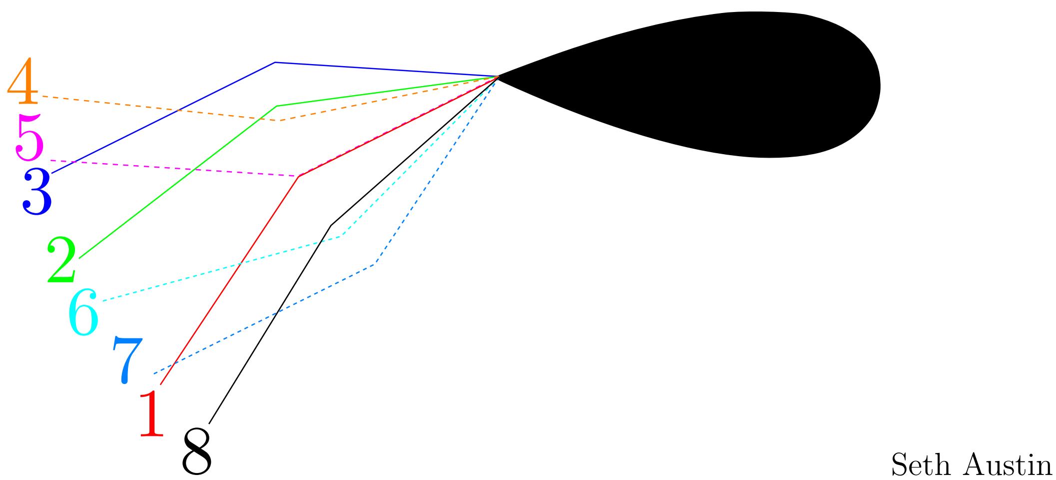

Figure 3.17: Diagram of a typical turning gait for $L = 1$ and $\psi_{\phi_{\mathrm{f},1}} = 90°$. The turning is achieved by setting $\overline{\phi}_{\mathrm{p},1} = \overline{\phi}_{\mathrm{f},1} \neq 0$. The numbers correspond to the order of the sequence of tail orientations. The “upstroke” is in solid lines, while the “down stroke” is in dashed lines.

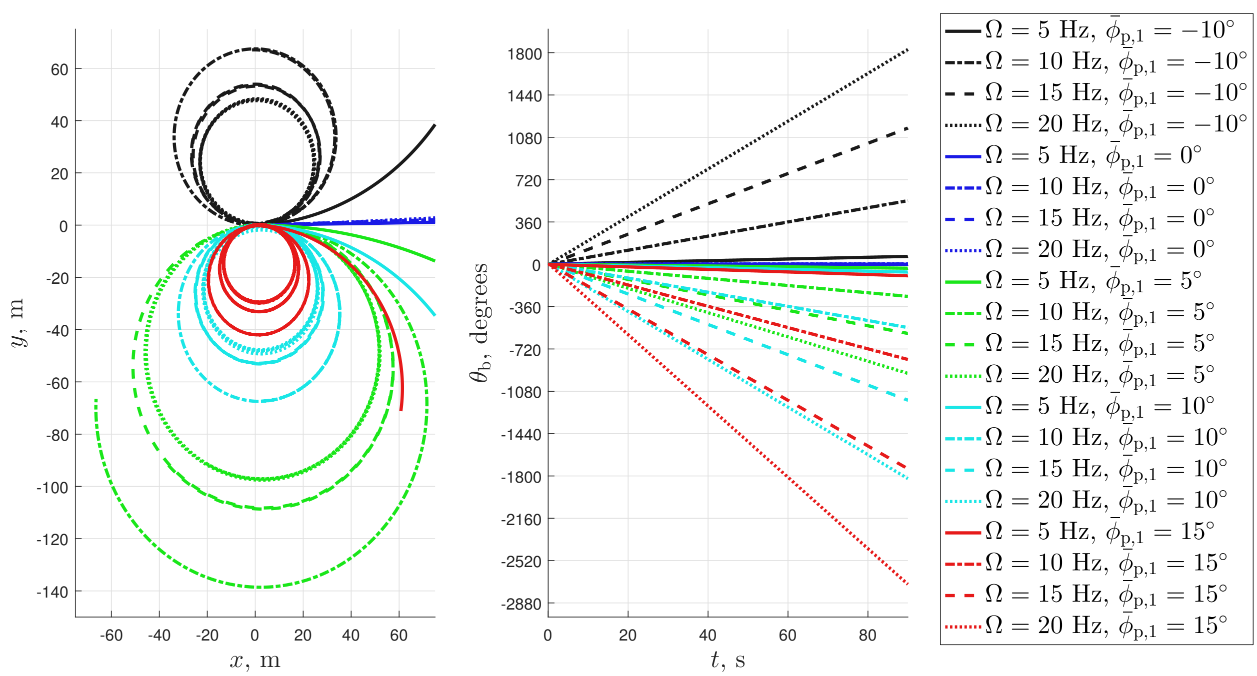

Figure 3.18: Path and turning angle of fish swimming with various values of Ω and $\overline{\phi}_{\mathrm{p},1}$. Other gait parameters are $\phi_{\mathrm{p},1,0}/\Omega = 30°$ and $\psi_{\phi_{\mathrm{p},1}} = 90°$.

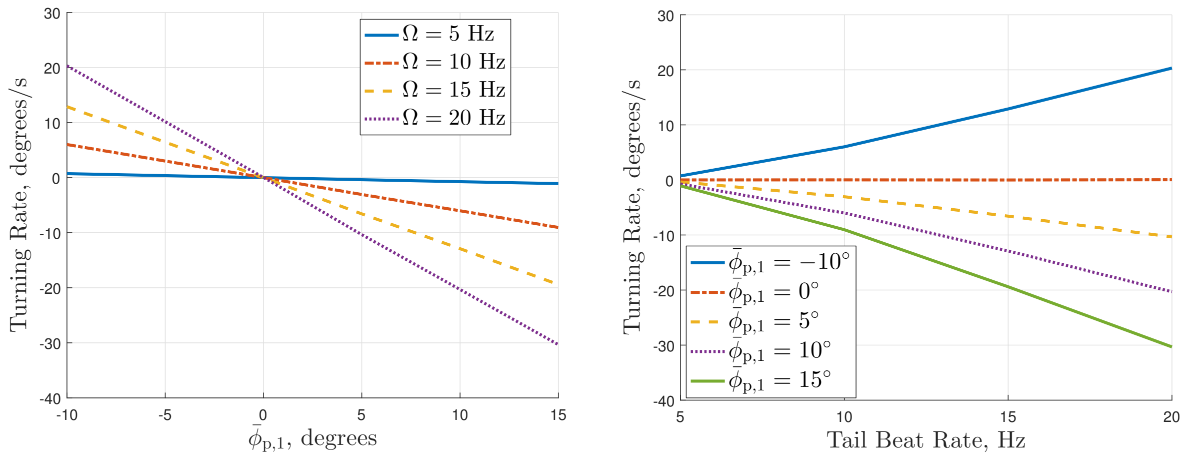

(a) Variation with $\bar{\phi}_{\mathrm{p},1}$ (b) Variation with Ω

Figure 3.19: Variation of the average turning rate with the tail beat rate and $\bar{\phi}_{\mathrm{p},1}$.

the tail beat rate on the turning rate; increasing the tail beat rate increases the magnitude of the turning rate, except for the case when $\bar{\phi}_{\mathrm{p},1} = 0$ (i.e. swimming in a straight line).

3.4 Experimental Work

Although not included in this research, there has been significant experimental work on pisciform locomotion. A summary of previous work done by others will be presented in this section. While there are many experimental studies, the ones presented here are the most relevant to the work presented in this dissertation. Additionally, only experimental studies are discussed here; purely analytical studies are not discussed here.

The first relevant study was complete by Kelly et al. [1998]. This study includes begins by developing a new model for carangiform locomotion that includes a body and a moving tail that is represented by a moving point vortex. This is an interesting model, but, for this discussion, the relevant portion is their experiments. Instead of attempting to build a submerged robot with a morphology representative of a carangiform fish, most of the experimental apparatus is housed above the water. The submerged components are a rectangular fin, a peduncle, and a rod. The fin is attached to the peduncle with is then attached to a rod. The rod is attached to a unsubmergered sled that rides on linear bearings. Actuation torques for the peduncle and fin are applied through this rod to the peduncle and fin from motors mount the sled. Kelly et al. [1998] present limited experimental results, but Kelly and Murray [2000] extend the work of Kelly et al. [1998]. In fact, Kelly and Murray [2000] appear to use an identical model and experimental apparatus as Kelly et al. [1998], but present significantly more detail results. The experimental results found by Kelly and

Murray [2000] agree well with the results generated by their model.

Mason and Burdick [2000] appear to use a similar apparatus as Kelly and Murray [2000], but add limited translational and rotational degrees of freedom. Furthermore, a representative body component is added ahead of the peduncle and tail. Mason and Burdick [2000] then proceed to perform several experiments. These experiments yield similar behavior to that seen in Section 3.3.

Morgansen et al. [2007] built a free-swimming carangiform robot. Although the model used by Morgansen et al. [2007] is different than the model used by Mason and Burdick [2000] (Morgansen et al. [2007] use the model presented by Morgansen et al. [2001, 2002]), the free-swimming carangiform robot could be thought of as a free swimming extension of the apparatus used by Mason and Burdick [2000]. Morgansen et al. [2007] develop a control methodology for this free-swimming carangiform robot that tracks a reference trajectory relatively well.[m] Although very different than the goals of this dissertation, the control methodology shares a similar motivation to the optimization technique presented in Section 4 in that it attempts to choose gaits that are parameterized by a few parameters.

Yu and Wang [2005]; Yu et al. [2004] present another free swimming pisciform robot. While the robot presented by Morgansen et al. [2007] is much more aligned with the model presented herein, the robot developed by Yu and Wang [2005]; Yu et al. [2004] is relevant because of the analysis conducted on this robot. The robot is first presented in Yu et al. [2004]. This robot is much more undulatory in nature than the robot developed by Morgansen et al. [2007] with several peduncles covered by a flexible skin. Yu and Wang [2005] then optimizes the length of the links. This is process is different from but similar to the optimization conducted in Section 4 and yields similar results.

3.5 Contributions

This section develops a new model for pisciform locomotion. This model is an adaptable model that can approximate the spectrum of pisciform locomotion from undulatory to oscillatory locomotion. If $L = 1$, this model is similar to the model presented by Morgansen et al. [2001, 2002], but is structured to allow significantly more complex gaits. A new hydrodynamic model was developed, but the primary contribution with respect to the hydrodynamics is the downwash model. The downwash model incorporates hydrodynamic coupling between components. Furthermore, the hydrodynamic model is designed to be modular, allowing different hydrodynamic models to be incorporated later. A new control technique is also developed. This technique is a feedback-inversion type technique that allows the inputs to be the shape coordinates, rather than joint forces.

[m](Morgansen et al. [2007] note that they should use some sort of system identification process for improving the controller.

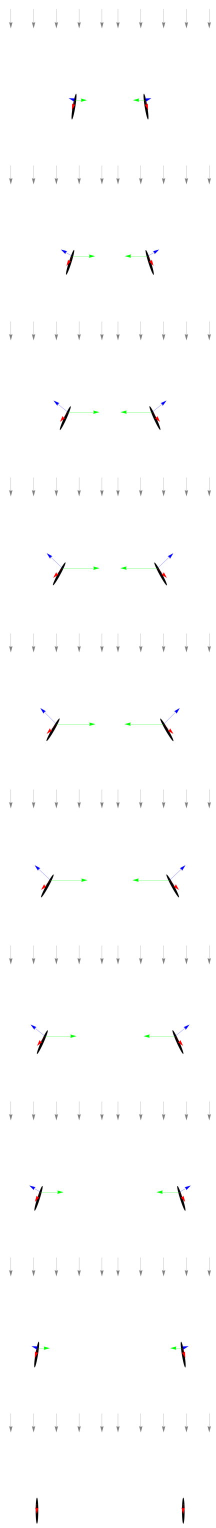

(a) Inertial Frame: Hydrofoil is allowed to move. The green arrow is the velocity of the quarter chord point.

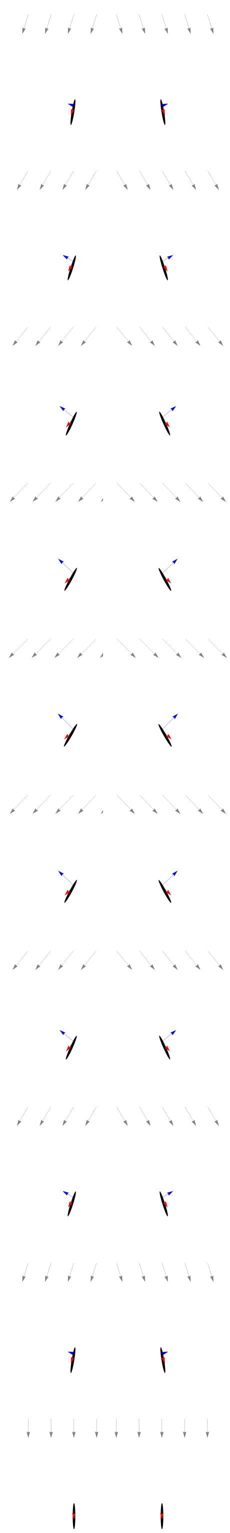

(b) Body Relative Frame: The quarter chord point is fixed and the relative flow velocity is shown.

Figure 3.20: Image montages of a hydrofoil moving perpendicular to the flow while simultaneously pitching. The system is defined by equation (3.22) and the parameters in Table 3.2. For these montages $\phi_\theta = -45°$. The blue arrow represents the lift force, the red arrow represents the drag force and the gray arrows represent the free stream flow velocity. The montages are equally sampled over one complete period of motion. The order is left to right along the top row and then left to right along the bottom row.

Chapter 4

Pisciform Optimization

The model of the multi-link fish model provides a rich structure for optimization. There are numerous parameters, such as lengths and masses of links, that can be varied to adjust performance. Furthermore, every fin and peduncle adds an additional degree of freedom that can be controlled. This chapter is divided into three sections; Section 4.1 presents details of the technique used, Section 4.2 presents a particular optimization problem that corresponds to thunniform locomotion, and Section 4.3 discusses the potential for future extensions and modifications to the optimization technique that may yield performance improvements.

4.1 Optimization Technique

The optimization technique used is a modification of the response surface technique developed specifically for this research. The response surface technique was developed by Box [1954]. The response surface technique was initially developed for chemical research, but Box [1954] correctly predicted that the response surface technique "may be of value in a wider field than that of chemical research." The response surface technique finds optima from multi-parameter sweeps by interpolating contours representing constant values of a cost functional to estimate the optimal point or contour.

For this research, the optimization will be conducted through a multi-parameter search of a grid populated using numerical simulation. A range of values for the design parameters are selected and the dynamics of the fish-like robot are numerically simulated at every combination of design parameters. Every combination of design variables is referred to as a "grid point."

This technique suffers from the curse of dimensionality [Bellman, 2003]; increasing the number of parameters included or the grid resolution greatly increases the computational time needed to perform the optimization. Fortunately, the most computationally intensive step in the optimization process, generating the grid of simulations, is "pleasingly parallel" or "embarrassingly parallel" [Moler, 1986]. That is, since every grid point is independent of all of the others, the process of parallelization is almost trivial. The grid simply needs to be divided into sections and sent to separate compute units. Thus, through parallelization, the challenges presented by the curse of dimensionality can be tackled using relatively modest computer hardware.[a]

One major distinction between the method used in this research and the traditional response surface technique is that the response surface technique typically seeks to find a single optimum, but the method used in this research seeks to find a family of optima. This family of optima corresponds to the optimal gaits for traveling at various speeds. This distinction arises from how the contours are utilized. In the response surface techniques, the contours are contours of constant cost, so they directly provide information about optima. In this research, the contours are contours of constant speed, representing a type of constraint. The optimization occurs along these constraints, finding the minimum cost necessary to travel at a particular speed.

4.1.1 Steady Locomotion and Gaits

In general, "gait" refers to the periodic movements performed by an animal for the purposes of locomotion. Depending on the situation, an animal may have several different gaits. For example, humans can alternately walk or run and horses can walk, trot, cantor, and gallop. Although these gaits accomplish the same basic task, forward locomotion, their energy requirements for moving at different speeds can vary greatly Alexander [1996].

Definition 4.1 ***Locomotion*** *is the use of periodic articulations to propel a multi-rigid-body mechanical system, either through contact with a surface or interaction with an ambient fluid.* ***Steady locomotion*** *is locomotion characterized by periodic gaits are described by constant average speed and angular velocities.*

For fish locomotion, "gait" specifically refers to the periodic motion of the fins and body that produces thrust and control. For BCF locomotion, this is the flexure of the body and caudal fins. This is the primary motivation for the development of the multi-link fish model, shown in Figure 3.2. The periodic motion the peduncles and fins is analogous to the gait of a BCF swimmer.

For the purposes of this research, only steady locomotion as defined in Definition 4.1 will be considered. Although pisciform locomotion is the topic of this optimization, the terms "locomotion" and "gait" apply more generally. Examples of steady locomotion include running at constant speed and turning at a constant rate while maintaining constant speed. The

[a]All computations in this dissertation were performed using consumer-grade desktop computers with quad-core CPUs. More complex optimization may require the use of computer clusters or GPU acceleration.

transition between two steady modes of locomotion is not considered. Also not considered is locomotion that requires acceleration, e.g. accelerating from zero speed to final speed. While constraining this research to steady locomotion is restrictive, the focus of this study is the assessment and optimization of steady locomotion, rather than attempting to control transient motion.

Although unsteady locomotion will not be considered, it is very interesting and rich topic worthy of future study. Apart from the simple accelerations between steady locomotive gaits, e.g. accelerating from a trot to a gallop, unsteady locomotion is often used to increase efficiency in non-intuitive ways. One example is the undulatory flight of many small birds, where a bird gains speed and altitude through flapping, then tucks its wings against its body to reduce drag and travels ballisticly until beginning to flap again. This “boost-glide” flight appears to be an adaptation for allowing higher speed flight without substantially modifying morphology [Alexander, 1996]. Another example of unsteady locomotion that enables higher speed locomotion is porpoising, which is seen in marine mammals. When swimming quickly, some animals accelerate to the surface, breaching it. The animals then fly through the air for a short time and then reenter the water. Although breaching the surface and flying through the air requires expending additional energy, the fact that there is significantly less drag when moving through air than through water more than recovers the energy spent while breaching [Fish and Rohr, 1999]. However, despite porpoising likely leading to energy savings, the claim that the primary purpose of porpoising is to save energy is not without controversy. Some observations of dolphins suggest that porpoising may be an adaptation to aid in respiration [Fish and Rohr, 1999]. Flying fish take the strategy of porpoising even further, having lifting surfaces that allow them to glide through the air. Flying squid actually use water jets to propel themselves while flying through the air.

4.1.2 Grid Generation

The optimization technique requires a grid representing the range of possible values of design parameters to be generated. The choice of the grid is simultaneously very important and relatively straightforward. There are three choices to make when generating the grid: 1) the parameters to include in the optimization, 2) the range of reasonable values for these parameters, and 3) the resolution of the sweep. This section will discuss the technical details of the choices with respect to the optimization technique. Analysis of these choices with respect to the application of the optimization of aquatic locomotion will be provided in Section 4.2.

4.1.2.1 Parameter Sweep Selection

The first step in the generation of the grid is the selection of the grid points. As these grid points are the result of a multi-parameter sweep, the choice of the range and resolutions of the sweeps define the grid points.

To demonstrate this, an example of a multi-parameter sweep is used. Suppose that there are three parameters selected for the sweep: $\mathfrak{a}$, $\mathfrak{b}$, and $\mathfrak{c}$. If the number of grid points (i.e. the resolution) for each of these parameters are $n_\mathfrak{a}$, $n_\mathfrak{b}$, and $n_\mathfrak{c}$, respectively. There is no requirement that $n_\mathfrak{a} = n_\mathfrak{b} = n_\mathfrak{c}$. Thus, the parameters are in the sets

$$\begin{aligned}
\mathfrak{a}_i &\in \mathfrak{A} = \{\mathfrak{a}_1, \mathfrak{a}_2, \ldots, \mathfrak{a}_{n_\mathfrak{a}-1}, \mathfrak{a}_{n_\mathfrak{a}}\} \\
\mathfrak{b}_j &\in \mathfrak{B} = \{\mathfrak{b}_1, \mathfrak{b}_2, \ldots, \mathfrak{b}_{n_\mathfrak{b}-1}, \mathfrak{b}_{n_\mathfrak{b}}\} \\
\mathfrak{c}_k &\in \mathfrak{C} = \{\mathfrak{c}_1, \mathfrak{c}_2, \ldots, \mathfrak{c}_{n_\mathfrak{c}-1}, \mathfrak{c}_{n_\mathfrak{c}}\}
\end{aligned} \tag{4.1}$$

where $\mathfrak{a}_1 < \mathfrak{a}_2 < \ldots < \mathfrak{a}_{n_\mathfrak{a}}$, $\mathfrak{b}_1 < \mathfrak{b}_2 < \ldots < \mathfrak{b}_{n_\mathfrak{b}}$, and $\mathfrak{c}_1 < \mathfrak{c}_2 < \ldots < \mathfrak{c}_{n_\mathfrak{a}}$. Thus, the minimum and maximum values of the parameters $\mathfrak{a}$ are $\mathfrak{a}_1$ and $\mathfrak{a}_{n_\mathfrak{a}}$, respectively, and likewise for $\mathfrak{b}$ and $\mathfrak{c}$.

Using these parameters, it is possible to define the set of grid points by taking the Cartesian product of these $\mathfrak{G} = \mathfrak{A} \times \mathfrak{B} \times \mathfrak{C}$ or as

$$\mathfrak{G} = \{\mathfrak{g}_{ijk} = (\mathfrak{a}_i, \mathfrak{b}_j, \mathfrak{c}_k) \,|\mathfrak{a}_i \in \mathfrak{A},\ \mathfrak{b}_j \in \mathfrak{B},\ \mathfrak{c}_k \in \mathfrak{C}\}$$

That is, every grid point is defined as $\mathfrak{g}_{ijk} = (\mathfrak{a}_i, \mathfrak{b}_j, \mathfrak{c}_k)$.

Now that the grid points are defined, it is straightforward to see where the curse of dimensionality arises [Bellman, 2003]. The number of grid points in this example is $n_\mathfrak{a} n_\mathfrak{b} n_\mathfrak{c}$. In a more general case, if there are m parameters with a resolution of n, the number of grid points is n^m. Thus, increasing the resolution or number of parameters increases the number of grid points, and thus the required compute time, exponentially. Because of the curse of dimensionality, it is imperative to carefully select both the grid resolution and number of parameters. The number of parameters is often defined by the optimization problem, so the choice that the user has the most freedom over is the resolution. Because the contour resolution technique uses interpolation, the resolution of the grid can be relatively low if the data is smooth and the contours are sufficiently spaced. More details are discussed in Section 4.1.3. Typically, the grid points are equally spaced, e.g. $\mathfrak{a}_{i+1} - \mathfrak{a}_i = \mathfrak{a}_{j+1} - \mathfrak{a}_j\ \forall\ i, j \in \{1, \ldots, n_\mathfrak{a} - 1\}$, but this is not a rigid requirement. This fact can be potentially used to reduce computation time or increase accuracy, which is discussed in Section 4.3.

4.1.2.2 Grid Population

Now that the grid points have been defined, the grid must be populated. While the response surface technique is usually applied to experimental data, the optimization technique presented here is applied to the results of numerical simulations. Specifically, it is applied to steady locomotion of fish-like robots, so the method of grid population is described in terms of steady locomotion. This implies that the parameters describe the gait. One constraint on the grid points is that the parameters must represent steady locomotion. It is difficult to verify the production of a steady gait without simulating the dynamics, so such verification occurs while populating the grid.

Before populating the grid, it is useful for purposes of parallelization to redefine the grid points as an unidimensional list rather than a multi-dimensional grid. This is a relatively straightforward task. Suppose the grid is a two dimensional grid with grid points $\mathfrak{g}_{ij}$, i.e. $\mathfrak{g}_{ij} = (\mathfrak{a}_i, \mathfrak{b}_j)$ with $\mathfrak{a} \in \mathfrak{A}$ and $\mathfrak{b} \in \mathfrak{B}$ as defined in Equation (4.1). Notice that the grid point has two indexes i and j that can take any value in $i = 1, \ldots, n_\mathfrak{a}$ and $j = 1, \ldots, n_\mathfrak{b}$, respectively. Thus, there are $n_\mathfrak{a} n_\mathfrak{b}$ grid points. These grid points can be written in a unidimensional list:

$$\begin{aligned}
\widetilde{\mathfrak{g}}_1 &= \mathfrak{g}_{11} = (\mathfrak{a}_1, \mathfrak{b}_1) \\
\widetilde{\mathfrak{g}}_2 &= \mathfrak{g}_{12} = (\mathfrak{a}_1, \mathfrak{b}_2) \\
&\vdots \\
\widetilde{\mathfrak{g}}_{n_\mathfrak{b}} &= \mathfrak{g}_{1n_\mathfrak{b}} = (\mathfrak{a}_1, \mathfrak{b}_{n_\mathfrak{b}}) \\
\widetilde{\mathfrak{g}}_{n_\mathfrak{b}+1} &= \mathfrak{g}_{21} = (\mathfrak{a}_2, \mathfrak{b}_1) \\
\widetilde{\mathfrak{g}}_{n_\mathfrak{b}+2} &= \mathfrak{g}_{22} = (\mathfrak{a}_2, \mathfrak{b}_2) \\
&\vdots \\
\widetilde{\mathfrak{g}}_{n_\mathfrak{a} * n_\mathfrak{b}} &= \mathfrak{g}_{n_\mathfrak{a} n_\mathfrak{b}} = (\mathfrak{a}_{n_\mathfrak{a}}, \mathfrak{b}_{n_\mathfrak{b}})
\end{aligned} \tag{4.2}$$

Now that the grid points have been re-described in terms of an unidimensional it is possible to populate the grid by performing the simulations at each grid point. As steady locomotion is desired, the value assigned to each grid point is the parameter that describes the steady locomotion. For this research, that parameter used is the average speed, which, for the multi-link fish model, is the average speed of the front of the body, i.e. the average of $\sqrt{\dot{x}^2 + \dot{y}^2}$. By simulating at every grid point and extracting the desired performance criteria, the grid is populated.

Notice that the simulation that occurs at each grid point is completely independent of all of the other simulations. Thus, the problem of populating the grid is "embarrassingly parallel" meaning that the task of distributing the conversation to multiple cores is trivial [Moler, 1986].[b] As the grid points are already described in a unidimensional list, the parallelization of the grid simply requires partitioning the list of grid points. This is handled automatically using MATLAB's `parfor` parallel `for`-loop, although it could be done using any job scheduling technique.

4.1.3 Contour Generation

At this point, the method for generating the grid is complete. Now the contours must be generated. This dissertation focuses on two parameter sweeps, which yield contours like

[b]The term "pleasingly parallel" is sometimes used in lieu of "embarrassingly parallel" to avoid negative connotations.

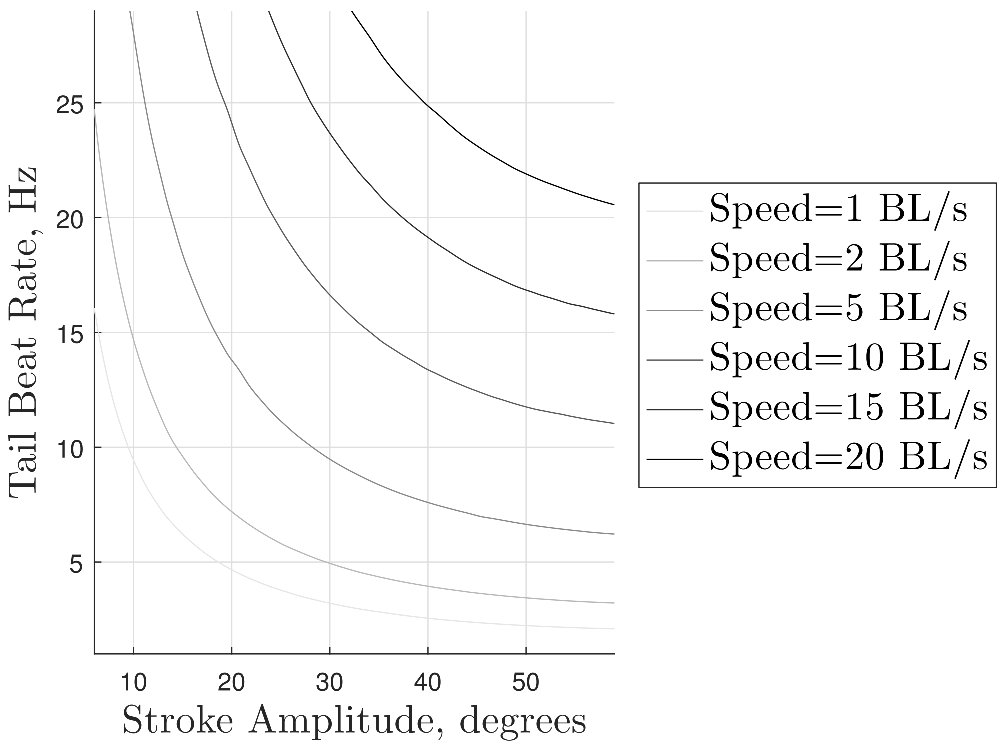

Figure 4.1: Example Speed Contours for Two-Parameter Sweep

those shown in Figure 4.1. The method used in this research is valid for multi-parameter sweeps, but the tool used, MATLAB's `scatteredInterpolant` algorithm, is only valid for two and three dimensional parameter sweeps. New tools will need to be implemented for higher dimensional parameter sweeps and will be discussed in Section 4.3. In two dimensional parameter sweeps the contours are represented by curves, in three dimensional parameter sweeps surfaces, and so on for higher dimensions. Since the grid is discrete and the contours need to be approximately continuous, interpolation between grid points is needed.

Recall that the response surface technique [Box, 1954] uses contours directly for optimization, which is not directly applicable to the optimization required here. The optimization method used herein searches for contours representing average values representative of steady locomotion, e.g. average speed or average turn rate. Because these contours do not represent constant cost and instead represent a value describing a steady gait, they should be interpreted as the set of parameters of that satisfy a constraint, i.e. the set of feasible solutions. These feasible sets are the sets of parameters that yield the desired performance, e.g. every gait capable of swimming at a particular speed.

4.1.4 Optimization

The contours described previously provide sets of parameters that yield desired performance. These sets include all possible parameters (within the grid) that can yield desired performance but provide no context as to which parameters are "best." This section provides a method for finding the optimal parameters within these sets and how these optimal solutions, taken together, from a family of optimal solutions.

At this point the cost functional is not defined, but one restriction is placed on it; the cost functional must be able to be computed independent of the simulations. A particular cost functional is presented in Section 4.2.1.2, but, as long as the cost functional is sufficiently smooth (at least once differentiable), the particular choice of cost functional is not important for the purposes of the description of the optimization method.

As the contours represent the entire set of solutions achieving desired performance and the cost functional can be computed for every point in the set, finding the optimal solution is very straightforward. By evaluating the cost functional at every point in this set and interpolating between discrete points (to increase resolution), the minimum value of the cost functional in the set can be found. That is, as the set is finite, it is reasonable to estimate the cost functional at every point using interpolation, and thus the optimum can be found by simply observing the minimum point.

One caveat is that this technique may not be applicable on the boundary of the grid. As the grid is inherently finite, finding an optimum on its boundary is likely representative of an optimum occurring outside of the grid. Such optima are ignored in this research, although if the boundary of the grid represents a physical limit the optima occurring on the boundary are admissible optima.

4.1.5 Comparison to Other Methods

The optimization method presented here is very useful for the purposes of this research, but it may not be the most efficient method for other applications. The method was chosen because it quickly yields a family of optimal solutions after populating the grid. Other methods may yield a particular solution faster, but are unlikely to yield a family of solutions with less computational expense.

One notable method that could improve efficiency of finding a particular optimum is a random search of the grid. Bergstra and Bengio [2012] showed that a random search is significantly faster than a grid search. This is a somewhat anticipated result; a complete grid search requires a complete population of the grid, while a random search will likely find an optimum prior to completing the grid. However, finding a family of optima would require multiple random searches, increasing the computational time beyond what is required to populate the grid once.

Another alternative would be to use a gradient based method. It is possible that a gradient based method could yield a particular result faster than the proposed method, it would likely be more computationally expensive to reproduce the family of optima generated by the grid search.

There are other methods for completing this optimization, such as genetic algorithms, but these alternatives will likely lead to similar issues: improved performance for finding a single optimum, but a significant penalty for finding a parameterized family of optima. A complete grid search requires the computationally intensive tasks to be performed once and separately from the actual optimization. Methods for future improvements to the optimization method are presented in Section 4.3.

4.2 Gait and Morphology Optimization

The primary goal of this optimization is to optimize a multi-link fish-like robot like the model developed in Section 3. The method is presented in terms of a single coherent example: the gait and morphology optimization of a thunniform robot. First, the specific optimization problem will be set up, with discussion of the parameterization and choice of cost functional. Then, the gait optimization of a single morphology is presented. This same optimization is then performed on multiple variations of the morphology.

4.2.1 Problem Setup

The optimization problem is to find the optimal gaits for traveling at different speeds. The system of interest is a fish-like robot with $L = 1$, i.e. a single caudal fin, which is representative of thunniform locomotion. Thus, the optimization problem can be stated as "determine the optimal gaits for traveling at a steady speed without turning."

4.2.1.1 Gait and Morphology Parameters

For this problem, a fish-like robot representative of thunniform locomotion is used. Most of the morphological parameters are the same as the system presented in Section 3.2.7. Therefore, $L = 1$ and

$$l_0 = 100 \text{ cm} \qquad \beta_\mathrm{b} = 0.8$$

where $\beta_1 = 1 - \beta_\mathrm{b} = 0.2$ and $\beta_{\mathrm{f},1}$ is left free at this point. Thus,

$$l_\mathrm{b} = l_0\beta_\mathrm{b} \qquad l_{\mathrm{p},1} = l_0\beta_1\left(1 - \beta_{\mathrm{f},1}\right) \qquad l_{\mathrm{f},1} = l_0\beta_1\beta_{\mathrm{f},1}$$

The remaining parameters are

$$
\begin{aligned}
&m_{\mathrm{b}} = 5\ \mathrm{kg}, && m_{\mathrm{p},1} = 0.75\ \mathrm{kg}, && m_{\mathrm{f},1} = 1\ \mathrm{kg}\\
&I_{\mathrm{b}} = \frac{1}{12} m_{\mathrm{b}} l_{\mathrm{b}}^2, && \frac{1}{12} m_{\mathrm{p},1} l_{\mathrm{p},1}^2, && I_{\mathrm{f},1} = \frac{1}{12} m_{\mathrm{f},1} l_{\mathrm{f},1}^2
\end{aligned}
$$

The hydrodynamic parameters are

$$
\begin{aligned}
&C_{\mathrm{L,b}} = 1, \quad C_{\mathrm{L,f},1} = 6, \quad C_{\mathrm{D,b}} = 2, \quad C_{\mathrm{D,f},1} = 2, \quad C_{\mathrm{D,linear,b}} = 2, \quad C_{\mathrm{D,linear,f},1} = 2\\
&b_{\mathrm{d,b}} = 0, \quad b_{\mathrm{d,p},1} = 0, \quad b_{\mathrm{d,f},1} = 0
\end{aligned}
$$

As previously mentioned, $\beta_{\mathrm{f},1}$, which is the ratio of the length of the tail fin to the combined length of the fin and peduncles as shown in Figure 3.14, is not specified at this point. Not specifying $\beta_{\mathrm{f},1}$ enables the study of the effects of varying the morphology on the optimal gaits.

The gaits are specified in the manner described in Section 3.2.7. For $L = 1$, these gaits are parameterized as

$$
\begin{aligned}
\phi_{\mathrm{p},1}(t) =& \overline{\phi}_{\mathrm{p},1} - \frac{\phi_{\mathrm{p},1,0}}{\Omega} \cos\left(\Omega t + \psi_{\phi_{\mathrm{p},1}}\right)\\
\phi_{\mathrm{f},1}(t) =& \overline{\phi}_{\mathrm{f},1} - \frac{\phi_{\mathrm{f},1,0}}{\Omega} \cos\left(\Omega t + \psi_{\phi_{\mathrm{f},1}}\right)
\end{aligned}
\tag{4.3}
$$

which are generated by the inputs

$$
\begin{aligned}
u_1(t) = \ddot{\phi}_{\mathrm{p},1}(t) =& \phi_{\mathrm{p},1,0} \Omega \cos\left(\Omega t + \psi_{\phi_{\mathrm{p},1}}\right)\\
u_2(t) = \ddot{\phi}_{\mathrm{f},1}(t) =& \phi_{\mathrm{f},1,0} \Omega \cos\left(\Omega t + \psi_{\phi_{\mathrm{f},1}}\right)
\end{aligned}
\tag{4.4}
$$

Following Tahmasian et al. [2016], we assign $\psi_{\phi_{\mathrm{p},1}} = 0$ without loss of generality. Furthermore, for this optimization problem, only non-turning motion is considered, which is prescribed by setting the mean stroke angles, $\overline{\phi}_{\mathrm{p},1}$ and $\overline{\phi}_{\mathrm{f},1}$, to zero. Lastly, following Mason and Burdick [2000], the phase $\psi_{\phi_{\mathrm{f},1}}$ is set to 90°. Thus, there are three parameters left unassigned, $\phi_{\mathrm{p},1,0}$, $\phi_{\mathrm{f},1,0}$, and Ω. Letting $\phi_{\mathrm{p},1,0} = \phi_{\mathrm{f},1,0}$ reduces these three parameters to two and yields realistic gaits, like the one shown in Figure 3.13.

Recall from Section 3.2.7 that the stroke amplitude is defined as $\phi_{\mathrm{p},1,0}/\Omega$, i.e. the ratio of $\phi_{\mathrm{p},1,0}$ to the tail beat rate Ω. Because the stroke amplitude has a more intuitive meaning than $\phi_{\mathrm{p},1,0}$[c], the two parameters used for the optimization are the tail beat rate, Ω, and the stroke amplitude, $\phi_{\mathrm{p},1,0}/\Omega$. For the generation of the grid, the tail beat rate is allowed to vary between 1 Hz and 30 Hz, while the stroke amplitude is allowed to vary from 5° to 60°.

[c]This parameterization arises from the parameterization used by Tahmasian et al. [2016] and presented in Section 2, which was selected to generate simple expressions describing the effects of symmetric product vector fields

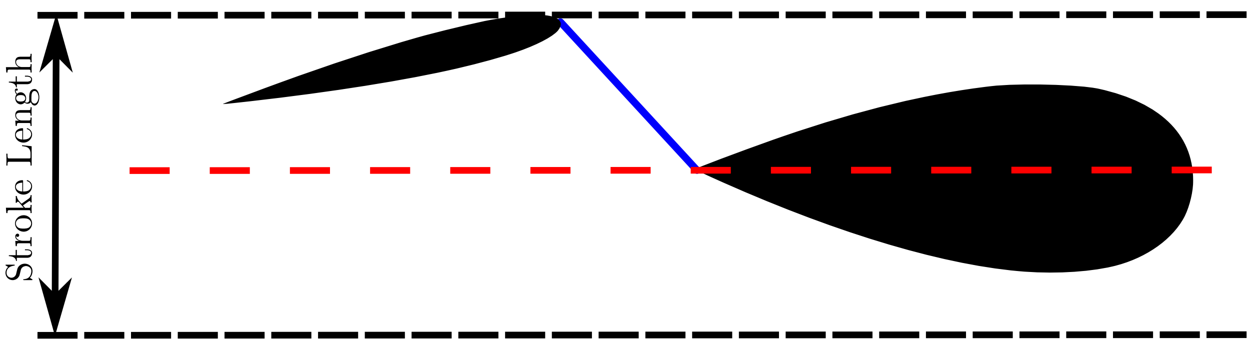

Figure 4.2: Illustration of the stroke when $\overline{\phi}_{\mathrm{p},1} = 0$ and $L = 1$. The black lines represent the bounds on the area occupied by the tail of a complete stroke.

4.2.1.2 Cost Functionals

The chosen cost functional contains two parts: input energy cost and stroke length cost. These are chosen for two reasons: 1) they penalize two distinct factors affecting the swimming speed, and 2) they have direct analogies to the propellers of ships.

When designing ship propellers, there is a direct trade-off between size and efficiency. In general, large propellers are more efficient in that they require less input power to generate the same amount of thrust. Unfortunately, it is not always practical to have a large propeller for physical considerations. A similar trade-off exists between the stroke length and input energy for fish-like robots.

As described in Section 2.2.2, the input energy should be interpreted as a signal energy and need not have units typically ascribed to energy. Tahmasian et al. [2016] note that sinusoids are the input energy minimizing input waveforms for vibrationally controlled systems. The input energy cost is computed using the T-averaged 2-norm (See Definition 2.3):

$$J_{\mathrm{E}} = \|\boldsymbol{u}(t)\|_{T,2} = \sqrt{\frac{1}{T}\int_0^T \boldsymbol{u}^T(t)\boldsymbol{u}(t)dt} \tag{4.5}$$

Using the parameterization for the gait presented in Section 4.2.1.1, the input energy cost is

$$J_{\mathrm{E}} = \frac{\Omega}{\sqrt{2}}\sqrt{\phi_{\mathrm{p},1,0}^2 + \phi_{\mathrm{f},1,0}^2} \tag{4.6}$$

or, since $\phi_{\mathrm{p},1,0} = \phi_{\mathrm{f},1,0}$,

$$J_{\mathrm{E}} = \phi_{\mathrm{p},1,0}\Omega \tag{4.7}$$

The stroke length is a measure of the total movement of the tail. Specifically, it is the length traced out by the peduncles and fins over one stroke. For the case where $\overline{\phi}_{\mathrm{p},i} = \overline{\phi}_{\mathrm{f},i} = 0$, the stroke length is twice the maximum distance between the centerline of the body and any point on the peduncles or fins. The case where $L = 1$ is illustrated in Figure 4.2. It should be noted that because the links are straight and slender, the maximum extents reached by the peduncle and fin are defined by their leading and trailing edges. As such, only these points must be considered while computing the stroke length.

For the gait described in Section 4.2.1.1, i.e. $L = 1$ and $\overline{\phi}_{\mathrm{p},1} = \overline{\phi}_{\mathrm{f},1} = 0$, only the trailing edges of the peduncle and fin need to be considered when computing the stroke length. Because the strokes are symmetric the two candidate stroke lengths are, from the peduncle,

$$\mathrm{SL_p} = 2\left(\max_{t\in[0,T]}\left[l_{\mathrm{p},1}\sin\left(\frac{\phi_{\mathrm{p},1,0}}{\Omega}\cos\left(\Omega t - \psi_{\phi_{\mathrm{p},1}}\right)\right)\right]\right)$$

and, for the fin,

$$\mathrm{SL_f} = 2\left(\max_{t\in[0,T]}\left[l_{\mathrm{p},1}\sin\left(\frac{\phi_{\mathrm{p},1,0}}{\Omega}\cos\left(\Omega t - \psi_{\phi_{\mathrm{p},1}}\right)\right) + l_{\mathrm{f},1}\sin\left(\frac{\phi_{\mathrm{f},1,0}}{\Omega}\cos\left(\Omega t - \psi_{\phi_{\mathrm{f},1}}\right)\right)\right]\right)$$

The stroke length cost function is

$$J_{\mathrm{SL}} = \max\left\{\mathrm{SL_p},\ \mathrm{SL_f}\right\} \tag{4.8}$$

which is the greater element of the set containing the peduncle and tail fin stroke lengths. For the gait shown in Figure 3.13, the stroke length is the distance between the tips of the tail fin in step "4" and "8."

The cost functional used for the optimization is

$$J = J_{\mathrm{E}} + \gamma k_1 J_{\mathrm{SL}} \tag{4.9}$$

where γ is a weighting factor that determines the relative importance of the input energy and stroke length cost functionals and k_1 is a scaling parameter. A scaling parameter is needed because typically $J_{\mathrm{E}} \gg J_{\mathrm{SL}}$.

4.2.2 Single Morphology

The first application of the optimization method is to determine the optimal gaits for various values of γ when $\beta_{\mathrm{f}} = 50\%$, i.e. the morphology discussed in Section 3.3. The grid was populated using the method described in Section 4.1.2.2. The contours were then generated using the method outlined in Section 4.1.3. The optimization outlined in Section 4.1.4 for the cost functional presented in Equation (4.9) with various values of γ.

The optimization process is illustrated in Figure 4.6. In this figure, the solid red curves are the speed contours and contours of constant cost are shown in dashed blue lines. The inclusion of the cost functional contours illustrates the optimization method; by including these contours it is possible to observe how the cost functional varies throughout the grid.

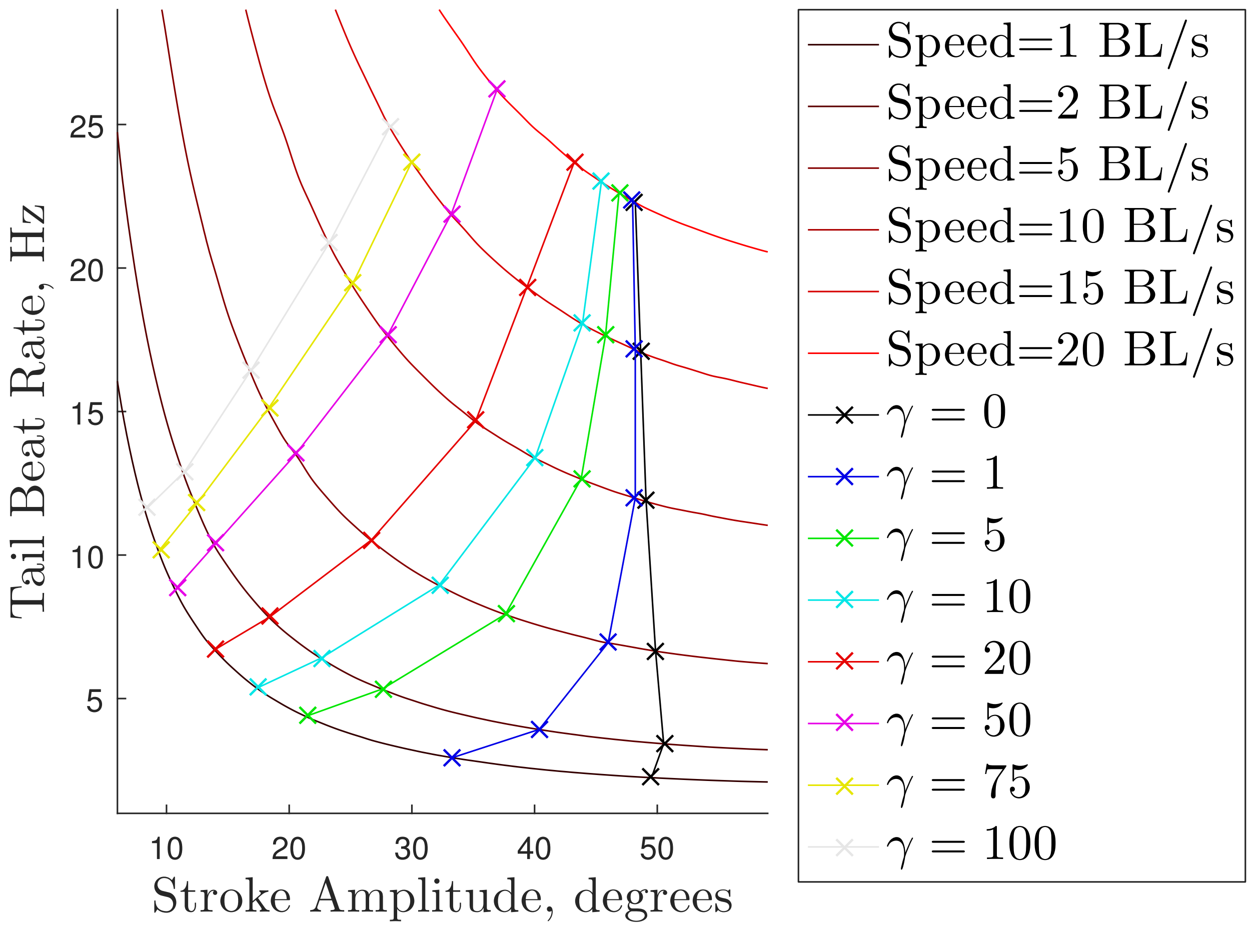

Figure 4.3: Optimal gaits for various values of γ.

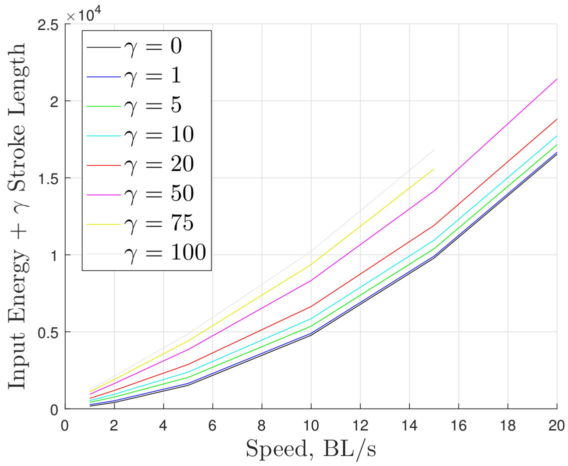

(a) Cost

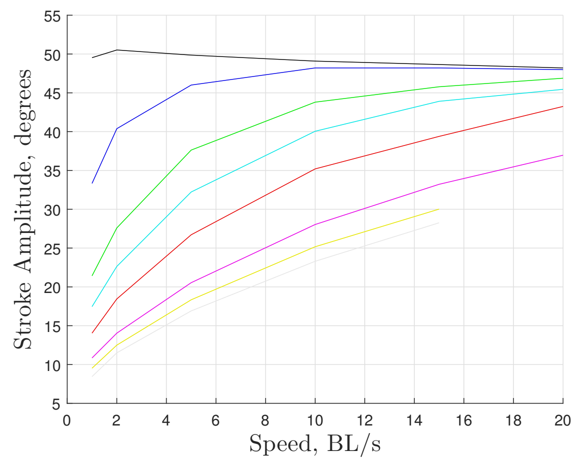

(b) Stroke Amplitude

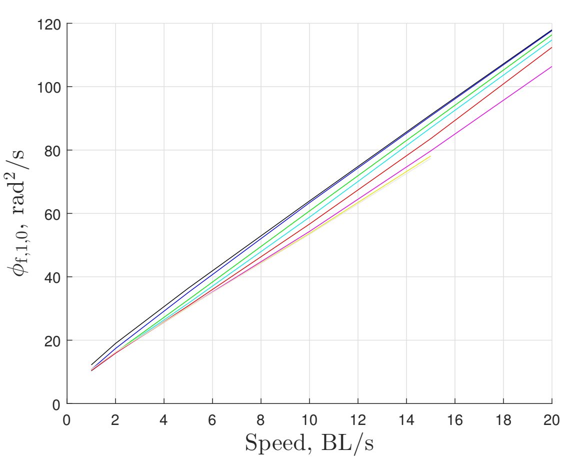

(c) $\phi_{\mathrm{f},1,0}$

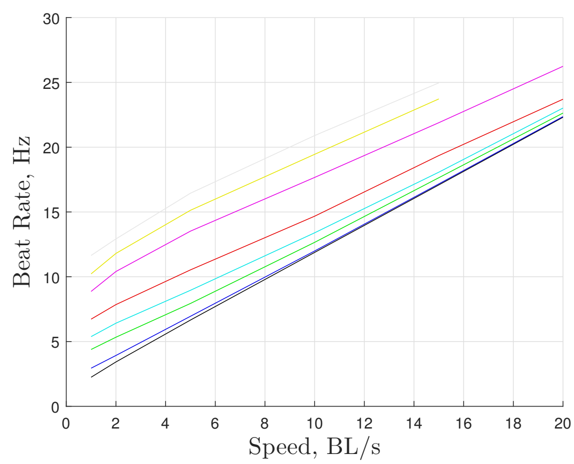

(d) Beat Rate

Figure 4.4: The optimal gaits for various values of γ. These figures represent the variation of the cost, stroke amplitude, $\phi_{\mathrm{f},1,0}$, and beat rate with speed. The legend in Figure 4.4(a) is consistent through all subfigures.

When $\gamma = 0$, the cost contours have a consistent convexity, but increasing γ leads to the generation of inflection points, with higher values of γ creating inflection points at lower stroke amplitudes. This inflection causes the optimal gait to shift to lower stroke amplitudes and higher tail beat rates. This is exactly the expected result because γ increases the penalty on the stroke length (which increases with the stroke amplitude) so it is intuitive that increasing γ would change the shape of the cost contours in such a way that the optimal gait would have a lower stroke amplitude (and thus a higher tail beat rate).

The optimal gaits for the various values of γ shown in Figure 4.6 and compiled into a single Figure 4.3. This figure shows the trend described previously; increasing γ and thus the penalty on stroke length causes the optimal gait to shift to lower stroke amplitudes and higher tail beat rates. This trend is intuitive, particularly in light of the analogy of a ship's propeller. In general, the most efficient propeller will accelerate a large mass of fluid a small amount, rather than accelerating a small mass of fluid a large amount. Thus, large propellers tend to be more efficient than small ones and, if no penalty is assigned to the size of the propeller, the optimal propeller will be a large propeller turning slowly. Likewise, if no penalty is assigned to the stroke length, the optimal gait will have a large stroke amplitude at a low tail beat rate.

The optimization procedure is illustrated in Figure 4.5. The contours shown are also shown in Figure 4.6 for the $\gamma = 10$ case. Figure 4.5(a) shows the contours. First one speed contour is selected as highlighted in Figure 4.5(b). Notice that this contour is approximately tangent to one of the cost contours. Because this cost contour divides a region of higher and lower cost, all of the speed contour lies in the region of higher cost except for the point of tangency. This can be seen in Figure 4.5(c). Because the point of tangency represents the lowest cost on the speed contour, this point represents the optimal gait for traveling at the selected speed for $\gamma = 10$, as seen in Figure 4.5(d).

The trends described here can be readily seen in Figures 4.4(b) and 4.4(d). Notably, when $\gamma = 0$ it can be seen in Figure 4.4(b) that the optimal stroke amplitude does not correspond to the boundary of the grid, rather it converges to some value from above, while non-zero values of γ yield a similar convergence to an optimal stroke amplitude, but from below. Sections 4.2.3 and 4.2.4 will examine this convergence further.

Figure 4.4(d) reveals that the optimal tail beat rate, Ω, follows an approximately linear trend with speed. Similar trends are seen for the swimming speeds of free swimming tuna [Yuen, 1966]. Similar trends were found by Yu and Wang [2005] using a similarly motivated but distinct optimization method. A similar trend is also seen for the thrust generated by an ornithopter as described in Section 5.2. Similar to the tail beat rate, $\phi_{\mathrm{p},1}$ follows a linear trend versus speed, which can be seen in Figure 4.4(c). Because both $\phi_{\mathrm{p},1}$ and the tail beat rate obey approximately linear trends and because the stroke amplitude is the ratio $\phi_{\mathrm{p},1}/\Omega$, the optimal gait can be described using two functions that are determined by γ. Increasing γ decreases the optimal $\phi_{\mathrm{p},1}$ and increases the optimal tail beat rates as can be seen in Figures 4.4(c) and 4.4(d). This is the intuitive result; increasing value of γ increases the penalty on

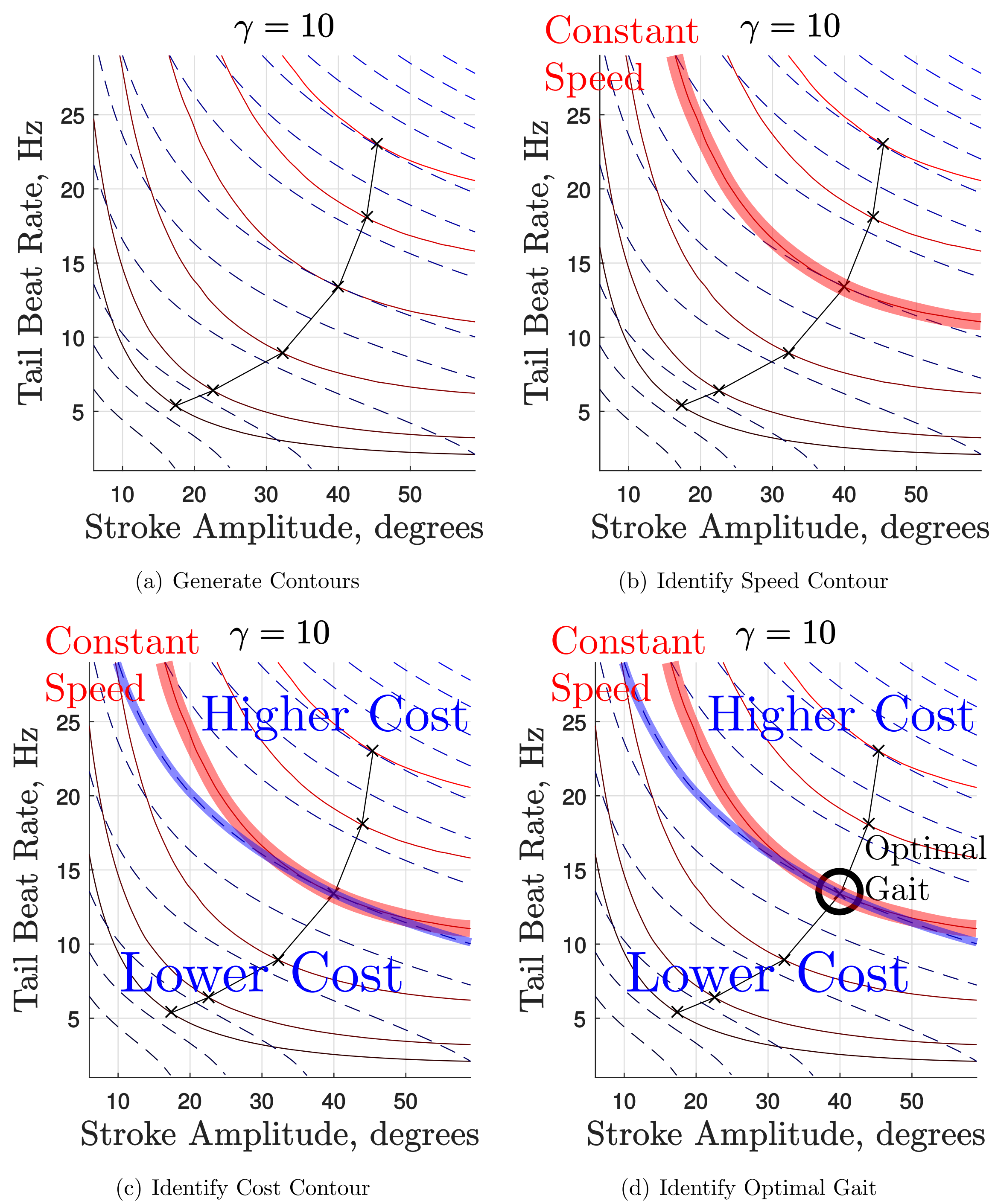

Figure 4.5: Illustration of the optimization procedure. The solid red lines are constant speed contours and the dashed blue lines are constant cost contours.

the stroke length, which scales directly with the stroke amplitude and therefore $\phi_{\mathrm{p},1}$. Thus, increasing γ effectively increases the penalty $\phi_{\mathrm{p},1}$. The tail beat rate must then be increased accordingly.

These linear trends can be used to describe the behavior of the stroke amplitude at both low and high speeds. As both $\phi_{\mathrm{p},1}$ and Ω obey linear trends they can be expressed for a specific γ as

$$\begin{aligned} \phi_{\mathrm{f},1,0}\left(v\right) &= m_{\phi_{\mathrm{f},1,0}} v + b_{\phi_{\mathrm{f},1,0}} \\ \Omega\left(v\right) &= m_{\Omega} v + b_{\Omega} \end{aligned} \tag{4.10}$$

where v is the desired swimming speed. Recall that the stroke amplitude can be computed as

$$\frac{\phi_{\mathrm{f},1,0}}{\Omega} = \frac{m_{\phi_{\mathrm{f},1,0}} v + b_{\phi_{\mathrm{f},1,0}}}{m_{\Omega} v + b_{\Omega}}$$

so the value of the stroke amplitude at low speeds will be approximately $b_{\phi_{\mathrm{f},1,0}}/b_{\Omega}$ while at high speed the stroke amplitude will be approximately $m_{\phi_{\mathrm{f},1,0}}/m_{\Omega}$. This behavior will be further discussed in Section 4.2.4.

The chosen structure of the cost functional allows the optimal gaits to be described as Pareto optimal fronts. There are two Pareto fronts shown in Figure 4.7. The traditional Pareto front, which illustrates the trade off between input energy and stroke length costs. This trade off is controlled by the choice of γ. This Pareto front is shown in Figure 4.7(a).

At first glance, one may assume that the speed contours (as seen in Figure 4.3) may represent these Pareto fronts, but that is not the case. Every point on the Pareto fronts represents an optimum with respect to some value of γ, there are points on the speed contours which are not optimal for any value of γ. The segments of the contours reached using the tested values of γ are shown in Figure 4.7(b).

The analysis and presentation of Figures 4.3 through 4.7 is the result of significant post processing. While this yields clearer results, providing results with minimal post processing can yield an intuitive presentation of the results. This can be seen in Figure 4.8 which shows the cost and speed of every data point in the optimization. The color of each data point represents the stroke amplitude. The bottom edges of the colored regions represent the optimal gaits and are represented by the curves in Figure 4.4(a). Thus, the qualitative behavior of Figure 4.4(b) can also be seen by examining the color of the bottom edge of the colored region. When $\gamma = 0$, the bottom edge has a relatively consistent color, which corresponds to a relatively constant value of the stroke amplitude. This is exactly behavior seen in Figure 4.4(b). In contrast, the bottom edge of the colored region for $\gamma = 20$ experiences a dramatic color shift, starting out as blue at low speed and shifting to orange at high speed. This is indicative of the behavior seen in Figure 4.4(b); increasing the value of γ produces smaller stroke amplitudes (represented by blue), particularly at low speeds.

It should be noted that the observations about the optimal gait using Figure 4.8 are significantly more qualitative in nature than those presented previously. However, the examination of Figure 4.8 provides a clearer picture of the effect of increasing γ. Looking at curves of constant color in Figure 4.8. These curves of constant color are curves of constant stroke amplitude. Increasing the value of γ causes the curves of stroke amplitude to shift upward. These shifts change the color of the bottom edge of the colored regions, which changes the optimal stroke amplitudes.

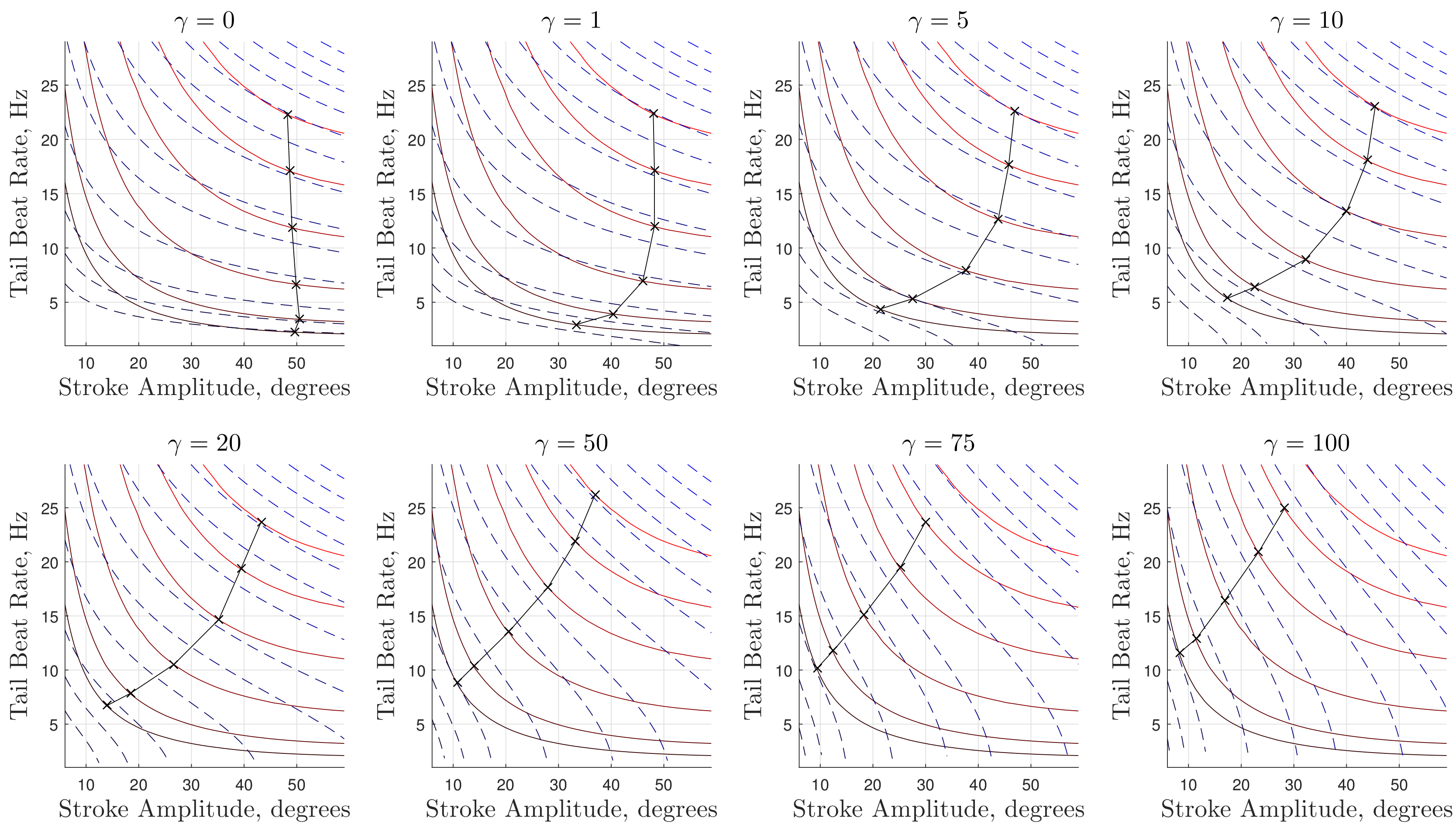

Figure 4.6: Speed and cost contours for various values of γ. The solid red contours represent constant speeds and the dashed blue contours represent constant values of the cost functions. The black line represents the optimal gait, which corresponds to the minimum value the cost along the speed contours.

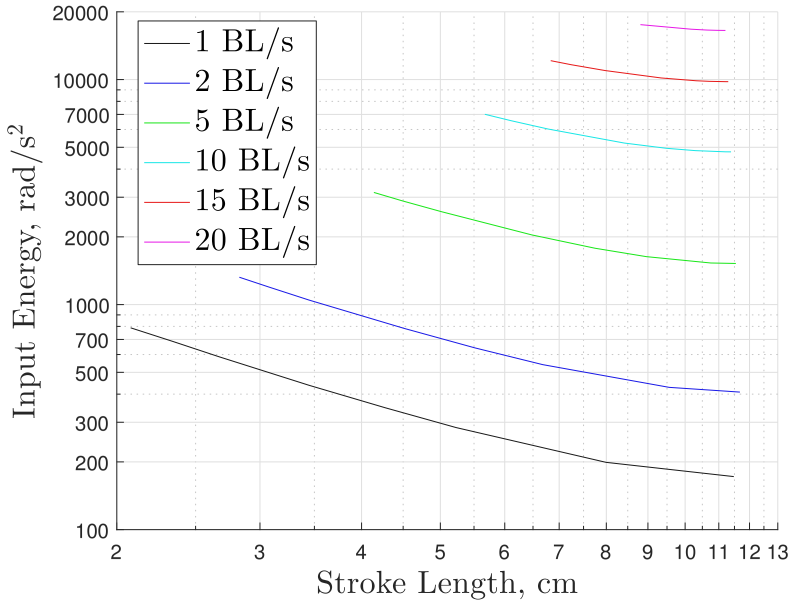

(a) Cost

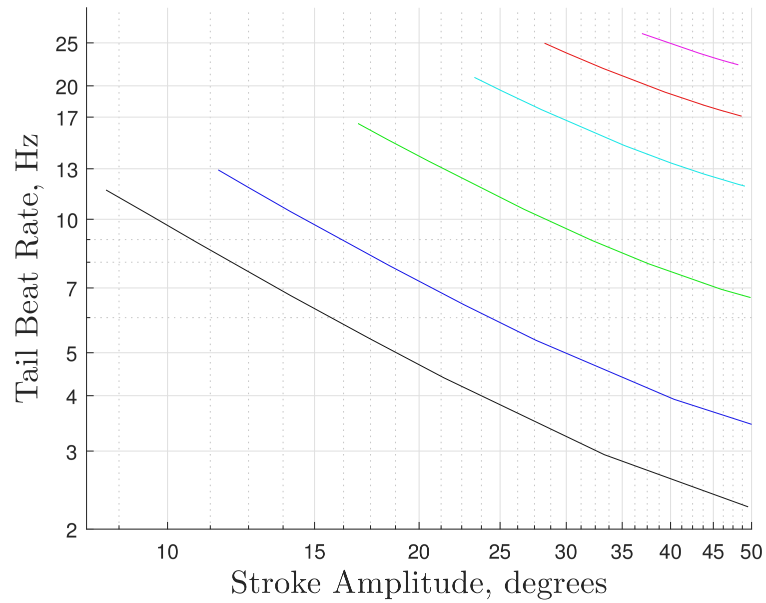

(b) Gait

Figure 4.7: Pareto Optimal Front for the gait at various swimming speeds. Figure 4.7(a) shows the traditional Pareto front, which is parameterized by the components of the cost functional, and Figure 4.7(b) shows the same Pareto front parameterized instead by the tail beat rate and stroke amplitudes.

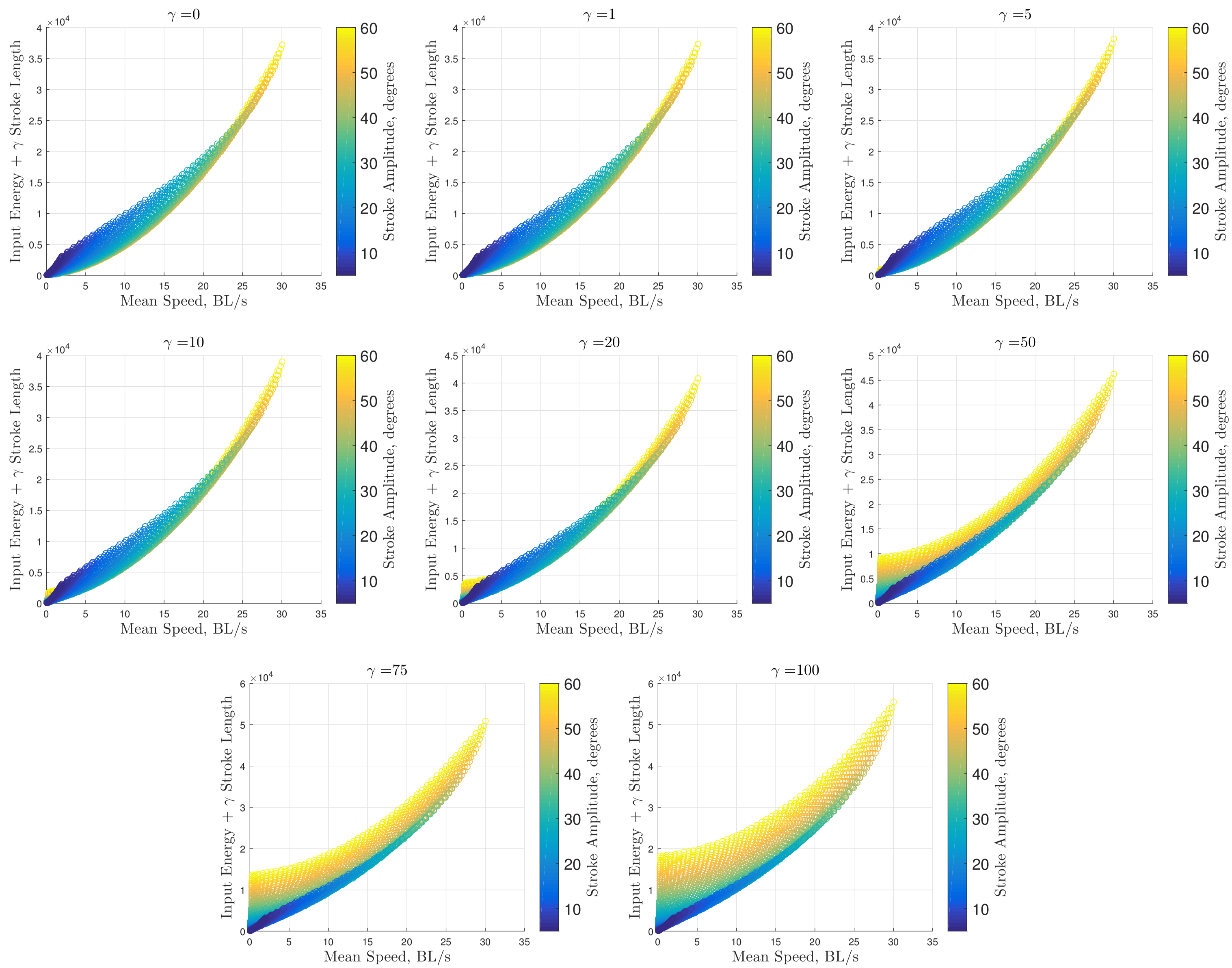

Figure 4.8: Cost vs speed for various values of γ. The bottom edge of the colored regions represent the optimal gaits and are shown in Figure 4.4(a).

4.2.3 Multiple Morphologies

Section 4.2.2 demonstrated the ability of the optimization technique to determine the optimal gaits for a particular morphology representative of thunniform locomotion:

$$l_0 = 100 \text{ cm} \qquad \beta_\mathrm{b} = 0.8 \qquad \beta_{\mathrm{f},1} = 0.5$$

By following the same procedure and varying $\beta_{\mathrm{f},1}$, the optimal gaits for the family of morphologies representative of thunniform locomotion can be determined. Observing how the optimal gait changes when the morphology changes allows one to tailor the optimal gait to behave as desired.

Figures 4.9, 4.10, and 4.11 show this process, with each figure being divided into subplots depending on the value of γ. One may notice that the optimal gaits shown in these figures start and stop at different speeds. There are two causes of this: 1) the speed is not achieved within the grid, or 2) the optimum does not occur within the grid.

Figure 4.9 shows the effects of changing the morphology on the optimal tail beat. Regardless of the value of γ, a similar trend emerges; increasing the length of the tail fin by increasing $\beta_{\mathrm{f},1}$ results in a higher optimal tail beat rate. This stems from the thrust generation mechanism. The thrust is generated by moving the fin perpendicular to the ambient flow and scales with the velocity perpendicular to this flow. Increasing the length of the tail fin decreases the length of the peduncle, which in turn decreases the speed of the fin perpendicular to the flow for a given tail beat rate. Thus, to maintain the same level of thrust, the tail beat rate must be increased. This increase generates the behavior of the trends seen in Figure 4.9.

Figure 4.10 shows the optimal stroke amplitudes for different morphologies. For every morphology, the behavior is qualitatively similar to the behavior seen in Section 4.2.2. There is one significant difference between the morphologies: increasing β_f tends to reduce the maximum optimal stroke amplitude. This can be clearly seen in Figure 4.10 from the case where $\gamma = 0$. For the other values of γ a new trend emerges. At low speeds, greater values of β_f result in higher stroke amplitudes, but the trend appears to reverse at higher speeds. These curves vary smoothly, so there is a point where the curves cross. The location of this point depends on the value of γ. As such it is not seen in Figure 4.10 for the cases where $\gamma \geq 50$.

Figure 4.11 shows the effect that the morphology has on the optimal values of $\phi_{\mathrm{f},1,0}$. As mentioned in Section 4.2.2, the optimal values of $\phi_{\mathrm{f},1,0}$ appear to follow a linear trend. Increasing the value of β_f increases the optimal value of $\phi_{\mathrm{f},1,0}$ for traveling a particular speed. As seen from Figure 4.4(c), increasing the value of γ decrease the value optimal values of $\phi_{\mathrm{f},1,0}$. This trend holds for all morphologies.

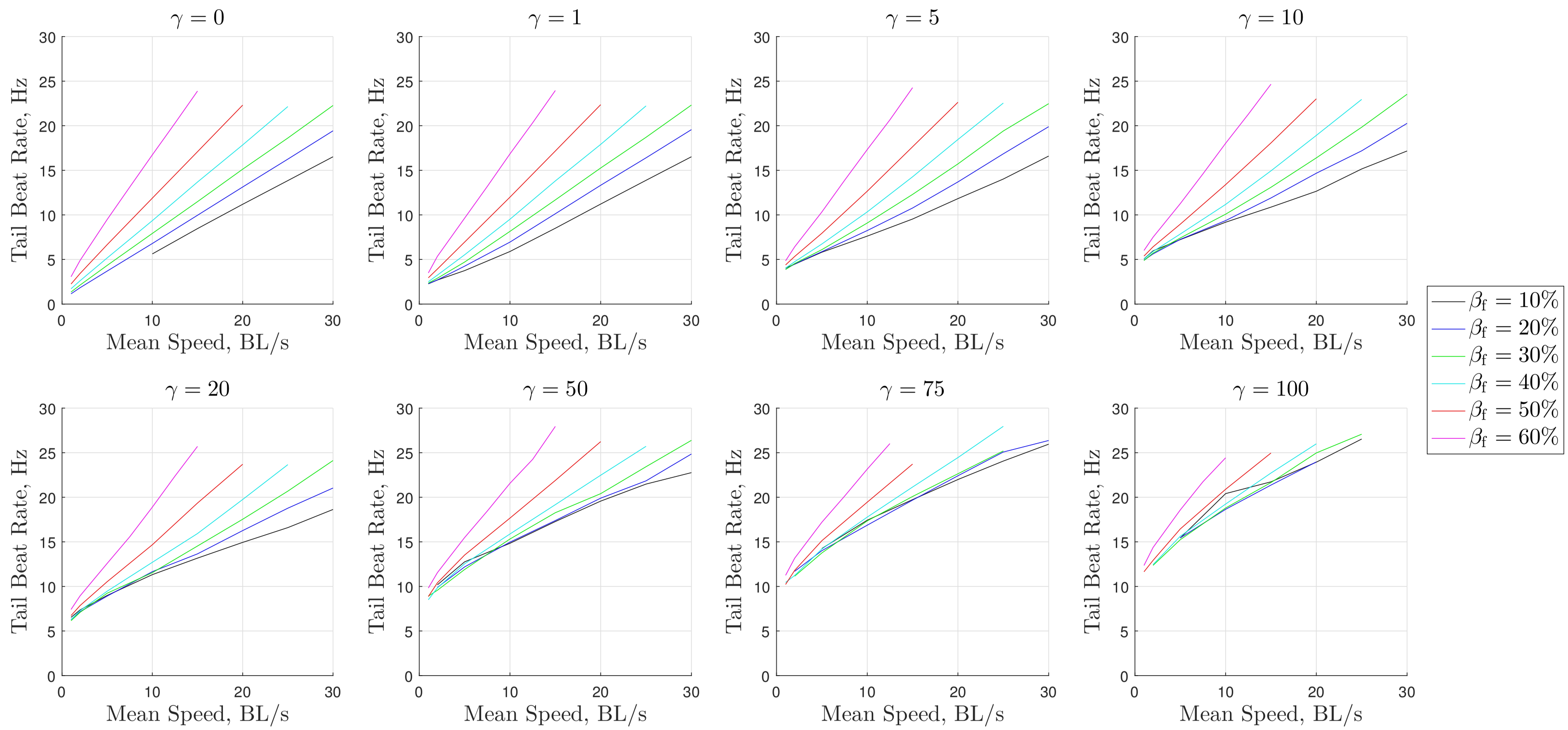

Figure 4.9: Optimal tail beat rates for traveling at various speeds for different morphologies and values of γ. Plots are separated by the value of γ.

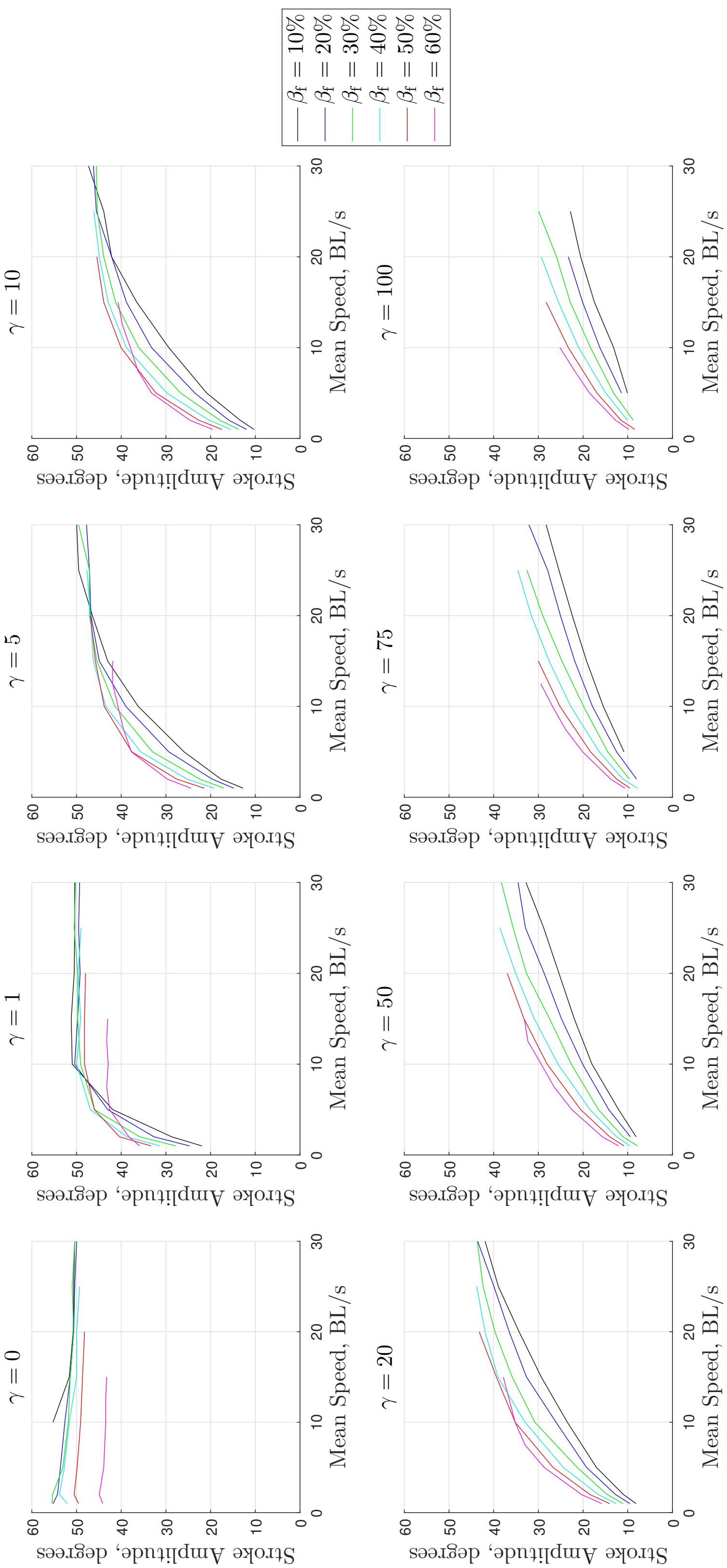

Figure 4.10: Optimal stroke amplitudes for traveling at various speeds for different morphologies and values of γ. Plots are separated by the value of γ.

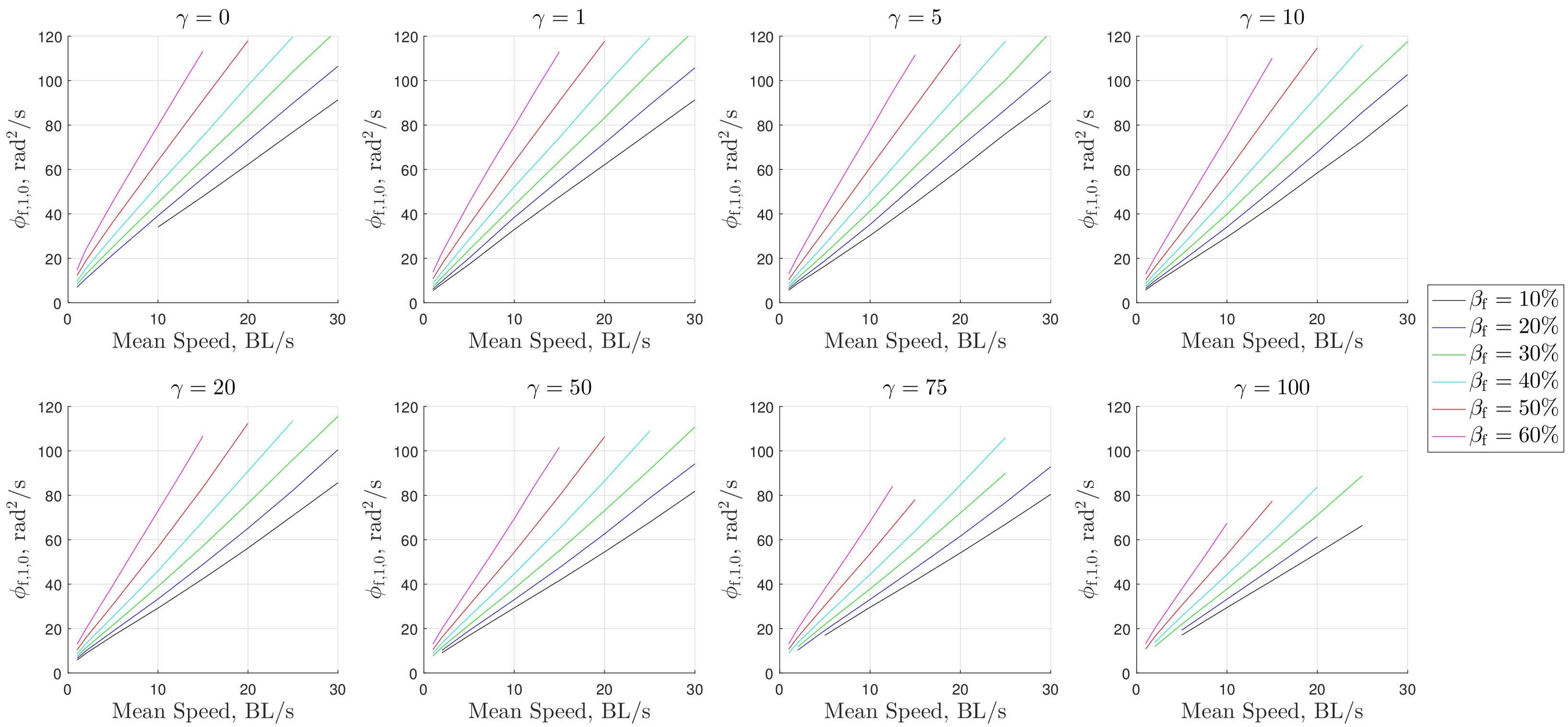

Figure 4.11: Optimal values of $\phi_{f,1,0}$ for traveling at various speeds for different morphologies and values of γ. Plots are separated by the value of γ.

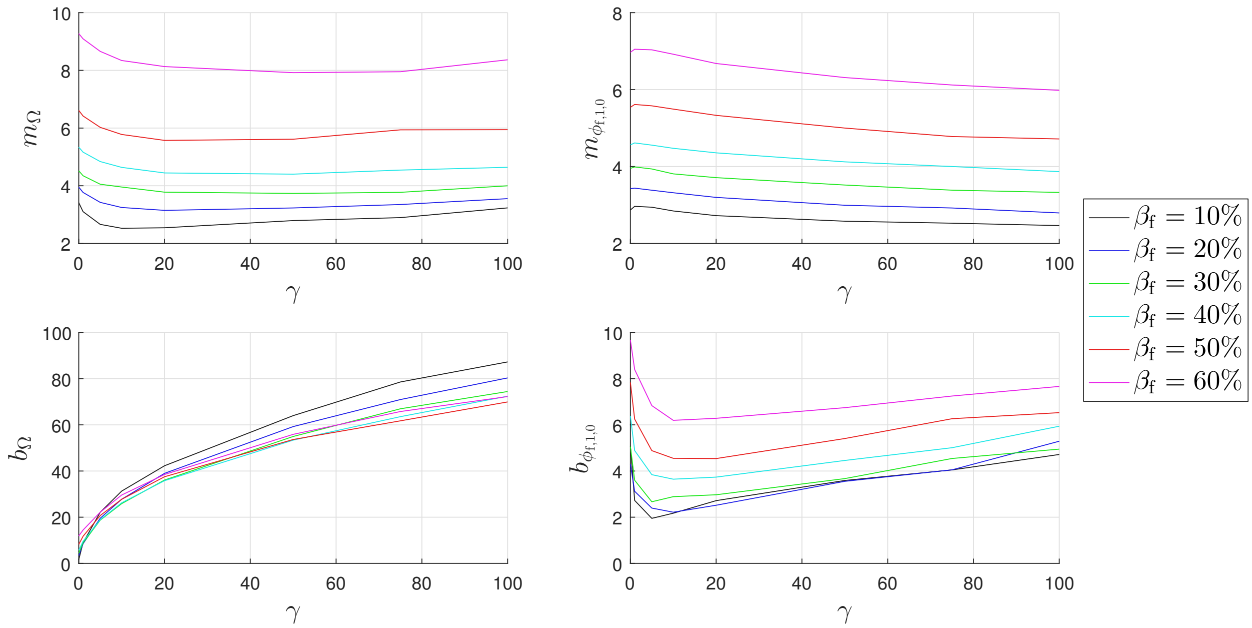

Figure 4.12: Coefficients for linear models presented in Equation (4.10) for various morphologies and values of γ.

4.2.4 Linear Model of Gaits

Recall the linear models for $\phi_{\mathrm{f},1,0}$ and Ω presented in Equation (4.10),

$$\begin{aligned}\phi_{\mathrm{f},1,0}\left(v\right) &= m_{\phi_{\mathrm{f},1,0}} v + b_{\phi_{\mathrm{f},1,0}}\\ \Omega\left(v\right) &= m_\Omega v + b_\Omega\end{aligned}$$

The optimal gaits show in Figures 4.9 and 4.11 are fitted to this model using a least-squares linear regression. The values of the coefficients from these linear fits are shown in Figure 4.12. The stroke amplitude is the ratio $\phi_{\mathrm{f},1,0}\left(v\right)/\Omega\left(v\right)$, so the ratio of the coefficients describe at high and low speeds. At high speeds, the optimal stoke amplitude is the ratio $m_{\phi_{\mathrm{f},1,0}}/m_\Omega$, which is displayed in the left plot in Figure 4.13. This plot shows that there is a peak in this stroke amplitude between $\gamma = 10$ and $\gamma = 20$. This is believed to be caused by the transition of a cost functional dominated by the input energy (for small γ) to one dominated by the stroke length (for large γ). Such a trend is not seen in the ratio $b_{\phi_{\mathrm{f},1,0}}/b_\Omega$ which is shown in the right plot in Figure 4.13. This ratio represents the stroke amplitude at low speeds. Increasing γ has the expected effect on this ratio; it reduces the stroke length.

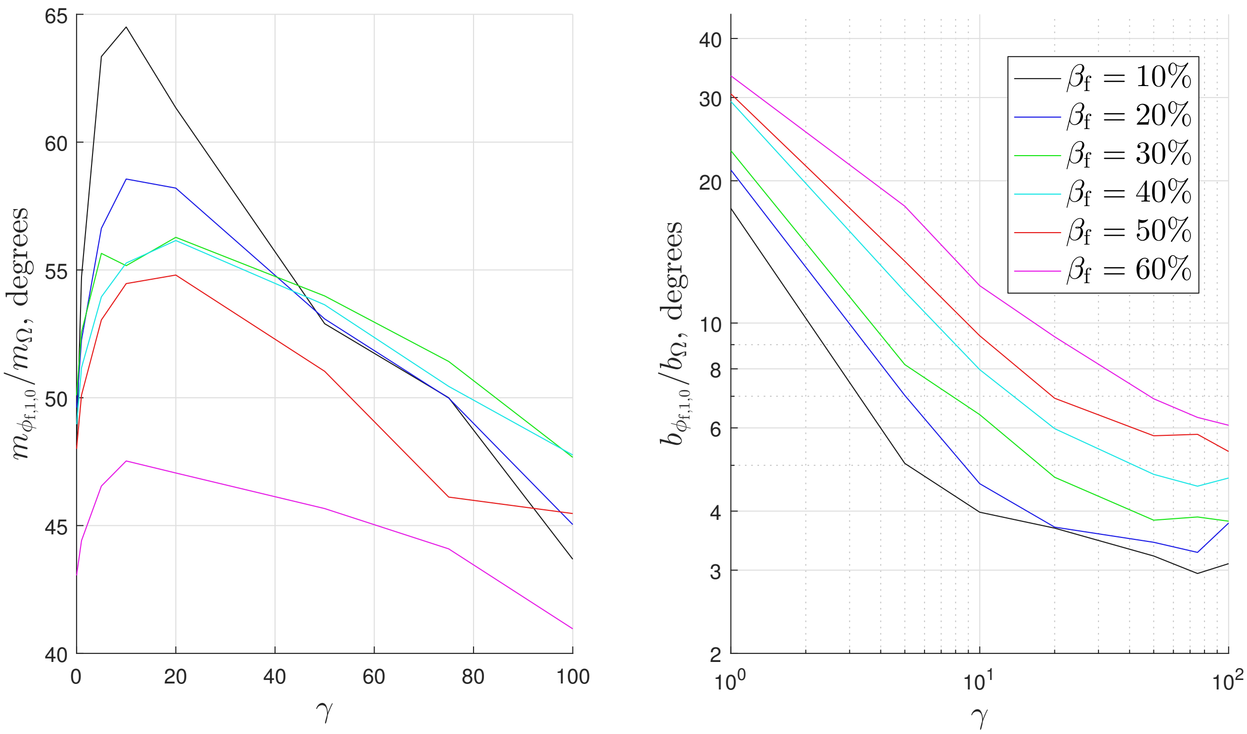

Figure 4.13: Ratio of the coefficients for linear models presented in Equation (4.10) for various morphologies and values of γ.

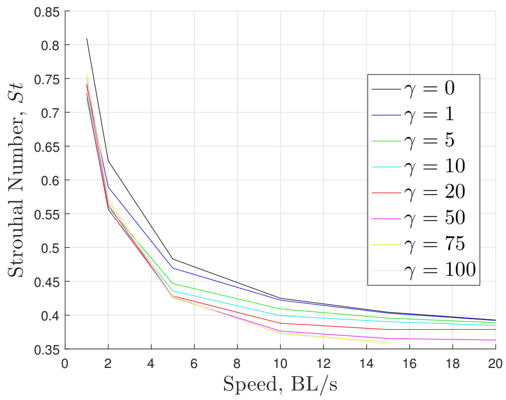

(a) Strouhal Number for Optimal Gaits for $\beta_\mathrm{f} = 0.5$

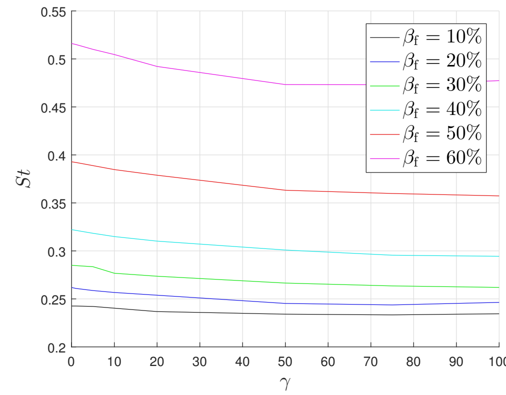

(b) Strouhal Number at Highest Speed for Various Morphologies

Figure 4.14: Strouhal Number for a fixed morphology and several morphologies. Figure 4.14(a) shows the variation of the Strouhal number with speed for a fixed morphology and Figure 4.14(b) shows the Strouhal number at the highest speed achieved for each morphology and γ.

4.2.5 Strouhal Number

The Strouhal number, St is a nondimensional parameter that relates to oscillatory phenomena in flows. It describes the vortex propagation in flows with pitching and heaving airfoils. It also appears to be useful for describing flapping flight and swimming. For flying and swimming animals, the Strouhal number is typically computed as

$$St = \frac{fA}{U}$$

where f and A are the stroke frequency and amplitude, respectively, and U is the free stream speed of the ambient flow, i.e. the flight speed or swimming speed relative to the ambient flow [Taylor et al., 2003]. For this model, the stroke frequency is the tail beat rate, the stroke amplitude is half the stroke length, and U is the swimming speed. Taylor et al. [2003] noted that, for flying and swimming animals, the range $0.2 < St < 0.4$ corresponds to maximum propulsive efficiency and most flying and swimming animals locomote in this range of Strouhal numbers.

Figure 4.14(a) shows the Strouhal numbers for the optimal gaits for the morphology described in Section 4.2.2 ($\beta_{\mathrm{f},1} = 0.5$). Specifically, Figure 4.14(a) shows the variation of the Strouhal number with swimming speed. It is immediately apparent that the Strouhal number is not constant for any choice of γ over the range of speed. This is somewhat expected due to the fact that $St \propto 1/U$, so low speeds tend to yield greater Strouhal numbers. At higher speeds, the Strouhal numbers of these gaits appear to approach a constant values slightly less than $St = 0.4$.

Since the Strouhal number for the optimal gaits appear to approach constant values, the values at the highest speed achieved are taken to be the Strouhal number of the gait. These Strouhal numbers were found for all of the optimal gaits found in Section 4.2.3. These Strouhal numbers are shown in Figure 4.14(b). Increasing β_{f} increases the Strouhal number, with most morphologies falling in the $0.2 < St < 0.4$ range seen in nature. The value of St does not vary much with γ, indicating that the morphology is the primary driver of the value of the Strouhal number, not the choice of cost function.

4.3 Future Extension of Optimization

Earlier discussion mentioned one unavoidable fact about the chosen optimization method: it is very computationally intensive. For a two or three parameter sweep, the computational expense is reasonable and the optimization can be performed on a relatively modest desktop computer.[d] Increasing the number of parameters or the resolution may make the optimization too computationally intensive to be practical to perform on modest hardware. Two solutions to this problem are proposed: 1) using more powerful computer clusters to distribute work over a greater number of compute units and 2) leveraging the linear model described in Section 4.2.4 to drastically reduce the simulations necessary.

The first alternative is more straightforward. As previously mentioned, the problem of generating the grid is embarrassingly parallel, so distributing the work over many cores is relatively simple. So long as a more powerful cluster of computers is available, it is always possible to accelerate computation. However, more powerful computers are not always available. Therefore, other alternatives should be considered.

One alternative is to leverage the linear gait model described in Section 4.2.4. As both $\phi_{\mathrm{p},1,0}$ and Ω appear to follow linear trends, only two points are need to define their variation with speed: a "low" and a "high" speed. So instead of populating the entire grid, only portions need to be populated. An approach to this is shown in Figure 4.15. Figure 4.15(a) shows the grid and the contour of interest, which is representative of the low speed. Figure 4.15(b) shows the grid search procedure. First the grid points highlighted in blue are populated. Since none of the points are above the contour, the grid points highlighted in green are populated. The contour is now bounded except for one point, so the grid point highlighted in red is populated. The contour can now be interpolated using the same procedure as described in Section 4.1.3. A similar approach can be used for the high speed contour which starts in the upper right hand corner of the grid and searches outward. This is illustrated in Figure 4.16, with the search proceeding from the blue, to the green, to the red, and finally to the yellow highlighted grid points. Unfortunately, this approach relies on the linear gait model, which may not be applicable for $L > 1$. Therefore further investigation is needed to

[d] The computer used was a desktop computer with a quad-core Intel i5-2500K CPU over-clocked to 4.2 GHz. The memory requirements are quite modest (less than 500 MB per core).

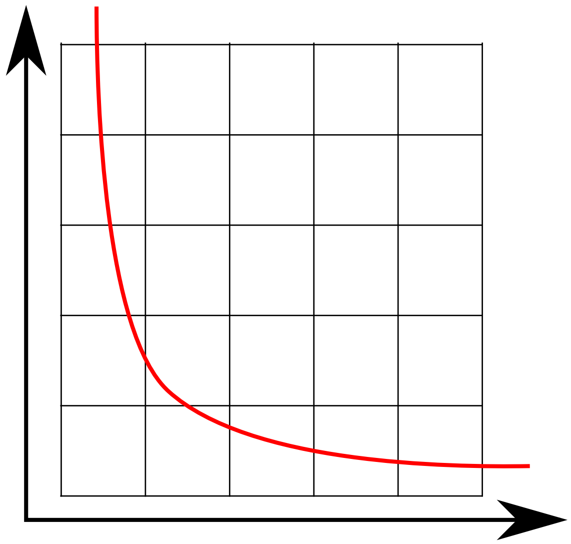

(a) Grid and Contour

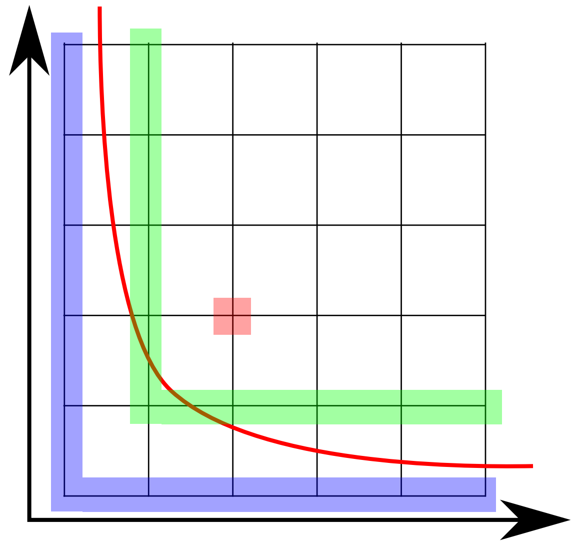

(b) Adaptive Grid Search

Figure 4.15: Illustration of proposed adaptive grid search technique.

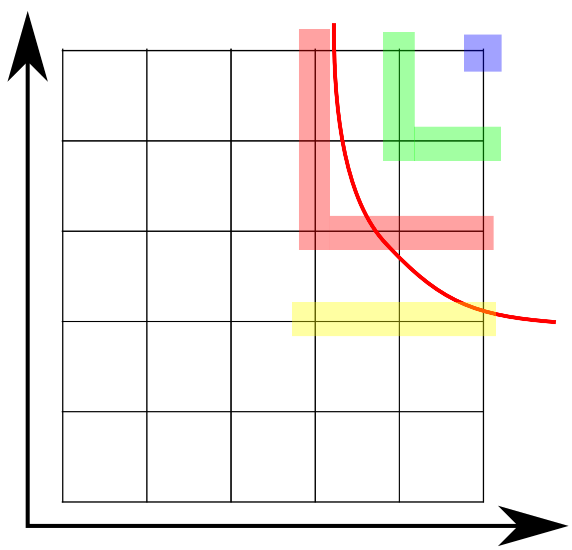

Figure 4.16: Adaptive grid search for the “high speed” contour.

determine if the linear gait model is valid $L > 1$ or if some extension is needed.

Another concern not addressed in this research is the application of the optimization technique to higher dimensional grids. All of the grids presented here are two dimensional and as such the contours are curves. These curves are found by interpolation using MATLAB's `scatteredInterpolant` function. This function could also be used for three dimensional grids, where it can be used to generate contour surfaces. Unfortunately, it cannot be used to generate contour hyper-surfaces for higher dimensional grids. The solution to this was actually already shown although not explicitly described. Recall the gait and morphology optimization described in Section 4.2.3. The optimization was described in terms of a two dimensional grid, but there were in fact three design variables, the tail beat rate, the stroke amplitude, and $\beta_{\mathrm{f},1}$. Thus, instead of attempting to develop a method for finding contour hyper-surfaces, the optimization can be performed on lower dimension grids by fixing one or more of the parameters and interpolating between these lower dimensional grids.

4.4 Contributions

The primary contributions of this section is the use of a modified response surface optimization technique to determine the optimal gaits and morphologies for pisciform locomotion. The optimization technique is a grid based method that searches for the optimal gaits for traveling at particular speeds. This is accomplished by simulating the motion of a pisciform system with many gaits and finding the contours of constant speed. A cost function is then computed at all points these contours yielding the optimal gait for traveling at particular speeds. Thus, this technique yields a family of optima corresponding to the optimal gait at various speeds. This technique was then applied to find the optimal gaits for several variations of a thunniform-like morphology. The results of this application led to the discovery of a new model for determining optimal gaits which specifies the gaits using two linear trends.

Chapter 5

Bio-Inspired Flight

In addition to the study of bio-inspired aquatic locomotion, experiments were performed on an ornithopter Ornithopters are small aerial vehicles that propel themselves using flapping wings in a manner similar to birds. Ornithopters can adapt their performance much more than traditional aircraft. Much of the work presented here was first presented in [Zakaria et al., 2016].[a]

Ward et al. [2015] presented the latest comprehensive bibliometric review of the research on biomimetic air vehicles (BAVs) known to the authors. They divided the research field into five primary areas of study. The most studied area is aerodynamics, with 46% of papers, focusing on this subtopic. In contrast, materials and structures of BAVs are the focus of only 14% of papers, and system design is the focus of only 9% of papers. Despite aerodynamics being the most studied area, relatively few (9%) of the aerodynamic studies have focused on the propulsive performance of BAVs. This study primarily seeks to evaluate the propulsive performance of an ornithopter.

The objective of this experimental investigation is to assess the behavior the cycle-averaged aerodynamic forcing with respect to varying flight conditions. This investigation differs from previous investigations in that it attempts to describe the performance of a flapping wing vehicle in the classical aircraft design framework. Most previous studies have approached the design of flapping wing vehicles from a perspective that focused on describing the interesting phenomena associated with flapping flight. While this perspective has revealed new insight into the physics of flapping flight, it may be foreign to those familiar with conventional aircraft who may wish to explore the merits of biomimesis. For this reason, the results of this investigation are presented in a manner that is more familiar to the broader community. Although many important characteristics of flapping flight, such as reduced frequency and flexibility effects, are not directly described in the classical aircraft design framework (e.g. the reduced frequency does not play a role in the design of fixed

[a]The work presented in this chapter is the result of close collaboration with Dr. Mohamed Zakaria.

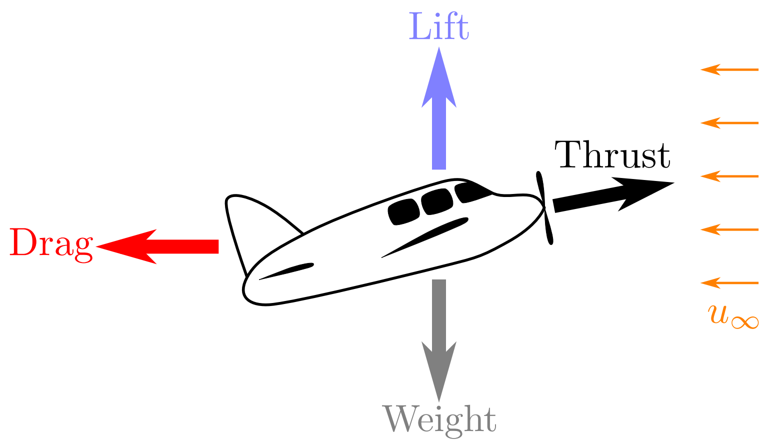

Figure 5.1: Free body diagram of a conventional aircraft.

wing aircraft), these characteristics appear in this investigation as parameters that affect the performance of the flapping wing vehicles in a manner familiar to the broader community.

When examining the longitudinal flight performance of aircraft, the forces are divided into lift, drag, and thrust, as shown in Figure 5.1. The lift and drag act perpendicular and parallel to the free stream, respectively, while the thrust acts in a direction defined by the orientation of the body. This fact belies an implicit assumption: the lift and drag producing mechanisms are separate from the thrust producing mechanisms. That is the lift is primarily produced by the wings, the drag by the wings and body, and the thrust by the propellers (or jet engines). Ornithopters do not have this distinction. The wings of ornithopters simultaneously produce both lift, drag, and thrust. This leads to the primary difficulty when discussing the flight performance of ornithopters; the vocabulary used to describe the performance of conventional aircraft assumes a distinction between purely thrust producing mechanics and purely drag and lift producing mechanics. Such a distinction does not exist for ornithopters, so it becomes difficult discuss the performance of ornithopters using standard terminology. This section seeks to do just that, adapt and expand the traditional terminology for longitudinal aircraft performance to make it useful for describing the flight of ornithopters.

A typical gait of a bird is illustrated in Figure 5.2. The pigeons shown in Figure 5.2 are different birds flying in close proximity. Unlike the airplane shown in Figure 5.1, the direction of the generated thrust is unclear. Recall the thrust generation mechanism described in Section 3.2.3.5. A flapping airfoil produces thrust by moving perpendicular to the ambient flow direction. This deflects the lift generated by the airfoil into the flow as seen in Figure 3.20. Although this is an appropriate description of the thrust generation mechanism, it is not amenable to the conventions shown in Figure 5.1. Because the thrust generation is a result of the aerodynamic force (the lift) being deflected in order to counteract another aerodynamic force (the drag), when describing the performance of ornithopters the concept of thrust is defined as “the force that acts in opposition to the drag”. Thus, there is not an explicit “thrust” force that acts on ornithopters separate from the other aerodynamic forces

Figure 5.2: Gait of domestic pigeons. Images are of different birds flying in approximately the same direction and in close proximity at different points in their gaits. This is not a sequence of images of the same bird. Used under the Creative Commons Attribution-ShareAlike License 3.0. Photo by Toby Hudson. Edited by Tony Wills.

Figure 5.3: The wind tunnel in Virginia Tech's Biomedical Engineering and Applied Mechanics (BEAM) Department

(the lift and the drag). Rather, the thrust is discussed as a "negative drag," a force acting anti-parallel to the free stream velocity regardless of the orientation of the body or the wings. This choice leads to interesting observations of the behavior, which will be described along with the experimental results later in this section.

5.1 Experimental Setup

5.1.1 Wind Tunnel

The experiments were performed in the low-speed wind tunnel at Virgina Tech's Biomedical Engineering and Mechanics (BEAM) department shown in Figure 5.3. The test section of the wind tunnel has a 52 cm square cross section and is 120 cm long. The wind tunnel is a suction type tunnel with a 1 m fan driven by a 15 hp motor. The inlet is a 1.2 m square bell mouth and contains a 9 cm long honeycomb flow straightener with a 1 mm cell size. Following the inlet, there are three additional turbulence-reducing screens. Airspeed were measured using a pitot-static system with an accuracy of 0.5% of the flow velocity.

5.1.2 Data Acquisition System

The data acquisition system consisted of an ATI Industrial Automation Mini40 force/torque sensor, a NI USB 6210 data acquisition card, and a Windows computer. The sting was attached to the sensor using a circular bracket and the fixed side of the sensor was attached

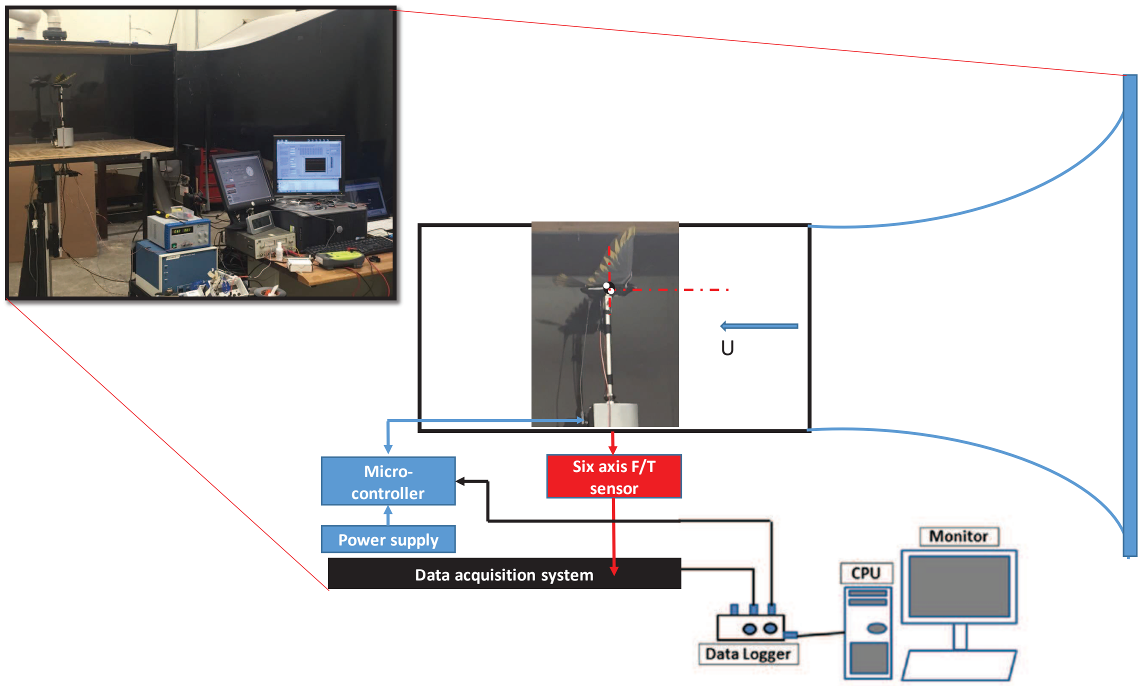

Figure 5.4: Schematic of the experimental apparatus and data acquisition system.

to a floor-mounted strut. The ornithopter was mounted to the sting as shown in Figure 5.4. A bracket holding a digital servo motor was fixed on the lower half of the sting in order to provide pitch control for the ornithopter. The servo motor is connected to the ornithopter fuselage rear end via an aluminum push rod. The Mini40 sensor is a six-component silicon strain gauge sensor capable of measuring forces up to ± 240 N in the axial direction and ± 80 N in other directions. It can also measure torques up to ±40 Nm in all three axes, although these measurements are not used in this experiment. The published resolution of the force measurements of the Mini40 is 20 mN. The measurement axes of the Mini40 are aligned with the wind tunnel, with the x-direction aligned with the flow direction, the z-direction pointing vertically up, and the y-direction completing the dextral basis.

For each experimental condition, two sets of experiments were conducted. First, tare experiments were conducted to determine forces generated when there is no airflow or flapping. Measurements from the tare experiments were then used to remove biases from the experiments with airflow and flapping. These experiments involved taking force measurements over 10 seconds. The data was then filtered with a fourth order Butterworth filter and a low pass frequency of at least twice the flapping frequency. This data was then averaged to generated the results presented later. As the length of data collection is significantly longer than the period of flapping, the effects of having incomplete cycles were ignored.

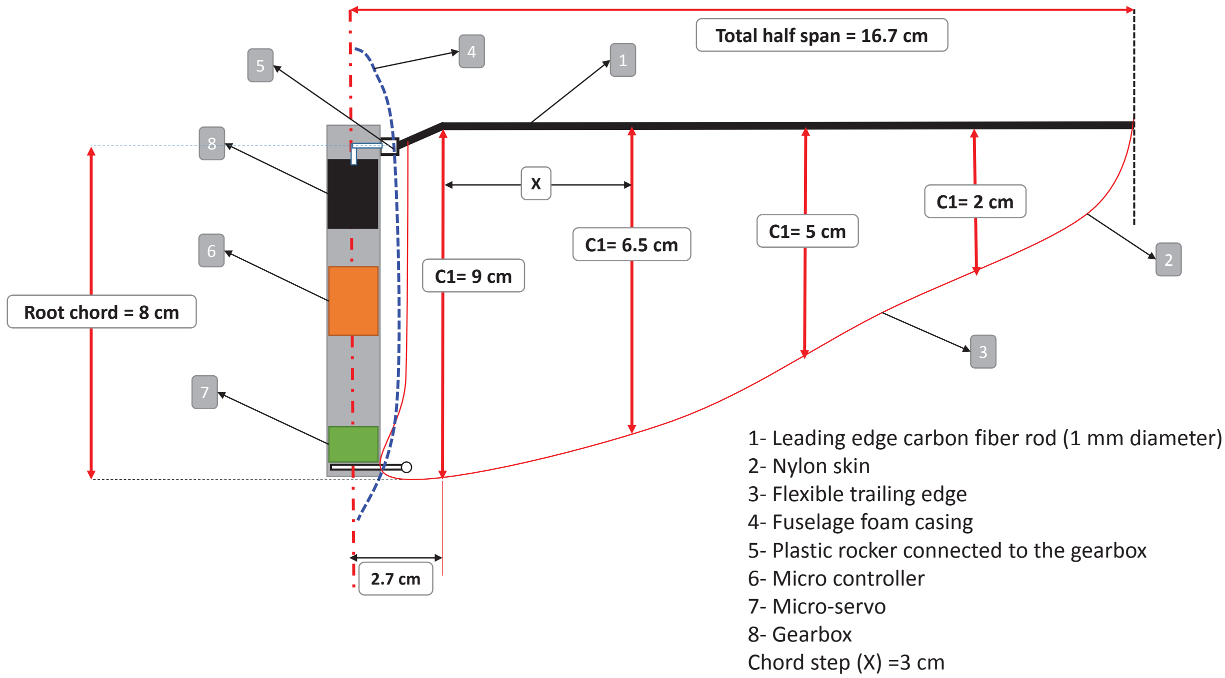

Figure 5.5: Schematic diagram for the tested ornithopter

5.1.3 Description of Ornithopter

Table 5.1: Kinematics and wing properties

Parameter	Value	Definition
$\overline{c}$	6.5 cm	Mean aerodynamic chord
$(\Gamma)_{max}$	35°	Maximum upstroke flapping angle
$(\Gamma)_{min}$	20°	Maximum down stroke flapping angle
W	13 g	Ornithopter mass
b	33.4 cm	Total span

The test article is a small ornithopter Figure 5.5 shows the main component of the tested ornithopter and provides the primary dimensions of the wing and the fuselage. Note that only the fuselage and right wing are shown; the left wing is symmetrical to the right wing about the center line of the fuselage. Four main chord values were used at fixed positions in the spanwise direction to indicate the spanwise variation of the chord length. The throttle is operated wirelessly and controls a motor which drives a rocker mechanism. This rocker mechanism is connected to the main spar of the flapping wing. The leading edge of the wing is attached to the main spar with adhesive. The trailing edge of the flapping wing is flexible and free to move except at the root of the wing, which is attached to the fuselage.

The kinematic parameters of the ornithopter are listed in Table 5.1. The angle of attack is measured with respect to line connecting the fixed roots of the leading and trailing edges of the wing.

5.2 Experimental Results

Table 5.2: Experimental operating parameters

Parameter	Value
Re: 1	6600
Re: 2	13000
Re: 3	21000
f: 1	7 Hz
f: 2	12 Hz
f: 3	15 Hz

Every test of the performance of the ornithopter involved controlling three parameters, the angle of attack, Reynolds number, and throttle setting, and collecting data for 10 seconds. As 10 seconds is significantly longer than the flapping period, errors introduce by averaging incomplete flapping cycles are ignored. For every combination of angle of attack, Reynolds number, and throttle setting three tests were performed. The throttle setting controls the flapping frequency and the Reynolds number is controlled by the wind tunnel. The values of the Reynolds numbers and approximate frequencies are listed in Table 5.2. Because the throttle setting controls the torque of the motor and not the flapping frequency, these frequencies represent the approximate frequencies corresponding to the three throttle settings.

The average lift and drag coefficients are shown with respect to the angle of attack at the range of Reynolds numbers and flapping frequencies in Figures 5.9 and 5.10. In this context, force coefficients are the force averaged over many cycles normalized by the planform area of the wings and the free stream dynamic pressure. The use of the free stream dynamic pressure obscures the fact that wings are moving relative to the body, so the velocity of the wings relative to the flow will be higher than the free stream leading to increased force coefficients. This problem is exacerbated at high flapping frequencies, when the speed from flapping is comparable to the free stream. These figures further obscure the fact that the flexibility of the wings allows the wings to deflect into the flow, changing the angle of attack of the wings with respect to the body. This is not practical to measure, so the angle of attack of the fuselage is used. Additionally, for some combinations of angles of attack, Reynolds numbers, and throttle settings the ornithopter is not capable of overcoming internal resistance and therefore cannot flap.

Figure 5.9 shows the relationship between the lift coefficient and angle of attack for various flapping frequencies and Reynolds numbers. An additional curve is provided, which represents a standard model of the lift coefficient, $\pi \sin 2\alpha$ [Karamcheti, 1966]. Instead of placing all of the data in a single plot, the data is divided into several plots by fixing either the Reynolds number or the flapping frequency setting. The top row of plots in Figure 5.9 group the data by Reynolds number while the bottom row groups the same data grouped by a flapping frequency. By grouping this data in this manner allows trends to be more easily observed.

At high angles of attack ($\approx 50°$), the slope of the lift coefficient decreases greatly or becomes negative indicating stall. This is significantly delayed in comparison to what is expected for fixed wing aircraft ($\approx 25°$). This is likely caused by the flexible wings deflecting into the flow, lowering the effective angle of attack. For many of the tests, the lift coefficient appears to be greater than the $\pi \sin 2\alpha$ prediction. This likely arises from the speed of the wing relative to the flow is greater than the free stream velocity, resulting in an artificially low dynamic pressure and thus and artificially high lift coefficient. Although this appears to be a limitation of the normalization, it is actually a useful feature; aircraft designers are likely more interested in the flight speed of the aircraft, so increasing the flapping frequency can be considered a lift enhancement mechanism.

Figure 5.10 shows the relationship between the drag coefficient and the angle of attack with data divided into several plots in the same way as Figure 5.9. In Figure 5.10, negative values for the drag coefficient correspond to the case where the ornithopter is producing thrust and would accelerate forward, were the test article not restrained. Thus, the operating conditions at which the drag coefficient is zero are the conditions when the thrust generated by the ornithopter balances the drag. Two general trends appear in Figure 5.10: 1) increasing the Reynolds number decreases the net thrust produced, and 2) increasing the flapping frequency increases the amount of thrust produced. Furthermore, because the drag coefficient is positive for almost all of the data corresponding to the highest Reynolds number the ornithopter is not capable of sustaining forward flight at this Reynolds number.

Figure 5.11 shows the variation of the drag to lift ratio with the angle of attack. The drag to lift ratio is used instead of the more common lift to drag ratio because of the nature of flapping flight. Using the conventions presented herein, steady flight corresponds to zero drag, which gives a singular value for the lift to drag ratio. In order to simplify the figure, the absolute value of the lift is used. Because of this, when the drag to lift ratio is negative, the ornithopter is producing enough thrust to overcome drag. There appears to be a large spike in the drag to lift ratio at low angles of attack, which is an artifact of the very small lift values at these angles.

Figure 5.6 shows the variation of the lift coefficient with the reduced frequency with each plot representing a different Reynolds number. The lines are linear least-squares fits for the data at different angles of attack. These lines represent the lift enhancement due to increasing the flapping frequency.

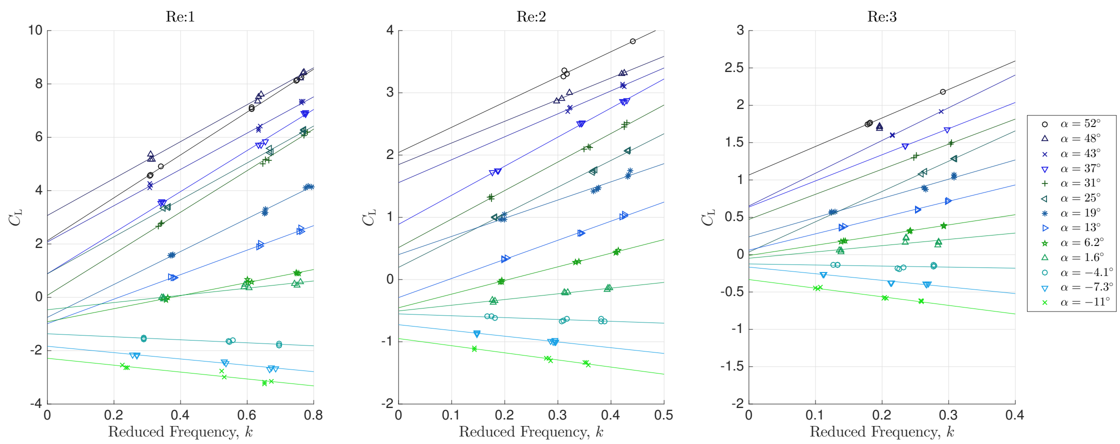

Figure 5.6: Variation of the cycle-averaged lift coefficient with reduced frequency. Lines are a linear least-squares fit.

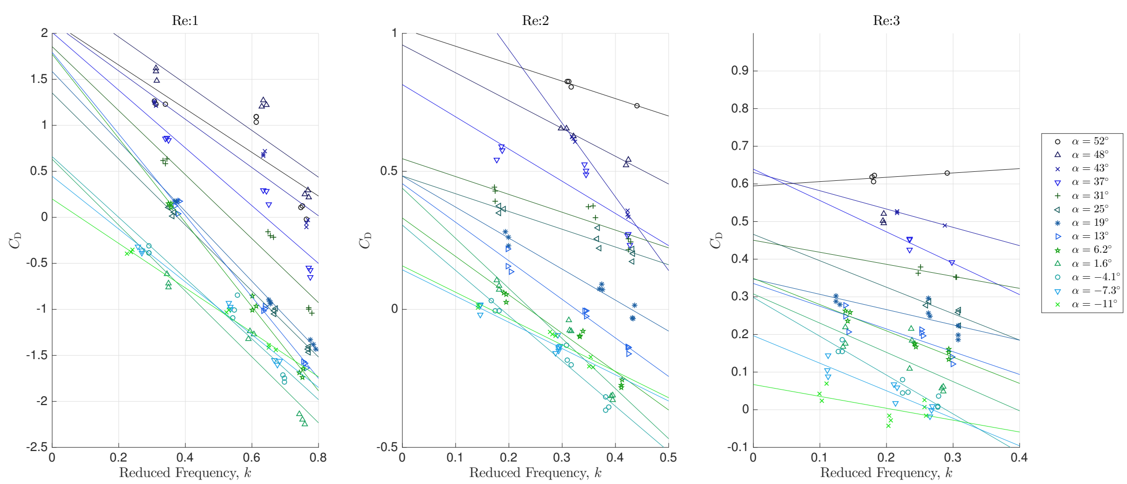

Figure 5.7: Variation of the cycle-averaged drag coefficient with reduced frequency. Lines are a linear least-squares fit.

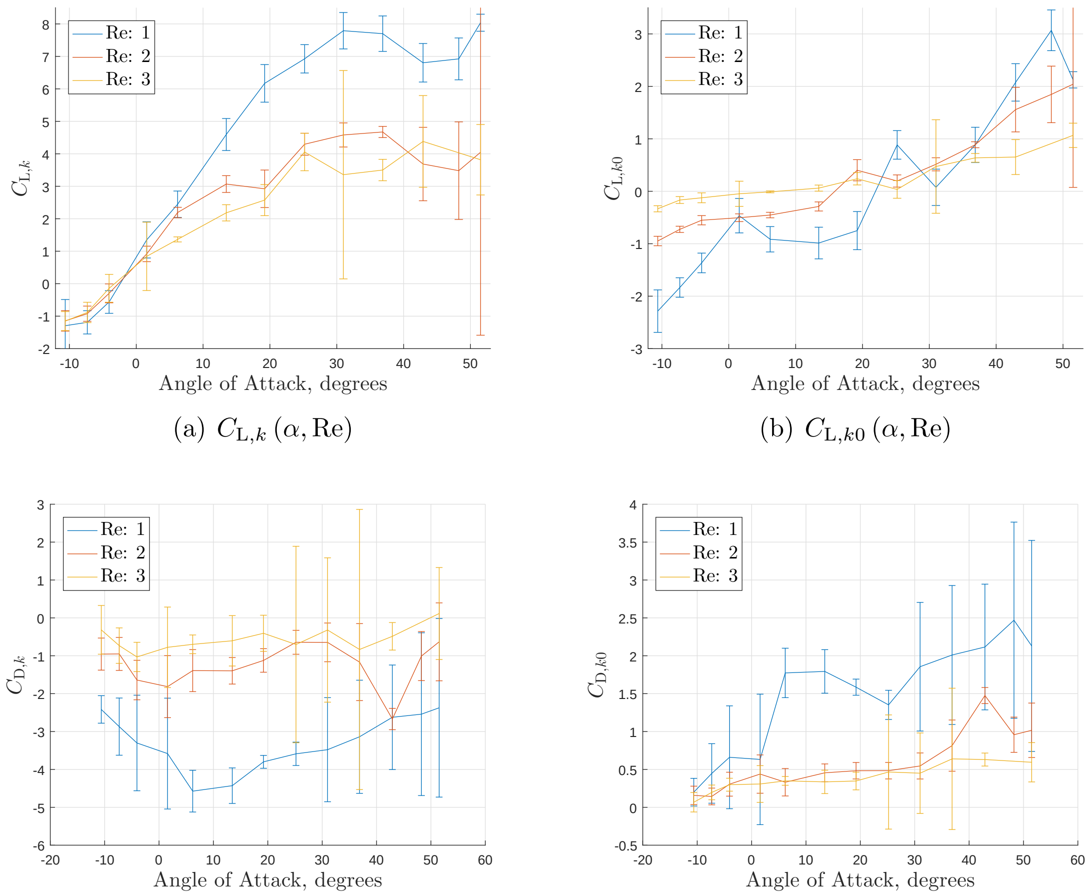

(a) $C_{\mathrm{L},k}\left(\alpha, \mathrm{Re}\right)$ (b) $C_{\mathrm{L},k0}\left(\alpha, \mathrm{Re}\right)$

(c) $C_{\mathrm{D},k}\left(\alpha, \mathrm{Re}\right)$ (d) $C_{\mathrm{D},k0}\left(\alpha, \mathrm{Re}\right)$

Figure 5.8: Coefficients for the linear model presented in Equation (5.1). Error bars represent the 3σ confidence interval.

Figure 5.7 shows the variation of the drag coefficient with reduced frequency. Again, the lines are linear least-squares fits. Note, in the case of the drag coefficient, that the linear fits are less accurate and trends related to angle of attack are harder to infer. Regardless, it is clear that almost all of these fits have negative slopes, indicating, as expected, that increasing the flapping frequency increases the thrust. The most prominent outlier is the highest angle of attack at the highest Reynolds number, which has a near-zero slope. This indicates that the ornithopter is not capable of generating thrust under these conditions.

The linear fits in Figures 5.6 and 5.7 provide a model for the variation of the lift and drag coefficients at a specific Reynolds number, i.e.

$$\begin{aligned} C_{\mathrm{L}}\left(\alpha, k, \mathrm{Re}\right) =& C_{\mathrm{L},k}\left(\alpha, \mathrm{Re}\right) k + C_{\mathrm{L},k0}\left(\alpha, \mathrm{Re}\right) \\ C_{\mathrm{D}}\left(\alpha, k, \mathrm{Re}\right) =& C_{\mathrm{D},k}\left(\alpha, \mathrm{Re}\right) k + C_{\mathrm{D},k0}\left(\alpha, \mathrm{Re}\right) \end{aligned} \tag{5.1}$$

One interesting feature of this model is that the lift and drag coefficient vary with the Reynolds number (i.e. the free stream flow velocity) even at zero flapping frequency. This is due to flexibility of the wings. The values of the coefficient in Equation (5.1) are shown in Figure 5.8. Figure 5.8(a) shows that the lower Reynolds number results in greater lift enhancement for given reduced frequency. Figure 5.8(b), which represents the lift coefficient without flapping, shows the effect of the flexibility of the wings (higher Reynolds numbers reduce the effective angle of attack). Figure 5.8(c) reveals that the same increase of reduced frequency produces a greater change of the drag coefficient for lower Reynolds number than higher Reynolds numbers. Figure 5.8(b) shows that the lower Reynolds numbers produce a greater drag coefficient at zero flapping frequency.

The conditions for steady, straight, and level flight that are such that the lift must overcome the weight and the thrust must balance the drag. Using this model and the conventions presented in this paper, these conditions become

$$\mathrm{W} = \frac{1}{2} C_{\mathrm{L}} \left(\alpha, k, \mathrm{Re}\right) \rho u_\infty^2 = \frac{1}{2} \left(C_{\mathrm{L},k} \left(\alpha, \mathrm{Re}\right) k + C_{\mathrm{L},k0} \left(\alpha, \mathrm{Re}\right)\right) \rho u_\infty^2$$

and

$$C_{\mathrm{D}} \left(\alpha, k, \mathrm{Re}\right) = C_{\mathrm{D},k} \left(\alpha, \mathrm{Re}\right) k + C_{\mathrm{D},k0} \left(\alpha, \mathrm{Re}\right) = 0$$

These conditions provide a structure for determining the angles of attack and flapping frequencies as would be required for a specific forward acceleration. For a given weight and forward flight speed, the values of W and Re are known; therefore the problem of satisfying these conditions becomes a matter of finding the angle of attack and flapping frequency which satisfy the conditions.

5.3 Contributions

The contributions of this section include both the experimental results and the new framework for discussing the performance of ornithopters. Wind tunnel testing was performed on a model ornithopter and the results are presented here. While these are unique tests, the main contribution arises from the interpretation. Most previous studies seek to describe the complex unsteady aerodynamics in detail. While this is a useful pursuit, analysis of the experimental data revealed that much of unsteady effects can be considered to be lift enhancement or thrust generation mechanism that vary linearly with reduced frequency. This observation arose from the application of a traditional aircraft performance to the performance of ornithopter, which is a unique contribution in its own right.

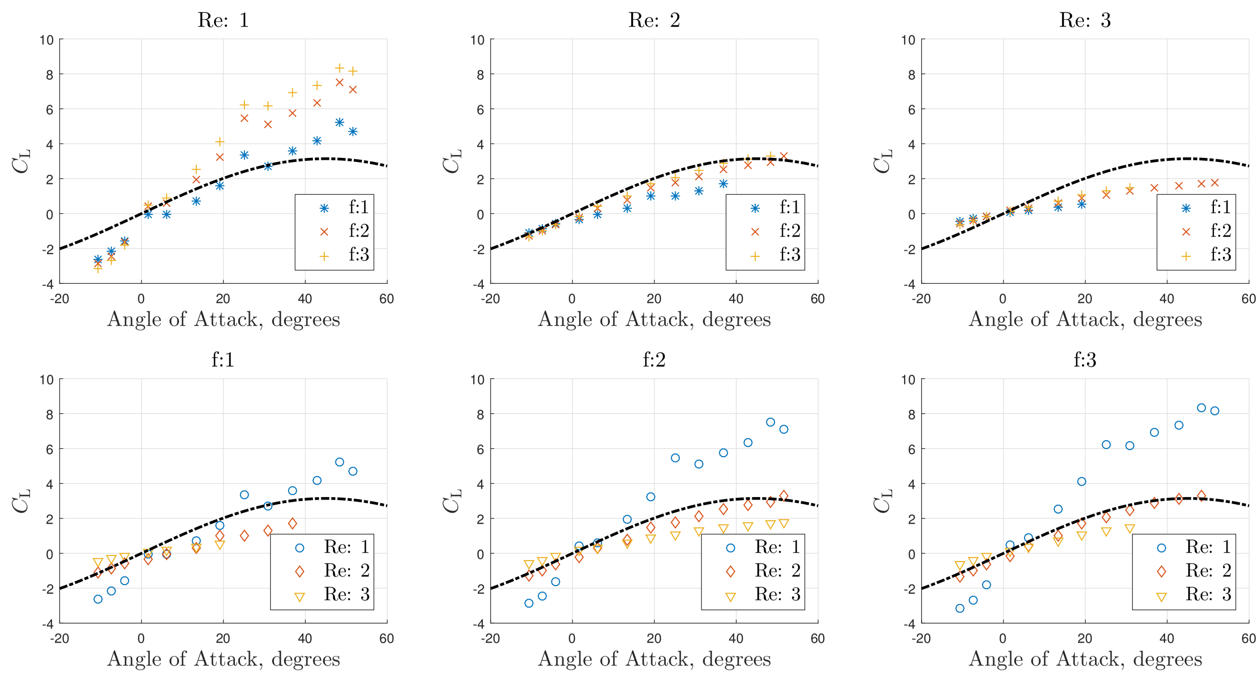

Figure 5.9: Variation of the cycle-averaged lift coefficient with the angle of attack with varying Reynolds number and flapping frequency.

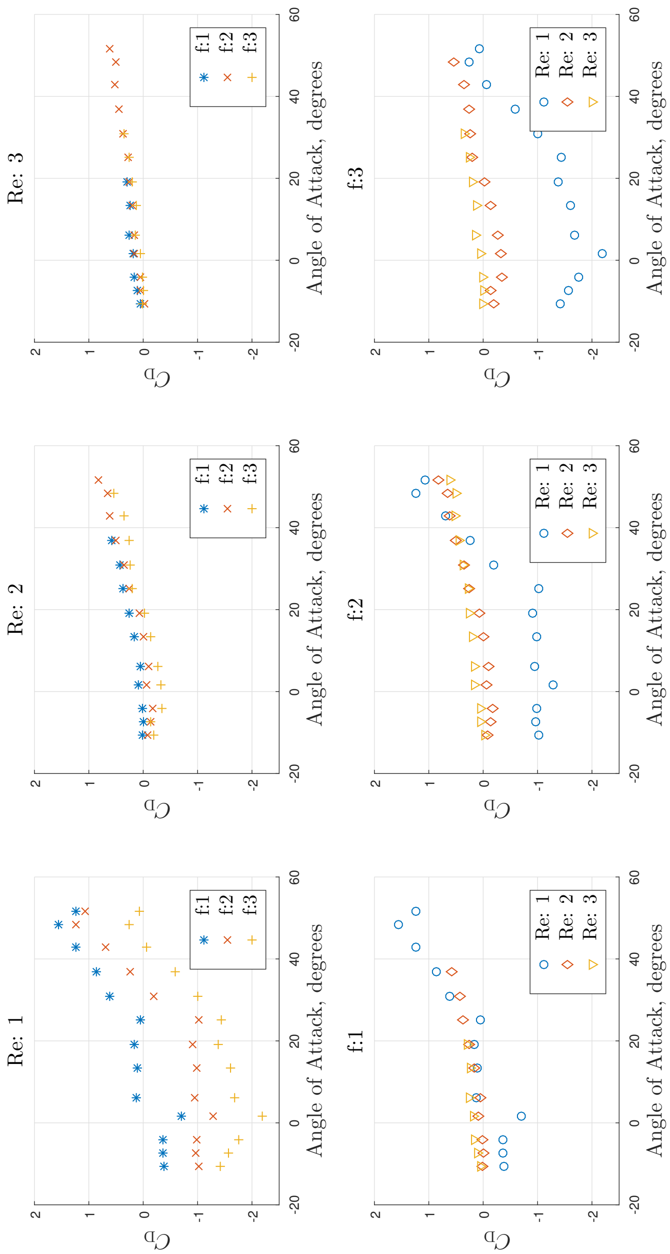

Figure 5.10: Variation of the cycle-averaged drag coefficient with the angle of attack with varying Reynolds number and flapping frequency.

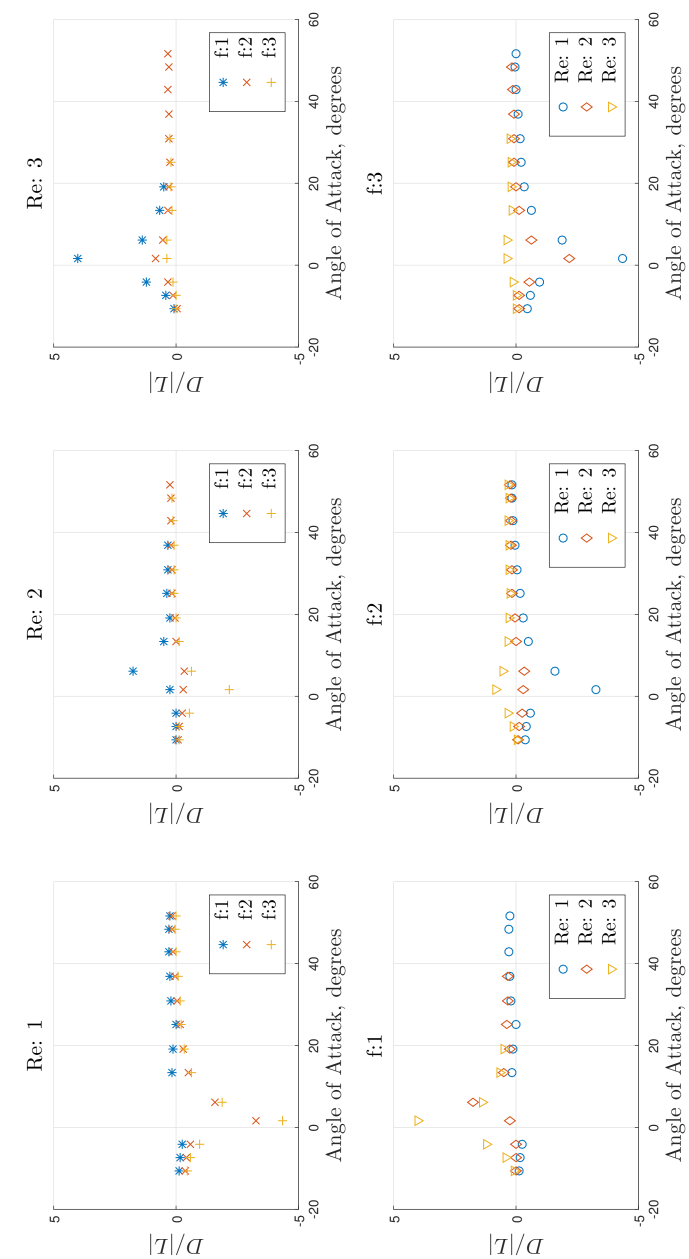

Figure 5.11: Variation of the cycle-averaged drag to lift ratio with the angle of attack.

Chapter 6

Conclusion and Future Work

Although this dissertation had one primary focus, the morphology and gait optimization of articulated bodies in fluids, the research presented here can be broadly divided into three topics: input waveform optimization, pisciform locomotion, and bio-inspired flight. These topics represent interrelated yet separate research efforts.

The first topic covered is input waveform optimization in Chapter 2. This section represents the author's contributions to the method presented by Tahmasian et al. [2016] as well as extensions to that work. The input waveform optimization method utilizes the geometric averaging technique presented by Bullo and Lewis [2005] to create a constrained optimization problem. This optimization problem selects the optimal input waveforms that will stabilize a system at a desired equilibrium. Three cost functionals are presented, each of which yield different optimal input waveforms. The observation that different input waveforms are optimal for different cost functionals inspired a more adaptable parameterization of the input waveform: truncated Fourier series. This parameterization allows for more complex input waveform although increases computational requirements for optimization.

The primary limitation of the input waveform optimization technique comes from the limitations of the averaging theorem on which the technique is built. The averaging theorem requires that the frequency of the input waveforms be "high enough," but does not provide a means for determining how high is "high enough." Further investigation may reveal methods of determining if a particular frequency is high enough, but, in general, this can be verified through simulation.

There are two useful extensions for input waveform optimization proposed here. The first is to incorporate the second order averaging technique presented by Vela [2003]. Implementing this will allow for frequency effects to be described and potentially allow for lower operating frequencies for averaging. The other extension would be to define the constraints to allow for constant average velocity motion. This would enable the input waveform optimization technique to be used to analyze the gait of flying and swimming systems.

Pisciform locomotion is the topic of Chapters 3 and 4. This work is divided into two parts. The first part, Chapter 3, develops a model of pisciform locomotion. This model is a control oriented model that can be adapted to approximate the spectrum of pisciform locomotion from undulatory to oscillatory locomotion. The second part, Chapter 4, utilizes the model developed in Chapter 3 to determine the optimal gaits for pisciform locomotion. A representative of thunniform locomotion is used to demonstrate the optimization technique.

The future development of the model presented in Chapter 3 should primarily focus on the development of more advanced and realistic hydrodynamic models. Some future work for the optimization was previously discussed in Section 4.3. Future work should primarily focus on moving to high performance computing and the development of new techniques to accelerate the optimization. Furthermore, experiments should be conducted on representative systems to verify the findings of the optimization method.

The final topic is bio-inspired flight, which is discussed in Chapter 5. This work discussed the results of wind tunnel experiments on an ornithopter. The primary contribution of these experiments was the use of a novel framework for discussing the results. By placing the results in the traditional longitudinal flight framework, new insight into how to make a practical ornithopter was generated. This insight provided a new model for the flight where the flapping frequency is both a thrust and lift generating mechanism.

Future work on bio-inspired flight should consist of additional testing. These future tests should use imaging systems to describe the flexure of the wing and attempt to tie the effects of flexure to the performance. Future work should also attempt to develop tests to describe the pitching moment and possibly the transverse flight dynamics. In the more distant future, studies attempting to describe the stability derivatives should also be conducted.

Bibliography

NJ Adams, CR Brown, and KA Nagy. Energy Expenditure of Free-Ranging Wandering Albatrosses Diomedea exulans. *Physiological Zoology*, 59(6):583–591, 1986. URL http://www.jstor.org/stable/30158606.

A A Agračev and R V Gamkrelidze. The Exponential Representation of Flows and the Chronological Calculus. *Mathematics of the USSR-Sbornik*, 35(6):727–785, 1979. ISSN 0025-5734. doi: 10.1070/SM1979v035n06ABEH001623. URL http://iopscience.iop.org/0025-5734/35/6/A01.

H. D. J. N. Aldridge. Flight kinematics and energetics in the little brown bat, Myotis lucifugus (Chiroptera: Vespertilionidae), with reference to the influence of ground effect. *Journal of Zoology*, 216(3):507–517, November 1988. ISSN 09528369. doi: 10.1111/j.1469-7998.1988.tb02447.x. URL http://doi.wiley.com/10.1111/j.1469-7998.1988.tb02447.x.

R. McNeill Alexander. The flight of the pterosaur. *Nature*, 371(6492):12–13, September 1994. ISSN 0028-0836. doi: 10.1038/371012a0. URL http://www.nature.com/doifinder/10.1038/371012a0.

R. McNeill Alexander. *Optima for Animals*. Princeton University Press, revised edition, 1996. ISBN 978-0691027999.

David W Allen. Database of Flying Animals. Technical report, Virginia Center for Autonomous Systems, Blacksburg, Virginia, USA, 2015.

David W Allen, Matthew Jones, Leigh Mccue, Craig Woolsey, and William B Moore. EUROPA: Exploration of Under-Ice Regions with Ocean Profiling Agents. Technical report, NIAC, 2013a. URL http://www.nasa.gov/directorates/spacetech/niac/2012_phase_I_fellows_mccue.html#.UnbPf_nksYw.

David W. Allen, Matthew C. Jones, Leigh S. Mccue, Craig A. Woolsey, and William B. Moore. Exploration of Under-ice Regions with Ocean Profiling Agents (EUROPA). Technical Report 01, Virginia Center for Autonomous Systems, Blacksburg, Virginia, USA, 2013b. URL http://www.unmanned.vt.edu/discovery/reports/VaCAS_2013_01.pdf.

David W. Allen, Matthew C. Jones, Craig A. Woolsey, William B. Moore, and Leigh McCue. Mapping a mission profile for the exploration of Europas ocean. In *AIAA SPACE 2013 Conference and Exposition*, San Diego, CA, USA, September 2013c. American Institute of Aeronautics and Astronautics. ISBN 978-1-62410-239-4. doi: 10.2514/6.2013-5474. URL http://arc.aiaa.org/doi/abs/10.2514/6.2013-5474.

David W. Allen, Matthew C. Jones, Leigh S. McCue, Craig a. Woolsey, Michael K. Philen, and William B. Moore. Exploring the Oceans of Europa with Biologically-Inspired Underwater Vehicles. *Journal of the British Interplanetary Society*, 68:251–264, 2015.

David William Allen. *Development of a Value System and Mission Architecture for the Exploration of the Oceans of Europa*. Master's thesis, Virginia Tech, 2014. URL http://scholar.lib.vt.edu/theses/available/etd-11122014-130031/unrestricted/Allen_DW_T_2014.pdf.

R. Bellman, J. Bentsman, and S. Meerkov. Stability of fast periodic systems. *IEEE Transactions on Automatic Control*, 30(3):289–291, mar 1985a. ISSN 0018-9286. doi: 10.1109/TAC.1985.1103936. URL http://ieeexplore.ieee.org/lpdocs/epic03/wrapper.htm?arnumber=1103936.

R. Bellman, J. Bentsman, and S. M. Meerkov. Stability of fast periodic systems. *IEEE Transactions on Automatic Control*, AC-30(3):289–291, 1985b.

Richard E. Bellman. *Dynamic Programming*. Dover Publications Inc., 2003. ISBN 9780486428093.

C Berg and J Rayner. The moment of inertia of bird wings and the inertial power requirement for flapping flight. *The Journal of experimental biology*, 198(Pt 8):1655–64, January 1995. ISSN 1477-9145. URL http://www.ncbi.nlm.nih.gov/pubmed/9319563.

Jordan M Berg and I.P Manjula Wickramasinghe. Vibrational control without averaging. *Automatica*, 58:72–81, 2015. doi: 10.1016/j.automatica.2015.04.028.

James Bergstra and Yoshua Bengio. Random Search for Hyper-Parameter Optimization. *Journal of Machine Learning Research*, 13:281–305, 2012. ISSN 1532-4435.

Gordon J. Berman and Z. Jane Wang. Energy-minimizing kinematics in hovering insect flight. *Journal of Fluid Mechanics*, 582:153, June 2007. ISSN 0022-1120. doi: 10.1017/S0022112007006209. URL http://www.journals.cambridge.org/abstract_S0022112007006209.

John J Bertin and Russell M Cummings. *Aerodynamics for Engineers*. Pearson Prentice-Hall, Upper Saddle River, NJ, USA, 5 edition, 2009. ISBN 0-13-227268-7.

G. E. P. Box. The Exploration and Exploitation of Response Surfaces: Some General Considerations and Examples. *Biometrics*, 10(1):16, mar 1954. ISSN 0006341X. doi: 10.2307/3001663. URL http://www.jstor.org/stable/3001663.

S. Boyd and L. Vandenberghe. *Convex Optimization.* Cambridge University Press, Cambridge, United Kingdom, 2004.

JC Brower and Julia Veinus. Allometry in Pterosaurs. Technical report, The University of Kansas Paleontological Contributions: Paper 105, 1981. URL http://hdl.handle.net/1808/3677http://kuscholarworks.ku.edu/handle/1808/3677.

Francesco Bullo. Series Expansions for the Evolution of Mechanical Control Systems. *SIAM Journal on Control and Optimization*, 40(1):166–190, January 2001. ISSN 0363-0129. doi: 10.1137/S0363012999364796. URL http://epubs.siam.org/doi/abs/10.1137/S0363012999364796.

Francesco Bullo. Averaging and Vibrational Control of Mechanical Systems. *SIAM Journal on Control and Optimization*, 41(2):542–562, January 2002. ISSN 0363-0129. doi: 10.1137/S0363012999364176. URL http://epubs.siam.org/doi/abs/10.1137/S0363012999364176.

Francesco Bullo and Andrew D. Lewis. *Geometric Control of Mechanical Systems.* Springer, 1 edition, 2005. ISBN 0-387-22195-6.

John A Burns. *Introduction to the Calculus of Variations and Control with Modern Applications.* CRC Press, Boca Raton, FL, USA, 2014. ISBN 9781466571396.

O. Chanute. *Progress in Flying Machines,.* Dover Publications, Inc.,, 1894.

Octave Chanute. *Progress in Flying Machines.* M. N. Forney, New York, New York, USA, 1899.

P. Chedmail and M. Gautier. Optimum choice of robot actuators. *ASME Journal of Engineering for Industry*, 112:361–367, 1990.

M. G. Chopra. Large amplitude lunate-tail theory of fish locomotion. *Journal of Fluid Mechanics*, 74(01):161, March 1976. ISSN 0022-1120. doi: 10.1017/S0022112076001742. URL http://www.journals.cambridge.org/abstract_S0022112076001742.

M. G. Chopra and T. Kambe. Hydromechanics of lunate-tail swimming propulsion. Part 2. *Journal of Fluid Mechanics*, 79(01):49, 1977. ISSN 0022-1120. doi: 10.1017/S0022112077000032.

Bruce B. Collette and Cornelia E. Nauen. FAO Species Catalogue: Vol. 2 Scombrids of the World. *FAO Fisheries Synopsis*, 2(125):137, 1983. URL http://www.fao.org/docrep/009/ac478e/ac478e00.htm.

Herbert C. Corben. Wing-beat frequencies, wing-areas and masses of flying insects and hummingbirds. *Journal of Theoretical Biology*, 102(4):611–623, June 1983. ISSN 00225193. doi: 10.1016/0022-5193(83)90394-6. URL http://linkinghub.elsevier.com/retrieve/pii/0022519383903946.

S Dhawan. Bird flight. *Sadhana*, 16(4):275–352, December 1991. ISSN 0256-2499. doi: 10.1007/BF02745345. URL http://link.springer.com/10.1007/BF02811356http://link.springer.com/10.1007/BF02745345.

C. P. Ellington. The Aerodynamics of Hovering Insect Flight. IV. Aeorodynamic Mechanisms. *Philosophical Transactions of the Royal Society B: Biological Sciences*, 305 (1122):79–113, February 1984a. ISSN 0962-8436. doi: 10.1098/rstb.1984.0052. URL http://rstb.royalsocietypublishing.org/cgi/doi/10.1098/rstb.1984.0052.

C. P. Ellington. The Aerodynamics of Hovering Insect Flight. V. A Vortex Theory. *Philosophical Transactions of the Royal Society B: Biological Sciences*, 305(1122):115–144, February 1984b. ISSN 0962-8436. doi: 10.1098/rstb.1984.0053. URL http://rstb.royalsocietypublishing.org/cgi/doi/10.1098/rstb.1984.0053.

C. P. Ellington. The Aerodynamics of Hovering Insect Flight. I. The Quasi-Steady Analysis. *Philosophical Transactions of the Royal Society B: Biological Sciences*, 305(1122): 1–15, February 1984c. ISSN 0962-8436. doi: 10.1098/rstb.1984.0049. URL http://rstb.royalsocietypublishing.org/cgi/doi/10.1098/rstb.1984.0049.

C. P. Ellington. The Aerodynamics of Hovering Insect Flight. VI. Lift and Power Requirements. *Philosophical Transactions of the Royal Society B: Biological Sciences*, 305 (1122):145–181, February 1984d. ISSN 0962-8436. doi: 10.1098/rstb.1984.0054. URL http://rstb.royalsocietypublishing.org/cgi/doi/10.1098/rstb.1984.0054.

C. P. Ellington. The Aerodynamics of Hovering Insect Flight. III. Kinematics. *Philosophical Transactions of the Royal Society B: Biological Sciences*, 305(1122):41–78, 1984e. ISSN 0962-8436. doi: 10.1098/rstb.1984.0051. URL http://rstb.royalsocietypublishing.org/cgi/doi/10.1098/rstb.1984.0051.

C. P. Ellington. The Aerodynamics of Hovering Insect Flight. II. Morphological Parameters. *Philosophical Transactions of the Royal Society B: Biological Sciences*, 305 (1122):17–40, February 1984f. ISSN 0962-8436. doi: 10.1098/rstb.1984.0050. URL http://rstb.royalsocietypublishing.org/cgi/doi/10.1098/rstb.1984.0050.

Charles P. Ellington. Power and efficiency of insect flight muscle. *The Journal of experimental biology*, 115:293–304, March 1985. ISSN 0022-0949. URL http://www.ncbi.nlm.nih.gov/pubmed/4031771.

Bernard Etkin and Lloyd Duff Reid. *Dynamics of Flight: Stability and Control*. Wiley, 3 edition, 1995.

John Farney and Eugene D. Fleharty. Aspect Ratio, Loading, Wing Span, and Membrane Areas of Bats. *Journal of Mammalogy*, 50(2):362–367, May 1969. ISSN 00222372. doi: 10.2307/1378361. URL http://www.jstor.org/stable/1378361http://www.jstor.org/stable/1378361?origin=crossref.

Frank E Fish and J J Rohr. Review of Dolphin Hydrodynamics and Swimming Performance. Technical report, SPAWAR Systems Center, San Diego, CA, USA, 1999.

Thor I. Fossen. *Guidance and Control of Ocean Vehicles*. John Wiley & Sons, Ltd, Chichester, West Sussex, UK, 1994. ISBN 0-471-94113-1.

Charles C. Frasier. An explanation of the relationships between mass, metabolic rate and characteristic skeletal length for birds and mammals. *Journal of Theoretical Biology*, 109 (3):331–371, August 1984. ISSN 00225193. doi: 10.1016/S0022-5193(84)80086-7. URL `http://linkinghub.elsevier.com/retrieve/pii/S0022519384800867`.

Crawford H Greenewalt. Dimensional Relationships for Flying Animals. *Smithsonian miscellaneous collections*, 144(2):1–46, 1962. URL `http://www.biodiversitylibrary.org/item/79674`.

Crawford H. Greenewalt. The Flight of Birds: The Significant Dimensions, Their Departure from the Requirements for Dimensional Similarity, and the Effect on Flight Aerodynamics of That Departure. *Transactions of the American Philosophical Society*, 65(4):1–67, 1975. ISSN 00659746. doi: 10.2307/1006161. URL `http://www.jstor.org/stable/1006161?origin=crossref`.

Donald T. Greenwood. *Classical Dynamics*. Dover Publications Inc., Mineola, New York, USA, 1977. ISBN 978-0-486-69690-4.

J. Guckenheimer and P. Holmes. *Nonlinear Oscillations, Dynamical Systems, and Bifurcations if Vector Fields*. Applied Mathematical Scinces, Springer-Verlag, New York, New York, USA, 1983.

Grant A Hazlehurst and Jeremy M V Rayner. Flight Characteristics of Triassic and Jurassic Pterosauria: An Appraisal Based on Wing Shape. *Paleobiology*, 18(4):447–463, 1992. URL `http://www.jstor.org/stable/2400829`.

A. Hedenstrom and T. Alerstam. Optimal Flight Speed of Birds. *Philosophical Transactions of the Royal Society B: Biological Sciences*, 348(1326):471–487, June 1995. ISSN 0962-8436. doi: 10.1098/rstb.1995.0082. URL `http://rstb.royalsocietypublishing.org/cgi/doi/10.1098/rstb.1995.0082`.

A. Hedenstrom and A. P. Moller. Morphological Adaptations to Song Flight in Passerine Birds: A Comparative Study. *Proceedings of the Royal Society B: Biological Sciences*, 247(1320):183–187, March 1992. ISSN 0962-8452. doi: 10.1098/rspb.1992.0026. URL `http://rspb.royalsocietypublishing.org/cgi/doi/10.1098/rspb.1992.0026`.

Glenn L. Jepsen, Robert J. Baker, Terry A. Vaughan, Robert T. Orr, Donald R. Griffin, Wayne H. Davis, Charles P. Lyman, and Robert M. Rosenbaum. *Biology of Bats: Volume I*. Academic Press, New York, New York, USA, 1 edition, 1970.

Oliver Junge, Jerrold E Marsden, and Sina Ober-Blöbaum. Discrete mechanics and optimal control. In Pavel Zítek, editor, *IFAC Congress*, pages 744–744, Prague, Czech Republic, July 2005. doi: 10.3182/20050703-6-CZ-1902.00745. URL `http://www.ifac-papersonline.net/Detailed/28026.html`.

E. Kanso, J. E. Marsden, C. W. Rowley, and J. B. Melli-Huber. Locomotion of Articulated Bodies in a Perfect Fluid. *Journal of Nonlinear Science*, 15(4):255–289, August 2005. ISSN 0938-8974. doi: 10.1007/s00332-004-0650-9. URL `http://link.springer.com/10.1007/s00332-004-0650-9`.

Eva Kanso and J.E. Marsden. Optimal Motion of an Articulated Body in a Perfect Fluid. In *Proceedings of the 44th IEEE Conference on Decision and Control*, volume 2005, pages 2511–2516. IEEE, 2005. ISBN 0-7803-9567-0. doi: 10.1109/CDC.2005.1582540. URL `http://ieeexplore.ieee.org/lpdocs/epic03/wrapper.htm?arnumber=1582540`.

Eva Kanso and Babak Ghaemi Oskouei. Stability of a coupled bodyvortex system. *Journal of Fluid Mechanics*, 600(2002):1–22, April 2008. ISSN 0022-1120. doi: 10.1017/S0022112008000359. URL `http://www.journals.cambridge.org/abstract_S0022112008000359`.

Krishnamurty Karamcheti. *Principals of Ideal-Fluid Aerodynamics*. Robert E. Krieger Publishing Company, Malabar, FL, USA, 1966. ISBN 0-89874-113-0.

M. Karpelson, G. Wei, and R. J. Wood. A review of actuation and power electronics options for flapping-wing robotic insects. In *Proc. IEEE International Conference on Robotics and Automation*, pages 779–786, Pasadena, CA, May 2008.

Scott D. Kelly and Richard M. Murray. Modelling efficient pisciform swimming for control. *International Journal of Robust and Nonlinear Control*, 10(4):217–241, April 2000. ISSN 1049-8923. doi: 10.1002/(SICI)1099-1239(20000415)10:4⟨217::AID-RNC469⟩3.0.CO;2-X. URL `http://doi.wiley.com/10.1002/%28SICI%291099-1239%2820000415%2910%3A4%3C217%3A%3AAID-RNC469%3E3.0.CO%3B2-X`.

S.D. Kelly, R.J. Mason, C.T. Anhalt, R.M. Murray, and J.W. Burdick. Modelling and experimental investigation of carangiform locomotion for control. *Proceedings of the 1998 American Control Conference. ACC (IEEE Cat. No.98CH36207)*, 2(June):1271–1276, 1998. URL `http://doi.wiley.com/10.1002/%28SICI%291099-1239%2820000415%2910%3A4%3C217%3A%3AAID-RNC469%3E3.0.CO%3B2-X`.

Hassan Khalil. *Nonlinear Systems*. Prentice Hall, third edition, 2001. ISBN 0130673897.

M J Lighthill. Hydromechanics of Aquatic Animal Propulsion. *Annual Review of Fluid Mechanics*, 1(1):413–446, January 1969. ISSN 0066-4189. doi: 10.1146/annurev.fl.01.010169.002213. URL `http://www.annualreviews.org/doi/abs/10.1146/annurev.fl.01.010169.002213`.

H Liu, Charles P. Ellington, K Kawachi, and C. A computational fluid dynamic study of hawkmoth hovering. *The Journal of experimental biology*, 201(Pt 4):461–77, February 1998. ISSN 1477-9145. URL `http://www.ncbi.nlm.nih.gov/pubmed/9438823`.

R. Mason and J.W. Burdick. Experiments in carangiform robotic fish locomotion. In *Proceedings 2000 ICRA. Millennium Conference. IEEE International Conference on Robotics and Automation. Symposia Proceedings (Cat. No.00CH37065)*, volume 1, pages 428–435. IEEE, 2000. ISBN 0-7803-5886-4. doi: 10.1109/ROBOT.2000.844093. URL `http://ieeexplore.ieee.org/lpdocs/epic03/wrapper.htm?arnumber=844093`.

SM Meerkov. Averaging of trajectories of slow dynamics system. *Differential Equation.—-9, c*, pages 1239–1245, 1973.

Cleve Moler. Matrix Computation on Dirstributed Memory Multiprocessors. In Michael T. Heath, editor, *Hypercube Multiprocessors*. SIAM, 1986. ISBN 9780898712094.

Enrique Morgado. On the allometry of wings. *Revista Chilena de Historia Natural*, 60:71–79, 1987. URL `http://rchn.biologiachile.cl/pdfs/1987/1/Morgado_et_al_1987.pdf`.

K.a. Morgansen, V. Duidam, R.J. Mason, J.W. Burdick, and R.M. Murray. Nonlinear control methods for planar carangiform robot fish locomotion. *Proceedings 2001 ICRA. IEEE International Conference on Robotics and Automation (Cat. No.01CH37164)*, 1: 427–434, 2001. ISSN 1050-4729. doi: 10.1109/ROBOT.2001.932588.

K.a. Morgansen, P.a. Vela, and J.W. Burdick. Trajectory stabilization for a planar carangiform robot fish. *Proceedings 2002 IEEE International Conference on Robotics and Automation (Cat. No.02CH37292)*, 1:756–762, 2002. ISSN 10504729. doi: 10.1109/ROBOT.2002.1013449.

Kristi A. Morgansen, Benjamin I. Triplett, and Daniel J. Klein. Geometric Methods for Modeling and Control of Free-Swimming Fin-Actuated Underwater Vehicles. *IEEE Transactions on Robotics*, 23(6):1184–1199, December 2007. ISSN 1552-3098. doi: 10.1109/LED.2007.911625. URL `http://ieeexplore.ieee.org/lpdocs/epic03/wrapper.htm?arnumber=4399955`.

Ulla M. Norberg. Allometry of Bat Wings and Legs and Comparison with Bird Wings. *Philosophical Transactions of the Royal Society B: Biological Sciences*, 292(1061):359–398, June 1981. ISSN 0962-8436. doi: 10.1098/rstb.1981.0034. URL `http://rstb.royalsocietypublishing.org/cgi/doi/10.1098/rstb.1981.0034`.

Colin J. Pennycuick. Thermal Soaring Compared in Three Dissimilar Tropical Bird Species, Fregata Magnificens, Pelecanus Occidentals and Coragyps Atratus. *Journal of Experimental Biologyx*, 102:307–326, 1983.

Jeremy M V Rayner. A new approach to animal flight mechanics. *Journal of Experimental Biology*, 80:17–54, 1979. URL `http://jeb.biologists.org/content/80/1/17.short`.

Jan A. Sanders, Ferdinand Verhulst, and James Murdock. *Averaging Methods in Nonlinear Dynamical Systems*. Springer, second edition, 2007. ISBN 978-0-387-48916-2.

Sanjay P. Sane. The aerodynamics of insect flight. *Journal of Experimental Biology*, 206 (23):4191–4208, December 2003. ISSN 0022-0949. doi: 10.1242/jeb.00663. URL http://jeb.biologists.org/cgi/doi/10.1242/jeb.00663.

Michael Sfakiotakis, D.M. Lane, and J.B.C. Davies. Review of fish swimming modes for aquatic locomotion. *IEEE Journal of Oceanic Engineering*, 24(2):237–252, April 1999. ISSN 03649059. doi: 10.1109/48.757275. URL http://ieeexplore.ieee.org/lpdocs/epic03/wrapper.htm?arnumber=757275.

Sevak Tahmasian, David W. Allen, and Craig A. Woolsey. On averaging and input optimization of high-frequency mechanical control systems. *Journal of Vibration and Control*, jul 2016. ISSN 1077-5463. doi: 10.1177/1077546316655706. URL http://jvc.sagepub.com/cgi/doi/10.1177/1077546316655706.

Graham K Taylor, Robert L Nudds, and Adrian L R Thomas. Flying and swimming animals cruise at a Strouhal number tuned for high power efficiency. *Nature*, 425(6959):707–11, October 2003. ISSN 1476-4687. doi: 10.1038/nature02000. URL http://www.ncbi.nlm.nih.gov/pubmed/14562101http://www.nature.com/nature/journal/v425/n6959/abs/nature02000.html.

R.J. Templin. The spectrum of animal flight: insects to pterosaurs. *Progress in Aerospace Sciences*, 36(5-6):393–436, August 2000. ISSN 03760421. doi: 10.1016/S0376-0421(00)00007-5. URL http://linkinghub.elsevier.com/retrieve/pii/S0376042100000075.

Xiaodong Tian, Jose Iriarte-Diaz, Kevin Middleton, Ricardo Galvao, Emily Israeli, Abigail Roemer, Allyce Sullivan, Arnold Song, Sharon Swartz, and Kenneth Breuer. Direct measurements of the kinematics and dynamics of bat flight. *Bioinspiration & biomimetics*, 1(4):S10–8, December 2006. ISSN 1748-3190. doi: 10.1088/1748-3182/1/4/S02. URL http://www.ncbi.nlm.nih.gov/pubmed/17671313.

Bret W Tobalske, Douglas R Warrick, Christopher J Clark, Donald R Powers, Tyson L Hedrick, Gabriel a Hyder, and Andrew a Biewener. Three-dimensional kinematics of hummingbird flight. *The Journal of experimental biology*, 210(Pt 13):2368–82, July 2007. ISSN 0022-0949. doi: 10.1242/jeb.005686. URL http://www.ncbi.nlm.nih.gov/pubmed/17575042.

C. van den Berg and Charles P. Ellington. The three-dimensional leading-edge vortex of a 'hovering' model hawkmoth. *Philosophical Transactions of the Royal Society B: Biological Sciences*, 352(1351):329–340, March 1997. ISSN 0962-8436. doi: 10.1098/rstb.1997.0024. URL http://rstb.royalsocietypublishing.org/cgi/doi/10.1098/rstb.1997.0024.

Joris Vankerschaver, Eva Kanso, and Jerrold Marsden. The geometry and dynamics of interacting rigid bodies and point vortices. *The Journal of Geometric Mechanics*, 1(2):223–266, July 2009. ISSN 1941-4889. doi: 10.3934/jgm.2009.1.223. URL http://arxiv.org/abs/0810.1490http://www.aimsciences.org/journals/displayArticles.jsp?paperID=4369.

Joris Vankerschaver, Eva Kanso, and Jerrold E. Marsden. The dynamics of a rigid body in potential flow with circulation. *Regular and Chaotic Dynamics*, 15(4-5):606–629, October 2010. ISSN 1560-3547. doi: 10.1134/S1560354710040143. URL http://arxiv.org/abs/1003.0080http://link.springer.com/10.1134/S1560354710040143.

P.A. Vela, K.A. Morgansen, and J.W. Burdick. Second order averaging methods for oscillatory control of underactuated mechanical systems. In *Proceedings of the 2002 American Control Conference (IEEE Cat. No.CH37301)*, volume 1, pages 4672–4677 vol.6. IEEE, 2002a. ISBN 0-7803-7298-0. doi: 10.1109/ACC.2002.1025395. URL http://ieeexplore.ieee.org/lpdocs/epic03/wrapper.htm?arnumber=1025395.

Patricio Antonio Vela. *Averaging and Control of Nonlinear Systems (with Application to Biomimetic Locomotion)*. PhD thesis, California Institute of Technology, 2003.

Patricio Antonio Vela, Kristi A. Morgansen, and Joel W Burdick. Underwater locomotion from oscillatory shape deformations. In *Proceedings of the 41st IEEE Conference on Decision and Control, 2002.*, volume 2, pages 2074–2080. IEEE, 2002b. ISBN 0-7803-7516-5. doi: 10.1109/CDC.2002.1184835. URL http://ieeexplore.ieee.org/lpdocs/epic03/wrapper.htm?arnumber=1184835.

Zhenlong Wang, Guanrong Hang, Yangwei Wang, Jian Li, and Wei Du. Embedded SMA wire actuated biomimetic fin: a module for biomimetic underwater propulsion. *Smart Materials and Structures*, 17(2):25039, April 2008. ISSN 0964-1726. doi: 10.1088/0964-1726/17/2/025039.

Thomas A Ward, M Rezadad, Christopher J Fearday, and Rubentheren Viyapuri. A Review of Biomimetic Air Vehicle Research: 1984-2014. *International Journal of Micro Air Vehicles*, 7(3):375–394, sep 2015. ISSN 1756-8293. doi: 10.1260/1756-8293.7.3.375. URL http://multi-science.atypon.com/doi/10.1260/1756-8293.7.3.375.

John Warham. Wing loadings, wing shapes, and flight capabilities of procellariiformes. *New Zealand Journal of Zoology*, 4(1):73–83, March 1977. ISSN 0301-4223. doi: 10.1080/03014223.1977.9517938. URL http://www.tandfonline.com/doi/abs/10.1080/03014223.1977.9517938.

Paul W. Webb. Form and Function in Fish Swimming. *Scientific American*, 251(1):72–82, July 1984. ISSN 0036-8733. doi: 10.1038/scientificamerican0784-72. URL http://www.nature.com/doifinder/10.1038/scientificamerican0784-72.

T Weis-Fogh. Energetics of Hovering Flight in Hummingbirds and in Drosophila. *Journal of Experimental Biology*, 56:79–104, 1972. URL http://jeb.biologists.org/content/56/1/79.short.

Torkel Weis-Fogh. Quick Estimates of Flight Fitness in Hovering Animals, Including Novel Mechanisms for Lift Production. *Journal of Experimental Biology*, 59(1):169–230, 1973. ISSN 0022-0949, 1477-9145. URL http://jeb.biologists.org/content/59/1/169.short.

D. R. Wilkie. The Work Output of Animals: Flight by Birds and by Man-power. *Nature*, 183(4674):1515–1516, May 1959. ISSN 0028-0836. doi: 10.1038/1831515a0. URL http://www.nature.com/doifinder/10.1038/1831515a0.

Junzhi Yu and Long Wang. Parameter Optimization of Simplified Propulsive Model for Biomimetic Robot Fish. In *Proceedings of the 2005 IEEE International Conference on Robotics and Automation*, volume 2005, pages 3306–3311. IEEE, 2005. ISBN 0-7803-8914-X. doi: 10.1109/ROBOT.2005.1570620. URL http://ieeexplore.ieee.org/lpdocs/epic03/wrapper.htm?arnumber=1570620.

Junzhi Yu, Min Tan, Shuo Wang, and Erkui Chen. Development of a Biomimetic Robotic Fish and Its Control Algorithm. *IEEE Transactions on Systems, Man and Cybernetics, Part B (Cybernetics)*, 34(4):1798–1810, August 2004. ISSN 1083-4419. doi: 10.1109/TSMCB.2004.831151. URL http://ieeexplore.ieee.org/lpdocs/epic03/wrapper.htm?arnumber=1315762.

Heeny S.H. Yuen. Swimming Speeds of Yellowfin and Skipjack Tuna. *Transactions of the American Fisheries Society*, 95(2):203–209, apr 1966. ISSN 0002-8487. doi: 10.1577/1548-8659(1966)95[203:SSOYAS]2.0.CO;2. URL http://www.tandfonline.com/doi/abs/10.1577/1548-8659{%}281966{%}2995{%}5B203{%}3ASSOYAS{%}5D2.0.CO{%}3B2.

Mohamed Y. Zakaria, David W. Allen, Craig A. Woolsey, and Muhammad R. Hajj. Lift and Drag of Flapping Membrane Wings at High Angles of Attack. In *34th AIAA Applied Aerodynamics Conference*, Reston, Virginia, jun 2016. American Institute of Aeronautics and Astronautics. ISBN 978-1-62410-437-4. doi: 10.2514/6.2016-3554. URL http://arc.aiaa.org/doi/10.2514/6.2016-3554.

Appendix A

Proofs

A.1 Proof of Equation (2.7)

The following sections contain proofs for the simplifications of the waveform shape parameters. These proofs are mostly straightforward calculus and algebraic manipulation. One useful fact is that the trigonometric functions in the definition of a Fourier series form an orthogonal basis. Thus, the following identities hold: If $n_i, n_j \in \mathbb{N}_+$[a], then

$$\int_0^T \cos(n_i \omega t)\cos(n_j \omega t)\,dt = \int_0^T \sin(n_i \omega t)\sin(n_j \omega t)\,dt = \begin{cases} 0 & \text{if } n_i \neq n_j \\ \frac{\pi}{\omega} & \text{if } n_i = n_j \end{cases} \tag{A.1}$$

and

$$\int_0^T \cos(n_i \omega t)\sin(n_j \omega t)\,dt = 0 \quad \forall n_i, n_j \in \mathbb{N}_+ \tag{A.2}$$

These proofs are presented with minimal commentary, as most intermediate steps are presented.

A.1.1 κ_i

$$\begin{aligned} \kappa_i =& \frac{1}{T}\int_0^T \int_0^t v_i(\tau)\,d\tau dt \\ =& \frac{1}{T}\int_0^T \int_0^t \omega \sum_{n=1}^{l} \left(a_{i,n}\cos(\omega n \tau) + b_{i,n}\sin(\omega n \tau)\right) d\tau dt \end{aligned}$$

[a] I.e. the set of natural numbers (which are positive by definition)

Since $\omega/T = 2\pi/T^2$,

$$\begin{aligned}
\kappa_i =& \frac{2\pi}{T^2}\int_0^T \int_0^t \sum_{n=1}^{l} \left(a_{i,n}\cos\left(\omega n\tau\right) + b_{i,n}\sin\left(\omega n\tau\right)\right) d\tau dt \\
=& \frac{2\pi}{T^2}\sum_{n=1}^{l}\left(a_{i,n} \underbrace{\int_0^T \int_0^t \cos\left(\omega n\tau\right) d\tau dt}_{=0} + b_{i,n} \underbrace{\int_0^T \int_0^t \sin\left(\omega n\tau\right) d\tau dt}_{=\frac{T^2}{2\pi n}} \right)
\end{aligned}$$

Thus

$$\kappa_i = \sum_{n=1}^{l} \frac{b_{i,n}}{n}$$

A.1.2 λ_{ij}

$$\begin{aligned}
\lambda_{ij} =& \frac{1}{T}\int_0^T \left(\int_0^t v_i(s_i) ds_i\right)\left(\int_0^t v_j(s_j) ds_j\right) dt \\
=& \frac{1}{T}\int_0^T \left(\int_0^t \omega \sum_{n=1}^{l} a_{i,n}\cos\left(\omega n s_i\right) + b_{i,n}\sin\left(\omega n s_i\right) ds_i\right) \\
& * \left(\int_0^t \omega \sum_{n=1}^{l} a_{j,n}\cos\left(\omega n s_j\right) + b_{j,n}\sin\left(\omega n s_j\right) ds_j\right) dt \\
=& \frac{\omega^2}{T}\int_0^T \left(\sum_{n=1}^{l}\left(\int_0^t a_{i,n}\cos\left(\omega n s_i\right)\right) ds_i + \sum_{n=1}^{l}\left(\int_0^t b_{i,n}\sin\left(\omega n s_i\right)\right) ds_i\right) \\
& * \left(\sum_{n=1}^{l}\left(\int_0^t a_{j,n}\cos\left(\omega n s_j\right)\right) ds_j + \sum_{n=1}^{l}\left(\int_0^t b_{j,n}\sin\left(\omega n s_j\right)\right) ds_j\right) dt \\
=& \frac{\omega^2}{T}\int_0^T \left(\sum_{n=1}^{l}\left(\frac{a_{i,n}}{\omega n}\sin\left(\omega n t\right) + \frac{b_{i,n}}{\omega n} - \frac{b_{i,n}}{\omega n}\cos\left(\omega n t\right)\right)\right) \\
& * \left(\sum_{n=1}^{l}\left(\frac{a_{j,n}}{\omega n}\sin\left(\omega n t\right) + \frac{b_{j,n}}{\omega n} - \frac{b_{j,n}}{\omega n}\cos\left(\omega n t\right)\right)\right) dt \\
=& \frac{1}{T}\int_0^T \left(\sum_{n_i=1}^{l}\left(\frac{a_{i,n_i}}{n_i}\sin\left(\omega n_i t\right) + \frac{b_{i,n_i}}{n_i} - \frac{b_{i,n_i}}{n_i}\cos\left(\omega n_i t\right)\right)\right) \\
& * \left(\sum_{n_j=1}^{l}\left(\frac{a_{j,n_j}}{n_j}\sin\left(\omega n_j t\right) + \frac{b_{j,n_j}}{n_j} - \frac{b_{j,n_j}}{n_j}\cos\left(\omega n_j t\right)\right)\right) dt
\end{aligned}$$

This can be expanded to

$$\lambda_{ij} = \frac{1}{T}\int_0^T \sum_{n_i,n_j=1}^{l} \left(\frac{a_{i,n_i}a_{j,n_j}}{n_in_j}\sin(\omega n_i t)\sin(\omega n_j t) + \frac{a_{i,n_i}b_{j,n_j}}{n_in_j}\sin(\omega n_i t) - \frac{a_{i,n_i}b_{j,n_j}}{n_in_j}\sin(\omega n_i t)\cos(\omega n_j t) \right.$$
$$+ \frac{b_{i,n_i}a_{j,n_j}}{n_in_j}\cos(\omega n_i t)\sin(\omega n_j t) + \frac{b_{i,n_i}b_{j,n_j}}{n_in_j}\cos(\omega n_i t) - \frac{b_{i,n_i}b_{j,n_j}}{n_in_j}\cos(\omega n_i t)\cos(\omega n_j t)$$
$$\left. + \frac{b_{i,n_i}a_{j,n_j}}{n_in_j}\sin(\omega n_j t) + \frac{b_{i,n_i}b_{j,n_j}}{n_in_j} - \frac{b_{i,n_i}b_{j,n_j}}{n_in_j}\cos(\omega n_j t) \right) dt$$

Switching the order of integration and summation[b] and applying the zero properties in equations (A.1) and (A.2) yields

$$\lambda_{ij} = \frac{1}{2}\sum_{n=1}^{l}\left(\frac{1}{n^2}\left(a_{i,n}a_{j,n} + b_{i,n}b_{j,n}\right)\right) + \sum_{n_i,n_j=1}^{l}\left(\frac{b_{i,n_i}b_{j,n_j}}{n_in_j}\right) \tag{A.3}$$

A.1.3 μ_{ij}

Notice that

$$\kappa_i\kappa_j = \sum_{n_i,n_j=1}^{l}\left(\frac{b_{i,n_i}b_{j,n_j}}{n_in_j}\right)$$

Thus,

$$\lambda_{ij} - \kappa_i\kappa_j = \frac{1}{2}\sum_{n=1}^{l}\left(\frac{1}{n^2}\left(a_{i,n}a_{j,n} + b_{i,n}b_{j,n}\right)\right)$$

and therefore

$$\mu_{ij} = \frac{1}{2}\left(\lambda_{ij} - \kappa_i\kappa_j\right) = \frac{1}{4}\sum_{n=1}^{l}\left(\frac{1}{n^2}\left(a_{i,n}a_{j,n} + b_{i,n}b_{j,n}\right)\right) \tag{A.4}$$

[b] This is valid because integration distributes over addition.

Appendix B

Lengthy Expressions

This appendix contains expressions that, although important, are too lengthy to include in the body of the text.

B.1 Multi-link Fish Model

B.1.1 Mass Matrix

The elements of $\boldsymbol{M}_{\mathbf{r}}$[a] can be found as follows.

$$m_{\mathbf{r},1,1} = m_{\mathbf{r},2,2} = m_{\mathrm{b}} + \sum_{i=1}^{L} m_{\mathrm{p},i} + m_{\mathrm{f},i}$$

$$m_{\mathbf{r},1,2} = 0$$

For find the remaining elements of the mass matrices, a slight change of notation is convenient. Rather than separately counting the peduncles and fins, all of the links will be counted sequentially. For example, the body relative angles $\phi_{\mathrm{p},1}$, $\phi_{\mathrm{f},1}$, and $\phi_{\mathrm{p},2}$ are now denoted ϕ_1, ϕ_2, and ϕ_3, respectively. The same notation will be used for the masses and lengths of the various peduncles and fins. Notice that the peduncles will be denoted by odd integers and the fins will be denoted by even integers.

$$m_{\mathbf{r},1,3} = \frac{m_{\mathrm{b}} l_{\mathrm{b}}}{2} \sin\left(\theta_{\mathrm{b}}\right) + \sum_{i=1}^{2L} m_i \left(l_{\mathrm{b}} \sin\left(\theta_{\mathrm{b}}\right) + \frac{l_i}{2} \sin\left(\phi_i + \theta_{\mathrm{b}}\right) + \sum_{j=1}^{i-1} l_j \sin\left(\phi_j + \theta_{\mathrm{b}}\right) \right)$$

$$m_{\mathbf{r},2,3} = -\frac{m_{\mathrm{b}} l_{\mathrm{b}}}{2} \cos\left(\theta_{\mathrm{b}}\right) - \sum_{i=1}^{2L} m_i \left(l_{\mathrm{b}} \cos\left(\theta_{\mathrm{b}}\right) + \frac{l_i}{2} \cos\left(\phi_i + \theta_{\mathrm{b}}\right) + \sum_{j=1}^{i-1} l_j \cos\left(\phi_j + \theta_{\mathrm{b}}\right) \right)$$

[a] The element in the ith row and jth column of $\boldsymbol{M}_{\mathbf{r}}$ is $m_{\mathbf{r},i,j}$. This notations also holds for $\boldsymbol{M}_{\mathbf{rs}}$ and $\boldsymbol{M}_{\mathbf{s}}$.

$$\begin{aligned} m_{\mathbf{r},3,3} =& I_{\mathrm{b}} + \left(\sum_{i=1}^{2L} I_i\right) + l_b \left[\frac{l_{\mathrm{b}} m_{\mathrm{b}}}{4} + \sum_{i=1}^{2L} m_i \left(l_{\mathrm{b}} + l_i \cos\left(\phi_i\right) + 2\sum_{j=1}^{i-1} l_j \cos\left(\phi_j\right)\right)\right] \\ &+ \left(\sum_{i=1}^{2L} l_i \left[\frac{l_i m_i}{4} + \sum_{j=i+1}^{2L} m_j \left(l_i + l_j \cos\left(\phi_j - \phi_i\right) + 2\sum_{k=i+1}^{j-1} l_k \cos\left(\phi_k - \phi_i\right)\right)\right]\right) \end{aligned}$$

Recall that $\boldsymbol{M}_{\mathbf{s}}$ is in $\mathbb{R}^{2L\times 2L}$. The values of the elements of $\boldsymbol{M}_{\mathbf{s}}$ depend on the value L. The diagonal elements can be determined using

$$m_{\mathbf{s},i,i} = I_i + \frac{m_i l_i^2}{4} + l_i^2 \sum_{j=i+1}^{2L} m_j$$

if $i = j$ and

$$m_{\mathbf{s},i,j} = \frac{l_i l_j}{2} \cos\left(\phi_i - \phi_j\right) \left(m_j + 2\sum_{k=j+1}^{2L} m_k\right)$$

if $i < j$. Notice that, since $M_{\mathbf{s}}$ is symmetric, under the assumption that $i < j$, which is equivalent to saying $m_{\mathbf{s},i,j}$ is an upper triangular element of $M_{\mathbf{s}}$, all of the elements of $M_{\mathbf{s}}$ will be defined. That is, if one desires to the value of an element where $j < i$, simply switch the values of i and j, and use the expression as normal.

The last sub-matrix is $\boldsymbol{M}_{\mathbf{rs}}$. Recall that $\boldsymbol{M}_{\mathbf{rs}} \in \mathbb{R}^{3\times 2L}$. The elements of $\boldsymbol{M}_{\mathbf{rs}}$ can be expressed using the following expressions.

$$m_{\mathbf{rs},1,i} = \frac{l_i}{2} \sin\left(\phi_i + \theta_{\mathrm{b}}\right) \left(m_i + 2\sum_{j=i+1}^{2L} m_j\right)$$

$$m_{\mathbf{rs},2,i} = -\frac{l_i}{2} \cos\left(\phi_i + \theta_{\mathrm{b}}\right) \left(m_i + 2\sum_{j=i+1}^{2L} m_j\right)$$

$$\begin{aligned} m_{\mathbf{rs},3,i} =& I_i + \frac{m_i l_i}{2} \left(\frac{l_i}{2} + l_{\mathrm{b}} \cos\left(\phi_i\right) + \sum_{j=1}^{i-1} l_j \cos\left(\phi_j - \phi_i\right)\right) \\ &+ l_i \sum_{j=i+1}^{2L} m_j \left(l_b \cos\left(\phi_i\right) + \frac{l_j}{2} \cos\left(\phi_j - \phi_i\right) + \sum_{k=1}^{j-1} l_k \cos\left(\phi_k - \phi_i\right)\right) \end{aligned}$$

B.1.2 Expressions for $c^k_{i,j}$

First, notice that $c^k_{1,1} = c^k_{2,2} = 0$ for all k. The remaining expressions are

$$c^1_{3,3} = -\frac{1}{2}\left(l_\mathrm{b}\cos\left(\theta_\mathrm{b}\right)\left(m_\mathrm{b} + 2\sum_{i=1}^{2L} m_i\right) + \sum_{i=1}^{2L} l_i\cos\left(\phi_i + \theta_\mathrm{b}\right)\left(m_i + 2\sum_{j=i+1}^{2L} m_j\right)\right)$$

$$c^2_{3,3} = -\frac{1}{2}\left(l_\mathrm{b}\sin\left(\theta_\mathrm{b}\right)\left(m_\mathrm{b} + 2\sum_{i=1}^{2L} m_i\right) + \sum_{i=1}^{2L} l_i\sin\left(\phi_i + \theta_\mathrm{b}\right)\left(m_i + 2\sum_{j=i+1}^{2L} m_j\right)\right)$$

$$c^3_{33} = 0$$

$$\begin{aligned} c^{3+i}_{3,3} =& \frac{l_i}{2}\left(m_i\left[\sum_{j=1}^{i-1} l_j\sin\left(\phi_j - \phi_i\right)\right] - l_\mathrm{b}\sin\left(\phi_i\right)\left(m_i + \sum_{j=i+1}^{2L} m_j\right)\right. \\ &\left. + \left[\sum_{j=i+1}^{2L} l_j\sin\left(\phi_i - \phi_j\right)\left(m_j + 2\sum_{k=j+1}^{2L} m_k\right)\right] - 2\left[\sum_{j=1}^{i-1} l_j\sin\left(\phi_j - \phi_i\right)\sum_{k=i+1}^{2L} m_k\right]\right) \end{aligned}$$

$$c^1_{3+i,3+i} = -\frac{l_i}{2}\cos\left(\phi_i + \theta_\mathrm{b}\right)\left(m_i + 2\sum_{j=i+1}^{2L} m_j\right)$$

$$c^2_{3+i,3+i} = -\frac{l_i}{2}\sin\left(\phi_i + \theta_\mathrm{b}\right)\left(m_i + 2\sum_{j=i+1}^{2L} m_j\right)$$

$$\begin{aligned} c^3_{3+i,3+i} =& \frac{l_i}{2}\left(\left[l_\mathrm{b}\sin\left(\phi_i\right)\left(m_i + 2\sum_{j=i+1}^{2L} m_j\right)\right] + \left[\sum_{j=i+1}^{2L} l_j\sin\left(\phi_i - \phi_j\right)\left(m_j + 2\sum_{k=j+1}^{2L} m_k\right)\right]\right. \\ &\left. - \left[\sum_{j=1}^{i-1} l_j\sin\left(\phi_j - \phi_i\right)\left(m_i + 2\sum_{k=i+1}^{2L} m_k\right)\right]\right) \end{aligned}$$

$$c^{3+j}_{3+i,3+i} = \begin{cases} -\frac{l_i l_j}{2}\sin\left(\phi_j - \phi_i\right)\left(m_i + 2\sum_{k=i+1}^{2L} m_k\right) & \text{if } j < i \\ \frac{l_i l_j}{2}\sin\left(\phi_i - \phi_j\right)\left(m_j + 2\sum_{k=j+1}^{2L} m_k\right) & \text{if } j > i \\ 0 & \text{if } i = j \end{cases}$$

For any i and j,

$$c^j_{1,i} = c^j_{2,i} = 0$$

$$c^1_{3,3+i} = -\, l_i \cos\left(\phi_i + \theta_b\right) \left(m_i + 2 \sum_{j=i+1}^{2L} m_j\right)$$

$$c^2_{3,3+i} = -\, l_i \sin\left(\phi_i + \theta_b\right) \left(m_i + 2 \sum_{j=i+1}^{2L} m_j\right)$$

$$\begin{aligned} c^3_{3,3+i} =& l_i \left(\left[l_{\mathrm{b}} \sin\left(\phi_i\right) \left(m_i + 2 \sum_{j=i+1}^{2L} m_j\right)\right] + \left[\sum_{j=i+1}^{2L} l_j \sin\left(\phi_i - \phi_j\right) \left(m_j + 2 \sum_{k=j+1}^{2L} m_k\right)\right] \right. \\ & \left. - \left[\sum_{j=1}^{i-1} l_j \sin\left(\phi_j - \phi_i\right) \left(m_i + 2 \sum_{k=i+1}^{2L} m_k\right)\right]\right) \end{aligned}$$

$$c^{3+j}_{3,3+i} = \begin{cases} -l_i l_j \sin\left(\phi_j - \phi_i\right) \left(m_i + 2 \sum_{k=i+1}^{2L} m_k\right) & \text{if } j < i \\ l_i l_j \sin\left(\phi_i - \phi_j\right) \left(m_j + 2 \sum_{k=j+1}^{2L} m_k\right) & \text{if } j > i \\ 0 & \text{if } i = j \end{cases}$$

Lastly, if $i \neq j$,

$$c^k_{3+i,3+j} = 0$$

Appendix C

Bioflyer Database

In addition to studying new modeling, optimization, and experimental techniques, a comprehensive and easily accessible database was developed. This database includes data from various sources. In addition, a text-based interface that utilizes MATLAB was developed that allows for easy access and editing the database. Additionally this interface can be used to create plots. These plots allow for the data to be sorted so that trends can be observed. These trends can be used to identify trends that form commonalities between diverse species as well trends that show difference between different flight strategies.

This database was constructed using data from several sources. These sources are [Jepsen et al., 1970], [Greenewalt, 1962], [Hazlehurst and Rayner, 1992], [Norberg, 1981], [Warham, 1977], and [Farney and Fleharty, 1969]. The primary source was [Greenewalt, 1962], which was a similarly motivated work, although its age makes it relatively difficult to access by modern standards. The other sources are included to improve the diversity of the data.

This database is stored as a MATLAB structure within a `*.mat` file. By itself, this data structure is not particularly accessible, so a custom text-based interface was developed. This interface allows the database to be accessed, edited, and appended. Furthermore, it provides a method for the generation of figures categorized by either class (e.g. Insecta or Aves) or "type" (e.g. dragonflies or hummingbirds). A few examples of such figures are included in Figures C.1, C.2, and C.3.

The user manual for this database is published as a Virginia Center for Autonomous Systems (VACAS) Technical Report [Allen, 2015]. If downloaded from the VACAS website, the database and interface are included as an attachment to the PDF. VACAS technical reports are available at `http://www.unmanned.vt.edu/discovery/reports.html`

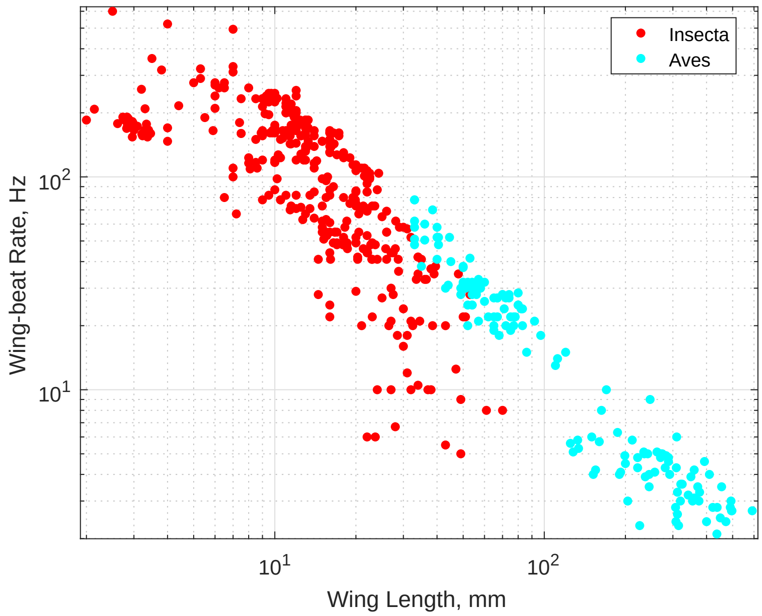

Figure C.1: Bioflyer database example. Wing beat rate vs wing length.

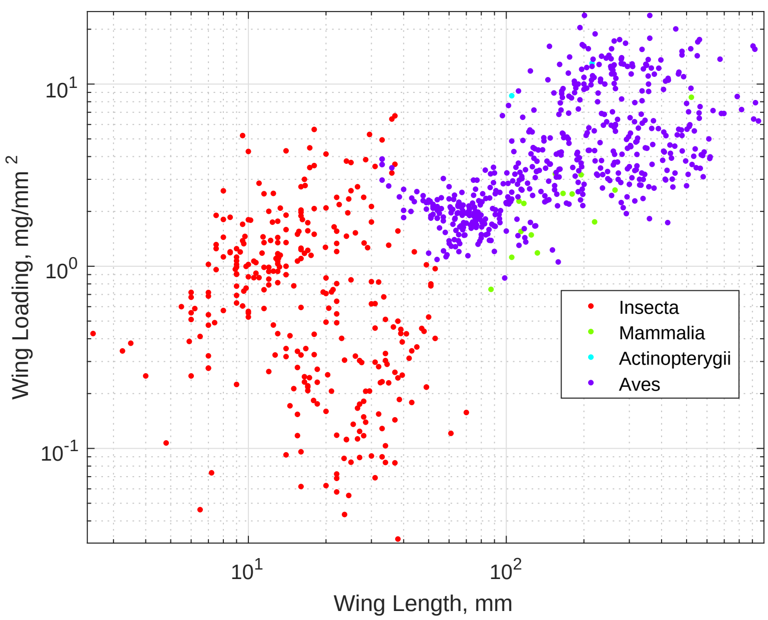

Figure C.2: Bioflyer database example. Wing loading vs wing length.

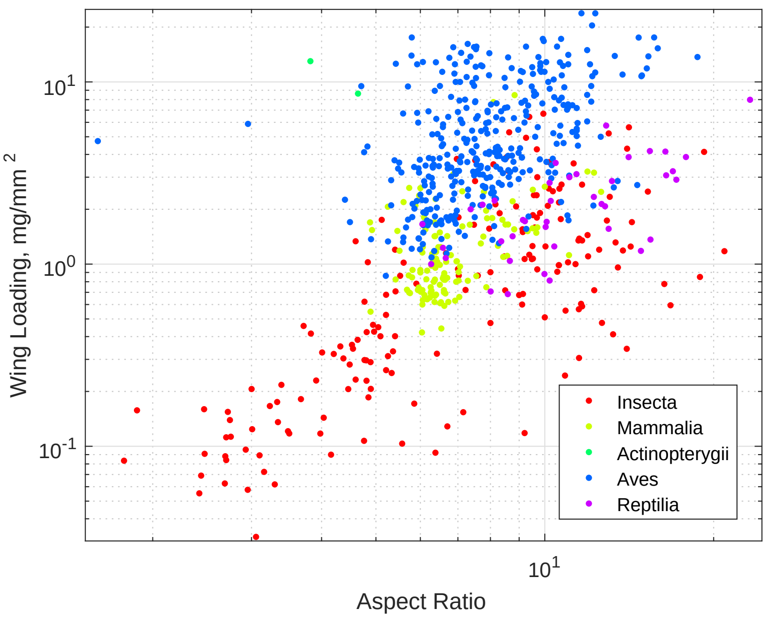

Figure C.3: Bioflyer database example. Wing loading vs aspect ratio.

Appendix D

Codes

This appendix contains a few selected MATLAB codes used in the gait an morphology optimization. These codes represent relatively high-level functions that call many other functions. These secondary functions are not included because they are excessively lengthy, especially in comparison to the amount of information they provide.

Section D.1 provides the code used for computing the equations of motion with the assumption of sinusoidal inputs. This function calls auto-generated MATLAB functions that actually compute the dynamics. These auto-generated functions were made by computing the system dynamics symbolically, then using the `matlabFunction` function to generate `*.m` files. This code also demonstrates the structures through which the parameters are passed to MATLAB, i.e. the `systemPARAMETERS`, `inputPARAMETERS`, `hydroPARAMETERS`, and `fluidPARAMETERS` structures.

Section D.2 shows how the system dynamics from Section D.1 are integrated to populate the grid. This shows how the grid points are defined and then compiled into a list. This list is then automatically distributed to multiple compute units using the `parfor` loop. The data is then saved to a `*.mat` for later use.

After the grid is populated, the next step is to find the contours of constant speed. More detail is required than what is provided by MATLAB's `contour` function, so a custom function was developed. This function is contained in Section D.3 and takes a set of grid points with values (speeds in this research) in order to generate contours.

The gait optimization code is provided in Section D.4. This takes the grid generated by the code in Section D.2 and, using the contour generation function contained in Section D.3, performs the optimization described in Chapter 4. This code also generates all of the appropriate plots.

D.1 System Dynamics with Chosen Gait

```
function dX = EOMfunc_StateOnly_SinusoidalInputs(X,t,...
    systemPARAMETERS,inputPARAMETERS,hydroPARAMETERS,fluidPARAMETERS)
% dX = EOMfunc_StateOnly_SinusoidalInputs(X,t,...
%     systemPARAMETERS,inputPARAMETERS,hydroPARAMETERS,fluidPARAMETERS)
%
% Computes the equations of motion (first order) of the state dynamics
% using sinusoidal inputs.
%
% Inputs:
%   X                          [r;dr] state position and velocity
%   t                          current time
%   systemPARAMETERS.L         number of fins
%                   .AM        Added Mass (0/1)
%                   .DW        Downwash (0/1)
%                   .ls        Lengths of links
%                   .ms        Masses of links
%                   .Is        Inertias of links
%   inputPARAMETERS.phibars    Vector of Mean Stroke Angles
%                  .phi0s      Vector of stroke amplitudes
%                  .Omega      Stroke Frequency
%                  .psis       Phase Shifts
%   hydroPARAMETERS.CLs        Lift Coefficients
%                  .CDs        Drag Coefficients
%                  .CDlins     Linear Drag Coefficients
%                  .CGammas    Circulation Coefficients
%                  .bds        Rotational Damping Coefficients
%   fluidPARAMETERS.rho        Density of fluid
%                  .vinf       Fluid Flow Velocity (typically [0;0;0])
%
% Written By:
%   David William Allen
%   8 April 2016
%   davidallen@vt.edu

%% Compute Inputs (and phis)
% Correct so psi_phip1=0
```

```
inputPARAMETERS.psis=inputPARAMETERS.psis-inputPARAMETERS.psis(1);

% Compute the "phased time" of the input
phasedTimes=inputPARAMETERS.Omega*t+inputPARAMETERS.psis;

% Generate phis, phidots, and phiddots
phis = inputPARAMETERS.phibars...
    -(inputPARAMETERS.phi0s./inputPARAMETERS.Omega).*cos(phasedTimes);

dphis = inputPARAMETERS.phi0s.*sin(phasedTimes);

u = (inputPARAMETERS.phi0s.*inputPARAMETERS.Omega).*cos(phasedTimes);

%% Get Generalized Coordinates
q=[X(1:3);phis];
qd=[X(4:6);dphis];

%% Compute Dynamics
[rdd,~,~]=stateDynamics(q,qd,u,...
    systemPARAMETERS.ls,systemPARAMETERS.ms,systemPARAMETERS.Is,...
    hydroPARAMETERS.CLs,hydroPARAMETERS.CDs,hydroPARAMETERS.CDlins,...
    hydroPARAMETERS.CGammas,hydroPARAMETERS.bds,...
    fluidPARAMETERS.vinf,fluidPARAMETERS.rho,...
    systemPARAMETERS.L,systemPARAMETERS.DW,systemPARAMETERS.AM);

%% Return First Order Acceleration dX
dX=[X(4:6);rdd];

end
```

D.2 Grid Generation

```
% run_Simulation
clearvars
close all
clc

currentFolder = pwd;
```

```
addpath(genpath([currentFolder,'/Functions']))

%% Set Parameters
systemPARAMETERS.L=1;
systemPARAMETERS.AM=1;
systemPARAMETERS.DW=1;

systemPARAMETERS.ls=[0.45;0.15;0.15];
systemPARAMETERS.ms=[5;0.75;1];
systemPARAMETERS.Is=[844;14;14]/(100^2);

inputPARAMETERS.phibars=[0;0]*pi/180;
% inputPARAMETERS.Omega=12*pi;
% inputPARAMETERS.phi0s=[30;30]*(pi/180)*inputPARAMETERS.Omega;
inputPARAMETERS.psis=[0;90]*pi/180;

hydroPARAMETERS.CLs=[1;6];
hydroPARAMETERS.CDs=[3;3];
hydroPARAMETERS.CDlins=[4;1];
hydroPARAMETERS.CGammas=[1;1];
hydroPARAMETERS.bds=[0;0;0];

fluidPARAMETERS.rho=1000;
fluidPARAMETERS.vinf=[0;0;0];

%% Get Initial Conditions
X0=zeros(6,1);X0(3)=0;X0(4)=0.3;

%% Create Data for Loops
gridResolution=100;
Omegas=linspace(1*(2*pi),40*(2*pi),gridResolution); % Range from Nature, See DOI:10.1577/1548-8659(1966)95[203:SSOYAS]2.0.CO;2
phi0s=linspace(5,55,gridResolution); % Both Amplitudes are the same

%% Create Cell for data

steps=length(Omegas)*length(phi0s);
stepCount=0;

%% Loop Through Data
phibars=inputPARAMETERS.phibars;
```

```
psis=inputPARAMETERS.psis;

% simDATA=cell(length(Omegas),length(phi0s));

testGaits=zeros(length(Omegas)*length(phi0s),2);

for ii=1:length(Omegas)
    for kk=1:length(phi0s)
        stepCount=stepCount+1;
        %           disp(['Run ',num2str(stepCount),' of ' num2str(steps) ,'..............'])

        testGaits(stepCount,:)=[Omegas(ii),phi0s(kk)];
    end
end

testGaits_Omega=testGaits(:,1);
testGaits_phi0=testGaits(:,2);

fprintf('\n\nGrid Generation Progress\n')
parfor_progress(length(testGaits));

parfor ii=1:length(testGaits)
    parfor_progress;

    TEMPinputPARAMETERS=compile_inputPARAMETERS(...
        phibars,...
        psis,...
        testGaits_Omega(ii),...
        [testGaits_phi0(ii);testGaits_phi0(ii)]*(pi/180)*testGaits_Omega(ii));


    %% Establish Functions
    odeFUNC=@(t,X)EOMfunc_StateOnly_SinusoidalInputs(X,t,...
        systemPARAMETERS,TEMPinputPARAMETERS,hydroPARAMETERS,fluidPARAMETERS);

    %% Simulate

    tspan=linspace(0,30,3000);
    [TOUT,XOUT]=ode45(odeFUNC,tspan,X0);
```

```
    %% Neglect First Second
    simDATA{ii}.meanSpeed=...
        mean(sqrt(XOUT(1000:end,4).^2 + XOUT(1000:end,5).^2));
    simDATA{ii}.meanAngSpeed=...
        mean(XOUT(1000:end,6));

    %% Store Rest of Data
    simDATA{ii}.inputPARAMETERS=TEMPinputPARAMETERS;
    simDATA{ii}.systemPARAMETERS=systemPARAMETERS;
    simDATA{ii}.hydroPARAMETERS=hydroPARAMETERS;
    simDATA{ii}.fluidPARAMETERS=fluidPARAMETERS;

end
parfor_progress(0);

save('StraightSwimData_wDW_nAM_Parallel_gridRes100_25Apr16','simDATA','Omegas','phi0s')
```

D.3 Contour Generation

```
function [Xvals,Yvals]=getContour(X,Y,V,cval,numSamples)
% [Xvals,Yvals]=getContour(X,Y,V,cval,numSamp)
%
% Computes the X and Y coordinates that correspond to the contour line cval
% with respect to the data X, Y, V. That is, Xvals and Yvals are vectors of
% values where V=cval. The data is interpolated between points. The data is
% sampled with numSamples in the X data. Xvals and Yvals are arbitrary
% lengths.

if size(X,2)~=1
    X=X';
end

if size(Y,2)~=1
    Y=Y';
end

```

```
if size(V,2)~=1
    V=V';
end

Xsamps=linspace(min(X),max(X),numSamples);
Ysamps=linspace(min(Y),max(Y),numSamples);

Xbnd=[min(X),max(X)];
Ybnd=[min(Y),max(Y)];

[Xsamps_grid,Ysamps_grid]=meshgrid(Xsamps,Ysamps);
% Vsamps_grid=griddata(X,Y,V,Xsamps_grid,Ysamps_grid)

% F=scatteredInterpolant(X,Y,V);
F=scatteredInterpolant(X,Y,V,'linear');

Vsamps_grid=F(Xsamps_grid,Ysamps_grid);


Xvals=[];
Yvals=[];

for ii=1:length(Xsamps)

    testfunc=@(y)(interp1(Ysamps_grid(:,ii),Vsamps_grid(:,ii),y)-
       cval);

    try
        Xval=Xsamps(ii);
        [Yval,~,~,~]=fzero(testfunc,Ybnd);

        Xvals(end+1)=Xval;
        Yvals(end+1)=Yval;
    catch
        % Continue if error occurs. This is usually caused if the
           point
        % cannot be found;
    end

end

Xvals=avgSmoothing(Xvals,3,0);
```

```
Yvals=avgSmoothing(Yvals,3,0);
```

D.4 Gait Optimization

```
% analyze_straightSwimData_18Apr16

clearvars;close all;clc;

betaf=0.5;
gammas=[0,1,5,10,20,50,75,100];
speedContourLines=[1,2,5,10,15,20];
gridRes=50;

numSamples=500; % How fine to make contour interpolation meshes

smoothingPasses=200;

fontSize=16;

%% Load Data
switch gridRes
    case 50
        switch betaf
            case 0.1
                load('
                   StraightSwimData_betaf10_gridRes50_13May16_1800
                   ')
            case 0.2
                load('
                   StraightSwimData_betaf20_gridRes50_13May16_2025
                   ')
            case 0.3
                load('
                   StraightSwimData_betaf30_gridRes50_13May16_2322
                   ')
            case 0.4
                load('
                   StraightSwimData_betaf40_gridRes50_14May16_0305
                   ')
            case 0.5
                load('
                   StraightSwimData_betaf50_gridRes50_14May16_0702
```

```
')
            case 0.6
                load('StraightSwimData_betaf60_gridRes50_14May16_1139')
            case 0.7
                load('StraightSwimData_betaf70_gridRes50_14May16_1649')
            otherwise
                error('Data not present')
        end
    case 75
        switch betaf
            case 0.3
                load('StraightSwimData_betaf30_gridRes75_11May16_1515')
            case 0.4
                load('StraightSwimData_betaf40_gridRes75_11May16_1845')
            case 0.5
                load('StraightSwimData_betaf50_gridRes75_11May16_2229')
            case 0.6
                load('StraightSwimData_betaf60_gridRes75_12May16_0227')
            case 0.7
                load('StraightSwimData_betaf70_gridRes75_12May16_0652')
            otherwise
                error('Data not present')
        end
    case 100
        switch betaf
            case 0.1
                load('StraightSwimData_betaf10_gridRes100_04May16_0508
```

```
')
            case 0.2
                load('StraightSwimData_betaf20_gridRes100_04May16_1911')
            case 0.3
                load('StraightSwimData_betaf30_gridRes100_05May16_0813')
            case 0.4
                load('StraightSwimData_betaf40_gridRes100_03May16_2113')
            case 0.5
                load('StraightSwimData_betaf50_gridRes100_04May16_2146')
            case 0.6
                load('StraightSwimData_betaf60_gridRes100_05May16_1834')
            case 0.7
                load('StraightSwimData_betaf70_gridRes100_05May16_0345')
            otherwise
                error('Data not present')
        end
    otherwise
        error('Data not present')
end


%% extract Data
script_extractAndSort_wDW_wAM_noSort
getYuenData


%% Make a New Color Space

temp=linspace(0.2,1,4);
count=0;
```

```
for ii=1:length(temp)
    for jj=1:length(temp)
        for kk=1:length(temp)
            count=count+1;
            colors(count,:)=[temp(ii),temp(jj),temp(kk)];
        end
    end
end

%% Define Contour Lines
numSpeedContourLines=length(speedContourLines);

normCostContourLines=[0.5,1,2,5,10,15:10:100]./100;
numNormCostContourLines=length(normCostContourLines);

speedContourlegendEntries=cell(numSpeedContourLines,1);
for ii=1:numSpeedContourLines
    speedContourlegendEntries{ii}=['Speed=',num2str(speedContourLines(ii)),' BL/s'];
end

normCostContourlegendEntries=cell(numNormCostContourLines,1);
for ii=1:numNormCostContourLines
    normCostContourlegendEntries{ii}=...
        ['Normalized Cost=',num2str(normCostContourLines(ii)*100),'\%'];
end

%% Speed Contours


axisLimits=[min(DATAvecs.wDW.wAM.strokeAmp_deg)+1,...
    max(DATAvecs.wDW.wAM.strokeAmp_deg)-1,...
    min(DATAvecs.wDW.wAM.Omegas./(2*pi)),...
    max(DATAvecs.wDW.wAM.Omegas./(2*pi))-1];

figure
customContour(...
    DATAvecs.wDW.wAM.strokeAmp_deg,...
    DATAvecs.wDW.wAM.Omegas./(2*pi),...
    DATAvecs.wDW.wAM.meanSpeed_BL,...
    speedContourLines,...
```

```
    numSamples,...
    '-',...
    getColorSeries(numSpeedContourLines,'k'));
hold on
grid on
h_legend=legend(speedContourlegendEntries{:});
set(h_legend,'Interpreter','latex')
set(h_legend,'Location','EastOutside')
set(h_legend,'FontSize',fontSize)
axis(axisLimits)
xlabel('Stroke Amplitude, degrees','Interpreter','latex','FontSize
    ',fontSize)
ylabel('Tail Beat Rate, Hz','Interpreter','latex','FontSize',
    fontSize)


%% Get Optimal Trend

% Resample Speed Contour Lines
% TEMPFUNC=@(index)interp1(1:numSpeedContourLines,
    speedContourLines,index);
% speedContourLines_resampled=...
%     TEMPFUNC(linspace(1,numSpeedContourLines,...
%     3*numSpeedContourLines));
speedContourLines_resampled=speedContourLines;

% Do the Optimization
for ii=1:length(gammas)
    [optStrokeAmp_degs{ii},optOmegas{ii},optSpeeds{ii},...
        optCosts{ii},optEnergyCosts{ii},optSLCosts{ii}]=...
        getOptimalGaitOnSpeedContour(...
        DATAvecs.wDW.wAM.strokeAmp_deg,...
        DATAvecs.wDW.wAM.Omegas,...
        DATAvecs.wDW.wAM.meanSpeed_BL,...
        speedContourLines_resampled,...
        gammas(ii),...
        k1,...
        DATAvecs.wDW.wAM.systemPARAMETERS{1}.ls,...
        DATAvecs.wDW.wAM.inputPARAMETERS{1}.psis,...
        numSamples,smoothingPasses);
end

```

```
%% Norm Cost Contours (Overlaid on Speed) as separate figures with
    optimal line
h_figure=figure;
for ii=1:length(gammas)
    subplot(2,floor(0.5+(length(gammas)/2)),ii)
    customContour(...
        DATAvecs.wDW.wAM.strokeAmp_deg,...
        DATAvecs.wDW.wAM.Omegas./(2*pi),...
        DATAvecs.wDW.wAM.meanSpeed_BL,...
        speedContourLines,...
        numSamples,...
        '-',...
        getColorSeries(numSpeedContourLines,'r'));
    customContour(...
        DATAvecs.wDW.wAM.strokeAmp_deg,...
        DATAvecs.wDW.wAM.Omegas./(2*pi),...
        DATAvecs.wDW.wAM.normCosts(:,ii),...
        normCostContourLines,...
        numSamples,...
        '--',...
        getColorSeries(numNormCostContourLines,'b'));
    hold on
    grid on
    plot(optStrokeAmp_degs{ii},optOmegas{ii}./(2*pi),'kx-')
    axis(axisLimits)
    xlabel('Stroke Amplitude, degrees',...
        'Interpreter','latex','FontSize',fontSize)
    ylabel('Tail Beat Rate, Hz',...
        'Interpreter','latex','FontSize',fontSize)
    title(['$\gamma=',num2str(gammas(ii)),'$'],...
        'Interpreter','latex','FontSize',fontSize)
end
h_figure.Position=[10 50 1500 750];

%% Plot Optimal Curves
gammalegendEntries=cell(length(gammas),1);

TEMP=linspace(0,0.9,ceil(length(gammas)^(1/3)));
count=0;
for ii=1:length(TEMP)
    for jj=1:length(TEMP)
```

```
            for kk=1:length(TEMP)
                count=count+1;
                gammaColors(count,:)=[TEMP(ii),TEMP(jj),TEMP(kk)];
            end
        end
end

h_figure=figure;
customContour(...
    DATAvecs.wDW.wAM.strokeAmp_deg,...
    DATAvecs.wDW.wAM.Omegas./(2*pi),...
    DATAvecs.wDW.wAM.meanSpeed_BL,...
    speedContourLines,...
    numSamples,...
    '-',...
    getColorSeries(numSpeedContourLines,'r'));
hold all
for ii=1:length(gammas)
    gammalegendEntries{ii}=['$\gamma=',num2str(gammas(ii)),'$'];
    plot(optStrokeAmp_degs{ii},optOmegas{ii}./(2*pi),'x-','Color',
       gammaColors(ii,:))
end
h_legend=legend(...
    {speedContourlegendEntries{:},...
    gammalegendEntries{:}});
set(h_legend,'Interpreter','latex')
set(h_legend,'Location','EastOutside')
set(h_legend,'FontSize',fontSize)
axis(axisLimits)
xlabel('Stroke Amplitude, degrees',...
    'Interpreter','latex','FontSize',fontSize)
ylabel('Tail Beat Rate, Hz',...
    'Interpreter','latex','FontSize',fontSize)


%% Plot Optimal Curves

figure
hold all
grid on
for ii=1:length(gammas)
    plot(optSpeeds{ii},optCosts{ii},'Color',gammaColors(ii,:))
```

```
end
xlabel('Speed, BL/s',...
    'Interpreter','latex','FontSize',fontSize)
ylabel('Input Energy + $\gamma$ Stroke Length',...
    'Interpreter','latex','FontSize',fontSize)
h_legend=legend(...
    gammalegendEntries{:});
set(h_legend,'Interpreter','latex')
set(h_legend,'Location','Best')
set(h_legend,'FontSize',fontSize)

figure
hold all
grid on
for ii=1:length(gammas)
    plot(optSpeeds{ii},optCosts{ii}./max(optCosts{ii}),'Color',
        gammaColors(ii,:))
end
xlabel('Speed, BL/s',...
    'Interpreter','latex','FontSize',fontSize)
ylabel('Normalized Cost',...
    'Interpreter','latex','FontSize',fontSize)
% h_legend=legend(...
%     gammalegendEntries{:});
% set(h_legend,'Interpreter','latex')
% set(h_legend,'Location','EastOutside')
% set(h_legend,'FontSize',fontSize)

h_figure=figure;
hold all
grid on
for ii=1:length(gammas)
    plot(optSpeeds{ii},optOmegas{ii}./(2*pi),'Color',gammaColors(
        ii,:))
end
xlabel('Speed, BL/s',...
    'Interpreter','latex','FontSize',fontSize)
ylabel('Beat Rate, Hz',...
    'Interpreter','latex','FontSize',fontSize)
% axis([0,max(DATAvecs.wDW.wAM.Omegas)/(2*pi),0,max(
    speedContourLines)])
% h_legend=legend(...
```

```
%       gammalegendEntries{:});
% set(h_figure,'Position',[520 378 700 420])
%
% set(gca,'Position',[0.1300 0.1291 0.6221 0.7959])
%
% set(h_legend,'Interpreter','latex')
% set(h_legend,'Location','Best')
% set(h_legend,'FontSize',fontSize-2)
% set(h_legend,'Position',[0.7878 0.2269 0.1838 0.5114])


h_figure=figure;
hold all
grid on
for ii=1:length(gammas)
    plot(optOmegas{ii}./(2*pi),optSpeeds{ii},'Color',gammaColors(
        ii,:))
end
% plot(YuenDATA.freqs,YuenDATA.skipjack.points,'k--')
% plot(YuenDATA.freqs,YuenDATA.yellowfin.points,'k-.')
ylabel('Speed, BL/s',...
    'Interpreter','latex','FontSize',fontSize)
xlabel('Beat Rate, Hz',...
    'Interpreter','latex','FontSize',fontSize)
% axis([0,max(DATAvecs.wDW.wAM.Omegas)/(2*pi),0,max(
    speedContourLines)])
h_legend=legend(gammalegendEntries{:});

set(h_figure,'Position',[520 378 700 420])

set(gca,'Position',[0.1300 0.1291 0.6221 0.7959])

set(h_legend,'Interpreter','latex')
set(h_legend,'Location','Best')
set(h_legend,'FontSize',fontSize-2)
set(h_legend,'Position',[0.7878 0.2269 0.1838 0.5114])

figure
hold all
grid on
for ii=1:length(gammas)
    plot(optSpeeds{ii},optStrokeAmp_degs{ii},'Color',gammaColors(
```

```
        ii ,:))
end
xlabel('Speed, BL/s',...
    'Interpreter','latex','FontSize',fontSize)
ylabel('Stroke Amplitude, degrees',...
    'Interpreter','latex','FontSize',fontSize)
% h_legend=legend(...
%     gammalegendEntries{:});
% set(h_legend,'Interpreter','latex')
% set(h_legend,'Location','EastOutside')
% set(h_legend,'FontSize',fontSize)

figure
hold all
grid on
for ii=1:length(gammas)
    plot(optSpeeds{ii},(optStrokeAmp_degs{ii}*(pi/180)).*optOmegas
        {ii},'Color',gammaColors(ii,:))
end
xlabel('Speed, BL/s',...
    'Interpreter','latex','FontSize',fontSize)
ylabel('$\phi_{\mathrm{f},1,0}$, rad$^{2}$/s',...
    'Interpreter','latex','FontSize',fontSize)
axis([0,20,0,120])

for speedIter=1:length(speedContourLines)


    paretoFronts{speedIter}.Speed=speedContourLines(speedIter);

    paretoFrontLegendEntries{speedIter}=...
        [num2str(speedContourLines(speedIter)),' BL/s'];

    count=0;
    for ii=1:length(optCosts)
        count=count+1;

        if min((optSpeeds{ii}-speedContourLines(speedIter)).^2)==0

            [~,optStep]=min((optSpeeds{ii}-speedContourLines(
                speedIter)).^2);

```

```
            TEMP=optEnergyCosts{ii};
            try
                paretoFronts{optStep}.energyCosts(ii)=TEMP(optStep);
            end

            TEMP=optSLCosts{ii};
            try
                paretoFronts{optStep}.SLCosts(ii)=TEMP(optStep);
            end

            TEMP=optStrokeAmp_degs{ii};
            try
                paretoFronts{optStep}.strokeAmps(ii)=TEMP(optStep);
            end

            TEMP=optOmegas{ii};
            try
                paretoFronts{optStep}.Omegas(ii)=TEMP(optStep);
            end
        else
            count=count-1;
        end

    end
end

%% Plot Pareto Fronts

paretoFrontColors=getColorSeries(length(paretoFronts),'f');

figure
hold on
grid on
plot(sqrt(paretoFronts{1}.SLCosts)*100,paretoFronts{1}.energyCosts,'Color',paretoFrontColors{1})
plot(sqrt(paretoFronts{2}.SLCosts)*100,paretoFronts{2}.energyCosts,'Color',paretoFrontColors{2})
plot(sqrt(paretoFronts{3}.SLCosts)*100,paretoFronts{3}.energyCosts,'Color',paretoFrontColors{3})
plot(sqrt(paretoFronts{4}.SLCosts)*100,paretoFronts{4}.energyCosts
```

```
    ,'Color',paretoFrontColors{4})
plot(sqrt(paretoFronts{5}.SLCosts)*100,paretoFronts{5}.energyCosts
    ,'Color',paretoFrontColors{5})
plot(sqrt(paretoFronts{6}.SLCosts)*100,paretoFronts{6}.energyCosts
    ,'Color',paretoFrontColors{6})

set(gca,'XScale','log')
set(gca,'YScale','log')

set(gca,'XLim',[2,13])
set(gca,'YLim',[100,2e4])
set(gca,'YTick'
    ,[100,200,300,500,700,1000,2000,3000,5000,7000,10000,20000])

xlabel('Stroke Length, cm','interpreter','latex','FontSize',
    fontSize)
ylabel('Input Energy, rad/s$^{2}$','interpreter','latex','FontSize
    ',fontSize)

h_legend=legend(paretoFrontLegendEntries{:});
set(h_legend,'Interpreter','latex')
set(h_legend,'Location','Best')
set(h_legend,'FontSize',fontSize)

figure
hold on
grid on
plot(paretoFronts{1}.strokeAmps,paretoFronts{1}.Omegas/(2*pi),'
    Color',paretoFrontColors{1})
plot(paretoFronts{2}.strokeAmps,paretoFronts{2}.Omegas/(2*pi),'
    Color',paretoFrontColors{2})
plot(paretoFronts{3}.strokeAmps,paretoFronts{3}.Omegas/(2*pi),'
    Color',paretoFrontColors{3})
plot(paretoFronts{4}.strokeAmps,paretoFronts{4}.Omegas/(2*pi),'
    Color',paretoFrontColors{4})
plot(paretoFronts{5}.strokeAmps,paretoFronts{5}.Omegas/(2*pi),'
    Color',paretoFrontColors{5})
plot(paretoFronts{6}.strokeAmps,paretoFronts{6}.Omegas/(2*pi),'
    Color',paretoFrontColors{6})

set(gca,'XScale','log')
set(gca,'YScale','log')
```

```

set(gca,'XLim',[8,50])
set(gca,'YLim',[2,30])
set(gca,'YTick',[1,2,3,4,5,7,10,13,17,20,25])

xlabel('Stroke Amplitude, degrees','interpreter','latex','FontSize
    ',fontSize)
ylabel('Tail Beat Rate, Hz','interpreter','latex','FontSize',
    fontSize)

% h_legend=legend(paretoFrontLegendEntries{:});
% set(h_legend,'Interpreter','latex')
% set(h_legend,'Location','Best')
% set(h_legend,'FontSize',fontSize)

%% Strouhal Number and Advance Ratio

for ii=1:length(optSpeeds)
    optSt{ii}=(optOmegas{ii}./(2)).*sqrt(optSLCosts{ii})./optSpeeds
        {ii};
    optAdvRatio{ii}=optSpeeds{ii}./((optOmegas{ii}./(2*pi)).*sqrt(
        optSLCosts{ii}));
end

advRatioColors=getColorSeries(length(optAdvRatio),'f');

h_figure=figure;
hold on
grid on
for ii=1:length(optAdvRatio)
    plot(optSpeeds{ii},optSt{ii},'Color',advRatioColors{ii})
end

xlabel('Speed, BL/s','interpreter','latex','FontSize',fontSize)
ylabel('Strouhal Number, $St$','interpreter','latex','FontSize',
    fontSize)

h_legend=legend(gammalegendEntries{:});
set(h_legend,'Interpreter','latex')
set(h_legend,'Location','Best')
set(h_legend,'FontSize',fontSize)

```

```
%% Save Figures
savefigs('strightSwim_GaitOptOnly_Fig')

%% Save Optimal Gait DATA
% FILENAME=...
%       ['OptGaitData_betaf',num2str(betaf*100),...
%       '_gridRes',num2str(gridRes),...
%       '_',datestr(now,'ddmmmyy_HHMM')];
%
% save(FILENAME,'gammas','optCosts','optOmegas','optSpeeds','
    optStrokeAmp_degs')
```